Modelling SEP events: latitudinal and longitudinal dependence of the injection rate of shock-accelerated protons and their flux profiles

Rosa Rodríguez Gasén

UNIVERSITAT DE BARCELONA

DEPARTAMENT D'ASTRONOMIA I METEOROLOGIA

Modelling SEP events: latitudinal and longitudinal dependence of the injection rate of shock-accelerated protons and their flux profiles

Memòria presentada per
Rosa Rodríguez Gasén
per optar al grau de Doctora
per la Universitat de Barcelona

Barcelona, Maig 2011

PROGRAMA DE DOCTORAT
D'ASTRONOMIA I METEOROLOGIA

BIENNI 2004-2006

Memòria presentada per

Rosa Rodríguez Gasén

per optar al grau de Doctora
per la Universitat de Barcelona

Directors de la tesi
Dr. Blai Sanahuja Parera
Dra. Àngels Aran i Sensat

Als meus pares

i al meu tete

Contemplant l'Univers,
tenia una increïble sensació de
benestar,
com si la infinitat de l'Univers
mostrés la seva pròpia eternitat.

Verònica decideix morir, Paulo
Coelho

Agraïments - Acknowledgments

Everybody has a reason to begin again.

Long Walk Home,
Bruce Springsteen

Aquesta tesi s'ha realitzat al departament d'Astronomia i Meteorologia de la Universitat de Barcelona. Agraeixo al departament tots els recursos dels que m'he pogut beneficiar durant aquests anys. Mil i una gràcies als informàtics, Gaby i Jordi, i a la gent de secretaria, Montse, Rosa i JR (no sé que fariem sense vosaltres). A tots els membres del departament, gràcies.

Voldria expressar el meu agraïment a tota la gent del CESCA (CEntre de Supercomputació de CAtalunya), en especial a en David Tur, l'Alfred Gil i la Ingrid Bàrcena, pel vostre suport inestimable. Gràcies també a en David Vicente i tot l'equip de suport del MareNostrum (BSC, Barcelona Supercomputing Center).

I am grateful to the faculty of ESA (European Space Agency) and Dr. R. G. Marsden for the finantial support that made possible my visit to ESA/ESTEC. I acknowledge ASTROSIM (European Network for Computational Astrophysics) and the Solar Network SOLAIRE for having granted me with the necessary finantial support to be able to participate in many courses and schools. And I am also thankful to Prof. R. Müller-Mellin for providing the particle data from the Helios/E6 instrument, as well as to Dr. A. de Lucas and Prof. R. Schwenn for providing the Helios plasma and IMF data.

I am really thankful to Prof. S. Poedts, Dr. C. Jacobs and all the (present and past) members of the CPA. Thank you very much for giving to me the opportunity to work with you. I have learned a lot, not only from the professional point of view. My most sincere thanks to Prof. S. T. Wu and M. Wu for your unvaluable (almost parental) kindness. Así como al Prof. A. Viñas por las discusiones productivas y por el entusiasmo que me has transmitido. I am also very thankful to Prof. X. Feng and all the team of the State Key Laboratory of Space Weather for your hospilatity and kindness during my stay in Beijing. Especially to Dr. F. Shen, I would like to be able, some day, to take care of you as you did of me. Thank you so much for everything.

A tota la gent de l'ARTista i a la Laya en especial, per cuidar tant bé del meu estat físic i, sobretot, mental: "Mens sana, in corpore sano". I a en Marc i en Victor per "recuperar" els meus músculs i, amb això, la meva serenor.

Vull agraïr d'una manera molt sincera els bons moments viscuts amb els meus companys, no, companys no, amics del departament. Gràcies DAMeros: Laura, Maria, Sinue, Jordi, Javi M., Albert, Héctor, Pol, Adolfo, Josep Maria, Àlvaro, Víctor, Pere, Pau, Felipe, Nadia, Eva, Andreu(s)... I molt, molt especialment a la Gemma, en Javi (nene) i la Carme (us adoro!). Un milió de gràcies pel bon rotllo "departamental".

Vull donar les gràcies a tots els meus amics, pel vostre suport incondicional i la infinita paciència que heu tingut amb la "meva agenda" d'aquests darrers anys. Un record molt especial per a les meves nenes de Lleida, l'equip de les boines (fu!), toda la comunidad "solar" que he conocido a lo largo de estos años y con quien he compartido momentos que nunca olvidaré (Jorge, Juan y Pris, Samuel, Bart, Patrick, Manuel, Roberto, Pedro, Fátima, Aimilia, Pia, Andrés, Eva ...), los "habitantes" de Bruxelles (mil gracias a todos por hacerme sentir una más de vosotros a pesar de vivir a unos cuantos kilómetros de distáncia), la meva tus preferida (per les "nits d'estudi" durant la nostra època al Penya i tot el que ha vingut després), i finalment en Joe, pels dos anys i mig de glòria i triomf que hem compartit (oh le le, oh la la, ser del Barça és, el millor que hi ha!).

A la meva compi, Dra. Neus Àgueda. T'he trobat a faltar aquests dos anys que has estat "rondant món". Gràcies per tots els moments compartits i per ser el meu model a seguir.

A la Dra. Àngels Aran, co-directora d'aquesta tesi. Tú millor que ningú saps com ha anat tot i lo que ha costat portar-la a terme. He après i continuo aprenent tantíssimes coses treballant al teu costat! Et dec una infinitat de gràcies. De tot cor. Per tot.

Al Prof. Blai Sanahuja, artífex d'aquest treball. Gràcies per la teva constància, la teva paciència i per transmetre'm el teu entusiasme per aquest món. T'agraeixo molt sincerament la confiança que un dia vas decidir posar en mi i espero haver estat a l'altura. Milions de gràcies per tot.

Als meus pares, al meu tete i a en Frank. Jo sense vosaltres no sóc jo, ja ho sabeu. A tota la meva familia i a tots els meus que ja no hi són, especialment al meu padrí i als meus abuelos.

E in un modo speciale al Dr. Lapo Bettarini. Perche tutti e due sappiamo che questa tesi è anche tua. Grazie.

Nella vita,
quando ti trovi di fronte a una cosa
importante,
no significa che devi rinunciare a
tutte le altre.

Brida, Paulo Coelho

Contents

Resum de la tesi

El uso del saber
para aprender a vivir.

PLATÓN

Introducció

Els esdeveniments de partícules energètiques[1] solars (SEP, acrònim de Solar Energetic Particle) són augments del flux de partícules en l'entorn solar detectats a l'espai, mitjançant sondes interplanetàries i satèl·lits, i a la Terra. Les energies involucrades s'estenen fins a centenars de MeV i, ocasionalment, fins a pocs GeVs pel cas de protons. Alguns esdeveniments intensos, amb energia $E > 30\,\mathrm{MeV}$, poden assolir fluències[2] de fins a $10^{10}\,\mathrm{protons\,cm^{-2}}$. La majoria de les partícules de baixa energia ($< 100\,\mathrm{MeV}$) detectades a l'espai formen part d'esdeveniments SEP. Aquests augments del flux poden durar des d'unes poques hores fins a diversos dies, depenent de l'origen de les partícules i de la connexió magnètica entre la font i l'observador.

Abans de la missió ACE[3], els esdeveniments SEP s'acostumaven a dividir en dues classes: els "impulsius" i els "graduals" (Reames 2000). Aquest darrer tipus d'esdeveniments, els graduals, són dels més perillosos en l'entorn espacial i és per aquest motiu que en aquest treball ens centrem en el seu estudi. Els esdeveniments graduals[4] tenen durades des d'un dia i mig fins a cinc dies, exhibeixen abundàncies coronals normals i estats de càrrega d'ions típics de plasmes coronals a 1 - 2 MK; són

[1] Una 'partícula energètica' és aquella que té 'velocitat diferent de zero en el sistema de referència del vent solar'. Per exemple, protons de 60 keV o electrons de 10 keV són 'partícules energètiques'.

[2] Fluència o fluència cumulativa: flux diferencial de partícules integrat en l'angle sòlid, per a un interval de temps donat i per sobre d'un cert llindar d'energia.

[3] ACE es va llançar el 25 d'Agost del 1997.

[4] L'esdeveniment SEP mostrat en la Figura 1.1 és un típic esdeveniment gradual de protons.

esdeveniments rics en protons i s'originen en un ampli rang d'heliolongituds (von Rosenvinge et al. 2001). Aquest tipus d'esdeveniments mostren fluències de protons $> 10^9$ protons cm^{-2} a 10 MeV i intensitats màximes[5] molt més grans que les dels esdeveniments impulsius. Pel que fa a la classificació dels esdeveniments, cal remarcar, però, que el paradigma dicotòmic dels esdeveniments SEP fou controvertit fins i tot abans de la seva pròpia formulació i, de fet, estudis més actuals apunten cap a un continu de possibilitats (Tylka et al. 2005; Cane & Lario 2006).

Els xocs interplanetaris forts, ones que es propaguen pel medi interplanetari originades per les ejeccions de massa coronal[6] (CMEs), són en bona part els responsables de l'acceleració de partícules energètiques (van Nes et al. 1984). Així doncs, els esdeveniments SEP[7] (Lindsay et al. 1994; Kahler 2001) són bàsicament deguts a la propagació d'aquests xocs conduïts per CMEs, amb una possible contribució d'una fulguració[8] concomitant en la fase inicial de l'esdeveniment (Cane et al. 2006).

Les partícules accelerades pels fronts dels xocs es propaguen en el medi interplanetari guiades per la topologia del camp magnètic interplanetari (IMF), descrivint òrbites helicoïdals al voltant de les línies de camp magnètic, mentre el xoc es propaga en el medi interplanetari (Cane & Lario 2006). L'acceleració de partícules s'ha estudiat des del punt de vista teòric i observacional, i són tres els principals processos cridats a explicar aquesta acceleració (Lee 1997, 2005), tot i que la contribució relativa d'aquests mecanismes depèn de les propietats del xoc. Paràmetres com la seva velocitat, el quocient de compressió, el nombre Mach Alfvénic i l'angle entre el camp magnètic en la part davantera del xoc (regió pre-xoc) i la normal a ell, així com l'existència de turbulència en les rodalies del xoc, són factors que poden

[5] Sovint referides com 'el pic de flux' o 'el pic d'intensitat'.

[6] Les ejeccions de massa coronal són ejeccions de plasma de la corona Solar, observades per coronògrafs (Hudson et al. 2006), que es propaguen en el medi interplanetari viatjant sobre el vent solar. Les CMEs es poden propagar a velocitats que van des dels pocs centenars fins als pocs milers de quilòmetres per segon. Donat que el vent solar té una velocitat típica d'uns $\sim 350\,\mathrm{km\,s}^{-1}$, les CMEs ràpides, super-Alfvéniques i supersòniques poden produir i conduir xocs interplanetaris. Aquests xocs són ones sense-col·lisions identificades per un augment sobtat de la densitat, la velocitat i la temperatura del plasma, i un salt en la força del camp magnètic.

[7] A menys que s'indiqui el contrari, d'ara en endavant per 'esdeveniment SEP', o simplement 'esdeveniment', s'entén 'esdeveniment SEP gradual de protons'.

[8] Les fulguracions solars són brillantors sobtades d'una petita regió del Sol, observades en raigs X, UV i línies d'emissió, però poques vegades observades en el continu visible. Els processos físics resultants d'una fulguració inclouen la reestructuració del camp magnètic, l'acceleració de partícules no-tèrmiques i l'escalfament del plasma coronal/cromosfèric fins a desenes de milions de graus Kelvin (Hudson 2010).

influenciar en aquesta contribució (Lario et al. 1998; Leske et al. 2008).

Els diferents processos que actuen sobre la població de partícules accelerades per un xoc durant el seu transport, modulen els perfils de flux i d'anisotropia[9] que observarà una sonda. Petites irregularitats del camp magnètic modifiquen el moviment regular de les partícules, la turbulència magnètica les dispersa, i es veuen sotmeses a la convecció i la desceleració adiabàtica degut a l'expansió del vent solar. Malgrat que no és possible observar les trajectòries completes de partícules individuals des de la font d'origen fins al punt de detecció, sí que es pot estudiar l'evolució de certes característiques, com ara el flux i les anisotropies, d'aquesta població de partícules. En qualsevol cas, els perfils de flux de protons i d'anisotropia són consistents amb la presència de xocs que es propaguen (Heras et al. 1992; Gosling 1993) i que poden omplir de partícules accelerades àmplies regions de l'heliosfera (Cliver et al. 1995). Per tant, la topologia a gran escala dels xocs interplanetaris juga un paper en el desenvolupament d'esdeveniments SEP, els quals mostren una organització respecte a l'heliolongitud de l'esdeveniment solar original (Cane et al. 1988).

Així doncs, els perfils observats es poden entendre com una superposició de partícules contínuament accelerades al front del xoc, amb llurs característiques modificades més endavant degut a la seva posterior propagació al llarg del IMF. Aquests perfils són el resultat de la interacció de molts factors, com ara la geometria local i la força del xoc, les condicions existents per a l'acceleració de partícules per part del xoc, la posició relativa en l'espai de l'observador respecte al front del xoc, les condicions de transport de les partícules energètiques en l'espai interplanetari i l'energia considerada. Per tant, hi ha una gran varietat de perfils[10], depenent de la posició

[9] Aquí 'perfil d'anisotropia de protons' es refereix a l'evolució de l'anisotropia de primer ordre normalitzada, A_1/A_0 (definida per Sanderson et al. 1985), en un esdeveniment de partícules. El perfil d'anisotropia de protons en la regió pre-xoc o en el moment de pas del xoc per la sonda clarament evidencia el paper del xoc interplanetari com a accelerador de partícules (Heras et al. 1994; Kallenrode 2002). Aquesta variable observacional s'ha de tenir en compte i ajustar quan es modelitzen esdeveniments de partícules.

[10] La Figura 1.4 mostra exemples de perfils d'esdeveniments SEP per a quatre observadors situats a 1 AU. En aquests perfils es pot veure com en la regió pre-xoc el camp magnètic és una espiral de Parker, mentre que darrera del xoc (la regió post-xoc) la propagació de la CME ha deformat l'estructura del camp. En direcció contra-rellotge, aquests esdeveniments s'identifiquen com oest, meridià central, est o est a prop del limbe, respectivament. És una identificació bastant poc intuïtiva (usada freqüentment pels modelitzadors): s'assumeix que el xoc es propaga en direcció CM i que hi ha diversos observadors localitzats normalment a 1 AU i a diferents heliolongituds. Per tant, un esdeveniment en el flanc oest (o esdeveniment W) té una bona connexió amb l'observador des de l'inici de l'esdeveniment, mentre que per un esdeveniment en el flanc est (o esdeveniment

relativa de l'observador respecte a la part central del xoc, 'el nas'[11].

En resum, els processos involucrats en el desenvolupament d'esdeveniments SEP inclouen l'acceleració i el transport de partícules en un sistema depenent del temps, format per la propagació del xoc, la topologia del camp magnètic evolutiu associat, i la formació, o existència, de fluctuacions del camp magnètic, les quals, al mateix temps, es veuen afectades per la mateixa propagació de les partícules. Així doncs, els components bàsics d'un model d'esdeveniments SEP són: (1) la propagació i l'evolució del xoc durant el seu trajecte interplanetari; (2) els diferents punts del front del xoc on l'observador es connecta magnèticament; i (3) les condicions de transport de les partícules que es propaguen en el medi interplanetari.

Els models actuals, però, són inadequats per a predir amb seguretat els principals detalls (i.e., inici, durada i perfils de flux) d'un esdeveniment individual, ja que la interpretació de les dades requereix d'una descripció molt més acurada de l'escenari solar-interplanetari del que som capaços de reproduir avui en dia. Les principals raons són que la naturalesa específica dels processos involucrats en la generació d'esdeveniments SEP encara no s'entén completament[12], i que les simulacions d'esdeveniments SEP requereixen un millor coneixement de les condicions inicials prop del Sol[13]. Fins ara aquestes condicions bàsicament s'obtenen de les observacions in situ a 1 AU i, quan és possible, s'extrapolen a distàncies properes al Sol. Per tant, donat que les observacions de xocs i de partícules lluny de l'òrbita terrestre són escasses (i les poques existents són difícils de relacionar), els models actuals difícilment es poden basar en observacions de diferents etapes dels processos físics que generen els esdeveniments.

La conclusió del treball d'en Lee (1997) diu: *"El desafiament pels teòrics és*

E), la connexió magnètica s'estableix tant sols unes poques hores abans del pas del xoc.

[11] Els 'nas' d'un xoc interplanetari és la seva regió central davantera, la qual s'assumeix que està dirigida en la direcció de llançament de la CME. Així doncs, un esdeveniment meridià central (CM) és un esdeveniment generat per un xoc interplanetari el nas del qual es propaga en la direcció Sol-Terra (o helilongitud W00); i, de manera similar, un esdeveniment oest (W)/est (E) és un esdeveniment en el qual el nas del xoc es mou en direcció oest/est (Cane et al. 1988).

[12] Anant des dels mecanismes que provoquen les CMEs al Sol i les acceleren (vegeu Manchester et al. 2008b, i les referències citades) fins als processos d'acceleració de partícules que tenen lloc al front del xoc (Cane et al. 1988; Reames 1999; Tylka et al. 2005; Li et al. 2005a; Manchester et al. 2005; Verkhoglyadova et al. 2009).

[13] Com per exemple, el vent solar de fons, les condicions de llançament de les CMEs, etc.

desenvolupar un model d'acceleració en el xoc que inclogui quantitativament la geometria 3D i el vent solar, el xoc evolutiu, un coeficient de difusió realista, les possibles ones excitades pels ions, i una transició entre el transport dominat per la dispersió i el transport gairebé lliure a l'espai interplanetari. Només llavors podrem usar els espectres observats d'energia de les partícules i els perfils temporals per a conèixer els orígens dels SEP a prop del Sol". I nosaltres afegiríem: per tal de, més tard, ser capaços de fer prediccions fiables.

En consonància amb Lee (1997), el treball de Cane & Lario (2006) ens indica els elements que els futurs models haurien d'incloure: (1) simulacions tridimensionals, 3D[14], de la propagació dels xocs des de la seva formació prop de la corona (e.g., a pocs radis solars) fins a la posició de la sonda. (2) Poblacions de partícules llavor pels mecanismes d'acceleració que donen compte de les possibles contribucions de restes supratermals d'esdeveniments anteriors i partícules accelerades durant els processos fulguratius concomitants. (3) L'evolució de les característiques del xoc, deguda a la seva expansió i propagació, i de la seva eficiència en accelerar partícules i injectar-les al medi interplanetari. (4) La influència de l'estructura de l'IMF en el transport de partícules. (5) Models de transport realistes en escenaris complexes (ja que els esdeveniments rarament succeeixen de manera aïllada). I (6) una expansió de les regions d'acceleració modelitzades, especialment prop del Sol.

Com ja s'ha comentat, els esdeveniments SEP graduals presenten un dels riscos més severs en l'entorn espacial, fet que és especialment important per al llançament i l'operació de vehicles en l'espai, per a les missions en l'interior del sistema solar, on s'assoleixen els més alts nivells de radiació, i per l'exploració humana de la Lluna i Mart[15]. Així doncs, donada la gran importància de les tempestes de radiació solar en meteorologia espacial, és essencial que siguem capaços de predir acuradament quan podria succeir un esdeveniment SEP, i de quina intensitat, en base a l'observació rutinària de la corona solar i del vent solar prop del Sol. En l'actualitat, però, existeix un gran buit entre el que prediuen els models i la realitat dels esdeveniments graduals. Per tant, es necessiten models que puguin descriure com es produeix

[14] D'ara en endavant, ens referirem a uni-, bi- i tridimensional com 1D, 2D i 3D, respectivament.

[15] En l'informe 'Severe Space Weather Events–Understanding Societal and Economic Impacts: A Workshop Report (2008)' es pot trobar una presentació global dels efectes de la meteorologia espacial. Els perills específics deguts a la radiació es tracten en 'Space Radiation Hazards and the Vision for Space Exploration: Report of a Workshop (2006)'.

l'acceleració de partícules per part d'un xoc i com aquestes partícules es propaguen en l'espai interplanetari. D'aquesta manera, en un futur, podríem ser capaços de predir amb èxit els esdeveniments SEP i avaluar correctament el risc que representen.

Objectius

El principal objectiu d'aquesta tesi és tractar alguns dels desafiaments mencionats per en Lee (1997) per avanar en el nostre coneixement de l'origne dels SEP per tal de, més endavant, poder-ne fer prediccions fiables. Una part important d'aquest treball tracta sobre simulacions magnetohidrodinàmiques (MHD) 3D de xocs que s'inicien prop del Sol, abordant la potencial rellevància de la latitud de l'observador (respecte al xoc interplanetari) i l'evolució de la força del xoc. La influència de la latitud no ha estat encara quantitativament considerada en simulacions d'esdeveniments SEP, bàsicament degut a que la majoria dels codis MHD utilitzats fins ara per simular els xocs associats a esdeveniments són 1D, 2D o 2.5D. Els pocs intents de simular esdeveniments usant models MHD 3D per a la propagació de la CME han estat aplicats a observacions prop de l'eclíptica. Així doncs, és essencial disposar de models 3D fora del pla de l'eclíptica per a poder reproduir les característiques que conformen un esdeveniment SEP. A més, l'evolució de les variables del xoc a prop del Sol és necessària per a reproduir la fase inicial d'alguns esdeveniments graduals.

Per tal de tenir un millor coneixement sobre la relació existent entre la força del xoc al seu front i el ritme d'injecció de partícules que accelera, així com sobre la influència de la latitud de l'observador en els perfils de flux de protons detectats, hem analitzat les principals característiques d'algunes variables al punt del xoc on l'observador està connectat magnèticament (anomenat cobpoint, vegeu la següent secció). Hem utilitzat el model MHD 3D desenvolupat per C. Jacobs (Jacobs 2007) per simular la generació i la propagació de xocs conduïts per CMEs. Així, hem simulat diversos xocs i hem seguit la seva evolució fins a un conjunt de sondes situades a 0.4 i 1.0 AU, i a diferents longituds i latituds. Donat que l'objectiu principal d'aquesta part del treball és l'estudi de la influència de la força del xoc en el ritme d'injecció de partícules, i, per tant, en els perfils de flux resultants, hem centrat el nostre interès en millorar la localització del cobpoint, la caracterització del front del xoc i la determinació dels salts en les variables del plasma a través d'ell. Per fer-ho, hem desenvolupat un procediment que té en compte el fet que estem tractant amb

una geometria 3D.

A més a més, presentem la simulació d'un esdeveniment observat per tres sondes utilitzant un nou model xoc-i-partícula desenvolupat dins del projecte SEPEM[16] (Aran et al. 2011). L'esdeveniment que hem estudiat va tenir lloc l'1 de Març de 1979 i fou observat per diferents sondes, Helios-1, Helios-2 i IMP-8/ISEE-3, situades a distàncies radials similars però a posicions angulars (respecte al lloc de la font solar associada a l'esdeveniment) molt diferents. Això ens dóna l'oportunitat de provar la capacitat del nostre model en l'estudi de la rellevància de les variacions longitudinals del punt d'observació en la forma dels perfils d'intensitat. El propòsit és extreure conclusions sobre la influència de la posició relativa de l'observador en el ritme d'injecció de partícules accelerades al xoc i en les condicions de transport de les partícules observades per cada sonda, i així estar en disposició de discutir la capacitat de predicció de la relació empírica (la relació Q(VR), vegeu la següent secció) derivada dels esdeveniments SEP modelitzats anteriorment.

Models xoc-i-partícula

El primer model xoc-i-partícula per SEPs va ser desenvolupat per Heras et al. (1992, 1995). Les principals característiques d'aquest model compost són: (1) la inclusió en l'equació de transport d'un terme font que representa el ritme d'injecció de partícules accelerades pel xoc que es propaga. I (2) la implementació explícita i quantitativa del concepte de "cobpoint" (Connecting with the OBserver POINT), el punt del front del xoc interplanetari connectat magnèticament amb l'observador[17]. Lario (1997) i Lario et al. (1998) van desenvolupar el model SaP98, una versió millorada del model d'Heras. Els components bàsics d'aquest nou model són una descripció apropiada d'ambdós, la propagació del xoc interplanetari i el transport de les partícules energètiques al llarg de les línies IMF.

Les equacions de transport de les partícules energètiques intenten reproduir les característiques dels processos que sofreixen les partícules en la seva propagació. Ruffolo (1995) va desenvolupar una equació explícita per al transport focalitzat-

[16] Solar Energetic Particle Environment Modelling (SEPEM) project: http://sepem.aeronomie.be

[17] En analogia amb el "footpoint", l'arrel solar d'una línia IMF, però associat a una font interplanetària de partícules que és mòbil.

difusiu[18] dels rajos còsmics, que inclou els efectes de la desceleració adiabàtica, la convecció del vent solar, els processos de dispersió degut a l'angle de batuda[19] i la focalització magnètica en el IMF. L'equació de transport (Equació 2.14) es pot aplicar només a una injecció limitada de partícules (solars, per exemple). No obstant, per a explicar els esdeveniments graduals es necessari assumir una injecció contínua de partícules accelerades al xoc que es mou. Per tant, per tal de descriure aquest ritme d'injecció, el model ha d'incloure un terme addicional (un terme font) en la part dreta de l'equació de transport (per a més informació, vegeu el Capítol 2).

Aquest nou terme dóna compte de l'"eficiència" del xoc com a accelerador de partícules, el qual comprèn l'eficàcia del xoc en accelerar protons, acoblat amb la seva eficiència en injectar-los a l'espai interplanetari. Aquesta eficiència depèn de les condicions entorn del xoc, com ara la presència o l'absència d'una regió turbulenta davant el xoc, o un intens fons de protons que actuen com a població de partícules llavor. És comú expressar, finalment, el ritme d'injecció de les partícules accelerades pel xoc a una energia, temps de la simulació i posició del cobpoint i de l'observador donats, en l'espai de les fases, Q[20] (e.g., Heras et al. 1992; Lario et al. 1998; Aran et al. 2007).

La principal millora del SaP98, respecte al model d'Heras, és la inclusió d'aquests efectes (la convecció del vent solar i la desceleració adiabàtica) en l'equació de transport de protons (Ruffolo 1995) així com el terme del ritme d'injecció. El model SaP98 utilitza el mateix codi MHD[21] per portar a terme les simulacions del xoc que usà Heras, i l'equació de transport més completa, tot just esmentada, per descriure la propagació de les partícules energètiques. El concepte de cobpoint permet connectar ambdós models: permet comparar en aquest punt, per a cada instant de temps donat, els valors de les variables del plasma i del camp magnètic del vent solar (derivats de la modelització de la propagació del xoc) amb els valors del ritme d'injecció de les partícules accelerades pel xoc (derivats de l'ajust dels perfils de flux

[18] D'ara en endavant, a l'equació de transport focalitzat que inclou els efectes de la desceleració adiabàtica i la convecció del vent solar ens referirem com a l'"equació de transport". El treball de Lario et al. (1997) estudia l'influència d'aquests termes en el model de transport.

[19] Caracteritzats pel recorregut lliure mig, $\lambda_{||}$, el qual dóna una descripció, en primer ordre, dels efectes de la interacció de les partícules amb el camp magnètic durant el seu viatge cap a l'observador.

[20] $[Q] = [\mathrm{cm}^{-6}\,\mathrm{s}^{3}\,\mathrm{s}^{-1}]$.

[21] El codi MHD desenvolupat per en Wu et al. (1983), el qual té el límit interior a $18\,\mathrm{R}_{\odot}$ del Sol i s'estén fins a 1.1 AU.

i d'anisotropia d'esdeveniments SEP observats a diferents energies). A mesura que el xoc es propaga i s'expandeix, el cobpoint es mou al llarg del seu front descrivint un camí que depèn de l'heliolongitud de l'activitat solar que genera el xoc; és a dir, de la posició de l'observador respecte a la direcció principal de propagació del front del xoc. Així doncs, per a un instant de temps donat, observadors posicionats en l'espai a distancies radials o heliolongituds diferents tindran diferents cobpoints en el front del xoc[22].

Els principals paràmetres del SaP98 són el ritme d'injecció, Q, i el recorregut lliure mig, $\lambda_{||}$, ambdós derivats de l'ajust de simulacions numèriques amb observacions. Altres sortides són els perfils simulats de flux i d'anisotropia i l'espectre d'energia de Q, per a un conjunt d'energies. Donat que la simulació de la propagació del xoc i l'ajust dels perfils de flux de partícules són independents, qualsevol relació empírica que es pugui trobar entre el ritme d'injecció de les partícules accelerades pel xoc, Q, i les variables del plasma i el camp magnètic del vent solar no dependrà dels processos que acceleren les partícules. Per tant, el model SaP98 és un model semi-empíric que se centra en l'anàlisi de l'eficiència del xoc com a injector interplanetari de protons accelerats.

L'aplicació dels models xoc-i-partícula a diversos esdeveniments SEP detectats per diferents sondes ens han permès establir i provar una relació empírica entre el ritme d'injecció de partícules accelerades pel xoc, Q, i el salt normalitzat de la velocitat radial a través del xoc, VR:

$$\mathrm{VR} = \frac{v_{r_d} - v_{r_u}}{v_{r_u}}, \tag{1}$$

on els subíndexs u i d signifiquen que la velocitat radial s'ha pres a les regions pre- i post-xoc, respectivament. Aquesta relació es coneix com la "relació Q(VR)" i es defineix com, per cada canal d'energia:

$$\log Q(r,t) \,=\, \log Q_0 \,+\, k\,\mathrm{VR}(r,t), \tag{2}$$

on r i t són les posicions i els moments en que té lloc l'injecció de partícules.

[22] En la Figura 2.1 es mostra un esbós de l'evolució del cobpoint al llarg del front del xoc (instantànies d'1 a 4): es mou cap al nas del xoc a mesura que s'apropa cap a l'observador. A Lario et al. (1998) i Aran et al. (2007) trobareu altres exemples d'esdeveniments SEP que mostren diferents comportaments del cobpoint.

Cal remarcar que el model no intenta simular els processos físics que donen lloc a l'acceleració de les partícules al front del xoc interplanetari. El xoc es tracta, tant sols, com a una font mòbil de partícules, sense explícitament considerar la física que hi ha darrera els mecanismes d'acceleració. En comptes d'això, el nostre objectiu és obtenir mesures de Q al cobpoint.

La dependència de Q amb el quocient de la velocitat del plasma VR al front del xoc considera, de manera implícita, la seva dependència temporal i longitudinal (latitudinal, en els models 3D) a mesura que el xoc s'expandeix i el cobpoint es mou al llarg del seu front. Q inclou, no només aquelles partícules accelerades pel xoc, sinó també aquelles que són reflectides al seu front; per tant, una simple dependència de Q amb VR hauria de ser concebuda només com una manera convenient de quantificar l'evolució temporal i la dependència longitudinal (latitudinal) de Q a través de relacionar-les amb l'expansió dinàmica del xoc. Altres paràmetres (com el nombre Mach o l'existència d'una població de partícules llavor (Tsurutani & Lin 1985; Desai et al. 2006)) poden ser rellevants a l'hora de caracteritzar les propietats de Q. El nostre coneixement de la dependència quantitativa de Q en aquestes variables o factors està lluny de ser definitiva. Són necessàries aproximacions més realistes de Q per tal de poder lligar, completament, les propietats del xoc que evoluciona amb la seva eficiència en l'acceleració i la injecció de partícules.

Assumint la relació Q(VR) (Equació 2), és possible invertir el procediment i computar perfils sintètics de flux i d'anisotropia. És a dir, per a un esdeveniment solar donat que genera un xoc: (1) el model de la propagació del xoc proporciona els valors de les variables MHD del xoc, al llarg del seu front i durant tot el seu viatge cap a l'observador, en particular al cobpoint; (2) això ens permet avaluar el nombre de partícules a injectar en la línia IMF arrelada al cobpoint; i (3) mitjançant l'equació de transport, s'estimen els efectes de la propagació d'aquestes partícules al llarg de la línia IMF. El resultat és un conjunt de perfils SEP per a un rang donat d'energies en un escenari solar-terrestre específic.

Dins el marc del projecte SEPEM, el nostre grup STP/SWG[23] i el grup del

[23] Solar-Terrestrial Physics and Space Weather Group, Departament d'Astronomia i Meteorologia, Universitat de Barcelona: http://www.am.ub.es/∼blai

CPA/KUL[24] (liderat pel professor S. Poedts) hem desenvolupat un nou model xoc-i-partícula, el model SaP10. La principal millora respecte al SaP98 és que la modelització del xoc comença més aprop del Sol ($\sim 4\,R_\odot$), fet que ens permet estendre les simulacions de partícules a més altes energies, fins a 200 MeV.

Donat que el nostre objectiu és modelitzar esdeveniments SEP, els codis MHD usats s'han d'adequar a aquesta finalitat. Això demana la incorporació de nous models MHD que permetin descripcions 2D i 3D dels xocs interplanetaris, començant tant a prop de la corona solar com sigui possible, tal i com succeeix en els models desenvolupats per C. Jacobs (CPA/KUL). Les principals característiques dels models MHD 2D i 3D emprats en aquest treball es troben exposades en la Secció 2.2.1.

Un punt clau dels models xoc-i-partícula és la identificació del front del xoc, és a dir, la determinació del cobpoint així com de les variables del plasma i del camp magnètic a ambdós costats del front del xoc (regions pre- i post-xoc). Degut a les tècniques numèriques de computació emprades per a resoldre les equacions MHD, els detalls del front del xoc poden no estar suficientment ben caracteritzats[25], especialment a les ales del xoc on la seva força esdevé més dèbil . Així doncs, és necessària una adequada identificació i caracterització[26] del xoc. La determinació de la posició del cobpoint i la caracterització del xoc 2D i 3D és una part important d'aquest treball. Un breu resum del procediment a seguir el trobareu en la Secció 2.3, mentre que l'explicació detallada per a cada cas s'exposa a mesura que es discuteixen les aplicacions d'aquests models a esdeveniments (o simulacions) específics (Capítols 3 i 5).

[24] Centrumm voor Plasma Astrophysics, Katholieke Universiteit Leuven, Belgium: http://wis.kuleuven.be/cpa/index.php

[25] Per exemple degut a salts de les variables del plasma massa petits o a una xarxa massa gruixuda.

[26] Això significa: determinar les característiques del xoc que, basat en el nostre coneixement, puguin ajudar a entendre millor la seva eficiència com a injectors de partícules energètiques, i millorar les simulacions d'esdeveniments SEP. No és fàcil; Lario et al. (1998) comenta: *"la identificació dels límits del xoc i els seus efectes en la població de partícules no són fàcils de definir. La interacció d'una partícula amb una discontinuïtat en el plasma depèn de l'energia de la partícula. Conseqüentment, és possible que un xoc pugui accelerar eficientment partícules de baixa energia en les seves ales mentre esdevé un ineficient accelerador a altes energies. O, que una partícula de baixa energia pugui "veure" una discontinuïtat en el plasma i en el camp magnètic com un xoc, mentre que un partícula a alta energia "veuria" només una petita irregularitat".*

3D. Modelització d'esdeveniments graduals de protons

Hem desenvolupat un procediment per determinar, de manera automàtica, la localització del cobpoint, la corresponent direcció normal al xoc i el punt post-xoc en simulacions 3D. L'hem aplicat a diversos observadors localitzats a 0.4 i a 1.0 AU, a punts estratègics amb diferents longituds i latituds heliocèntriques (nou posicions en total; vegeu la Figura 3.2). Hem emprat un model MHD 3D per simular la propagació d'un xoc ràpid i un lent.

Hem analitzat l'evolució de la intensitat del camp magnètic, la densitat numèrica i la velocitat radial per aquests observadors i aquests escenaris, discutint la rellevància de la latitud de l'observador. Hem trobat que l'observador que detecta els majors salts del plasma al pas del xoc és l'observador que està situat en la mateixa direcció en qu'e hem llançat la pertorbació, direcció en la que el xoc és més ràpid i més fort. Aquest comportament es manté a ambdues distàncies i pels dos escenaris de velocitats de propagació tractats. També hem vist que hi ha una considerable disminució en els valors del plasma enregistrats quan l'observador se situa lluny del nas del xoc, ja sigui en longitud com en latitud. A més, hem comprovat que el comportament general dels salts del plasma i del camp magnètic són qualitativament similars a ambdues distàncies estudiades, essent els salts més petits a 1.0 AU; això és degut a que el xoc s'afebleix mentre s'expandeix pel medi interplanetari. També per tots dos escenaris, els salts del plasma i del camp magnètic mostren el mateix comportament, amb salts majors pel cas del xoc ràpid que pel lent.

Com a conseqüència de les variacions de la velocitat del vent solar amb la latitud (estructura bimodal), hem corroborat que el xoc mateix es propaga a diferents velocitats depenent de la velocitat de fons sobre la que ho fa; per tant, també la velocitat de propagació del xoc depèn de la latitud. Això es tradueix en que, per observadors amb la mateixa longitud, el xoc arriba abans a aquells que estan localitzats a latituds més altes (les quals tenen un vent solar més ràpid). Per a observadors amb la mateixa latitud, el xoc arriba més tard com més gran és la separació entre la posició de l'observador i el nas del xoc.

D'altra banda, hem estudiat l'evolució del salt normalitzat de la velocitat radial,

VR (Equació 1, com a paràmetre que caracteritza la força del xoc. Hem mostrat que: (1) les simulacions MHD de xocs han d'incloure l'evolució de les variables del plasma i del camp magnètic a prop del Sol ($< 18\,R_\odot$), ja que la força del xoc disminueix ràpidament amb la distància radial i, per tant, la seva eficiència com a accelerador de partícules, fet que és especialment important a altes energies; i (2) la VR també depèn de la latitud, no només de la longitud. L'observador que enregistra el major valor de VR és el que té una connexió magnètica més propera al nas del xoc, punt que depèn tant de la posició radial de l'observador com de la seva latitud. Així doncs, els models MHD haurien de considerar la influència de les variacions amb la latitud de les variables del plasma i del camp magnètic al front del xoc.

Per cadascun dels casos estudiats, hem derivat els corresponents perfils sintètics de flux dintre el marc del nostre model xoc-i-partícula. Hem presentat exemples que il·lustren la importància de la latitud de l'observador en aquests perfils i hem mostrat que, dins de la mateixa simulació, els perfils de flux (i també de fluència) poden variar fins a un ordre de magnitud per observadors amb la mateixa longitud però amb diferents latituds, tant pels observadors a 0.4 com a 1.0 AU[27]. Per ambdues simulacions i per les dues energies estudiades, l'observador N22W00[28] enregistra la màxima intensitat. Totes aquestes diferències en els perfils de flux impliquen una variació en l'eficiència del xoc en injectar partícules accelerades, essent major pel cas d'un xoc ràpid que pel cas d'un xoc lent, i pels observadors a 0.4 AU que pels observadors a 1.0 AU.

Hem estat capaços de reproduir la fase inicial dels esdeveniments SEP graduals amb una bona connexió. Això és degut al fet que estem en disposició de simular de manera consistent la injecció de partícules a alta energia a prop del Sol, ja que amb el nou model podem traçar el cobpoint des de posicions més properes al Sol que no pas ho fèiem amb els antics models. Hem corroborat que, en general, la fase inicial és més intensa pels observadors a 0.4 AU que pels observadors a 1.0 AU, així com pel cas del xoc ràpid que pel cas del xoc lent, fins i tot tenint en compte que la fase inicial pot dependre de la connexió magnètica de l'observador amb el front del xoc, el qual, al mateix temps, depèn de la latitud (degut a les diferències en la velocitat

[27] Això es deu al fet que els seus cobpoints poden estar més a prop o més lluny de la regió central del xoc, depenent de la latitud en la qual es troben els observadors.

[28] Aquest és l'observador que està situat en la mateixa direcció en que hem llançat la pertorbació. Per a més informació sobre la notació emprada vegeu la Secció 3.2.

del vent solar).

Hem computat els pics d'intensitat en cada cas, adonant-nos que també aquests poden canviar molt, fins a un ordre de magnitud, per observadors a qualsevol distància o longitud, depenent de la seva latitud. Pel xoc ràpid, el pic de l'esdeveniment de protons associat és major que pel xoc lent, essent la diferència molt més gran a alta energia que a baixa.

Hem notat que la presència d'una regió turbulenta davant del xoc pot àmpliament modificar la forma dels perfils de flux i, per tant, els valors del pic d'intensitat i el moment en què es donen: a alta energia, el pic acostuma a aparèixer en la fase inicial; però a baixa energia, es pot veure superat per un màxim absolut en el moment del pas del xoc. Pels pics que tenen lloc en la fase inicial de l'esdeveniment, com millor és la connexió magnètica entre l'observador i el front del xoc, major és el pic; mentre que pels casos en que el pic té lloc al pas del xoc, aquest és major com més aprop del nas del xoc es troba l'observador. Els valors del pic d'intensitat també depenen de la velocitat del xoc; això és especialment important per esdeveniments ben connectats magnèticament generats per xocs ràpids, on el valor del pic d'intensitat varia considerablement amb la longitud i la latitud de l'observador.

Finalment, hem estudiat la dependència del pic d'intensitat amb la posició radial de l'observador. Aquesta dependència no es pot quantificar adequadament ja que mostra una alta variabilitat en funció de la longitud i la latitud: observadors amb la mateixa longitud però diferent latitud proporcionen índexs radials considerablement diferents, i viceversa. Al derivar la dependència del pic d'intensitat amb la velocitat del xoc, podem conclure que com més ràpid és el xoc, més aviat ocorre el pic d'intensitat.

La principal conclusió de l'estudi presentat en aquesta secció de la tesi és la rellevància de la latitud en l'evolució del plasma i del camp magnètic del vent solar, així com en la força del xoc i la seva evolució, en els perfils de flux derivats, i en els valors del pic d'intensitat i la seva suposada (o esperada) dependència amb la distància radial. La importància de la latitud és un factor tot just esmentat i pràcticament no tractat anteriorment en simulacions numèriques d'esdeveniments SEP. Actualment, pràcticament tots els esforços en aquest sentit s'han focalitzat en

la longitud (o heliolongitud), degut, principalment, a que: (1) el gruix d'observacions provenen de sondes localitzades prop d'1 AU i prop del pla de l'eclíptica; i (2) la modelització 3D d'esdeveniments SEP és una tasca complexa i requereix d'una capacitat computacional difícilment assequible, fins i tot avui en dia.

Sostenim que la inclusió de la latitud és important per a l'avenç en meteorologia espacial i, per tant, requereix una major atenció. Cal afegir que serien necessàries moltes més simulacions (amb altres distàncies radials, latituds, velocitats i formes del xoc, etc.) per tal refermar aquestes conclusions.

2D. Simulació d'un esdeveniment gradual de protons multi-sonda

Els perfils d'intensitat de partícules d'un esdeveniment SEP gradual observat per diverses sondes situades a diferents longituds prop del pla de l'eclíptica, fins i tot estant a distàncies radials similars, mostren formes diferents. Per tal de modelitzar aquesta variabilitat hem realitzat la simulació de l'esdeveniment multi-sonda que va tenir lloc l'1 de Març de 1979 emprant un nou model xoc-i-partícula 2D, el model SaP10 (Aran et al. 2011). L'esdeveniment va ser observat per diverses sondes, Helios-1, Helios-2 i IMP-8/ISEE-3, les quals estaven situades a distàncies radials semblants, des de 0.925 fins a 0.99 AU, però a posicions angulars (respecte al lloc de la font solar associada a l'esdeveniment) molt diferents, des de E50 fins a W08. Amb el nou model MHD 2D estem en disposició de seguir el xoc que es propaga des de $4\,R_\odot$, fet que ens permet determinar el ritme d'injecció de partícules accelerades pel xoc prop del Sol, on normalment té lloc l'acceleració de la major part de partícules d'alta energia.

Amb la simulació de la propagació del xoc hem estat capaços de reproduir el seu temps d'arribada, la seva velocitat de trànsit i els principals dels salts del plasma en les tres sondes. També hem desenvolupat i hem aplicat un nou procediment automàtic per tal de localitzar el cobpoint i el punt post-xoc per a les tres sondes, per a cada instant temporal (i.e., instantània), així com determinar el front del xoc mitjançant el càlcul de la direcció normal a ell. Hem comprovat la solidesa d'aquest procediment i també n'hem discutit les seves limitacions.

Amb el nou model SaP10 hem simulat els perfils de flux de protons de 4 canals

d'energia observats durant l'esdeveniment a Helios-1 i a Helios-2, així com de 14 canals d'energia observats a IMP-8. El model reprodueix el perfils en la regió pre-xoc vista per cada sonda, per diferents canals d'energia amb protons entre 3.77 i 81 MeV. Així, hem vist que les intensitats assolides en el moment del pas del xoc disminueixen amb l'augment de l'energia dels protons, deduint que l'eficiència del xoc disminueix amb l'augment de l'energia. També hem derivat les condicions de transport a partir dels perfils de flux mesurats per cada sonda.

Podem, d'aquesta manera, quantificar l'eficiència del xoc en injectar partícules en el seu camí cap a cada observador i extreure conclusions de la influència de la posició relativa de l'observador (respecte a la direcció principal del nas del xoc) en el ritme d'injecció de partícules accelerades pel xoc, Q. Per energies semblants, el ritme d'injecció derivat a Helios-1 és més alt que a Helios-2, i aquest és més gran que a IMP-8 (tal i com s'espera de les intensitats mesurades per cada sonda). En el cas d'Helios-1, la ràpida disminució de Q indica una forta injecció de partícules a alta energia accelerades pel xoc quan aquest es troba prop del Sol, seguida d'una ràpida disminució en la seva eficàcia quan es mou cap a l'observador. El ritme d'injecció derivat per Helios-2 i IMP-8 mostra la mateixa tendència però amb una evolució de Qmés suau (en comparació amb la d'Helios-1). Aquest comportament diferent reflecteix el fet que els seus respectius cobpoints es mouen al llarg de diferents regions del front del xoc. Per Helios-1, el cobpoint recorre una regió del front del xoc que s'estén des de l'ala esquerra del xoc fins al seu nas, mentre que els respectius cobpoints d'Helios-2 i IMP-8 estan sempre localitzats al llarg de l'ala esquerra del xoc.

Hem estudiat la correlació entre la Q i la VR a les tres sondes. Tot i que la correlació trobada és alta (els valors del coeficient de la regressió són, en general, majors que 0.95), l'evolució de la Q i de VR no ens permet derivar una relació Q(VR) per aquestes sondes. Això ens confirma la necessitat de modelitzar un conjunt molt més gran d'esdeveniments SEP per tal de refinar aquesta relació empírica.

Finalment, hem discutit els factors importants que el model SaP10 encara no pot tenir en compte, essent els més rellevants l'existència d'una població de partícules llavor, la possible contribució al flux de partícules accelerades en la fulguració, i la forma del xoc quan aquest es troba encara a prop del Sol.

Chapter 1

Introduction

> La mente no es una vasija que haya que llenar, sino un leño que hay que hacer arder para que avive el placer por la investigación y el amor por la verdad.
>
> PLUTARCO

1.1 Solar energetic particle (SEP) events

1.1.1 Main features

Solar energetic particle (SEP) events are particle flux enhancements regularly detected in space by spacecraft and satellites, and at Earth[1]. First Earth-based measurements of solar flare generated particles date from 1946 whereas spacecraft measurements were only systematic from about twenty years later[2]. The energy of the involved particles extends up to hundreds of MeV and, occasionally, to a few GeVs, for protons. The Space Environment Center of the National Oceanic and Atmospheric Administration[3] defines a SEP event as the flux[4] of interplanetary particles that exceeds the threshold of 10 pfu[5] during 15 minutes for $E > 10$ MeV. Intense SEP

[1] SEP events detected at Earth are known as Ground Level Events (GLEs): high energy (> 500 MeV) solar particle events observed with neutron monitors (Kallenrode 2004).

[2] Forbush (1946), but see also comments by Shea & Smart (1990).

[3] SEC/NOAA: http://www.swpc.noaa.gov/ftpdir/indices/SPE.txt

[4] Otherwise indicated, 'particle flux' means the differential particle intensity derived from the measured count rate of particles detected by an instrument: the number of particles per unit of time, area, solid angle, and energy in a given energy range. Differential flux units: [particles $\mathrm{cm}^{-2}\,\mathrm{s}^{-1}\,\mathrm{sr}^{-1}\,\mathrm{MeV}^{-1}$] (or keV^{-1} in some cases).

[5] Particle Flux Units, pfu: [particles cm^{-2} s^{-1} sr^{-1}].

events can reach fluences[6] as high as 10^{10} protons cm^{-2} for E > 30 MeV. Most of the low energy (< 100 MeV) particles detected in space form part of SEP events. SEP flux enhancements may last from few hours to several days depending on the origin of the particles and on the magnetic connection between the source and the observer (usually near or at Earth's orbit).

Figure 1.1 shows an example of a large SEP event (115 keV < E < 131 MeV), occured on 4 - 7 April 2000, as detected by different instruments on board ACE[7] and SOHO[8] spacecraft, as well as the evolution of the solar wind and interplanetary magnetic field (IMF) in this time interval[9]. The vertical arrow marks the time of the triggering solar activity (located at heliolongitude W66) and the vertical line the shock passage (see Aran et al. 2011, for a full description of this event). The different shapes of the flux profiles at high and low energies reflect the capability of the interplanetary shock (the main source of accelerated particles in this SEP event-scenario) at accelerating particles of different energies.

The Sun is the most powerful natural particle accelerator in our solar system: it is able to accelerate ions mainly as a consequence of transient phenomena like solar flares and coronal mass ejections (CMEs)[10]. A solar flare is a sudden brightening of a small region of the Sun observed in X-rays, UV and emission lines, but rarely observed in the visible continuum. The physical processes resulting in a flare include restructuring of the magnetic field, acceleration of non-thermal particles and heating of coronal/chromospheric plasma up to tens of millions of Kelvins (Hudson 2010). Several mechanisms of particle acceleration at flares have been proposed, as resonant wave-particle interactions (Roth & Temerin 1997) and stochastic acceleration with a complex spectrum of cascading waves (Miller & Viñas 1993). These processes occur in connection with the magnetic reconnection at the time of the flare and are confined to the site where the flare takes place.

[6] Fluence or cumulative fluence: particle differential flux integrated over the solid angle, for a given time interval and above a certain threshold energy.

[7] ACE: Advanced Composition Explorer. http://www.srl.caltech.edu/ACE/

[8] SOHO: SOlar and Heliospheric Observatory. http://sohowww.nascom.nasa.gov/

[9] ACE Science Center: http://www.srl.caltech.edu/ACE/ASC/

[10] Large flares frequently accompany CMEs, being both different aspects of a large scale coronal field reconfiguration that finally results in a release of mass and energy. It does not exist a cause-effect relation among them but a co-evolution of both processes (Aschwanden 2006).

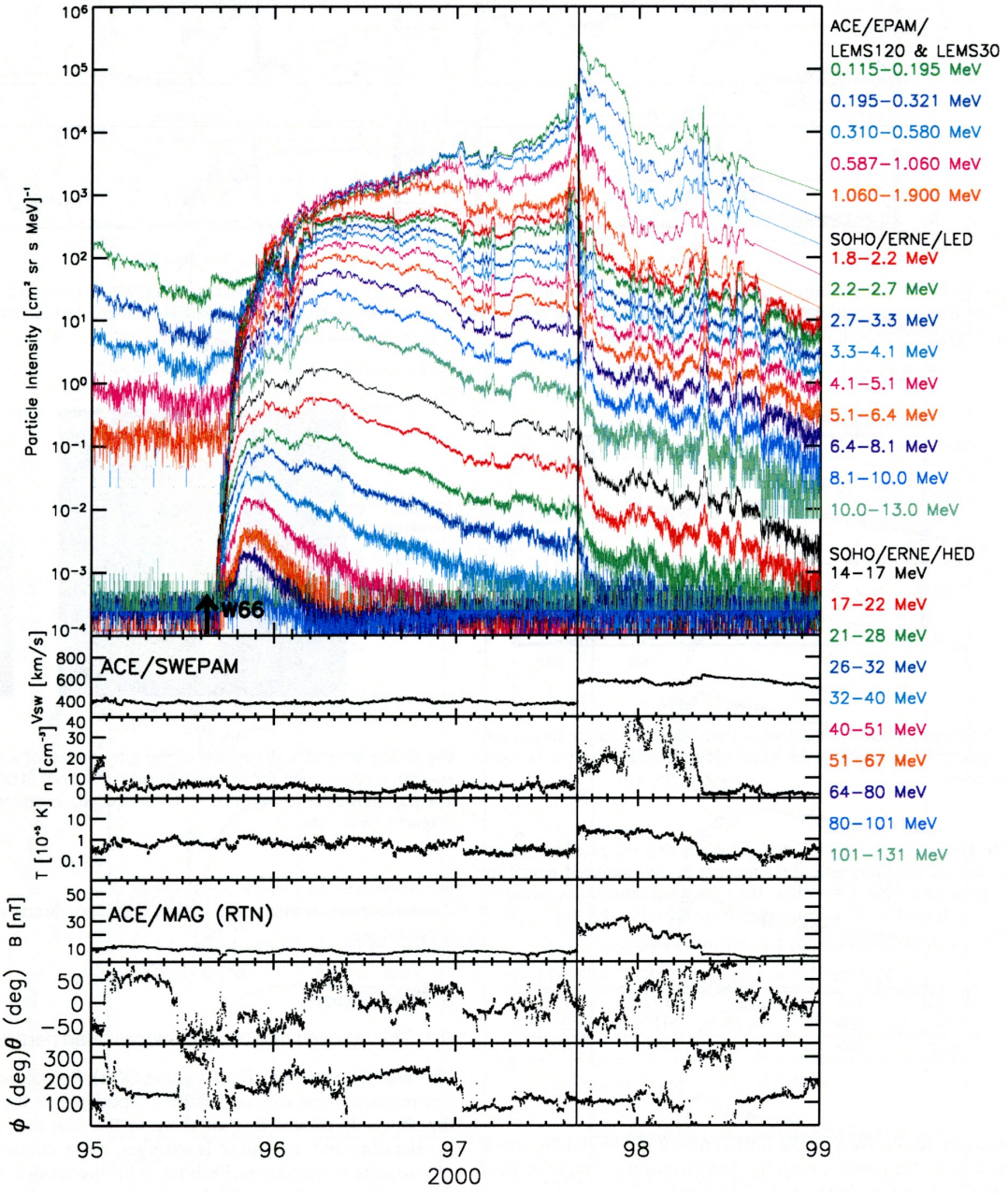

Figure 1.1: SEP event of 4 April 2000. From top to bottom: proton intensities observed by ACE/EPAM instrument and SOHO/ERNE instrument; solar wind velocity, density and temperature observed by ACE/SWEPAM instrument; and magnetic field magnitude, latitude and longitude measured by ACE/MAG Experiment (from Aran et al. 2011).

CMEs are ejections of coronal plasma, observed by coronagraphs (St. Cyr et al. 1997; Hudson et al. 2006), that propagate into interplanetary space ploughing through

in the solar wind. CMEs can travel in the solar wind at speeds from a few hundreds to a few thousands of kilometres per second. Since the solar wind has a typical speed of $v \sim 350\,\mathrm{km\,s^{-1}}$, fast super-Alfvénic and supersonic CMEs can produce and drive interplanetary shocks. These physical shocks are collisionless waves identified in space by a sudden increase in plasma density, speed and temperature, and a jump in the IMF strength: in Figure 1.1, for example, the shock passage takes place on doy[11] 97, marked by the solid line. Strong interplanetary shocks are largely responsible for the acceleration of energetic particles[12] (e.g., van Nes et al. 1984); these particles propagate along the magnetic field lines as the shock propagates outward from the Sun in interplanetary space (Cane & Lario 2006). Not all CMEs result in SEP events; in fact, only 1 - 2 % of CMEs have SEP events associated with them (Gopalswamy et al. 2002). In many SEP events, specially below $\sim 2\,\mathrm{MeV}$, detectors measure large flux increases in advance of the shock passage at the spacecraft position. This increase is historically known as the Energetic Storm Particle (ESP) component[13] (Bryant et al. 1962).

Particle acceleration at interplanetary shocks has been theoretically and observationally investigated. Three processes are mainly invoked to explain such acceleration (Lee 1997, 2005): (1) shock drift acceleration that takes advantage of the electric induction field existing in the shock front and the motion of particles that drift along the shock front (Armstrong et al. 1977). (2) Diffusive shock acceleration mechanism where particles undergo repeated reflections between converging scattering centres formed by magnetohydrodynamic (MHD) waves propagating in the vicinity of the shock (Lee & Fisk 1982; Lee 1982). During the wave-particle interactions there is an energy transfer between the wave and the particle as well as a change in the direction of motion of the particle. And (3) stochastic acceleration in the turbulent medium existing downstream of the shock. Particles moving in this region may interact with uncorrelated magnetic inhomogeneities moving in arbitrary direction resulting in a net energy gain if a strong downstream turbulence exists (e.g., Campeanu & Schlickeiser 1992; Vainio & Schlickeiser 1999). The relative contribution of these three shock-acceleration mechanisms depends on the properties

[11] Doy: day of the year.

[12] 'Energetic particle' means a 'particle whose velocity is not zero in the solar wind frame'. Therefore, 60 keV-protons or 10 keV-electrons are 'energetic particles', for example.

[13] A few unusual events may show an ESP component extending up to 100 MeV (Lario & Decker 2001).

of the shock (Jokipii 1982)[14]. Shock parameters such as shock speed, compression ratio, alfvénic Mach numbers, and the angle between the upstream magnetic field and the normal to the shock (θ_{Bn}) as well as the existence of turbulence in the vicinity of the shock are all factors that can influence the relative contribution of the particle acceleration (e.g., Lario et al. 1998; Sokolov et al. 2006b; Tylka & Lee 2006; Leske et al. 2008).

Other sources of energetic particles are Corotating Interaction Regions (CIRs), Galactic Cosmic Rays (GCRs) and certain planetary and cometary environments (Richardson 1985; Kallenrode 2004; Prölss & Bird 2004). Proton fluxes associated with CIRs are smaller than those associated with interplanetary shocks whereas GRCs are only relevant with respect to SEPs at energies higher than several GeVs[15].

Prior to ACE mission[16], SEP events were usually divided in two classes: "impulsive" and "gradual" events (Reames 1999, 2000). Impulsive events are of short duration, several hours, and they are originated in a limited range of heliolongitudes around W60; their fluence at 10 MeV is usually smaller than 10^8 protons cm^{-2}; they show enrichment in electrons, ^{3}He and heavy ions, and have ion charge states typical of high-temperature plasma (~ 5 - 10 MK). Impulsive events are associated with solar flaring acceleration (Kahler 2001; Mason et al. 2002). Figure 1.2 shows an example of an impulsive SEP event of electrons and protons, with a rapid main phase of ~ 2 hours followed by a slow decay phase of about ~ 12 hours; it has low H/He ratios and high Fe/O and ^{3}He/^{4}He ratios characteristic of impulsive events (Agueda et al. 2008).

Gradual SEP events last from one and a half to five days, exhibit normal coronal abundances and ion charge states, typical of a 1 - 2 MK coronal plasma; they are proton-rich events and are originated in a wide-spread range of heliolongitudes (von Rosenvinge et al. 2001). Gradual events display > 10 MeV-proton fluences higher

[14] In situ observations of shocks and particles suggest that multiple acceleration processes may occur (van Nes et al. 1984; Tsurutani & Lin 1985; Lario et al. 2005).

[15] GCRs are highly energetic nuclei mainly in the range between 100 MeV and 10 GeV per nucleon. Solar energetic particles were historically understood as the low-energy component (< 0.5 GeV) of GCRs. GCRs of non-solar origin in the 10 - 100 MeV energy range are one or two orders of magnitude less abundant than solar energetic particles (Fisk et al. 1998; Bieber et al. 2000).

[16] ACE was launched on 25 August 1997.

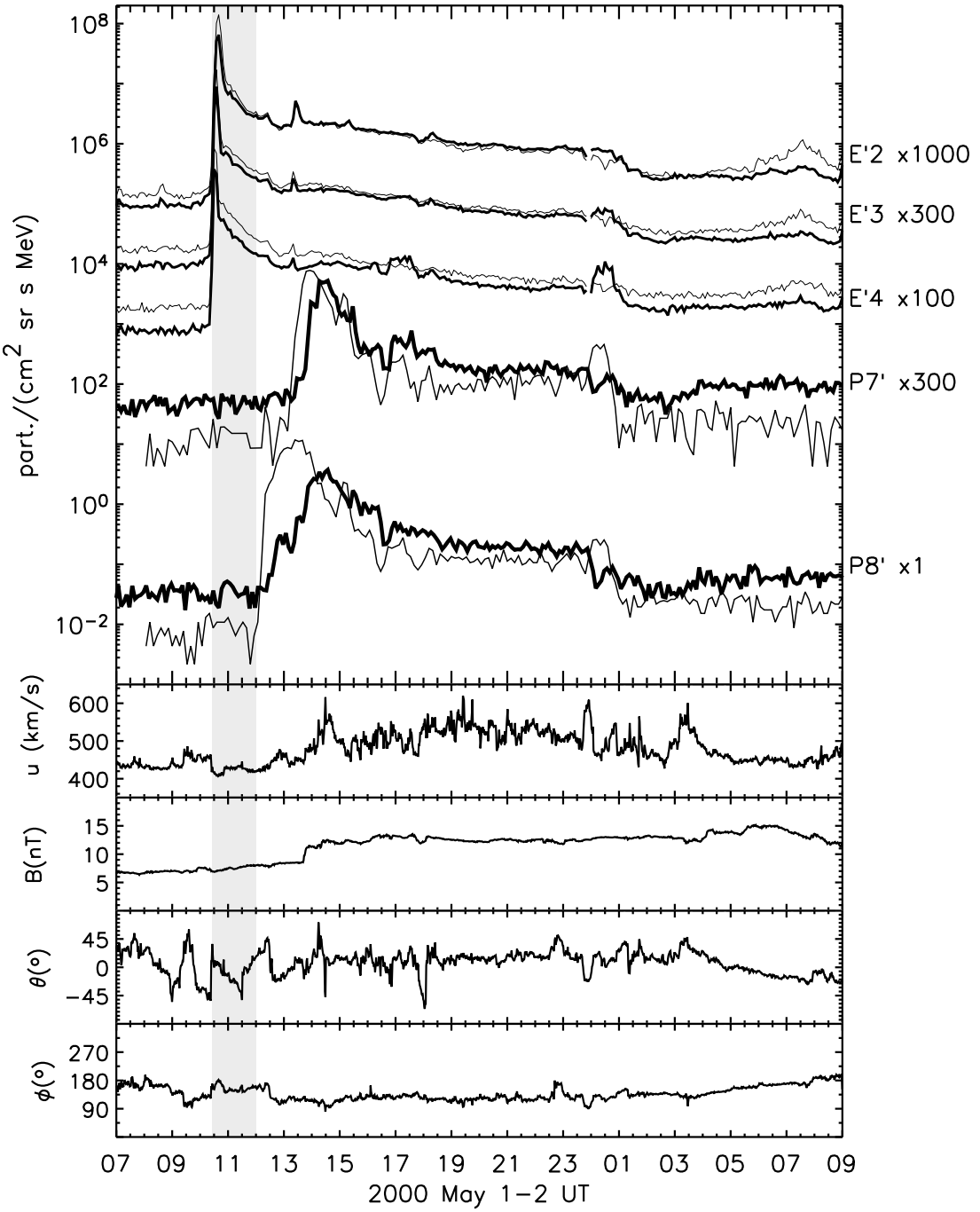

Figure 1.2: Impulsive SEP event on 1 May 2000. From top to bottom: electron and proton spin-averaged intensities observed by ACE/LEFS60 and LEMS120 telescopes; solar wind velocity observed by ACE/SWEPAM instrument; magnetic field magnitude, latitude and longitude measured by ACE/MAG Experiment (from Agueda et al. 2008).

than 10^9 protons cm^{-2} and maximum particle intensities[17] much larger than those of impulsive events; the SEP event shown in Figure 1.1 is a typical gradual proton event. Whereas smaller impulsive flare-associated events can occur at any time during the solar cycle, large SEP events occur most frequently during periods of increased solar activity.

Such dichotomous paradigm was controversial even before its formulation[18] (Cliver 1996). Hybrid events are large SEP events that show at their prompt phase ion abundances similar to those seen in impulsive events (Kallenrode et al. 1992; Cliver 1996; Ruffolo 2002), or simply an enhancement relative to coronal values (Cane et al. 2010). Different studies point towards a continuum of possibilities from pure impulsive to pure gradual events (i.e., Tylka et al. 2005; Cane & Lario 2006; Klecker et al. 2006; Mewaldt et al. 2006). Cane et al. (2010) study the composition and solar events associations for 280 SEP events in the period of 1997 - 2006. Based on abundance ratios and the shape of particle intensity-time profiles they divide these events in five groups and find a continuum of event properties that does not permit to clearly filter out groups of events: from a group of electron-rich events, most of which might be classified to be impulsive (with associated narrow CMEs) to a group of events primarily composed of shock-accelerated particles, associated with interplanetary shocks observed at 1 AU. Cane et al. (2010) show that, in these events, the early (<12 h) proton peak intensity increases as a function of both the flare and the CME properties examined (e.g., angular size and projected speed for CMEs and duration and X-ray intensity peak for flares), which is not surprising due to the close physical relationship between flares and CMEs[19]. Further conclusions of Cane et al. (2010) are that it is not necessary to appeal for a hypothetical leftover particle population from unrelated flares as a seed for shock acceleration, and that it is difficult to evaluate the involvement of quasi-perpendicular shocks due to the poor knowledge of the configuration of CME-driven shocks near the Sun. What remains to be

[17] Hereafter, frequently referred as the 'peak flux' or 'peak intensity'.

[18] The usage of these terms has been critically reviewed by Cliver & Cane (2002).

[19] As stated by Cane et al. (2010): *"We would not necessarily expect 'flare particles' in energetic SEP events to have abundances identical to those of impulsive flare events. We reiterate that the term 'flare' is used in a broad sense. In energetic SEP events the flare impulsive phase is followed by extended magnetic reconfiguring and particle acceleration... This later acceleration is likely to be the same basic process as in the impulsive phase but in an environment with different physical properties"*. These authors use the term 'flare' to mean: *"particle acceleration involving some sort of reconnection, and, in particular, including widespread magnetic reconfiguring in the aftermath of a CME"*.

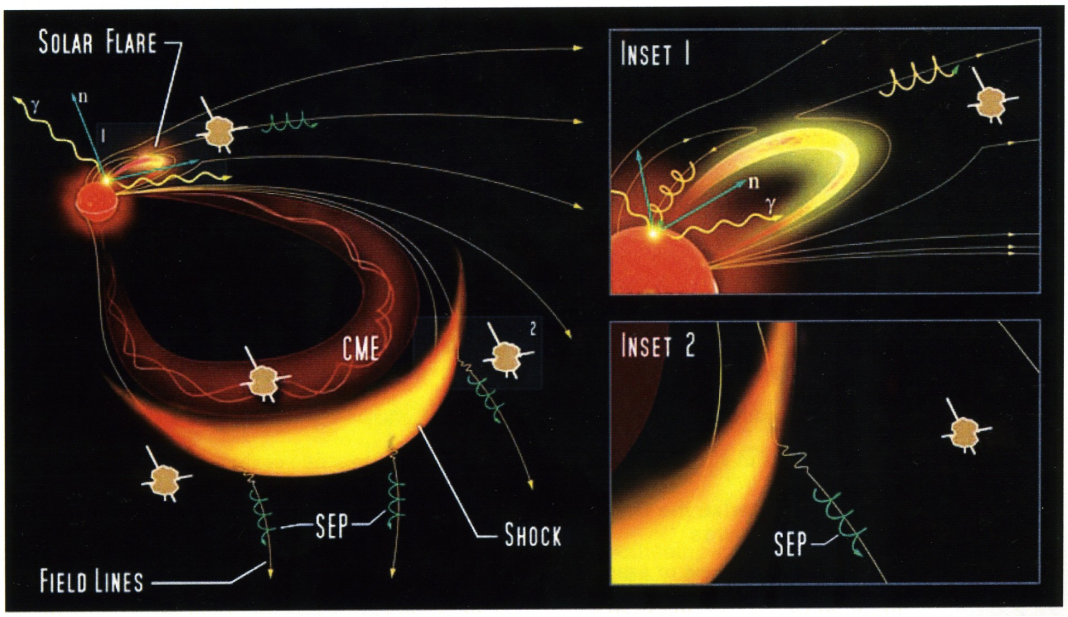

Figure 1.3: Sketch of the two principal sources of energetic particles: a flare (inset 1) and an interplanetary shock (inset 2), both responsible of the accelerated particles that propagate along the IMF lines (from the NASA/TM-2006-214137 (2006) report).

clarified is up to what extend (dependent on the energy) and how flare-accelerated particles play a role in large SEP events (Cane et al. 2003; Tylka et al. 2005; Cliver & Ling 2007, and see also Section 1.1.1.c of the NASA/TM-2006-214137 (2006) report).

Figure 1.3 shows a sketch of these two possible sources of energetic particles: on one hand, inset 1 depicts the occurrence of a flare that may be able to accelerate energetic particles that travel directly along the IMF line toward the position of the detector; on the other hand, inset 2 shows a CME-driven shock propagating away from the Sun whose front intersects different IMF lines, with shock-accelerated particles streaming away along them.

1.1.2 Current understanding of gradual events

The main responsible of SEP events[20] are shocks driven by CMEs[21] (Lindsay et al. 1994; Kahler 2001), with a possible contribution from a concomitant flare[22] at the

[20] Otherwise indicated, hereafter 'SEP event' is a short for 'proton gradual SEP event'.
[21] The interplanetary counterpart of CMEs is often referred as 'Interplanetary CME', ICME (Figure 1.4).
[22] The flare that occurs in temporal association with the CME lift-off.

prompt phase of the event (Cane et al. 2002, 2006). Proton flux and anisotropy[23] profiles of gradual events are consistent with the presence of travelling CME-driven shocks (i.e., Heras et al. 1992, 1995; Kahler 1992; Gosling 1993). The shock can fill with accelerated particles broad regions of the heliosphere (Cliver et al. 1995); hence, the large-scale topology of interplanetary shocks plays a role in the development of SEP events, and the shape of the particle flux profiles displays an organization with respect to the heliolongitude of the solar parent event (e.g., Cane et al. 1988; Domingo et al. 1989; Reames 1990; Richardson et al. 1991).

The observed profiles can be understood as a superposition of particles continuously accelerated at the front of the shock, with their characteristics later on modified by their subsequent propagation along the IMF. There is a large variety of SEP profiles: Figure 1.4 shows four examples of SEP events profiles. Upstream of the shock the IMF is a Parker spiral, while downstream of the shock the propagation of the CME has deformed the structure of the IMF. Due to the relative position of the four observers located at 1 AU (hereafter 1 AU-observers) with respect to the central part[24] of the shock, 'the nose', these proton events are respectively identified (counter-clockwise direction) as western, central meridian, eastern and near eastern-limb[25] SEP events.

These profiles result from the interplay of many factors, as the local geometry and strength of the travelling shock, the existing conditions for shock-particle acceleration, the relative position in space of the observer with respect to the front of

[23] Here 'proton anisotropy profile' refers to the evolution of the normalized first-order anisotropy, A_1/A_0 (defined by Sanderson et al. 1985), in a particle event; see also comments in Section 2.4. The anisotropy profile of the proton population in the upstream part (ahead of the shock) or at the time of the shock passage clearly evidences the role of the interplanetary shock as particle-accelerator (Heras et al. 1994; Kallenrode 2002). This observational variable must be taken into consideration and be fitted when modelling particle events.

[24] The 'nose' of an interplanetary shock is its frontal central region, which is assumed to be in the direction of launch of the CME. Therefore, a central meridian (CM) event is a SEP event generated by an interplanetary shock whose nose travels in the Sun-Earth direction (or W00 heliolongitude); and similarly, a west (W)/east (E) event is a SEP event whose nose moves in west/east direction (Cane et al. 1988), as seen from the Sun.

[25] This is a qualitative identification of SEP events frequently used by modellers and when analysing a set of events or multispacecraft events. It assumes that the shock propagates in CM direction and that several observers are located usually at 1 AU and at different heliolongitudes. Hence, a western event (or W event) has a good IMF connection between the shock front and the observer from the beginning of the event whereas for an eastern event (or E event), the magnetic connection is only established a few hours before the shock passage by the observer.

the shock, the conditions for transport of energetic particles in interplanetary space and the energy of the particles; more details about these factors can be found in recent review papers such as Lario & Simnett (2004); Lee (2005); Vainio et al. (2009); Watermann et al. (2009). For example, CME speeds and SEP intensities are well correlated (Kahler 2001), but for a given CME speed the SEP intensity can vary over four orders of magnitude (Gopalswamy et al. 2003). Gopalswamy et al. (2002) found that 4500 CMEs were observed between 1996 and 2001, but only ~ 100 SEP events with intensity of $> 10\,\mathrm{MeV}$ protons exceeding 1 pfu. Reinard & Andrews (2006) compared those CMEs that do result in SEP events and those that do not, more specifically investigating the differences in CME/flare combinations including the importance of CME velocity, flare duration and CME-flare time delays. The study took a list of SEP events and a list of non-SEP events with similar characteristics. The flare durations and difference in onset time from the CME launch time were not found to be significantly different. They concluded that for SEP events the speeds of the CME are a determining factor but probably in addition to the seed population which could have a dominant effect on the potential for SEP production (see however Cane et al. 2010).

Current models are inadequate to predict with confidence the main features (i.e., onset, duration and flux profiles) of an individual SEP event, because the interpretation of SEP data requires a more accurate description of the solar-interplanetary scenario than we are able to perform at present. Two main reasons can account for this situation: (1) the specific nature of the processes involved in the generation of SEP events is not completely understood, going from the mechanisms that trigger and accelerate CMEs at the Sun (see Manchester et al. 2008b, and references quoted there) to the particle acceleration processes at work at the front of the shock (Cane et al. 1988; Reames 1999; Tylka et al. 2005; Li et al. 2005a; Manchester et al. 2005; Verkhoglyadova et al. 2009). And (2) SEP event simulations require knowledge of the initial conditions near the Sun (e.g., solar wind and magnetic field conditions, etc.). Observations of shocks (plasma and magnetic field measurements) and particles are basically at 1 AU and, whenever possible, they are extrapolated back to near Sun. Hence, as shock and particle observations out of 1 AU are scarce and those existing ones are difficult to link to 1 AU observations, models can hardly rely on observations at the different stages of the generation of SEP events.

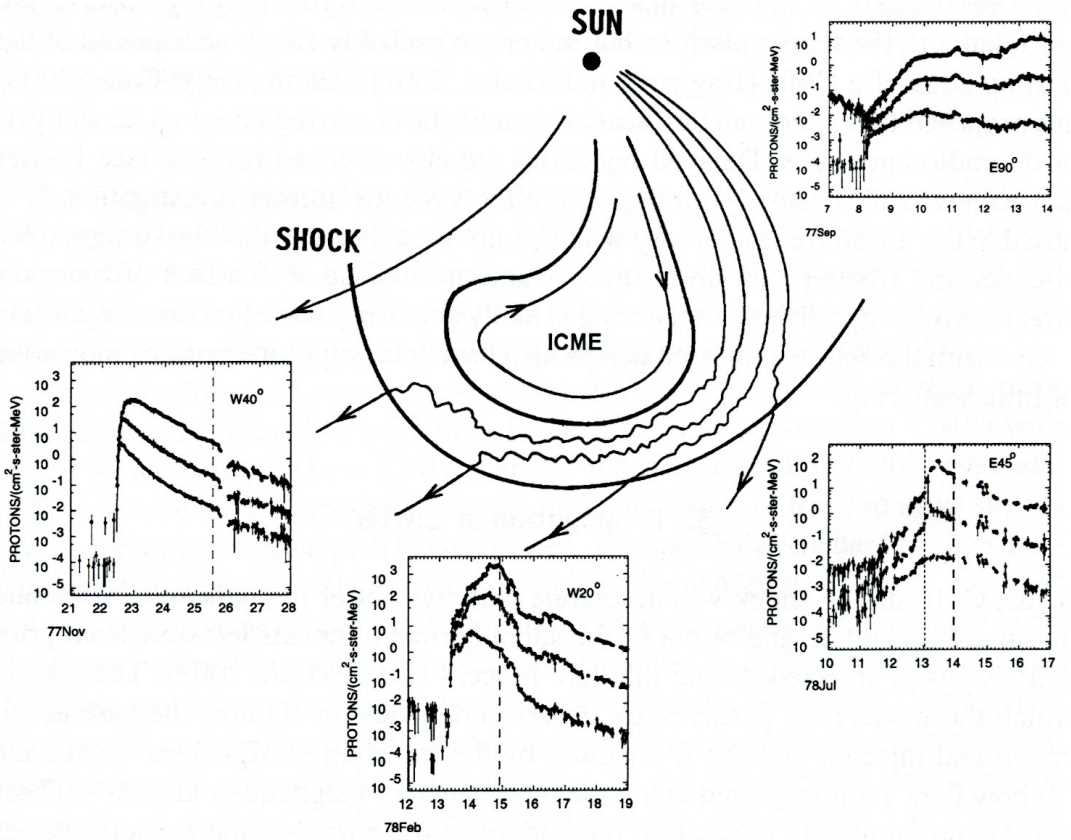

Figure 1.4: Cartoon showing the shape of an interplanetary shock, its ICME driver and the surrounding IMF structure. Proton flux profiles for three energies (approximately 5, 15 and 30 MeV) are shown. The dashed lines in the plots indicate the passage of shocks (from Cane & Lario 2006).

Cane & Lario (2006) point out the elements that future SEP models should include: (1) three-dimensional, 3D[26], simulations of the propagation of shocks from their formation low in the corona (e.g., at few solar radii) to the spacecraft location. (2) Seed particle populations for the mechanisms of shock acceleration that account for possible contributions of the suprathermal remnants from previous SEP events and particles accelerated during the concomitant flaring processes. (3) The evolution of the shock characteristics, due to its expansion and propagation, and of its efficiency at accelerating particles and injecting them into the interplanetary medium. (4) The influence of the IMF structure on the particle transport; for example, on determining the onset times, spectra, time-intensity and anisotropy profiles of the SEP events at different regions of the heliosphere. (5) Realistic transport models in

[26] Hereafter, we will usually refer to one-, two- and three-dimensional as 1D, 2D and 3D, respectively.

complex scenarios formed during SEP events that rarely happen in isolation. And (6) an expansion of the modelled regions of acceleration, specially close to the Sun.

Shocks may accelerate electrons, protons and other ions. However, the high frequency turbulence of the magnetic field required for the scattering of low-energy electrons is often not present. Likely this is the reason why interplanetary shocks are quite inefficient at electron-acceleration (Lee 1997). Therefore, the shock-accelerated component in gradual SEP events is usually a not dynamically significant component (Lee 2005). This inefficiency accounts for the high proton-to-electron ratios observed in gradual events (see, for example, Cane et al. 1986).

1.2 Modelling gradual events

Processes involved in the development of SEP events include the acceleration and transport of particles in a time-dependent system formed by a propagating shock, the associated evolving magnetic field topology, and the formation or existence of magnetic field fluctuations, which, in turn, are also affected by the propagating particles. Therefore, the basic components of a SEP event model are a description of both the propagation of the travelling interplanetary shock and the transport of energetic particles along the IMF lines. As consequence, the modelling of such events has to consider: (1) the propagation and evolution of the shock during its interplanetary journey; (2) the region of the front of the shock where the observer is magnetically connected to; and (3) the conditions of the transport of the particles that propagate along the IMF lines toward the observer's position. Each model has its own simplified assumptions in order to be able to deal with the complex development of SEP events.

Large efforts are devoted to understand the triggering mechanisms of CMEs. This is, to identify and simulate the processes responsible for the chromospheric and coronal instabilities leading to magnetic rearrangement, which finally results in a launch of a CME and its immediate propagation close to the Sun. But not so much efforts are done to track its further interplanetary evolution, for example up to 1 AU[27]. There are also many studies addressing the role and influence of the

[27] Odstrčil et al. (2002b) reads: *"Although significant attention has been given to numerical MHD modeling of CMEs, the focus has generally been divided between considerations of their origin in*

solar wind in the propagation of CMEs as coronal/interplanetary phenomena. Nevertheless, only few of such models pay attention to particle acceleration processes[28]. Conversely, many particle transport models assume that the source of accelerated particles is fixed, usually at or close to the solar surface[29]. In what follows we present a brief overview[30] of the existing models for gradual SEP events, mainly focusing on those that are relevant or face up together the coronal/interplanetary shock formation and propagation, and the transport of energetic particles.

1.2.1 Simulation of the shock

Approximations used to describe the propagation of the coronal/interplanetary shocks had ranged from considering a simple semicircle centred at the Sun propagating radially at a constant velocity, up to fully sophisticated MHD models. Formerly, heliospheric disturbances were often modelled by driving the inner boundary conditions placed upstream of the critical point of the solar wind (at $\sim 20\,R_\odot$); e.g., Wu et al. (1983); Smith & Dryer (1990); Vandas et al. (2002). These models provided basic physical insight into how a large solar disturbance propagates and interacts with the large-scale solar wind. However, there are very few observable parameters at these distances to constrain the boundary conditions. Recently, due to the availability of CPU power and huge computer memories and storage capacity, the propagation of a CME and its driven shock from the inner corona up to 1 AU have been simulated in 2D and 3D geometries. These models may account for new physical and geometrical effects and may allow CME modellers to start incorporating observational data as boundary conditions. Then, simulations have started to become realistic enough to allow detailed comparison with observations. Here we do not intend to review the state-of-the-art of the field, but just to present a summary of the main recent studies. Poedts & Arge (2007) review the recent developments in relation to the solar wind models and the superposed CME-triggering simulations

the solar corona or of their propagation in interplanetary space. Very few attempts have been made to simulate these two aspects simultaneously (...)".

[28] Section 2.3 of the NASA/TM-2006-214137 (2006) report reads: "*Combining the acceleration and the transport of energetic particles is very challenging.*". See also comments on Section 1.1.2 of the same document.

[29] This "fix-source" hypothesis is valid for impulsive events because its duration is short enough to consider that their source remains at the same location on the Sun (e.g., Agueda et al. 2008). This is not true for gradual events.

[30] See the review papers by Vainio et al. (2009) and Watermann et al. (2009) for a detailed description about the actual situation of gradual SEP events modelling, both from the scientific and engineering point of view.

in the solar corona, and the CME propagation in the interplanetary medium. The different CME initiation theories and models are revised by Klimchuk (2001); Forbes et al. (2006); Roussev & Sokolov (2006); Mikić & Lee (2006).

Gibson & Low (1998) developed one of the first 3D CME propagation models. This analytical model is used as a CME generation mechanism in numerical simulations, for example by Manchester et al. (2004b) or Lugaz et al. (2005b); in these simulations the evolution of the CME is followed while it is interacting with a bimodal background solar wind. Manchester et al. (2004a, 2005, 2006) present a 3D numerical MHD model[31] describing the evolution of a CME from the solar corona up to 1 AU, by using the BATS-R-US[32] code. This model is used to explore the sheath region that forms behind the shock because particle acceleration processes strongly depend on the topology of such region. The authors conclude that the sudden post-shock increase in magnetic field strength is effective at accelerating particles to the GeV range and they state that *"this simulation represents and ongoing effort to develop global space weather models that can track and resolve shocks to accurately derive MHD quantities from which SEP properties are calculated."*.

Lugaz et al. (2007) study an event with three interacting CMEs[33], mainly focusing on the interactions among the shocks and reproducing the line-of-sight observations and plasma measurements at 1 AU. They conclude that the main limitations of these simulations are due to the too simple solar wind and CME models adopted[34]. Then, Manchester et al. (2008a) and Manchester et al. (2008b) examine the Thomson-scattered white-light appearance of 3D MHD simulations of CMEs to address the interpretation of the 2D projections of 3D structures observed by

[31] The steady-state corona and bimodal solar wind are based on the model of Groth et al. (2000), that includes open polar field lines and low latitude closed field lines forming a streamer belt (as described in Section 2.2.3); the CME initiation is simulated assuming a 3D magnetic flux rope, picked up from the family of analytical solutions of Gibson & Low (1998).

[32] BATS-R-US: Block Adaptive Tree Solar-Wind Roe Upwind Scheme code (Powell et al. 1999). http://ccmc.gsfc.nasa.gov/models/modelinfo.php?model=BATS-R-US

[33] The background solar wind is based on the varying polytropic index model of Roussev et al. (2003b); the CMEs are initiated using the out-of-equilibrium semicircular flux rope model developed by Roussev et al. (2003a).

[34] Lugaz et al. (2007) stress: *"Getting accurate velocities and compression ratio of shocks in the corona is important, because the acceleration of SEPs is thought to occur within 10* $R_\odot$*. Out-of-equilibrium flux rope models, such the one used in this study, cannot be used if one wishes to reproduce the gradual acceleration of the CME and the formation of shock waves in the corona."*

SOHO/LASCO and STEREO/SECCHI[35] coronagraphs. They find close quantitative comparison with LASCO observations and produce shapes at large elongations as seen by SECCHI. Recently, Lugaz et al. (2009) have performed a similar study for the 24 - 25 January 2007 CMEs and filled the 20 hour gap in SECCHI coverage. This kind of works show the potentiality of numerical simulations to disentangle observational from physical effects and, therefore, to allow the modellers' community to study the 3D nature of the ejections and their evolution in the inner heliosphere[36].

Odstrčil et al. (2002b) present a merged coronal and heliospheric 2D MHD models. For the inner region ($< 20\,R_\odot$), they use the coronal MHD model developed by Mikić & Linker (1994) and Linker & Mikić (1995); whereas for the outer region (from 20 to $220\,R_\odot$) they use the heliospheric axisymmetric MHD model of Odstrčil & Pizzo (1999), being directly driven by the output from the coronal solution. They conclude that the merging of the models enable accurate tracking of a CME from its origin in the solar atmosphere to its arrival at Earth. Riley et al. (2003), using the coupled model of Odstrčil et al. (2002b), perform a MHD simulation to interpret the global context of a CME observed by two spacecraft on February 1999[37]. Odstrčil et al. (2004) and Odstrčil et al. (2005) simulate the 12 May 1997 ICME event trying to reproduce the plasma parameters near Earth, by coupling the ENLIL inner-heliosphere solar wind model (Odstrčil et al. 2002a; Odstrčil 2003; Odstrčil et al. 2004) together with the MAS[38] coronal model. They reconstruct the ambient solar wind from photospheric magnetograms and they simulate a perturbation based on the 3D cone model of Zhao et al. (2002) and Odstrčil et al. (2004), which uses geometrical and kinematic fitting of coronagraph observations of CMEs.

[35] STEREO: Solar TErrestrial RElations Observatory. http://stereo.gsfc.nasa.gov/

[36] They conclude: *"This study reflects the start of a new era where, on one hand, models of CME propagation and interaction can be fully tested by using heliospheric observations and, on the other hand, observations can be better interpreted by using global numerical models."*

[37] They present a detailed analysis of the plasma, magnetic field and composition signatures of two interplanetary shocks observed in late February 1999 by ACE spacecraft at 1 AU in the ecliptic plane, and thirteen days later by Ulysses at 5 AU and 22° S. Using a MHD simulation of a fast CME initiated at the Sun by magnetic flux cancellation and propagated out into the solar wind, they argue that both spacecraft observed the same CME-driven shock.

[38] MAS: Magnetohydrodynamics Around a Sphere coronal model (Linker et al. 1999; Mikić et al. 1999; Riley et al. 2001).

Lee et al. (2009) couple ENLIL with the MAS or the WSA[39] coronal models to investigate how well the models describe the solar wind structure from the Sun out to 1 AU. The 3D outputs of these simulations are compared with ACE solar wind measurements for the time period of the declining phase of Solar Cycle 23. They find an overall agreement for the general large-scale structures and trends, such as the timing of the high-density structures and the low- and high-speed winds. Recently, Falkenberg et al. (2010) investigate the sensitivity of the ENLILv2.5b[40] model to its solar input parameters, by reproducing the CME event of 25 July 2004. They find that the largest effects on the outputs are the fast solar wind velocity and the CME density, and that though the model currently does not include the magnetic cloud of the ICME, it reproduces well the signal at L1 in the studied event since the arrival time difference between simulations and satellite data is less than 30 minutes.

Chané et al. (2005, 2006) and Jacobs et al. (2005, 2006a,b) thoroughly analyse the initialization and propagation of a CME (by using an initial density-driven perturbation) up to $30\,R_\odot$, checking how the global characteristics of the CME as well as the evolution of the interplanetary shock wave rely on the background wind model used or on the magnetic polarity of the initial perturbation. They conclude that this initial magnetic polarity strongly relates to the geo-effectiveness of the CME and to its arrival time at the position of the observer. Jacobs et al. (2007) extend these analyses to 3D modelling to point out the differences between the 2.5D and 3D simulations, and conclude that the 2.5D MHD simulations are a good approach to estimate the arrival time of the shock. In addition, the results obtained with this model resemble well those obtained with the 3D simulations. Jacobs (2007) modifies and extends up to 1 AU the previous model to compare the results with LASCO observations. They conclude that the white light images of the simulated CME were clearly missing the three part front-cavity-core structure which is described as the typical CME morphology. However, the simulated CME event showed similarities with the observed SEP event, as can be a strong deceleration of a fast CME, the shock strength and the arrival time. More recently, Chané et al. (2008) use a 2.5D axisymmetric model to simulate a CME by superimposing a high-density and high-

[39] WSA: Wang-Sheeley-Arge coronal model (Wang & Sheeley 1990; Arge et al. 2004). http://ccmc.gsfc.nasa.gov/models/modelinfo.php?model=WSA/PF%20with%20CS

[40] This ENLIL version uses the cone model of Zhao et al. (2002) and Odstrčil et al. (2004) to initialize the perturbation.
http://ccmc.gsfc.nasa.gov/models/modelinfo.php?model=ENLIL%20with%20Cone%20Model

velocity magnetized plasma blob on the background solar wind and they discusse how to combine observations (from ACE, for this particular case) with the numerical simulations to determine the initial characteristics of the solar parent activity.

Tsurutani et al. (2003) use a 2.5D MHD code to study the formation properties of a CME-driven shock and its propagation toward 1 AU. Their case of study is the 6 January 1997 event. Starting from the inner corona, they find that a fast forward shock forms at $\sim 3.2\,R_\odot$ from the solar surface in the ecliptic plane, and at $\sim 3.6\,R_\odot$ at higher latitudes ($\sim 30°$), because the higher the latitude, the higher the local magnetosonic speed that the original disturbance must exceed to become a shock; finally, they find that the shock becomes symmetric at $16\,R_\odot$. These shock properties are relevant to the ability of the shock to accelerate particles up to 100 MeV. Wu et al. (2005b) develop a 3D MHD model to investigate the criteria for initiating a solar eruptive phenomena; this model can incorporate realistic photospheric dynamics together with the differential rotation and meridional flow. Then, Wu et al. (2006) study the nature of interacting CME shocks, extending their previous work on the Halloween 2003 events (Wu et al. 2005a). Their results show that the solar wind speed might increase about $\sim 25\%$ after the collision of two shocks, pointing out that this kind of interaction can affect the accuracy of the identification of the solar source that causes the interplanetary event.

Shen et al. (2007) use the halo-CME event of 6 January 1997 to test the dynamical interaction of a CME with the non-homogeneous background solar wind flow constructed on the basis of the observations of the solar magnetic field and K-coronal brightness. They find that the 3D MHD model, with the self-consistent structures on the source surface as input, provides a relatively satisfactory comparison with Wind spacecraft[41] observations of this event. Recently, Shen et al. (2010, private communication) have presented an improved version of this model[42], where the main change is the introduction of a simple flux rope model with a given initial velocity and launch direction in order to simulate the CME. Such model, based on the flux rope developed by Chané et al. (2008), consists of a 3D high density and high velocity magnetized plasma blob superposed on a background steady state solar wind. They have compared the simulation outputs with the ACE spacecraft

[41] Wind spacecraft. http://wind.nasa.gov/
[42] This model will be further commented in Chapter 7.

observations of the halo-CME event of 4 April 2000 finding satisfactory results.

1.2.2 Determination of plasma variables at the front of the shock

There is a well developed body of models and procedures to determine, from solar wind plasma and IMF observations, the main features of interplanetary disturbances (e.g., shocks, discontinuities) that sweep a given observer in space. Although important for modelling SEP events, these tools have been rarely worked out in the context of shock propagation modelling[43]. Hsieh & Richter (1986) stated, *"to identify observed plasma and magnetic field discontinuities in interplanetary space as MHD shocks requires fitting the plasma and magnetic field data to the Rankine-Hungoniot conditions"*. It is usually assumed an ideal shock to determine the shock features, with a well-defined pre-shock (upstream) medium of uniform plasma and magnetic field, and a well-defined post-shock (downstream) medium. Plasma density and velocity, and magnetic field intensity values across the shock must satisfy the conservation laws and Maxwell's equations, known as the Rankine-Hugoniot conditions[44] (Courant & Friedrichs 1948; De Hoffmann & Teller 1950).

Unfortunately, the interplanetary medium is never uniform, even in the absence of shocks. Actually, observations show the frequent presence of large deviations from stationary state in the 'quiet solar wind'. Moreover, shocks may be followed by great fluctuations in both the plasma and magnetic field which largely extend in the downstream region. Then, it is when the problem of choosing the supposedly constant upstream and downstream parameters appears. Colburn & Sonett (1966); Lepping & Argentiero (1971); Abraham-Shrauner (1972); Abraham-Shrauner & Yun (1976); Chao & Hsieh (1984) show how to estimate the shock normal $\hat{n}$, the shock velocity v_s, the θ_{Bn} angle, the Alfvén Mach number M_A, and other parameters that characterize the shock. But none of these works directly deals with the issue of where the upstream and downstream values should be taken.

Most of the existing methods for the determination of interplanetary shocks use temporal solar wind and magnetic field data series; i.e., time-averaged data

[43] Except in theoretical models of particle acceleration at shocks (perpendicular, oblique or parallel), but rarely linked to specific events and usually only presented as a cartoon.

[44] Hereafter referred as R-H conditions or, simply, the "jump conditions".

taken immediately in front and behind the discontinuity. Viñas & Scudder (1986); Berdichevsky et al. (2001); Szabo (1994); Koval & Szabo (2008) developed algorithms based on least squares minimization of the set, or a subset, of the R-H conditions; even when trying to understand some observational features by comparing them with simulations, the identification is done by using time-averaged data (Vourlidas et al. 2003). On the other hand, Lin et al. (2006); Feng et al. (2007); Lin et al. (2008) propose a method of shock fitting based on the full set of the R-H relations and the coplanarity property, within which they use a Monte Carlo calculation together with the least squares technique. These models are usually applied to a single-point shock measurements (or to a couple of them in the scarce existing interplanetary multi-spacecraft studies), and they do require visual inspection of the data in order to choose regions close to the shock passage and at its both sides (upstream and downstream regions) where to evaluate the MHD variables[45]. Hence, these methods are not well suited for automated detection in a shock simulation, which must deal with a huge amount of data that renders impossible an individual visual approach.

Based on these methods, Lario et al. (1998) tackle this problem since plasma parameter values at the shock front are needed for SEP modelling; in particular, the location and the strength of the simulated interplanetary shock. Luhmann et al. (2010) have recently developed a shock finder program that searches for the largest gradients in the MHD parameters along an observer-connected field line at a particular time step: starting at the 1 AU-observer end of the IMF line and mapping it back toward the Sun, the shock location is identified as the largest gradient found for a specific MHD variable[46]. From that point, the upstream and downstream regions are identified[47]. The density compression ratio and other shock parameters are calculated at the point of the largest gradient. But, as Luhmann et al. (2010) comment, the downstream values used to compute the jump conditions are difficult to determine because usually there is no plateau (or it is very small) in the downstream region where the peak value is identified. It is worth to point out that the use of the gradient method along the field line can underestimate the shock strength for

[45] Frequently supported by a further statistical analysis (Richter et al. 1985).

[46] They find that both dynamic pressure and density provide the clearest identification of shock gradients, being those of the dynamic pressure the most robust ones.

[47] Outward, the upstream point is located there where the MHD variable drops to less than 10 % of its value at the shock location; while going inward, the downstream point is situated where the gradient is zero or changes sign.

quasiperpendicular shocks, but the authors assume that the shock is so large-scale that the quasiparallel geometry adequately describes the scenario. This assumption allows them to skip considerable numerical complications when computing the jump conditions along the shock normal, with the final results providing the most direct test of such assumption. However, as Luhmann et al. (2010) note: *"We plan to eventually revise the shock finder program to use the shock normal direction to define the shock jump, however, this more desirable but more computationally intensive option will still be subject to the same difficulties of identifying what is upstream and what is downstream in a highly structured medium.(...) In any case shock identification in the MHD codes remains a key challenge for SEP event modelling."*.

1.2.3 Modelling the transport of energetic protons

Many efforts have been made to include the mechanisms of particle acceleration in interplanetary shocks, mainly based on the assumption that the diffusive shock acceleration mechanism is responsible for particle energization.

Heras et al. (1992) and Heras et al. (1995) reproduce the low-energy fluxes and anisotropies of several large particle events associated with interplanetary shocks triggered by solar activity. They use a compound model to describe the evolution of the shock and the particle propagation in the interplanetary medium (see Chapter 2). They derive the injection rate of shock-accelerated particles as a function of time and the mean free path for their propagation along the IMF, and they relate the variations of the efficiency of such injection with the plasma conditions at the shock region magnetically connected to the observer (i.e., the cobpoint, see Section 2.1). Lario (1997) and Lario et al. (1998) improve this approach by including the solar wind convection and the adiabatic deceleration effects in the particle transport equation. This model has been successfully applied to reproduce low-energy ($< 20\,\mathrm{MeV}$) proton flux and anisotropy profiles, as well as high-energy (up to $200\,\mathrm{MeV}$) flux profiles (A. Aran, 2010, private communication) for a number of SEP events, some of them observed by several spacecraft (Aran et al. 2007). An extensive description of these models and their applications is given in Section 2.1.

Kallenrode & Wibberenz (1997a) and Kallenrode (2001) adopt the same scheme as these previous works but, instead of a MHD model to describe the shock, they use a semicircle perturbation propagating radially from the Sun at a constant speed.

They also arbitrary parametrize the injection rate of shock-accelerated particles in terms of a radial and azimuthal variation, which represents the temporal and spatial dependences of the shock efficiency at accelerating particles. This model allows for particle propagation in the downstream region, but it does not take into consideration that different topologies of the shocked IMF lines may lead to different effects in the particle transport, yielding different results (Lario et al. 1999). Torsti et al. (1996) adopt a similar scheme as that of Lario et al. (1998), but assuming that the distance from the front shock to the observer along the IMF line decreases linearly with time[48].

Ng et al. (1999) and Ng et al. (2001) have developed a numerical model where the particle transport includes the effect of self-generated Alfvén waves by streaming protons. Ng (2007) also considers wave evolution by means of wave excitation and damping. For particles, this model incorporates magnetic focusing, scattering by Alfvén waves, solar wind convection and adiabatic deceleration. They apply this model to simulate several gradual SEP events in order to derive the time variations and energy spectra of elemental abundance ratios, the Fe/O and He/H ratios. An advantage of this model with respect to the above-described ones is that the particle pitch-angle diffusion coefficients are described in terms of wave intensities[49]. However, a disadvantage of this model is that it does not consider the evolution of the shock as a mobile source of particles as it propagates throughout the heliosphere.

The numerical approach of Vainio & Laitinen (2007) addresses the time dependence in particle acceleration and Alfvén waves generation at quasi-parallel shocks. Their results show that these processes can be described by quasi-stationary state models of shock acceleration, being its main drawback the treat of the shock as a boundary condition.

Zank et al. (2000) present a dynamical model of particle acceleration at evolving interplanetary shocks. This model assumes that the solar wind suprathermal particles are injected into the shock at certain energy, with the diffusive shock accel-

[48] Differences among the above models have been described in Sanahuja & Lario (1998) and Kallenrode (2001).

[49] The spectrum of scattering waves is developed self-consistently with the spectrum of energetic particles, which are themselves assumed to be generating the waves resonantly (Lee 1983; Ng et al. 2003).

eration process at work[50]. The basic success of this model is that it can reproduce the observed spectral break in the energy spectrum of energetic particles (when integrated over the transit from the Sun up to 1 AU). Rice et al. (2003) and Rice & Zank (2003) extend the work of Zank et al. (2000) to shock waves of arbitrary strength. The model is able to calculate the minimum and the maximum energy of the particles as the shock propagates out and can determine the evolution of the spectra of particles escaping into the upstream and downstream region. Li et al. (2003) simulate the transport of shock-accelerated particles by using a Monte-Carlo approach. Coupling it with the work of Rice et al. (2003) on particle acceleration at shocks, they are able to investigate the characteristics (intensity profiles, angular distribution, particle anisotropies) of high-energy particles arriving at various distances from the Sun, mainly addressing the affectation of interplanetary turbulence on particle transport.

Based on these former works, Verkhoglyadova et al. (2009) use the PATH code[51] to model the gradual SEP event observed on the 29 September 2001. The study is restricted to 1D modelling, that is, they consider a spherically symmetric shock and assume that all physical parameters only depend on the radial distance from the Sun. This implies that the shock connection to the spacecraft by the IMF remains in a quasi-parallel configuration as it propagates from the solar corona to 1 AU. Verkhoglyadova et al. (2010) modify the PATH code to accommodate the simulation of flare-accelerated particles in their model in order to simulate mixed SEP events. In particular they study the event on 13 December 2006. They assume, again, a shock propagating with a fixed obliquity and modify the particle transport conditions of previous works by introducing a particle perpendicular diffusion coefficient. For this event, they find a good agreement with observed proton, oxygen and iron ion spectra, whereas their resulting intensity-time profiles reproduce only some aspects of the measured proton and ion profiles. Actually, Verkhoglyadova et al. (2010) stress the fact that an important modification that remains to be done to

[50] This initial approach has important limitations (see Lee 2005). Furthermore, the interplanetary transport of particles is scarcely developed.

[51] PATH: Particle Acceleration and Transport in the Heliosphere (Zank et al. 2000; Rice et al. 2003; Li et al. 2003, 2005b). This code has two parts: the simulation of an interplanetary shock and particle acceleration (based in the ZEUS code; see Rice & Zank 2003), and the transport of particles through the heliosphere. Thus, it includes local particle injection at an evolving quasi-parallel shock, first-order Fermi acceleration, and self-consistent excitation of MHD waves to enhance particle scattering, trapping and escape from the shock, and transport.

the PATH code is the inclusion of 2D shock modelling in order to simulate shocks of changing geometry.

Lee (2005) presents an analytical quasilinear theory for the evolution of a gradual event that generalizes the approach of Lee (1983). The upstream transport of particles is based on the two-stream moments of the focused transport equation, which accommodate the large streaming anisotropies and escape far from the shock. The model includes diffusive shock acceleration, ion advection with the solar wind, magnetic focusing and wave excitation by the energetic protons. The predictions reproduce the onset, the 'plateau' and the flux enhancement prior to shock passage, as well as the decaying invariant spectra after the shock passage. However, there are relevant discrepancies with observations when comparing the resulting energy spectra, spatial gradients and high-energy cut-off of the ion distributions.

1.2.4 CSEM and CISM Modelling Frameworks

Two groups, the Center for Space Environment Modelling (CSEM)[52] and the Center for Integrated Space Weather Modelling (CISM)[53], are developing space weather-oriented models of the inner heliosphere. Their aim is to link models to describe different physical environments from the solar corona up to the orbit of Mars, including the Earth magnetosphere.

The CSEM group has developed the Space Weather Modelling Framework[54], which is designed to couple self-consistently a number of independent physics-based models covering from the surface of the Sun to the upper atmosphere of the Earth. Within this framework, J. Kota[55] has developed a numerical model for particle propagation based on the coupled solution of the focused transport equation and the wave kinetic equation, including shock acceleration by imposing a boundary condition of the transport equation at the shock. This model uses one IMF line advected with

[52] The CSEM is a consortium of a dozen US institutions leaded by University of Michigan (see Gombosi et al. 2004; Tóth et al. 2005). http://csem.engin.umich.edu

[53] The CISM is a NSF center at Boston University, consisting of research groups at eight universities and several US governmental research organizations (see Luhmann et al. 2004). http://www.bu.edu/cism/index.html

[54] SWMF: http://butch.engin.umich.edu/swmf

[55] Private communication to Manchester et al. (2005) and Tóth et al. (2005); quoted there as 'submitted manuscript to The Astrophysical Journal (2005)', but so far not published. For announced preliminary results of this model see Kota et al. (2004) or Kóta et al. (2005).

the plasma, whose geometry and the plasma parameters along it are obtained from a CME model, calculated with the the global BATS-R-US code. Roussev et al. (2004) constructed a fully 3D MHD model of a CME that incorporates solar magnetogram data and a loss-of-equilibrium mechanism, and they show that a CME-driven shock can develop close to the Sun ($\sim 4\,R_\odot$) and that it is of a strength sufficiently high to have accelerated ($> 2\,GeV$) SEPs during the solar eruptive event that took place on 2 May 1998.

Sokolov et al. (2004) extend these previous works by developing a new code, the FLAMPA[56] code, with the aim of simulating the time-dependent transport and diffusive acceleration of particles at CME-driven shocks. FLAMPA is coupled with the CME model developed by Manchester et al. (2005) to simulate the effects of particle transport and diffusive acceleration as the shock evolves between $4\,R_\odot$ and $30\,R_\odot$. Then, they compare the outputs of the simulation at 1 AU with the high-energy proton fluxes observed by GOES-8 satellite for the 2 May 1998 event. Recently, Sokolov et al. (2009) have included wave dispersion due to Alfvénic turbulence in the particle transport equation. They simulate the 21 April 2002 SEP event by coupling the FLAMPA code with the derived wave spectrum evolution[57]. Their main conclusions are that the outgoing waves, which are resonantly generated by the upstream particles, are strongly enhanced in front of the CME-driven shock[58], and that the waves propagation sunwarding become dominant in the downstream region for a wide range of wave frequencies.

Luhmann et al. (2004) perform a SEP event simulation employing the coupled model approach of the CISM framework. The simulation uses coronal, solar wind, and magnetosphere MHD models (the so-called CORHEL[59] model), and an upper atmosphere/ionosphere fluid dynamic model. Luhmann & Mann (2007) use the heliospheric MHD simulation of the 12 May 1997 ICME performed by Odstrčil et al. (2004) with the aim of illustrating an approach to model the associated SEP

[56] FLAMPA: Field Line Advection Model for Particle Acceleration.

[57] Extending, in this way, the work performed previously by Sokolov et al. (2006a).

[58] This effect is responsible for the capture and scatter of upstream electrons, which allows the SEPs to be repeatedly involved in the acceleration process.

[59] CORHEL: Corona-Heliosphere. The last version of CORHEL offers six possible model combinations and works with synoptic magnetograms from six observatories. It supports two coronal models (MAS and WSA method), and two heliospheric models (MAS and ENLIL). Either of the coronal models can be coupled with either of the heliospheric models. http://ccmc.gsfc.nasa.gov/models/corhel-note.php

event, which emphasizes the importance of knowing the observer connected shock source time history. From their study the authors conclude that the combination of a relatively simple shock source description and a scatter-free propagation can approximate an observed SEP time profile. More recently, Luhmann et al. (2010) extend the study to two other SEP events, in order to illustrate the potential utility of such model for interpretation of separated multipoint measurements, such as those expected from the STEREO mission. The two main differences with respect to other models (as, for example, Aran et al. 2007; Kocharov et al. 2009) are: (1) they assume that the influence of the shock evolution, as particle accelerator, dominates over the diffusive transport when deriving the SEP time profiles; and (2) that the particles accelerated around the time of the observer connection dominate what is detected.

All models, so far, include rough approximations, being the most evident: (1) prescribed ideal IMF configurations (e.g., stable Parker spiral). (2) The use of 1D models in some cases (e.g., PATH code) while the simulation of in-ecliptic spacecraft SEP observations requires the use of, at least, 2D models for the shock and particle propagation[60]. (3) The assumption that a specific shock-acceleration particle mechanism works at the travelling shock is an oversimplification in view of the rich diversity of events observed in association with the passage of interplanetary shocks (Tsurutani & Lin 1985; Lario et al. 2003). (4) The existence, or not, of a background population that could act as seed population for further shock-particle acceleration (Desai et al. 2006). And (5) the introduction of shocks at arbitrary ($\sim 20\,R_\odot$) distances from the Sun, when there is strong evidence that particle acceleration may start closer to the Sun ($\sim 2\,R_\odot$). The number of variables needed to describe the overall SEP scenario is large and hard to handle.

The conclusion of Lee (1997) reads: *"The challenge to theoreticians is to develop a model of shock acceleration which includes quantitatively the 3D geometry and solar wind, the evolving shock wave, a realistic diffusion coefficient, possibly ion-excited waves, and a transition from scatter-dominated transport near the shock to nearly scatter-free transport in interplanetary space. Only then can the observed particle energy spectra and time profiles be used to learn about the origins of solar energetic*

[60] For example, the longitudinal dependence of SEP flux profiles observed can not be reproduced if the IMF connection between the shock and the observer is assumed to be a purely radial IMF (as in Reames et al. 1996).

particles close to the Sun". And we add: in order to later on be able to make reliable predictions.

1.3 Space Weather interest

Gradual SEP events present one of the most severe hazards in space environment, specially important for the launch and operation of space vehicles, for space missions to the inner solar system, where the radiation levels are the highest, and for human exploration of the Moon and Mars[61]. The NASA Radiation Working Group Report (Golightly et al. 2005) stated: *"It is still not possible to forecast with accuracy whether a particular observed CME will result in a SEP event at Earth, and if so the intensity or duration of the event"*. A relevant issue of the Space Situation Awareness Programme of the European Space Agency (ESA) is the research oriented to reduce the vulnerability of space assets. Furthermore, the 7th EU Framework Programme for Research and Technological Development specifically supports producing *"space weather models to improve specification and prediction capabilities, with emphasis on the linkage of the different physical processes that occur simultaneously or sequentially in many domains"* (2009 FP7 call, "SPA.2010.2.3-01 Security of space assets from space weather events")[62].

Solar radiation storms are of most interest in space weather. So, it is important to be able to predict when and how strong a SEP event might be on the basis of routine observations of the solar corona and the near-Sun solar wind. But at present, there is a wide gap between what models predict and the reality of gradual SEP events. Hence, models that can describe how shock-acceleration of particles occurs

[61] An overall presentation of the space weather effects can be found in 'Severe Space Weather Events–Understanding Societal and Economic Impacts: A Workshop Report (2008)'. Specific hazards due to radiation are addressed in 'Space Radiation Hazards and the Vision for Space Exploration: Report of a Workshop (2006)'.

[62] As a matter of fact, European institutions are following the objectives of the U.S. National Space Weather Program Strategic Plan, created in 1995 (http://www.nswp.gov), which has been recently (June 2010) reviewed and redefined (available at http://www.ofcm.gov). This new plan describes how to capitalize on advances in science and forecasting to better cope with the adverse impacts of space weather on human activity and on advanced technologies that underlie the global economy and national security. This plan defines five goals: (1) discover and understand the physical conditions and processes that produce space weather and its effects; (2) develop and sustain necessary observational capabilities; (3) provide tailored and accurate space weather information where and when needed; (4) raise national awareness of the impacts of space weather; and (5) foster communications among government, commercial and academic organizations (from Williamson et al. 2010).

and how these particles propagate throughout the interplanetary space are needed. In this way, some time, we might be able to successfully forecast SEP events and correctly evaluate the risk they represent.

In fact, CSEM and CISM consortia are space weather-oriented interdisciplinary groups (Section 1.2.4) and the NASA CCMC[63] is a multi-agency partnership to enable support and perform the research and development for next-generation space science and space weather models. Recently, the Earth-Moon-Mars Radiation Exposure Module (EMMREM) has been developed in the frame of the CSEM and CISM consortia (Schwadron et al. 2010). EMMREM is aimed at characterizing the time-dependent radiation exposure in interplanetary space environments and it has been used to study the radial and longitudinal dependence of proton peak intensities and fluences, and radiation dose equivalents of SEPs at eight different locations between 1 AU and 5 AU (Dayeh et al. 2010). This coupled solar wind-energetic particles code uses initial conditions derived from solar wind and energetic particle observations at 1 AU to produce predictions at radial distances beyond 1 AU, up to $\sim$5 AU (Dayeh et al. 2010; Kozarev et al. 2010).

1.4 Aims of this thesis and outline

The aim of this thesis is to tackle some aspects of the challenge mentioned by Lee (1997). An important part of this work deals with 3D MHD simulations of the shock starting close to the Sun, addressing the potential relevance of the heliolatitude (i.e., latitudinal angular location of the observer with respect to the interplanetary shock) and the evolution of the strength of the shock. The influence of the latitude has not been quantitatively considered yet in simulations of gradual SEP events, basically because most of the codes used until now to model shocks associated with gradual SEP events are 1D, 2D or 2.5D codes. The scarce number of attempts to simulate SEP events using 3D models for CME propagation have been applied to near-ecliptic SEP observations. Nevertheless, the Sun does not necessarily launch CMEs in the direction of the ecliptic plane! Hence, 3D models out of the ecliptic plane are essential to reliably reproduce the features that account for a SEP event. Moreover, the evolution of the shock variables near the Sun are necessary to reproduce the onset phase of many gradual events.

[63] CCMC: Community Coordinated Modeling Center. http://ccmc.gsfc.nasa.gov

To gain knowledge about the relation between the strength of a shock at its front and the injection rate of shock-accelerated particles in interplanetary space, as well as the influence of the latitude of the observer in the derived proton flux profiles, we have analysed the main features of several shock variables at the the point of the shock where the observer is magnetically connected to (i.e., the cobpoint). We have used the 3D MHD model developed by C. Jacobs (Jacobs 2007) to simulate the generation and propagation of CME-driven shocks. We have simulated several shocks and we have followed their evolution up to a set of spacecraft situated at 0.4 AU and 1.0 AU, and at different heliolongitudes and heliolatitudes. Our main goal in this part of the work is to study the influence of the strength of a 3D shock on the injection rate of shock-accelerated particles, and, thus, on the resulting SEP flux profiles. We focus our interest in improving the location of the cobpoint, the characterization of the front of the shock and to get a better determination of the jumps of the plasma variables across the shock front. To do it, we have developed a procedure which takes into account the fact that we are dealing with a 3D geometry.

Moreover, we present the simulation of an event observed by three spacecraft by using a new 2D MHD model developed by C. Jacobs (Aran et al. 2011) under the SEPEM project[64]. Such event took place on 1 March 1979 and has the particular interest that it was observed by four different spacecraft, located at similar radial distances from the Sun but at significantly different angular positions from the site of the associated solar source. Therefore it gives us the opportunity to test the capability of the model to study the relevance of the longitudinal variations on the shape of the SEP intensity profiles. The main aim is to draw conclusions on the influence of the relative position of the observer on the injection rate of shock-accelerated particles and on the particle transport conditions observed by each spacecraft.

The outline of this report is as follows. Chapter 2 deals with the specific scenario and the models we are going to work with. We summarize the main characteristics of the shock-and-particle models and we describe in detail their basic components, pointing out those parts that are being presently improved as well as those downsides that should be considered for a future work. Chapter 3 presents the 3D scenario,

[64] Solar Energetic Particle Environment Modelling, SEPEM, project (supported through an ESA contract): http://sepem.aeronomie.be

together with a detailed description of the new procedure developed in order to determine, classify and characterize the shock. In Chapter 4 we discuss its application to 3D shock simulations up to several spacecraft located at different radial, longitudinal and latitudinal positions and we derive conclusions on the influence of the latitude of the observer and of the strength of the shock on the derived synthetic flux profiles. Chapter 5 and 6 show an application of a new shock-and-particle model. We have performed the simulation of the SEP event observed on 1 March 1979 by Helios-1, Helios-2 and IMP-8/ISEE-3 spacecraft. We describe the 2D scenario of this particular event and present the shock propagation modelling results in Chapter 5. In Chapter 6 we present the fitting of the observed proton intensities and we draw conclusions on the influence of the relative position of the observer on the injection rate of shock-accelerated particles and on the particles transport conditions found for each spacecraft. In Chapter 7 we summarize the main results obtained with these studies and we comment some future perspectives.

This work has been supported by the Spanish projects AYA2004-03022 (Ministerio de Educación y Ciencia) and AYA2007-60724 (Ministerio de Ciencia e Innovación). We also acknowledge the computational support provided by the Centre de Supercomputació de Catalunya (CESCA), the VIC cluster at the Katholieke Universiteit Leuven and the MareNostrum cluster of the Barcelona Supercomputing Center (BSC). We acknowledge the use of the 2D MHD model developed under the frame of the SEPEM project.

Chapter 2

Shock-and-particle models

> Detrás de lo que creemos conocer
> de sobra se esconde una cantidad
> equivalente de desconocimiento.
>
> *Sputnik, mi amor*, Haruki Murakami

2.1 Overall description of the SaP98 model

The first Shock-and-Particle (SaP) propagation model for SEPs was developed by Heras et al. (1992, 1995). The main features of this compound model are: (1) the inclusion in the focused-diffusion transport equation of a source term representing the injection rate of particles accelerated at the travelling shock. Solving this equation allowed us to reproduce the large and long-lasting anisotropies frequently observed in gradual SEP events (Heras et al. 1994). And (2) the explicit and quantitative implementation of the "cobpoint" (Connecting with the OBserver POINT) concept by analogy with footpoint, the solar root of an IMF line, but associated with an interplanetary mobile source of particles. This model uses the MHD code of Wu et al. (1983) to perform simulations of the interplanetary shock propagation from $18\,R_\odot$ from the Sun up to 1.1 AU.

Lario (1997) and Lario et al. (1998) developed the SaP98 model, an improved version of Heras' model. The basic components of SaP98 are two models that provide a suitable description of both the propagation of the travelling interplanetary shock and the transport of the energetic particles along the IMF lines. The main improvement of SaP98 is the inclusion of the solar wind convection and adiabatic

deceleration effects in the transport equation of protons (Ruffolo 1995). Then, the resulting set of linked transport equations (for different energies) yields a large reduction on the number of free parameters with respect to former approaches that solved the transport equation independently for each energy considered.

SaP98 uses the same MHD code as Heras et al. (1995) for the simulation of the interplanetary shocks, plus the aforementioned more complete transport equation to describe the propagation of the energetic particles. The cobpoint concept permits us to connect both models; particularly, to compare at the cobpoint, for each given time, the values of the solar wind plasma variables and magnetic field, derived from modelling the shock propagation, with the values of injection rate of shock-accelerated particles, derived from fitting the flux and anisotropy profiles of SEP events observed at different energies. As the shock propagates and expands, the cobpoint moves along its front. The cobpoint describes different paths there, depending on the heliolongitude of the solar activity that generates the shock; that is, depending on the position of the observer with respect to the leading direction of the shock front. Thus, at a given time, observers in space located at different radial distances or heliolongitudes may define different cobpoints in the shock front. Figure 2.1 sketches the evolution of the cobpoint along the front of a shock (snapshots 1 to 4): it moves toward the shock nose as it approaches the observer. Examples of SEP events showing different behaviours of the cobpoint can be found in Lario et al. (1998) and Aran et al. (2007).

The main parameters of SaP98 are Q and $\lambda_{||}$, both derived from the fitting of observed particle intensity-time profiles and first-order parallel anisotropies. The variable Q is the injection rate of shock-accelerated particles at a given energy, time of the simulation and position of the cobpoint. By fitting simultaneously several particle differential intensity channels we derive the spectrum evolution of Q. The parallel mean free path of the protons, $\lambda_{||}$, is a first order description of the effects of the particles interaction with the IMF during their journey towards the observer. The remaining outputs of the particle transport model are the simulated flux and anisotropy profiles for a set of energies. Since the simulation of the shock propagation and the fitting of particle flux profiles work independently, any empirical relation found between the injection rate of shock-accelerated particles, Q, and the solar wind plasma and magnetic field variables does not depend on the processes

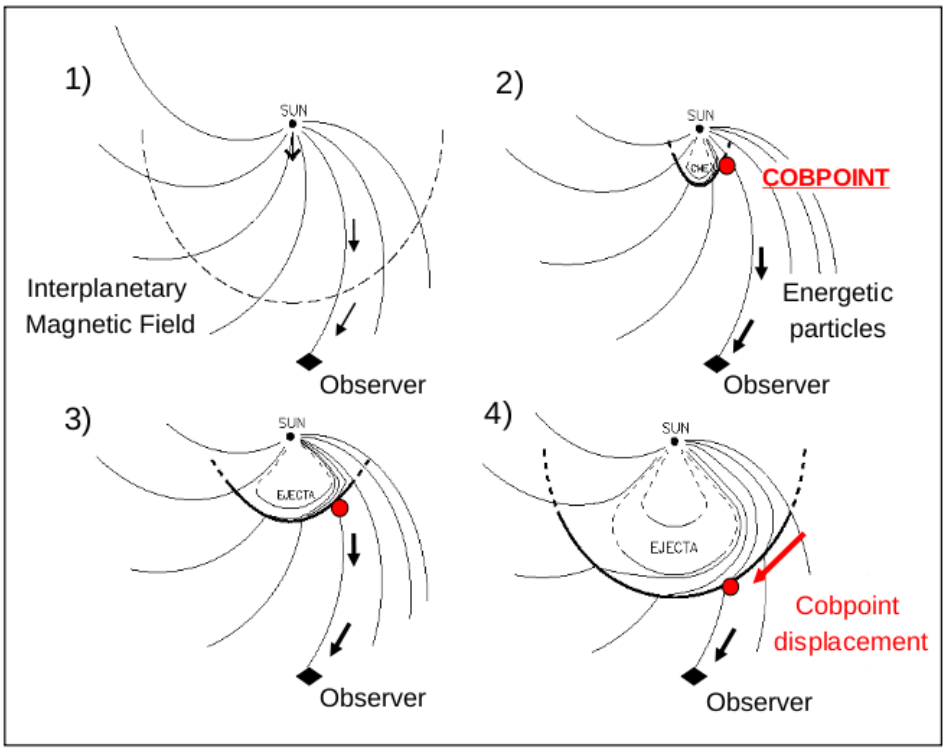

Figure 2.1: Sketch of the evolution of the cobpoint (red point) for an interplanetary shock propagating away from the Sun. In snapshot 2 the shock front intersects the IMF line (black thin line) connecting with the observer (black diamond) and shock-accelerated particles stream away along it (upstream region, black arrows). The red arrow indicates the movement of the cobpoint along the front (from Aran 2007).

that accelerate particles. Therefore, the SaP98 model is a semi-empirical model that focuses on the analysis of the efficiency of the shock as interplanetary injector of accelerated protons. It is worth to note that SaP98 is a bidimensional spatial model, which allows the description of the longitudinal structure of the expanding shock; this renders the model useful for simulating and predicting SEP fluxes at different locations in the inner space.

The Shock-and-Particle models have been applied to model several SEP events (< 100 MeV) detected by the Helios-1, Helios-2, IMP-8, ISEE-3, ACE and SOHO spacecraft among others. Heras et al. (1992, 1995) show how the efficiency of the shock evolves as a result of the combination of two factors: (1) the expansion and weakening of the shock as it moves away from the Sun, and (2) the way the observer establishes magnetic connection with the shock front. Therefore, different intensity

profiles result from different relative locations of the observer with respect to the nose of the shock. Lario et al. (1999) demonstrate that different topologies of the shocked IMF field lines might lead to different effects in the particle transport, and, thus, to different results. Aran et al. (2007) show the capability of the SaP98 model to describe SEP events seen by different spacecraft located at different radial distances from the Sun.

A key subject in space weather is the prediction of the radiation environment that a given mission may encounter in the interplanetary space. Lario et al. (2006) perform a statistical study of a set of 72 SEP events observed simultaneously by, at least, IMP-8 and one of the two Helios spacecraft. The main conclusion of this study is that the dominant parameter that governs the 2D-spatial distribution of peak intensities and fluences is the angular distance between the parent active region and the longitudinal position of the spacecraft, not the heliocentric distance[1]. Vainio et al. (2007) also illustrate this with the simulation of the proton gradual event observed on 6 June 2000 by ACE and IMP-8 spacecraft. These authors use the SaP98 model to reproduce the particle intensities at 1 AU and to calculate the time-intensity profiles for observers located at 0.3 AU and 0.7 AU, along the same IMF line. The peak intensities and the upstream fluence values derived for each observer do not show evidence of any dependence with the radial distance of the observer. These results are in discrepancy with the formerly accepted dependences that were deduced from assuming simple scenarios (see footnote 1) and are in agreement with the observational results of Lario et al. (2006). The reason is the contribution of the interplanetary shock as a source of particles.

A complete description of the transport processes is also necessary to infer SEP flux profiles out of 1 AU. Lario et al. (2007) analyse the dependence of peak intensities and fluences of SEP events with radial distance, by assuming: (1) a fixed solar source of particles, with a particle injection rate given by a Reid-Axford profile[2]

[1] The radial dependences found by Lario et al. (2006) show variations that range from $r^{-2.7}$ to $r^{-1.9}$ for 4 - 13 MeV and 27 - 37 MeV proton peak intensities, respectively; and from $r^{-2.1}$ to $r^{-1.0}$ for the respective proton fluences. These radial dependences are weaker than those formerly inferred from transport models (Hamilton 1988; Hamilton et al. 1990) and than those recommended to extrapolate peak intensities and fluences to radial distances out of 1 AU (Feynman & Gabriel 1988), both assuming particle sources fixed at the Sun.

[2] The Reid-Axford profile (Reid 1964) is: $I(t) = (\frac{N}{t}) \exp{(\frac{\beta}{t} - \frac{t}{\tau})}$. This profile shows a fast rise to maximum intensity, followed by a monotonic decay; the respective rates depend on the values assumed for β and τ.

and (2) that particles propagate along a nominal IMF line where several observers are placed at different radial distances. These authors conclude that the use of a complete focused-diffusion transport equation (like the one in the SaP98 model) to model the transport processes undergone by energetic particles is a better framework than pure diffusive models since the radial dependences are gentler than those recommended for radial extrapolations (Feynman & Gabriel 1988) and closer to those deduced observationally by Lario et al. (2006).

The SaP98 model allowed Lario et al. (1998) to establish, for the first time, a relation between the injection rate of shock-accelerated particles, Q, and the normalized radial velocity jump across the shock front, VR:

$$\mathrm{VR} = \frac{v_{r_d} - v_{r_u}}{v_{r_u}}, \tag{2.1}$$

where the subscripts u and d mean that the radial speed is taken at the upstream and downstream regions of the shock, respectively. This relation is known as the Q(VR) relation, and its functional form is:

$$\log Q(r,t) \;=\; \log Q_0 \;+\; k\,\mathrm{VR}(r,t). \tag{2.2}$$

This functional dependence has been derived from the modelling of several SEP events by using the SaP98 model (Lario et al. 1998; Aran 2007). Once a relation of this type is established, it permits obtaining particle flux profiles at different locations in space (provided by the knowledge of the MHD variables evolution up to these locations). For example, Aran et al. (2007) model a SEP event observed by IMP-8 and Phobos-2 spacecraft orbiting Mars (1.6 AU). They apply the SaP98 model to reproduce the particle intensities seen by IMP-8 and deduce a Q(VR) relation at different energies. They use this relation to successfully predict the flux profiles observed at 1.6 AU.

The potential forecasting capability of such relation led us to develop the tool SOLPENCO (SOLar Particle Engineering Code, Aran et al. 2004, 2006; Aran 2007) based on the SaP98 model. SOLPENCO is an engineering code, for space weather purposes, whose core is a database that contains a large number of pre-calculated energetic particle flux profiles for different solar-interplanetary scenarios, at two different radial distances (0.4 AU and 1.0 AU). This database permits the user to

obtain a rapid computation by interpolation of SEP fluxes and fluences for other interplanetary scenarios[3].

Finally, at present, within the SEPEM project, our STP/SWG[4] group and the CPA/KUL[5] group (leaded by Prof. S. Poedts) have developed a new shock-and-particle model, the SaP10 model. The main improvement of this model with respect to SaP98 is that shock modelling starts closer to the Sun ($\sim 4\,R_\odot$), which allows us to extend particle simulations to higher energies, up to 200 MeV (see more details in Section 2.2.2). Aran et al. (2011) have used the SaP10 model to derive the injection rate of shock-accelerated for the 4 April 2000 SEP event (Figure 1.1). They reproduce the proton intensity-time profiles measured by ACE/EPAM and SOHO/ERNE instruments for a total of twenty-two energy channels, ranging from 0.1 MeV up to 80 MeV, concluding that this large set of proton flux and anisotropy profiles can be fitted without including any ad hoc solar source additional to the interplanetary shock.

2.2 The MHD modelling of shocks

The modelling of the formation and propagation of interplanetary shocks driven by CMEs is governed by means of the MHD equations of mass, momentum and energy conservation. The success of its description depends on how accurate are both the input pulse and the assumed background medium. Interplanetary shocks can only be detected by spacecraft with in situ observations of solar wind plasma and magnetic field; thus, it is difficult to obtain observational details of the evolution of these large-scale structures, as well as of the interplanetary plasma over which they propagate. The formation of shocks in the solar corona, their relation with CMEs and how they can become interplanetary disturbances are a controversial issue today (Gopalswamy et al. 2001; Mann et al. 2003; Cane & Erickson 2005; Temmer et al. 2011).

[3] The tool SOLPENCO is of free acess on the European Space Weather Portal, http://www.spaceweather.eu/en/model_access_interface
It can be downloaded under demand from: http://www.am.ub.es/∼blai/indexsol.php

[4] Solar-Terrestrial Physics and Space Weather Group, Departament d'Astronomia i Meteorologia, Universitat de Barcelona: http://www.am.ub.es/∼blai

[5] Centrumm voor Plasma Astrophysics, Katholieke Universiteit Leuven, Belgium: http://wis.kuleuven.be/cpa/index.php

Tsurutani et al. (2003); Roussev et al. (2004); Jacobs (2007); Aran et al. (2011) have developed models capable to reproduce the location and strength of CME-driven shocks and they show that shocks may form very close to the surface of the Sun ($\sim 4\,R_\odot$). These models demonstrate the capability to produce quantitative descriptions of the undisturbed and disturbed physical parameters of simulated shocks that propagate from the Sun towards the Earth, as well as of the relevant shock parameters to be considered in connection with particle shock-acceleration[6]. Solar wind models are necessary for an accurate description of the background over which CMEs and interplanetary shocks extend and propagate. Current global MHD models can reproduce some aspects of the ambient solar corona and wind conditions from initial states of density, velocity and temperature at the coronal base and, in some cases, the large structure of the solar wind from magnetograms.

Since our main objective is SEP event modelling, the MHD codes used must focus on this aim. This requires to incorporate new MHD models that allow 2D and 3D descriptions of the interplanetary shocks starting as close as possible to the solar corona, as in the models developed by C. Jacobs (CPA/KUL). The main features of these models are described in next Section and their specific details and applications for SEP events modelling will be presented in the next chapters.

2.2.1 The Versatile Advection Code

To perform MHD simulations of interplanetary shocks we use the Versatile Advection Code (VAC), a finite volume code designed for solving the MHD equations working on structured grids. VAC was developed by G. Tóth at the Astronomical Institute (Utrecht) from 1994 to 1997 (Tóth 1996)[7]. The philosophy behind VAC is using a single versatile software with options and switches for various problems, rather than developing a different method or version for each problem. Such general

[6] The work of Tsurutani et al. (2003) helps to understand the present context of our models: *"We suggest that the shock conditions (i.e., Mach number, absolute magnetic field and velocity jumps) along the global shock configuration are, as suggested by Heras et al. (1995) and others, relevant to any study of the efficiency of the shock energization processes. The next step is to couple the predicted shocks and their shocked plasma properties to develop a more complete particle acceleration model (Tsurutani & Lin 1985; Heras et al. 1995; Lario et al. 1998; Zank et al. 2004). The model can then be tested with observed SEP events".*

[7] G. Tóth and R. Keppens are responsible for the development and maintenance of this software, as well as for its distribution and management. VAC is distributed at no charge. More information of the code can be found at http://grid.engin.umich.edu/∼gtoth/VAC

approach results in a significant reduction of overall time for software development, easy maintenance, compatibility of different parts and automatic extension of new features to all existing applications. However, the price to pay is some added complexity in the source: VAC is not a fool-proof black-box design; therefore, the user must understand how the different parameters change the behaviour of the code, and he has to be able to complete their own subroutines (for source terms, special boundary conditions, etc.) when needed. VAC aims to advance a system of hyperbolic equations by a number of different numerical schemes. The dimensionality of the problem as well as the selection of the equations, which are stored in separate modules, can be set by simple configuration. The code uses the Loop Annotation Syntax (LASY)[8], making it flexible and easy to use for 1D, 2D and 3D problems (Tóth 1997). It can run on parallel machines using the Message Passing Interface (MPI).

From the basic structure of VAC, a more sophisticate code is being developed: the Adaptive Mesh Refinement Versatile Advection Code, AMRVAC (Keppens et al. 2003). This new code uses an adaptive mesh refinement technique based on the superimposition of finer subgrids over the basic grid on those regions where a higher resolution is required, and by means of some parameter characterizing the solution (for instance, the local truncation error). AMRVAC has been extensively tested and validated on analytical known solutions, and it is expected to be a useful and powerful improvement for the correct determination of the shock features throughout its evolution, but an effective version for SEP event modelling is still under development[9].

2.2.2 The 2D MHD model

• Background Solar Wind

Parker (1958) was the first to predict a transonic outflow from the Sun. From his analytical solution for a stationary, spherical symmetric, isothermal flow a unique solution for the velocity can be obtained, which starts subsonically at the solar

[8] The LASY Preprocessor is a syntax which allows to write general simulation codes where the number of grid dimensions is a parameter that depends on the preprocessor; hence, with VAC the user can perform simulations in any (up to 3) number of dimensions.

[9] Keppens et al. (2004) and Meliani et al. (2006) present examples of AMRVAC applications for the study of accretion disk-jet systems and ultra-relativistic Gamma Ray Burst (GRB) afterglows, respectively.

surface and monotonically increases to supersonic speed for larger distances. The adopted initial condition for the simulated background solar wind is derived from the model of Weber & Davis (1967), an extension of Parker's model taking into account the effect of the solar rotation and the magnetic field. In order to simulate the subsonic-supersonic transit of the solar wind a frequent applied approach is to assume a polytropic relation between pressure and density, as:

$$p = K n^{\alpha}, \tag{2.3}$$

where p is the pressure of the gas, n the total particle density ($n = n_p + n_e$), α the polytropic index and K the parameter that relates the pressure and the density. It is also assumed that the plasma has the same number of protons and electrons ($n_p = n_e = n/2$) and that they are in thermal equilibrium ($T_p = T_e = T$).

Totten et al. (1995) conclude from the analysis of Helios-1 data that the solar wind shows an almost polytropic behaviour between 0.3 AU and 1.0 AU, with an average value of $\alpha = 1.46$, which implies that the polytropic index is rather independent of the solar wind speed. With the aim of reproducing the observations of Totten et al. (1995), we construct a spatially variable polytropic relation between density and pressure. This model should obey the observational constraints near the solar surface and reproduce the pre-event solar wind conditions at 1 AU. Combining Equation 2.3 with the law of the ideal gas we obtain:

$$K = k_b \, T \, n^{1-\alpha}, \tag{2.4}$$

where k_b is the Boltzmann constant. Therefore, the value of K can be derived if the values of T, n and α are known.

We assume that the profile of the polytropic index depends on the radial distance, $\alpha(r)$, having a constant value near the Sun and at large distances (α_0 and α_1, respectively), with a soft-evolving transition (a quadratic sinusoidal dependence) within an intermediate critical region (r_1, r_2). That is:

$$\alpha(r) = \begin{cases} \alpha_0 & \text{if} \quad r < r_1 \\ \alpha_0 + (\alpha_1 - \alpha_0) \sin^2(\dfrac{\pi}{2} \dfrac{r - r_1}{r_2 - r_1}) & \text{if} \quad r_1 < r < r_2 \\ \alpha_1 & \text{if} \quad r_2 < r \end{cases} \tag{2.5}$$

In this way, it is possible to simulate the transition of the solar wind from their slow regime near the solar corona to their fast interplanetary behaviour, without the necessity of assuming two different models[10]. The functional form of K is chosen accordingly:

$$K(r) = K_0\, n_0^{\alpha_0-\alpha(r)} f(r), \tag{2.6}$$

where $f(r)$ is:

$$f(r) = \begin{cases} 1 & \text{if} \quad r < r_1 \\ 1 + (K_1 - 1)\sin^2(\dfrac{\pi}{2}\,\dfrac{r - r_1}{r_2 - r_1}) & \text{if} \quad r_1 < r < r_2 \\ K_1 & \text{if} \quad r_2 < r \end{cases} \tag{2.7}$$

with $K_1 = \dfrac{K_{1AU}}{K_0 n_0^{\alpha_0-\alpha_1}}$ and $K_0 = \dfrac{T_0 k_b}{n_0^{\alpha_0-1}}$, and where n_0, T_0 and α_0 are the coronal values of the density, temperature and polytropic index, respectively. Table 3 of Totten et al. (1995) provides a list of the values of K_{1AU} depending on the solar wind speed ranges considered[11].

The solar wind is simulated on a 2D polar grid, covering the equatorial plane, in spherical geometry (r, φ), and it assumes symmetry in the azimuthal direction ($\frac{\partial}{\partial\varphi} = 0$). The computational domain of the grid used extends from $1.03\,\mathrm{R}_\odot$ to $364\,\mathrm{R}_\odot$ (1.7 AU) in the radial direction from the Sun, r, and from 0° to 360° in longitude, φ. The grid has 1804×364 points including four ghost-cells for each direction, with an accumulation of cells towards the Sun and towards the longitude $\varphi = 180°$.

The radial step varies from $\delta r = 0.005\,\mathrm{R}_\odot$ at the inner boundary, to $\delta r = 0.2\,\mathrm{R}_\odot$ at $20\,\mathrm{R}_\odot$ (approximately) and further on. The minimum longitudinal step is $\delta\varphi = 0.5°$ at $\varphi = 180°$. Within the interval $\varphi \in [120°, 240°]$ the cell size varies from $\delta\varphi = 0.5°$ to $\delta\varphi = 0.75°$, while outside of this interval $\delta\varphi$ increases linearly from $\delta\varphi = 0.75°$ to $\delta\varphi = 4°$ (at $\varphi = 0°$). The main direction of the shock propagation is chosen along the negative X-axis, in coincidence with the highest resolution of the grid[12]. For SEP events modelling this high resolution is needed to get a good capture of the shock structure (upstream-downstream regions). Figure 2.2 depicts two fields of

[10] As BATS-R-US code does, for example.

[11] For example, for a typical solar wind velocity within 300 and $400\,\mathrm{km\,s^{-1}}$, $K_{1AU} = 2.32 \pm 0.34 \times 10^{22}\,\mathrm{N\,m^{3\,\alpha-2}}$.

[12] For CM events, the Earth would be located in the negative X-axis.

the grid showing the different size of the cells and their accumulation toward the inner boundary in radial direction ($x = 0$) and toward the region that corresponds to $\varphi = 180°$ in longitude ($y = 0$). The red arrow marks the direction of the shock propagation.

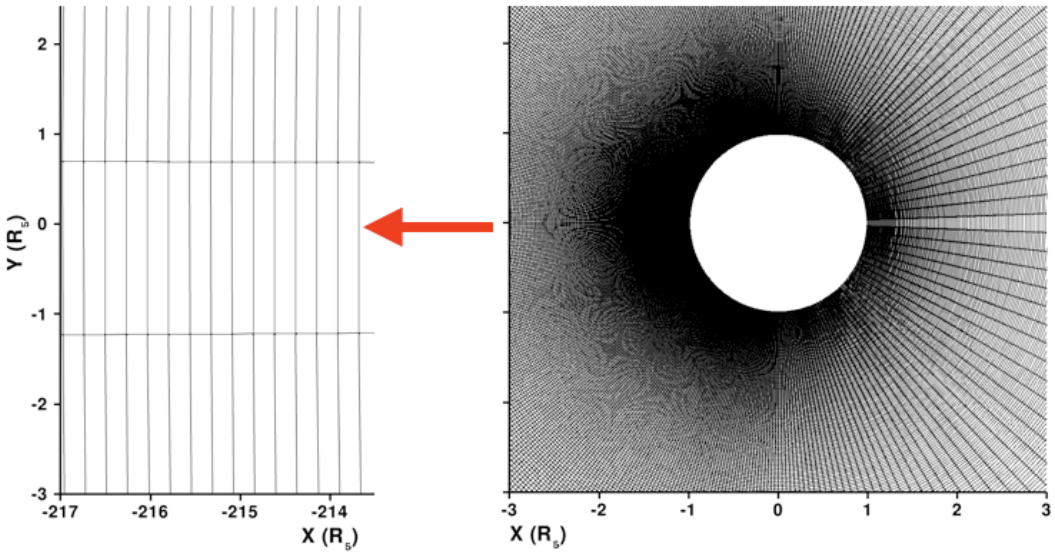

Figure 2.2: Variable (r, φ)-grid (converted to Cartesian coordinates) used in the 2D MHD model presenting the difference on the cells size. The red arrow marks the direction of launch of the perturbation. Left side: part of a network grid around $(-215, 0)$. Right side: network grid around $(0, 0)$, the location of the Sun. Radial distances are given in solar radii (R_s).

The reference values are set at the inner boundary ($r_0 = 1.03\,R_\odot$): $n_{0p} = 1.5 \times 10^8\,\mathrm{cm}^{-3}$, $T_0 = 1.4 \times 10^6\,\mathrm{K}$ and $\omega_0 = 2.66 \times 10^{-6}\,\mathrm{rad\,s}^{-1}$. The radial component of the magnetic field is set to $B_{0r} = B_r(r_0) = 2.1 \times 10^5\,\mathrm{nT}$ and it falls as r^{-2}. At the outer boundary, the flow is continuous and all the variables can be extrapolated, because all information propagates outward.

• Simulation of the shock

The perturbation is generated by superimposing a high-density and high-pressure plasma blob on the background solar wind. The velocity and density profiles of the initial disturbance are given by:

$$\alpha_{extra} = \alpha_{cme}\, A\, r'\, \exp(-A\, r' + 1)\, f(\varphi), \tag{2.8}$$

where α_{extra} indicates the extra density or radial velocity added to the background plasma, α_{cme} is the maximum density or radial velocity introduced and the constant A defines the shape of the exponential pulse profile in the radial direction. These density/velocity profiles vary in radial and longitudinal direction as:

$$r' = (r_{cme} + \frac{d_{cme}}{2}) - r \tag{2.9}$$

$$f(\varphi) = \begin{cases} \sin^2\left(\frac{\pi}{2}\,\frac{\frac{a_{cme}}{2} - |\varphi - \varphi_{cme}|)}{\Delta\varphi}\right) & \text{if} \quad \frac{a_{cme}}{2} - |\varphi - \varphi_{cme}| < \Delta\Phi \\ 1 & \text{else,} \end{cases} \tag{2.10}$$

where r_{cme} is the initial radial position of the perturbation, d_{cme} its diameter, φ_{cme} the initial longitudinal position and $\Delta\Phi$[13] the extend of the wings of the initial pulse. The initial disturbance is limited to the region defined by $\left[r_{cme} - \frac{d_{cme}}{2},\, r_{cme} + \frac{d_{cme}}{2}\right]$ in radial direction, and by $\left[\pi - \frac{a_{cme}}{2},\, \pi + \frac{d_{cme}}{2}\right]$ in longitudinal direction. Figure 2.3 shows an example of the initial radial velocity profile of a plasma blob introduced on the background solar wind.

The ideal MHD equations describing the evolution of the perturbation are solved by means of the Total Variation Diminishing Lax-Friedrichs scheme with a diffusive but stable minmod slope limiter for second-order reconstructions[14]. To advance in time the Courant-Friedrichs-Lewy (CFL) condition is applied[15]. The magnetic field is divergence free ($\boldsymbol{\nabla}\cdot B = 0$) by means of satisfying the projection scheme[16] (Brackbill & Barnes 1980). To give an idea of the computational workload, for a pre-calculated solar wind, one simulation of a shock from the Sun up to 364 $R_\odot$ takes ~ 4.5 hours of elapsed time using 24 processors of the SGI-Altix 3700 machine of the CESCA supercomputing center.

[13] $\Delta\Phi$ is expressed as percentage of the initial angular extend, a_{cme}.

[14] The TVDLF and other methods of computational fluid dynamics are described in detail in Anderson (1995) or in Goedbloed et al. (2010).

[15] The CFL condition states that, for stability, the physical domain of dependence must be fully contained in the numerical domain of dependence (Courant et al. 1967).

[16] In the projection scheme the 'violating' magnetic field is projected onto the space of divergence-free magnetic fields after each time step at the expense of requiring the solution of a Poisson equation.

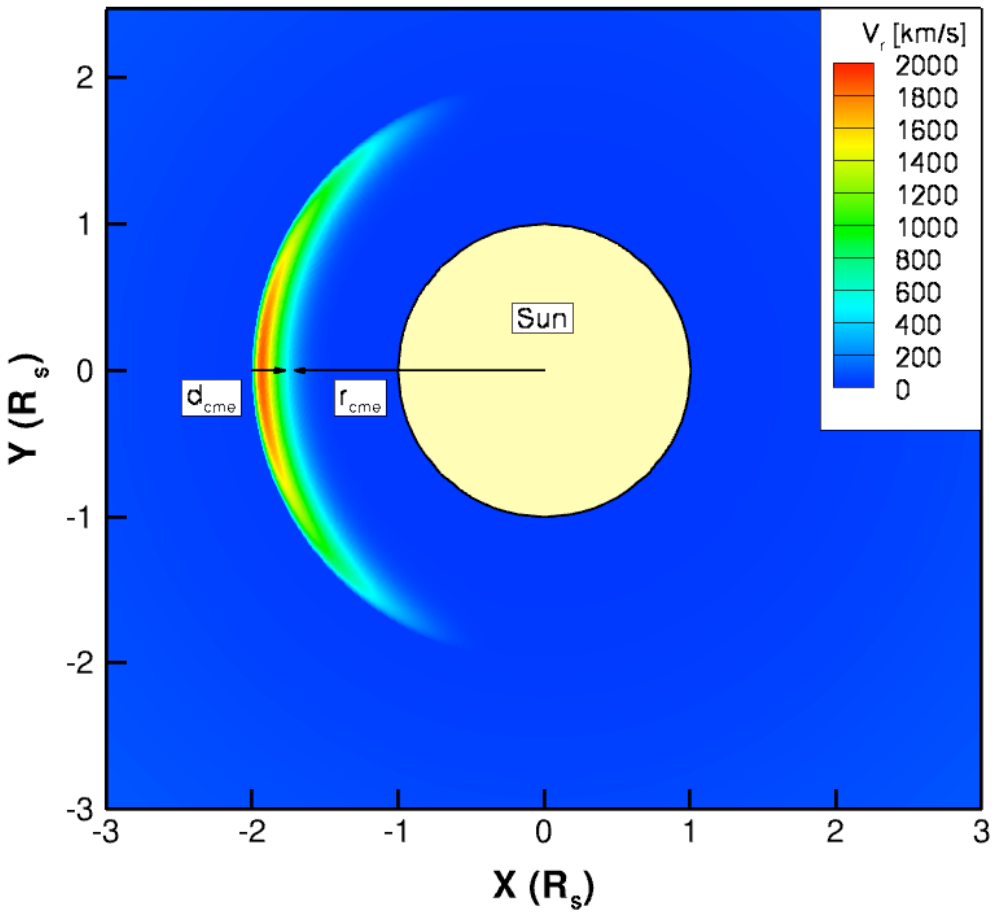

Figure 2.3: Example of an initial radial velocity profile of a plasma blob introduced on the background solar wind used in the 2D MHD model. Colour-code as indicated.

2.2.3 The 3D MHD model

• Background solar wind

The adopted initial condition to construct the background solar wind is the hydrodynamic solution of Parker (1958), with a supplementary dipolar magnetic field. As the initial solution relaxes to reach the steady state[17], the original magnetic dipole configuration is lost and regions of open and closed field lines develop. To reproduce the fast and slow solar wind regimes, we adopt the semi-empirical approach

[17] Such assertion hides a non-trivial technical problem: the reduction to a non-significant level (10^{-5} relative to local values) of the numerical instabilities of the computed solar wind. This precision is crucial in order to avoid potential problems of magnification of such instabilities when the perturbation propagates over them. This implies hard computing: as an example, the 3D stable solar wind presented here has been achieved after 150 000 iterations, which means $\sim$17 hours of elapsed time using 240 processors of the KUL VIC cluster.

of Groth et al. (2000) that introduces an additional heating term in the energy equation. Particularly, we take the expressions given by Jacobs et al. (2007), frequently used in this type of simulations (Manchester et al. 2004a,b; Lugaz et al. 2005a,b; Soenen et al. 2009; Zuccarello et al. 2009). Such term reads:

$$Q = \rho\, q_0 (T_0 - \gamma \frac{p}{\rho}) \exp\left(-\frac{(r - \mathrm{R}_\odot)^2}{\sigma^2}\right), \tag{2.11}$$

depending both on the radial and the latitude coordinates[18]. The temperature T_0 is set to $4.375 \times 10^6\,\mathrm{K}$ poleward from a critical angle $\theta_0(r)$, and to $2.5 \times 10^6\,\mathrm{K}$ equatorward of $\theta_0(r)$. This critical angle varies with the radial distance as:

$$\theta_0(r) = \arctan\left[(1 + \log(r)) \tan\theta_t\right], \tag{2.12}$$

where $\theta_t = 28°$. This latitudinal dependence of the heating term determines the regions of open and closed field lines and the corresponding fast and slow wind speeds.

The axisymmetric[19] solar wind model is simulated on a 3D spherical grid (r, θ, φ), where r is the radial distance to the Sun, θ the latitude and φ the longitude. The computational domain is defined as: $1 \leq r \leq 220\,\mathrm{R}_\odot$, -90° $\leq \theta \leq$ 90°, and 0° $\leq \varphi \leq$ 360°. The grid has $1104 \times 95 \times 184$ points including four ghost-cells for each direction, with an accumulation of cells towards both the Sun and towards the equator. The radial step varies from $\delta r = 0.02\,\mathrm{R}_\odot$ near $1\,\mathrm{R}_\odot$ to $\delta r = 0.24\,\mathrm{R}_\odot$ at $30\,\mathrm{R}_\odot$ and further on. The grid in θ-direction varies from a maximum angular step, $\delta\theta = 3.88°$, near the poles to a minimum value, $\delta\theta = 0.8°$, at the equator. In φ-direction the grid is uniform, with $\delta\varphi = 2°$.

The inner boundary of the simulation is at the base of the corona ($r_0 = 1\,\mathrm{R}_\odot$); there, the assumed reference values are: $n_{0p} = 1 \times 10^8\,\mathrm{cm}^{-3}$, $T_0 = 1.50 \times 10^6\,\mathrm{K}$ and $\omega_0 = 2.77 \times 10^{-6}\,\mathrm{rad\,s}^{-1}$. For the magnetic field, $B_{0r} = 2.10 \times 10^5\,\mathrm{nT}$ at the poles and $B_{0r} = 2.66 \times 10^5\,\mathrm{nT}$ at the solar equator. All the flow variables are extrapolated at the outer boundary.

[18] The scale height $\sigma(r, \theta)$ is taken as: $\sigma(r, \theta) = 4.5\,(2 - \frac{\sin^2\theta}{\sin^2\theta_0})$, from which $\sigma = 9$ near the poles (for $\theta > \theta_0(r)$), and $\sigma = 4.5$ toward the equator (for $\theta < \theta_0(r)$).

[19] It does not show a dependence on the azimuthal direction, $\dfrac{\partial}{\partial\varphi} = 0$.

• **Simulation of the shock**

The shock is generated by superimposing a high-density and high-pressure plasma blob on the background solar wind, with a certain velocity v_{cme} in a given direction $(\theta_{cme}, \varphi_{cme})$. The velocity and density profiles of this disturbance are given by:

$$\alpha = \frac{\alpha_{cme}}{2}(1 - cos\,\pi\frac{d_{cme} - d}{d_{cme}}), \tag{2.13}$$

where α can be density or radial velocity, α_{cme} is the maximum value of α, d_{cme} is the radius of the plasma bubble and d the distance to its centre (see Jacobs et al. 2005; Jacobs 2007, for more details). Figure 2.4 shows an example of the initial radial velocity profile of a plasma blob added over the background solar wind. This is a cut on the plane of launch of the perturbation, which is described by the 3D orientation axis.

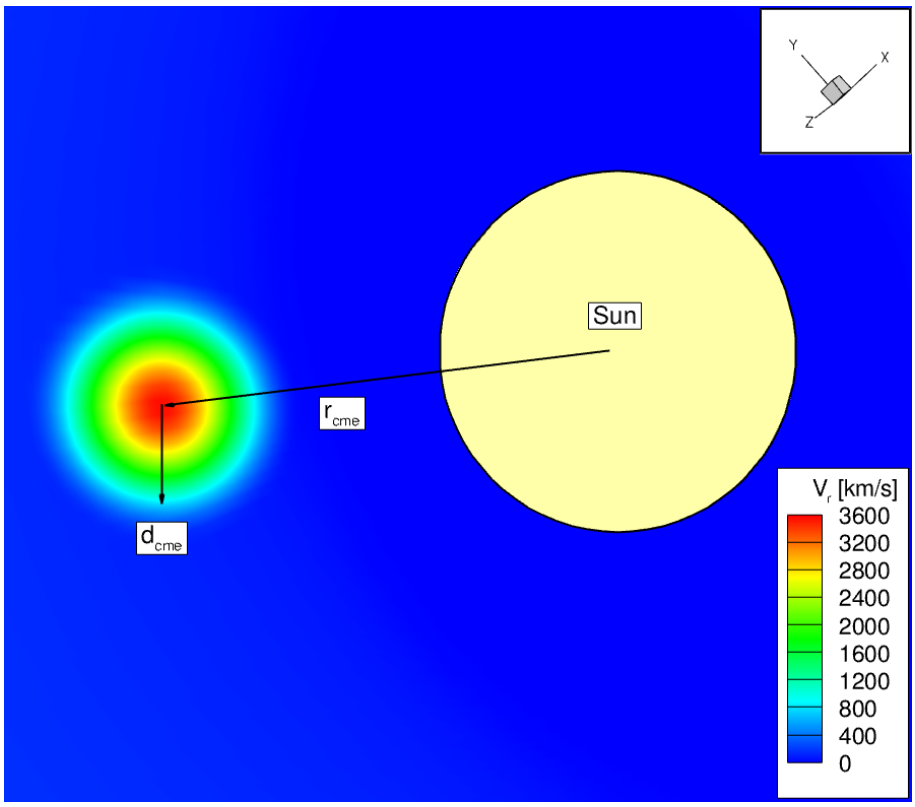

Figure 2.4: Example of an initial radial velocity profile of a plasma blob introduced on the background solar wind used in the 3D MHD model. The image shows a cut in the plane of launch of the perturbation. Colour-code as indicated.

The numerical techniques applied to solve the ideal MHD equations and advance the evolution of the perturbation in time are the same as for the 2D MHD code. In this case, however, the maintenance vanishing divergence of the magnetic field down to machine round-off error is guaranteed at all time by using the vector potential at the nodes according to the constrained transport method[20] (Evans & Hawley 1988). Approximately, one run for a shock simulation from the Sun to 100 $R_\odot$ (Mercury's orbit) takes about 48 000 hours of elapsed time using 64 processors of the SGI-Altix 3700 machine of the CESCA supercomputing center. A run from the Sun up to 215 $R_\odot$ (Earth's orbit) takes about 110 000 hours of elapsed time using 440 processors of the KUL VIC cluster.

In our simulations of SEP events, either 2D or 3D, we have to choose the initial input conditions that better reproduce the arrival time and speed of the shock at the observer, as well as the observed jumps of the plasma parameters. Such observations strongly constraint the initial set of values to be adopted for the perturbation. Hence, to simulate a given event it is necessary to perform a number of runs (usually many of them!) to ensure that the final fit of the aforementioned observations is the best[21] affordable in such scenario. It is important to stress the fact that our aim is not to describe the initiation of the CME itself but to perform simulations of coronal/interplanetary shocks driven by CMEs that can yield plasma inputs well suited and good enough to be useful for energetic particle modelling. Our actual limited knowledge[22] on the formation of shocks in the solar corona and their transition to the interplanetary medium, implies that characterizing a shock so close to the Sun by its initial velocity is an ad hoc assumption, because it is not a real-time observable variable. For example, the 3D shock-and-particle model developed recently by Luhmann et al. (2010) uses a high pressure 'gust' with an overdensity of four times the ambient density taken at the inner boundary of the ENLIL solar wind model (some point between 20 $R_\odot$ and 30 $R_\odot$).

[20] The constrained transport method is based on a staggered collocation of the magnetic and electric field components; it employs a special discretization of Faraday's law to satisfy the constraint $\nabla \cdot B = 0$.

[21] Here the term 'the best' means using the 'eye-ball' test by several (three) researchers.

[22] *"The processes leading to the magnetic rearrangement after a relatively slow buildup of basic causes of CMEs are still not known in any detail, so prediction is difficult."* (Space Radiation Hazards and the Vision for Space Exploration: Report of a Workshop 2006).

2.3 The cobpoint at the shock front

A key issue of the shock-and-particle models is the identification of the front of the shock; this is, the determination of the cobpoint as well as the plasma variables and magnetic field at both sides of the shock front (upstream and downstream regions). Due to the computational numerical techniques used to solve the MHD equations, the details of the front of the shock might be not enough well characterized, specially at the flanks of the shock where its strength weakens (for example due to too small fluctuations of the plasma variables across the shock front or to a too coarse grid). Therefore, a proper identification and characterization of the shock is required. Lario (1997) and Lario et al. (1998) developed simple procedures[23] to locate the cobpoint and to determine the regions upstream and downstream of the shock where to measure the values of the plasma variables. Since these methods are of limited precision, we have had to improve such procedures.

The spiral IMF line passing through each observer is constructed from the MHD simulation. Starting from the position of the observer and going back to the Sun, we search for the cobpoint location along the IMF line by requiring a density or radial velocity higher than a given threshold over the background solar wind. Figure 2.5 shows the location of the cobpoint (at a given time, or for a given snapshot of a simulation) at the front of an interplanetary shock. It is identified by its distance from the Sun and the angle subtended with the main direction of the shock propagation.

Once identified the cobpoint, it is necessary to determine the direction of the shock normal[24] at this position, $\hat{\mathbf{n}}$, in order to characterize the shock. Therefore, we must choose where to evaluate the plasma variables in the downstream region. We locate the downstream point as the first point after the cobpoint, going from the cobpoint toward the Sun, where the velocity and the density start decreasing. The final step of this procedure is to calculate the upstream-to-downstream ratio across the shock front, for the plasma variables of the simulation we are interested

[23] The *radial cut method* uses the location of the beginning (radial position where the plasma parameters start to increase at a given time) and the end (radial position where the plasma parameters begin to decrease at a given time) of the shock front. The *time profile method* uses the time profiles of plasma and magnetic field data at the observer position. These methods can give different results at the wings of the shock or if the shock has a downstream region too wide. For more details see Section 3.3 of Lario (1997).

[24] The normal direction to the shock front is taken as directed sunward, hence, in the opposite sense of the plasma flow.

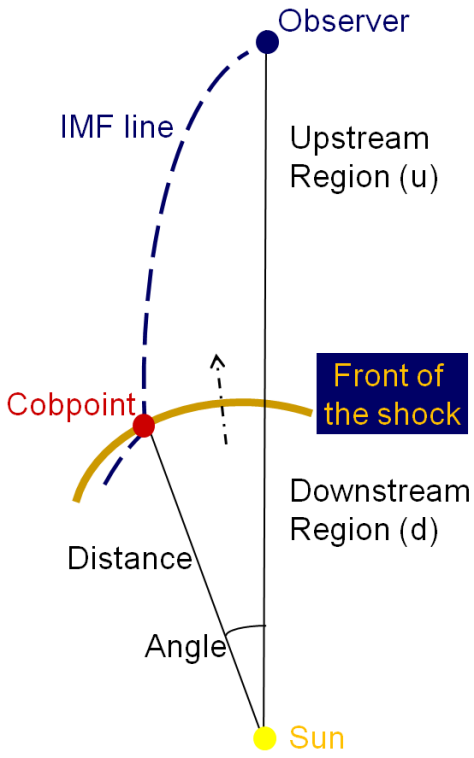

Figure 2.5: Sketch of the location of the cobpoint (red point) at the front of the shock (brown surface). The Sun is the yellow point and the blue dashed trace indicates the IMF line that connects the observer (blue point) with the shock front. The arrow marks the direction of propagation of the nose of the shock.

in studying: velocity, density and magnetic field ratios or the θ_{Bn} angle, for example. In our case, we mainly concentrate in the normalized radial velocity jump, VR (Equation 2.1), because this is the variable used so far in the shock-and-particle models to quantify the strength of the shock at the cobpoint (Heras et al. 1995; Lario 1997; Lario et al. 1998; Aran et al. 2007, 2011).

Figure 2.6 shows an example of the evolution of the cobpoint associated with two spacecraft, as the interplanetary shock expands in the heliosphere. Top panel depicts the position of IMP-8 (orbiting Earth) and Phobos-2 (orbiting Mars) and their corresponding cobpoints at the front of the shock. The bottom panel shows the evolution of the position of the respective cobpoints (radial and angular distance) as well as the evolution of the magnetic field jump, BR (Equation 3.17), and the normalized radial velocity jump, VR, derived from the simulation of this event.

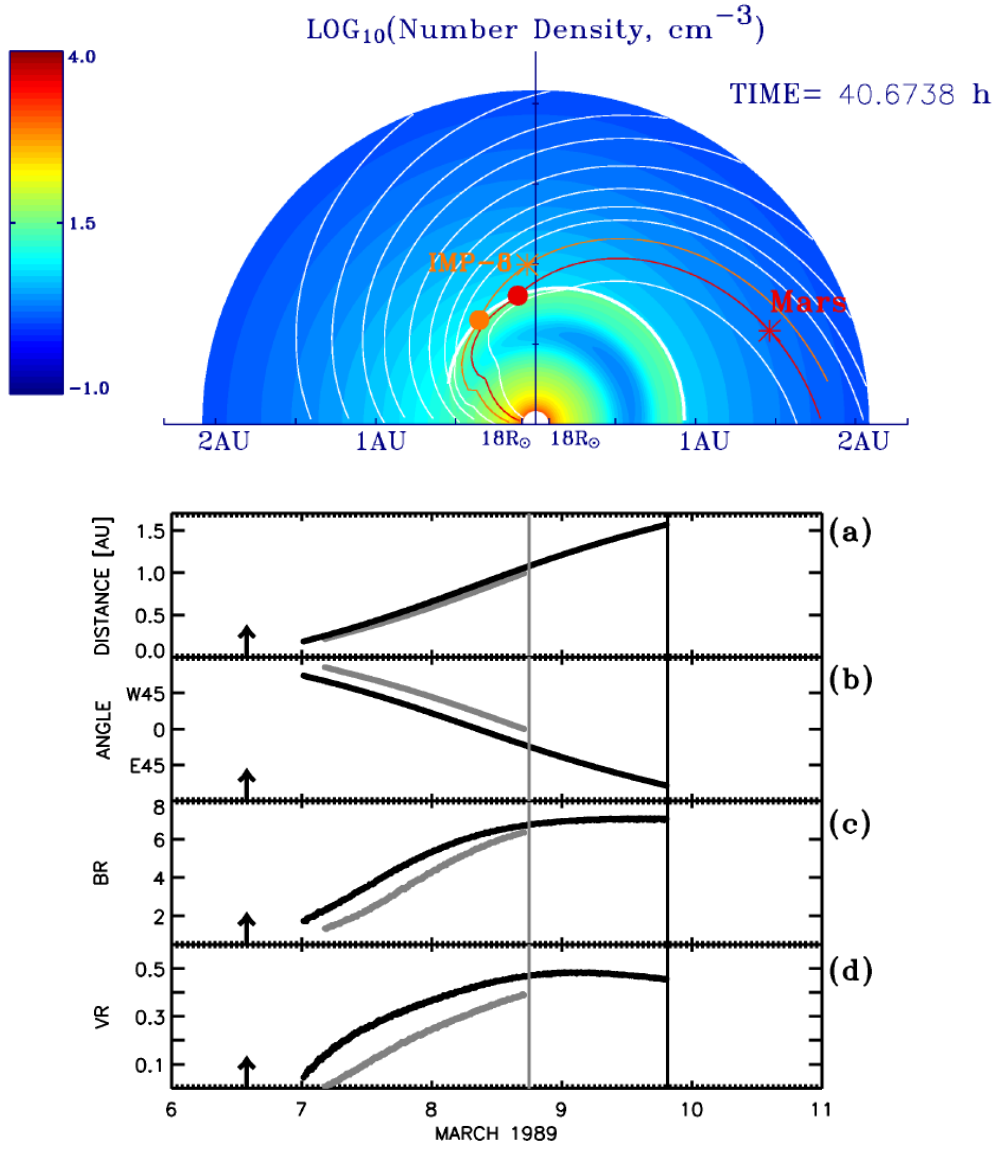

Figure 2.6: Evolution of the cobpoint in the 6 March 1989 SEP event. Top panel: snapshot of the shock simulation 40.7 hours after the parent solar event showing density contours and some IMF lines. Orange and red asterisks mark, respectively, the location of IMP-8 and Phobos-2 spacecraft, and their corresponding cobpoints are indicated by orange and red dots. Bottom panel: evolution of the cobpoint features, for IMP-8 (grey) and Phobos-2 (black); (a) cobpoint heliocentric radial distance and (b) heliolongitude; (c) BR and (d) VR. The vertical arrows indicate the onset time of the solar parent activity and the vertical lines the time of shock passage by each spacecraft (adapted from Aran et al. 2007).

The determination of the cobpoint position and the characterization[25] of the shock in 2D and 3D is a main aim of this work. We will comment on them in more detail in the following Chapters when discussing the application of these models to specific events.

2.4 Transport model for energetic particles

Energetic particles propagate through the interplanetary medium guided by the topology of the IMF, describing helical orbits around magnetic lines of force. Therefore, the particle flow is structured by the IMF in the expanding solar wind. Particle flux and anisotropy profiles observed by spacecraft are modulated by different processes acting on the particle population during its transport. Small magnetic field irregularities modify the regular motion of the particles, which are scattered by the magnetic turbulence and undergo outward convection with the solar wind and adiabatic deceleration due to the expansion of the solar wind. It is not possible to observe the complete trajectories of individual energetic particles from its source to the point of detection, but the evolution of certain features, as the flux and anisotropies, of this particle population.

The transport equations for energetic particles try to reproduce such features and their evolution. Parker (1965) use a Fokker-Planck equation to describe the evolution of a cosmic ray population as a function of the distance from the Sun, including the effects of spatial diffusion, convection and deceleration. Jokipii (1966) incorporate some terms to describe the pitch-angle scattering and streaming in order to explain the large anisotropies observed. Later on, Roelof (1969) adds the effect of focusing on transport; Roelof's equation has been widely used to study anisotropic distributions in numerical simulations of interplanetary transport[26].

[25] It would mean: to determine the shock features that, to our knowledge, can help to better understand the efficiency of interplanetary shocks as injectors of energetic particles in space, and to improve SEP simulations. Lario et al. (1998) reads: *"the identification of the limits of the shock and its effects on particle population are not easy to define. The interaction of a particle with a plasma discontinuity depends on the energy of the particle. As a consequence, it is possible that a shock could efficiently accelerate low-energy particles at its wings while becoming an inefficient accelerator at high energy. Or, a low-energy particle could 'see" a discontinuity on the plasma and magnetic field as a shock, while a high-energy particle will "see" just a small irregularity".*

[26] This focused-diffusion model neglects the solar wind velocity and it assumes that the magnitude of the particle velocity is conserved by both focusing and diffusion effects. Furthermore, it does not include convection or adiabatic deceleration effects, which becomes increasingly important

2.4.1 The transport equation and the injection rate Q

Ruffolo (1995) developed an explicit equation for the focused-diffusion[27] transport of solar cosmic rays, including the effects of adiabatic deceleration and convection by the solar wind. This focused transport approximation considers the particle streaming along the IMF lines, the pitch-angle scattering processes, the adiabatic deceleration, the solar wind convection and the magnetic focusing in the outward magnetic field, and it is given by[28]:

$$\begin{aligned}
\frac{\partial F(t,\mu,r,p)}{\partial t} &= -\cos\psi\,\frac{\partial}{\partial r}\left\{\upsilon\mu F(t,\mu,r,p)\right\} - \\
&-\cos\psi\frac{\partial}{\partial r}\left\{\left(1-\mu^2\frac{\upsilon^2}{c^2}\right)\upsilon_{sw}\sec\psi\,F(t,\mu,r,p)\right\} - \\
&-\frac{\partial}{\partial\mu}\left\{\frac{\upsilon}{2L(r)}\left[1+\mu\frac{\upsilon_{sw}}{\upsilon}\sec\psi-\mu\frac{\upsilon_{sw}\upsilon}{c^2}\sec\psi\right](1-\mu^2)\,F(t,\mu,r,p)\right\} + \\
&+\frac{\partial}{\partial\mu}\left\{\upsilon_{sw}\left(\cos\psi\frac{d}{dr}\sec\psi\right)\mu(1-\mu^2)F(t,\mu,r,p)\right\} + \\
&+\frac{\partial}{\partial\mu}\left\{\varphi(\mu)\frac{\partial}{\partial\mu}\left\{\left(1-\mu\frac{\upsilon_{sw}\upsilon}{c^2}\sec\psi\right)F(t,\mu,r,p)\right\}\right\} + \\
&+\frac{\partial}{\partial p}\left\{p\upsilon_{sw}\left[\frac{\sec\psi}{2L(r)}(1-\mu^2)+\left(\cos\psi\frac{d}{dr}\sec\psi\right)\mu^2\right]F(t,\mu,r,p)\right\},
\end{aligned} \tag{2.14}$$

where t is the time, μ the pitch-angle cosine of the particles, r the heliocentric distance, p the particle momentum, υ the velocity of the particles, ψ the angle between the magnetic field, B, and the radial direction, L the focusing length, $\varphi(\mu)$ the diffusion coefficient in the μ-space and υ_{sw} the solar wind radial speed[29].

as lower energies are considered.

[27] Hereafter, the focused transport equation including adiabatic deceleration and solar wind convection effects will be referred to as the "transport equation". Lario et al. (1997) study the influence of these terms in the transport equation model.

[28] Lario (1997) assumes that $dr = dz\cos\psi$, where z is the distance along the IMF line, and ψ the angle between the radial and the IMF directions.

[29] This equation is expressed in mixed coordinates: the coordinates p, υ and μ are referred to the local solar wind frame, co-moving with the inhomogeneities of the IMF, whereas r and t are referred to a frame fixed at the Sun.

In Equation 2.14 it is assumed that the distribution of particles shows symmetry with respect to the magnetic field line (i.e., gyrotropicity). Then, the distribution of particles inside a magnetic flux tube, $F(t, \mu, r, p)$, of cross-sectional area $A(r)$ is related to the particle distribution function in the phase space[30], $f(t, \mu, r, p)$, as $F(t, \mu, r, p) = A(r)\, f(t, \mu, r, p)$ (Ng & Wong 1979).

The transport model for energetic particles assumes a stable solar wind regime with an Archimedian topology for the IMF (Parker 1958). Then, we have that

$$\tan\, \psi \;=\; \frac{\omega\, r}{\upsilon_{sw}}, \tag{2.15}$$

$$A(r) \;=\; \frac{A(r_0)\, r^2}{(1 \,+\, \tan^2 \psi)^{1/2}} \tag{2.16}$$

and

$$L \;=\; \frac{r}{\cos\, \psi\, (1 \,+\, \cos^2\, \psi)}, \tag{2.17}$$

where ω is the solar angular rotation speed and r_0 is a given radial distance. For a constant solar wind speed, $A(r)$, ψ and L are unequivocally determined.

The approximation of pitch-angle scattering describes the interaction between the energetic particles and the irregularities superposed on the averaged magnetic field, created by the magnetic field fluctuations. The pitch-angle diffusion coefficient used comes from the standard model for the IMF fluctuations, which assumes that such irregularities are small when compared with the large-scale magnetic field strength. Then it is possible to consider the interaction between waves and particles only to the first order (Quasi-Linear Theory, QLT, approximation Jokipii 1966). In the QLT model, the pitch-angle diffusion coefficient, $\varphi(\mu)$, can be parametrized in terms of the particles mean free path parallel component to the magnetic field, $\lambda_{||}$, that depends on the rigidity[31] of the particles, R, (Hasselmann & Wibberenz 1970) as

$$\lambda_{||}(R) \;=\; \lambda_{||0}(R/R_0)^{2-q}. \tag{2.18}$$

The index q is the spectral index of the magnetic field fluctuations and $\lambda_{||0}$ and

[30] The distribution function gives the number of particles per unit volume of the six-dimensional phase space.

[31] The rigidity of a particle gives its resistance to deflection by a magnetic field, and it is defined as $R = pc/\tilde{q}$, where $\tilde{q}$ is the particle charge, p its momentum and c the speed of light.

R_0 are the mean free path and the particle rigidity, respectively, at a specific energy E_0. Measured magnetic field spectra give values of q in the range of $1.3 \leq q \leq 1.9$, with an average value[32] of $q = 1.63$ (Kunow et al. 1991).

Equation 2.14 can only apply to a limited injection of particles (solar, for example). Nevertheless, to explain gradual events it is necessary to assume a continuous injection of particles accelerated at a moving shock. Therefore, to describe the injection rate of shock-accelerated particles, the model must include an additional term (a source term) in the right hand side of the transport equation; this is (Lario 1997):

$$\frac{\partial F(t,\mu,r,p)}{\partial t} \;=\; [\text{right hand side of Equation 2.14}] + G(t,\mu,r,p). \tag{2.19}$$

This new term accounts for the "efficiency" of the shock as particle accelerator, which comprises the effectiveness of the shock in accelerating protons, coupled with its efficiency on injecting these protons into interplanetary space. This efficiency depends on the conditions around the shock, such as the presence or absence of a turbulent foreshock region ahead of the shock, or a large background of protons acting as a seed particle population.

It is usual (e.g., Heras et al. 1992; Lario et al. 1998; Aran et al. 2007) to finally express the injection rate in terms of the distribution function f instead of the axisymmetric distribution function F. If Q is the injection rate of shock-accelerated particles in phase space[33], then

$$G(t,\mu,r,p) \;=\; A(r)\, Q(t,\mu,r,p), \tag{2.20}$$

with $A(r)$ computed at the cobpoint. Figure 2.7 shows an example of the evolution of G and Q variables for the simulation of the SEP event observed by ISEE-3 on the 24 April 1979.

It is worth to point out that the model does not intend to simulate the physical processes which lead to the acceleration of particles at the front of the interplanetary shock. The shock is just treated as a moving source of particles, not explicitly considering the physics underlying the particle-shock acceleration mechanisms. In-

[32] Lario (1997) concludes that the influence of the adopted values of q in the results is minimal.
[33] $[Q] = [\mathrm{cm}^{-6}\,\mathrm{s}^{3}\,\mathrm{s}^{-1}]$.

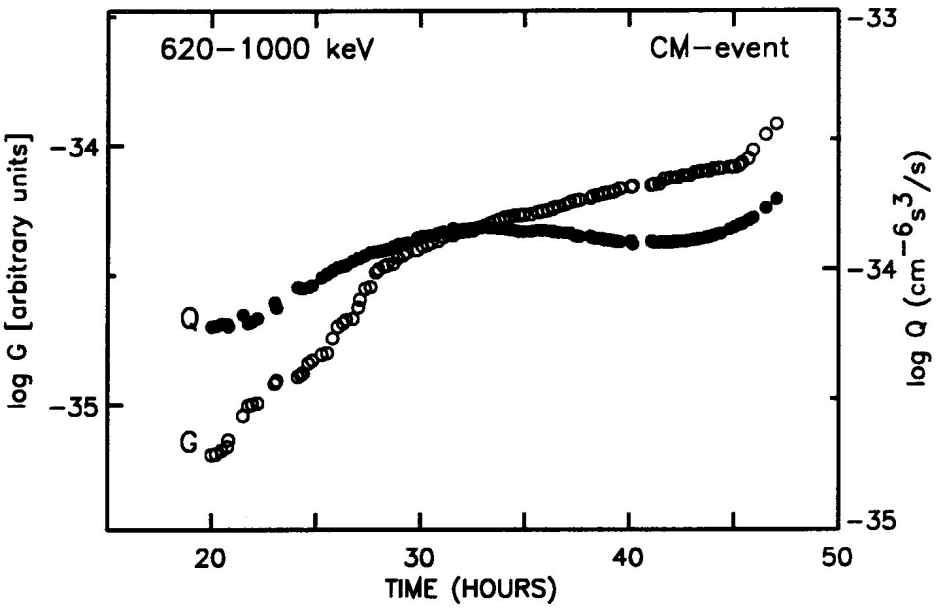

Figure 2.7: Evolution of G and Q derived from the simulation of the 24 April 1979 SEP event, at 620 - 1000 keV (from Lario 1997).

stead, our aim is to obtain measures of the injection of shock-accelerated particles rate, Q, at the cobpoint. Thus, the basic free parameters of the model, required to fit the particle flux and anisotropy profiles, are $\lambda_{\parallel}$ and G (or Q) at a given energy, as well as the spectral index of the injection rate, γ.

The transport equation is solved by splitting it in four time-dependent equations, further solved by means of a finite-difference method[34]. The fitting of particle flux and anisotropy profiles is performed at a fiducial energy, E_0, while for the other energies (from half a dozen to two dozens of energy channels, depending on the SEP event considered) we assume that G is proportional to $E^{-\gamma}$; example of such fittings can be found in Lario (1997); Lario et al. (1998); Aran et al. (2006); Aran (2007); Aran et al. (2007, 2011).

Figure 2.8 is an example of the outputs that the model can provide, from the fitting of observed proton flux and anisotropy profiles. It depicts the evolution of Q at the cobpoint for the 4 April 2000 event, for five energy channels between 195 keV

[34] For an extensive explanation of the method used to solve the transport equation see Lario (1997) or Lario et al. (1998).

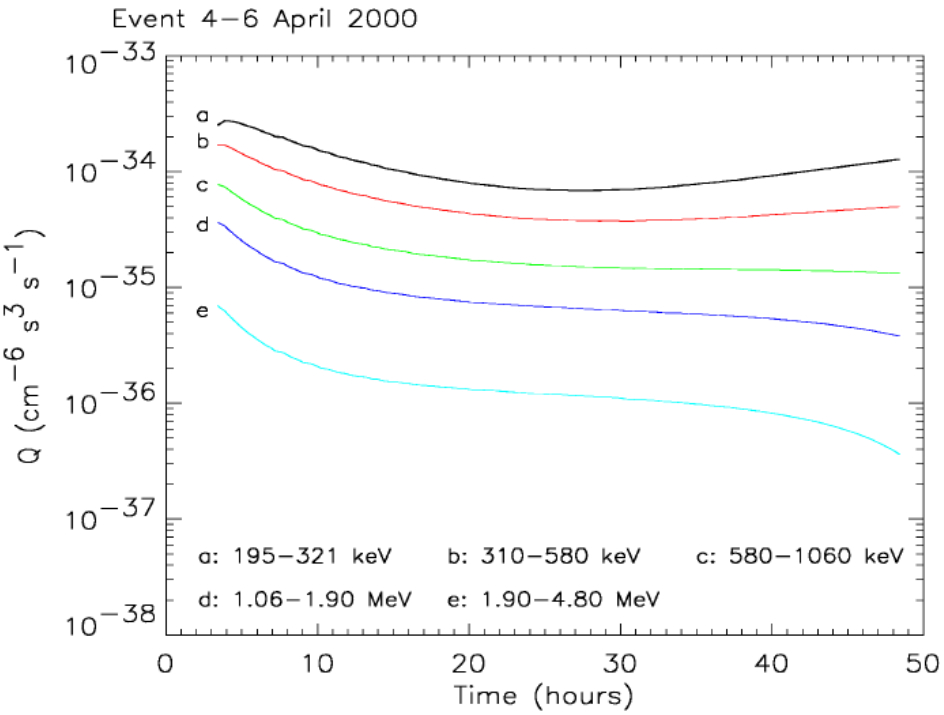

Figure 2.8: Evolution of Q for the 4 April 2000 SEP event for five energy channels, as labelled (from Aran 2007).

and 4.80 MeV, once the magnetic connection between the observer and the shock front is established ('first cobpoint') up to the shock passage by the observer's position. The connecting time, t_c, is the elapsed time period from the launch of the perturbation, $t = 0$, to the occurrence of the first cobpoint (see Lario et al. 1998).

The transport model assumes that the observer is connected back to the cobpoint by an unique flux tube, where particles are successively injected and propagate. In fact, during the development of a SEP event several flux tubes will sweep the spacecraft, due to the corotation of the solar wind, which carries out magnetic field tubes (Kallenrode 1997). Each one of these flux tubes contains different populations of energetic particles with not identical history of shock parameters. Therefore, the observed particle flux and anisotropy profiles are the result of successive samples of flux tubes seen by the spacecraft. At present, only Kallenrode & Wibberenz (1997b) and Lario et al. (1998) have modelled and evaluated the relevance of this corotation effect[35].

[35] While the shock is propagating out from the Sun, the background medium is rotating westward

The arrival of the shock at the observer is frequently accompanied by the ESP component, a flux enhancement produced by a quasi-isotropic population of particles. We reproduce this flux increase by assuming that it exists a foreshock region preceding the shock arrival, a high scattering region for the particles with self-generated waves. To model this region we assume a small mean free path there, since the transport equation does not include wave-related terms (as Ng et al. 2001, model does, for example). Interplanetary foreshock turbulence and waves have been observed (see, for example, Tsurutani et al. 1983; Russell 1988; Russell et al. 2009; Aguilar-Rodriguez et al. 2010), but only at the shock passage at 1.0 AU and they have not been extensively studied yet. Hence, assumptions about its characteristics (at and out of 1.0 AU) should be made in order to take into account its effects throughout the event (e.g., Aran et al. 2007)[36].

A limitation of the transport model is that it can only be applied to the upstream part of the SEP events (i.e., ahead of the shock). As the model assumes a Parker description for the IMF, it cannot be applied to simulate SEP events with a highly perturbed solar wind regime. The shock front is a mobile source of particles that can inject them into both the upstream and the downstream regions. However, the post-shock region is highly modified by the shock itself and evolves rapidly as the shock moves away from the Sun. Tan et al. (1992); Lario et al. (1999); Kallenrode (2002) study the distortion of the IMF structure due to the presence of a driver or magnetic cloud in the downstream region of an interplanetary shock and the effects that such variations might produce on the propagation of energetic particles[37]. But at present, it does not exist any reliable model that can describe the particle propagation in

at a rate of 13.6° per day. Therefore, an Earth-orbiting observer at L1, for example, will scan different magnetic flux tubes; as the shock propagates more slowly, more tubes will sweep the spacecraft before the shock arrival. A direct consequence of including corotation in a model is the considerably increase of the computing time needed to produce a fitting, because it is necessary to include to the flux the contribution coming from a different magnetic tube at each time/snapshot.

[36] Different studies (see quoted references) have described the presence of long-period amplitude waves upstream of interplanetary shocks. These waves guarantee multiple shock encounters of the particles and, consequently, a large energy gain in the acceleration process and storage of particles just ahead of the shock front. This turbulent foreshock usually appears at low energies, rarely at energies larger than 5-10 MeV. Figure 2 of Lee (2005) sketches the scenario proposed, where enhanced fluctuations and restricted particle propagation (so, particle storage) only exists in the vicinity of the shock.

[37] These works basically address and model, for specific situations, how the disturbance generated by the presence of a driver or magnetic cloud deforms the spiral field, which leads to transient local changes in the focusing length, L, that in turn influences the propagation of energetic particles.

the turbulent downstream region.

2.4.2 The Q(VR) relation

The values of $Q(r,t)$ are set by iteratively fitting the computed particle fluxes and anisotropies with the observational data. That is, for a given SEP event, the explicit procedure is as follows: we fit the flux and anisotropy (when they are available) profiles for the energy channel of reference, E_0, which yields to $\lambda_{\parallel 0}$ and Q_0. Then, assuming the functional dependence already described for Q and $\lambda_{\parallel 0}$ on the energy, we derive the best fit for the fluxes and anisotropies at all energies. The differential flux profiles derived are given in physical units after calibration, following the procedure described in Appendix E. Once the model has reproduced the profiles observed at different energies, we can compare the evolution of Q with the evolution of the plasma variables that characterize the shock strength at the cobpoint, inferred from the shock simulation: the normalized velocity ratio across the shock, VR, the magnetic field ratio, BR, or the angle between the magnetic field strength in the upstream region and the normal direction of the front shock, θ_{Bn}. We then analyse whether there is a functional dependence between Q and some of these parameters. From the simulation of several SEP events Lario et al. (1998), determine an empirical relation between Q and VR[38] at the cobpoint, the so-called Q(VR) relation; for a given energy, this relation has the form (Equation 2.2):

$$\log Q(r,t) = \log Q_0 + k\,\mathrm{VR}(r,t). \tag{2.21}$$

Figure 2.9 shows a representative example of the Q(VR) relation derived from the modelling of four SEP events, for several energy channels (between 56 keV and 57 MeV, depending on the event). The four SEP events correspond to a central meridian (CM) event, an east (E) event and two west (W) events (fast and slow case, WF and WS, respectively). The two upper panels display the correlation between Q and VR for the CM and E events (top) and the WS and WF events (middle) at low energy (two channels). The lower panel shows this correlation for high energies (one energy per event). Each point represents a time step of the numerical integration at which particle injection occurs. The thin arrows in the top two panels

[38] Trials to derive a relation between Q and BR were also performed, but the derived fits only showed circumstantial evidence of a relation in few cases, and it was not always possible to identify an evolution as did for VR. No indications of any relation was found for θ_{Bn}. This point is discussed in Lario (1997) and Lario et al. (1998).

indicate the direction of increasing time. In the top panel, the points on the left correspond to the MHD conditions of the shock when it is still close to the Sun, whereas the points on the right indicate when the shock is close to 1.0 AU. The opposite is true for the middle panel; in the bottom panel, each set tracks the evolution of the corresponding event in the upper panels. Straight dashed lines show the result of a simple linear regression to each set of points: they follow a $\log Q \propto \mathrm{VR}$ dependence.

The dependence of Q with the plasma velocity ratio, VR, at the shock front implicitly considers its time and longitudinal (and latitudinal, in 3D models) evolution as the shock expands and as the cobpoint moves along its front. Q includes not only those particles accelerated by the shock, but also those reflected at its front; therefore, a simple dependence of Q and VR should be thought only as a convenient way to quantify the time evolution and longitudinal (latitudinal) dependence of Q by relating them to the dynamic expansion of the shock. As commented, other parameters than VR are also probably relevant to characterize the properties of Q (as in this model we considered BR and θ_{Bn}), as the Mach number or the existence of a seed population (Tsurutani & Lin 1985; Desai et al. 2006). Our knowledge of the quantitative dependence of Q on those variables or factors is far from being definitive. More realistic approaches for the injection rate Q are required in order to fully link the shock evolving properties with its efficiency in particle acceleration and injection. Sokolov et al. (2006b) revisit the diffusive shock acceleration theory of charged particles by shocks, concluding that *"the quantitative model of particle acceleration at shock waves is more tightly coupled to the models of the background solar corona and the CME than is usually assumed. Apart from the compression ratio, other important factors that determine the particle production at shocks are the shock angle, φ, the Alfvén Mach number, and the level of turbulence, along with its power spectrum and extent anisotropy"*. Our group has been considering many of these factors since the first shock-and-particle model, by Heras et al. (1992), and we always work keeping in mind to consider many factors as possible (at least those related with the shock determination).

Our experience in modelling SEP events has shown that, in order to simultaneously fit several energy channels (from ~ 0.3 MeV to ~ 200 MeV), it is necessary to consider that the slope of the power law, $Q \propto E^{-\gamma}$, at high energies can be different than at low energies (Lario et al. 1998), which is consistent with the fact

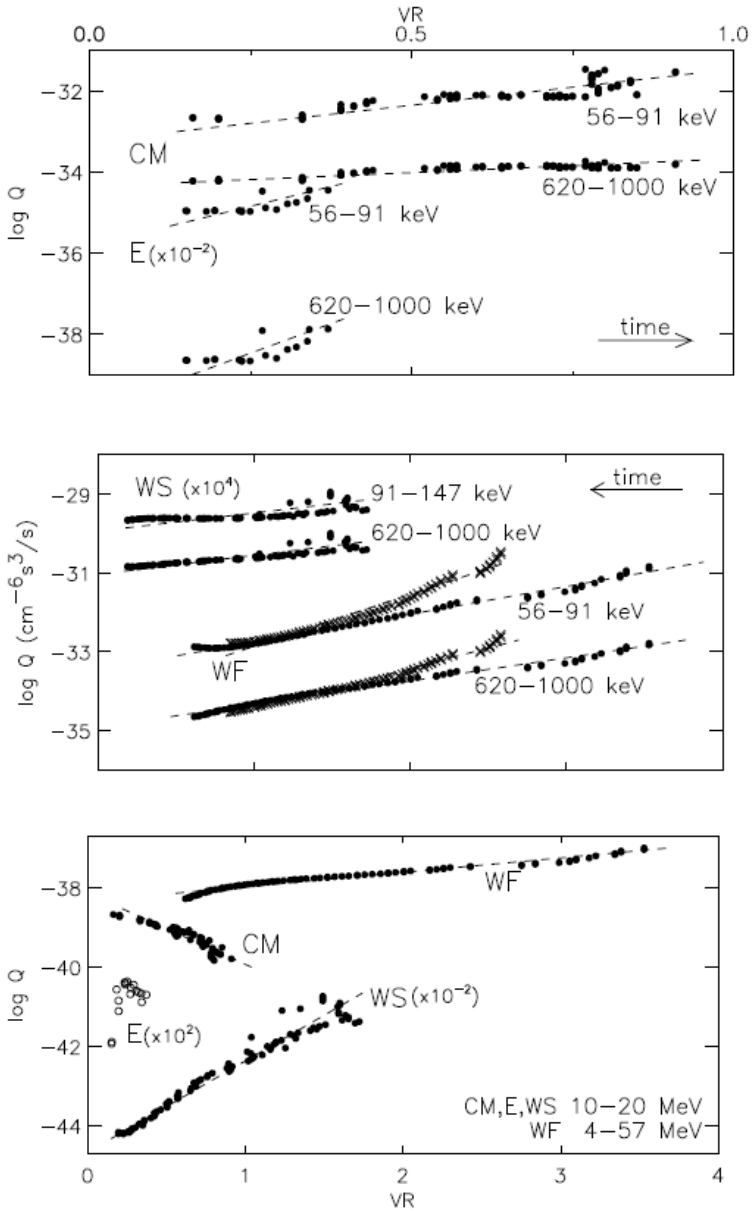

Figure 2.9: Examples of the dependence of Q on VR. Top panel: low-energy fits for CM and E events; middle panel: low-energy fits for WS and WF events; bottom panel: high-energy fits for the four events. The top scale of VR only applies to the top panel (from Lario et al. 1998).

that the efficiency of the shock as particle accelerator sharply decreases with energy (Armstrong et al. 1977). Furthermore, SEP fluxes frequently show a knee or rollover energy (somewhere between $\sim 5\,\mathrm{MeV}$ and $\sim 400\,\mathrm{MeV}$) where the spectral index softens, i.e, becomes more negative (Tylka et al. 2000; Xapsos et al. 2000). The only way to asses the validity of the $Q(\mathrm{VR})$ relation (and maybe extending it

to BR) is modelling a large set of various types of SEP events, mainly originated from solar longitudes between W50 and E10.

Assuming the Q(VR) relation, it is then possible to invert the procedure and compute synthetic flux and anisotropy profiles. That is, for a given solar event that triggers a shock: (1) the shock propagation model provides the values of the MHD variables of the shock all along its front (in particular, at the cobpoint) and throughout its travel toward the observer; (2) this allows us to evaluate the number of particles to be injected into the IMF line rooted at the cobpoint; and (3) the effects of the propagation of these particles through the interplanetary medium, along the IMF, are estimated by means of the particle transport equation. The output is a set of SEP profiles for a given range of energies in such specific solar-terrestrial scenario.

For space weather purposes it is important to estimate the proton flux at high energy ($>20\,\mathrm{MeV}$). This requires to assume $Q \propto E^{-\gamma}$, and the spectral index can then be compared with observations. However, the slope of observed energy spectrum highly varies from event to event and, thus, it is hard (if possible) to define average values of fluxes at high energies for different types of SEP events (i.e., average spectral indices). For example, there are SEP events generated by CMEs of similar characteristics that show high energy fluxes differing by 3 or 4 orders of magnitude (e.g., Kahler 2001). Figure 14 of Cane et al. (1988) clearly illustrates this point: the spectral index for $24 < \mathrm{E} < 81\,\mathrm{MeV}$-protons derived at the peak intensity for 235 proton events varies from 1.5 to 7.1 from event to event, as function of the position of the observers (for an extended discussion, see Section 5.3.2 of Aran 2007).

The Q(VR) relation permitted us to build SOLPENCO (see Section 2.1). The parameters selected to generate its database are basically derived from modelling individual SEP events (using the SaP98 model), by carefully fitting simultaneously both the upstream proton flux and the first order anisotropy profiles for various (usually eight) energy channels between $\sim 0.1\,\mathrm{MeV}$ and $5\,\mathrm{MeV}$. The main parameters used to build such database are: Q, which has been calculated at the cobpoint position for each case assuming $\log Q = \log Q_0 + k\,\mathrm{VR}$, taking $k = 0.5$ for all energies; and the energy dependence of Q_0, which has been considered to be a power law of the form $Q_0 \propto E^{-\gamma}$, with index $\gamma = 2$ for $\mathrm{E} < 2\,\mathrm{MeV}$ and $\gamma = 3$ for $\mathrm{E} \geq 2\,\mathrm{MeV}$. These are averaged values derived from modelling several SEP events for $0.5\,\mathrm{MeV}$-

protons (see details in Aran 2007, and references therein). These are the parameters that we will use to derive the synthetic flux profiles presented in Chapter 3. Figure 2.10 shows an example of different synthetic proton flux profiles of the database of SOLPENCO, at 0.5 MeV, for an observer located at 1.0 AU, and for eight interplanetary shocks with initial velocities between 750 km s^{-1} and 1800 km s^{-1}.

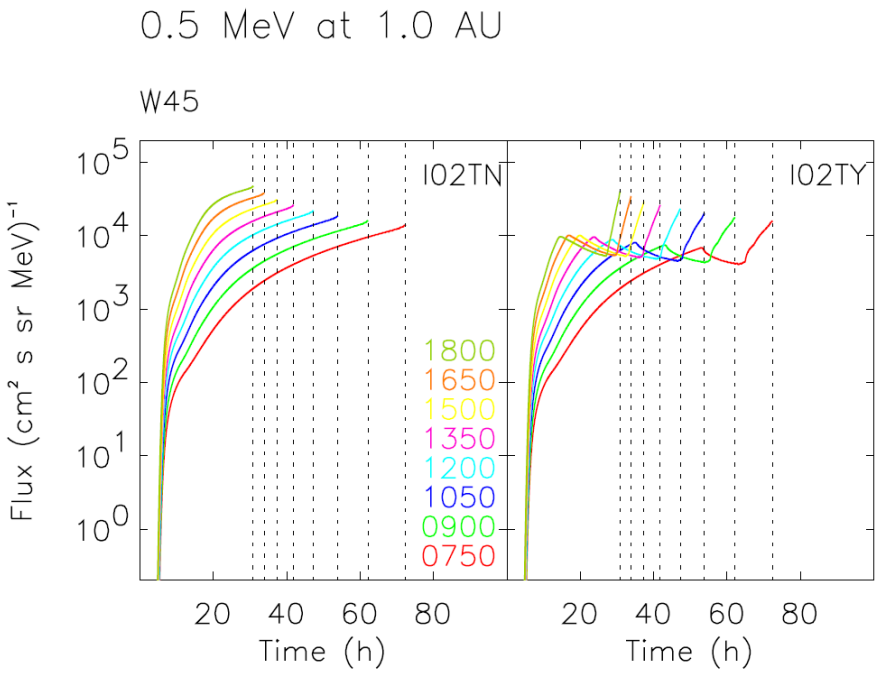

Figure 2.10: SOLPENCO: two examples of the flux profiles of the database. Synthetic 0.5 MeV-proton flux profiles for a 1.0 AU-observer at W45. The initial velocity of the eight simulated shocks is colour coded as indicated. Vertical dashed lines mark the arrival time for each shock at the observer's location. Left panel: derived flux profile without assuming the existence of a foreshock; right panel: assuming a foreshock (from Aran et al. 2005).

Part I

3D modelling of proton gradual events

Chapter 3

Scenario and shock determination

> Posa una cosa al lloc equivocat,
> i encara que hi sigui -molt
> possiblement just davant teu-
> pot desaparèixer per sempre
>
> *Invisible*, Paul Auster

3.1 Introduction

The shape of the flux profiles of gradual SEP events depends on several, not completely understood, factors. In this part of the thesis we focus on two of them: the influence of the shock strength and of the relative position of the observer. Two observers located at the same radial distance and with the same longitude, detecting the same shock, would not necessarily measure the same particle flux profile if they are at different latitudes with respect to the incoming disturbance. The reason is that their magnetic connection with the shock front may scan different regions with different conditions for particle acceleration and, hence, the observed flux profiles will differ[1].

To study the influence of these factors in the SEP flux profiles and how relevant they can be, we simulate the propagation of two interplanetary shocks (slow and fast) up to several observers placed at different radial distances, and at different angular positions with respect to the nose of the shock. We evaluate the plasma conditions at the cobpoint as derived from the 3D MHD shock simulation and we discuss the influence of the latitude on these changing conditions. We use these

[1] Chapters 3 and 4 are based on Rodríguez-Gasén et al. (2011)

outputs to study the influence of the position of the observer on the injection rate of shock-accelerated particles and on the resulting proton flux profiles to be measured by each observer (e.g., detected by each spacecraft).

3.2 Solar source and interplanetary scenarios

3.2.1 Background solar wind

To simulate the 3D background solar wind we use the model described in Section 2.2.3. Figure 3.1 presents several solar wind profiles as a function of the radial distance (left) and of the latitude (right) used in both shock simulations. Panels from top to bottom display the magnetic field strength, B, the number density, n, and the radial velocity, v_r, profiles. Each panel shows three curves corresponding to latitudes 45°, 22° (the latitude of the CME-launch direction, see below), and 7° (approximately the latitude of the ecliptic plane). The two regimes of the solar wind can be clearly differentiated in the bottom panel: a fast regime ($\sim 700\,\mathrm{km\,s^{-1}}$) at high latitudes, and a slow regime ($\sim 400\,\mathrm{km\,s^{-1}}$) near the equator. The three right panels show the dependence of the same variables with the latitude at $15\,\mathrm{R_\odot}$. Table 3.1 summarizes the derived values of B, n and v_r at 0.4 AU and at 1.0 AU, and at latitudes 7°, 22° and 37° over the solar equator, respectively. Note that: (1) the solar wind speed matches the observed values at 0.4 AU and at 1.0 AU; (2) at 0.4 AU, B varies in latitude from 7 nT to 11 nT, slightly underestimating observations near the ecliptic plane at such distance (Mariani & Neubauer 1990); and (3) the solar wind density is too high when compared to observations (e.g., at 1 AU in the ecliptic plane, the model gives $\sim 35\,\mathrm{cm^{-3}}$ whereas the observed average value is $\sim 6\,\mathrm{cm^{-3}}$, Kivelson & Russell 1995).

3.2.2 CME initial conditions

For the simulation of the fast shock, we assume that the plasma bubble has a radius $d_{cme} = 0.75\,\mathrm{R_\odot}$ and that its centre is placed at $2.5\,\mathrm{R_\odot}$. The extra density and velocity introduced (see Section 2.2.3) are: $n_{cme} = 7 \times 10^8\,\mathrm{cm^{-3}}$ and $v_{cme} = 3500\,\mathrm{km\,s^{-1}}$. These values yield a total mass of $\sim 1.4 \times 10^{17}$ g and a kinetic energy of $\sim 2.5 \times 10^{33}$ erg, both quantities within the range of estimated values for fast CMEs (Vourlidas et al.

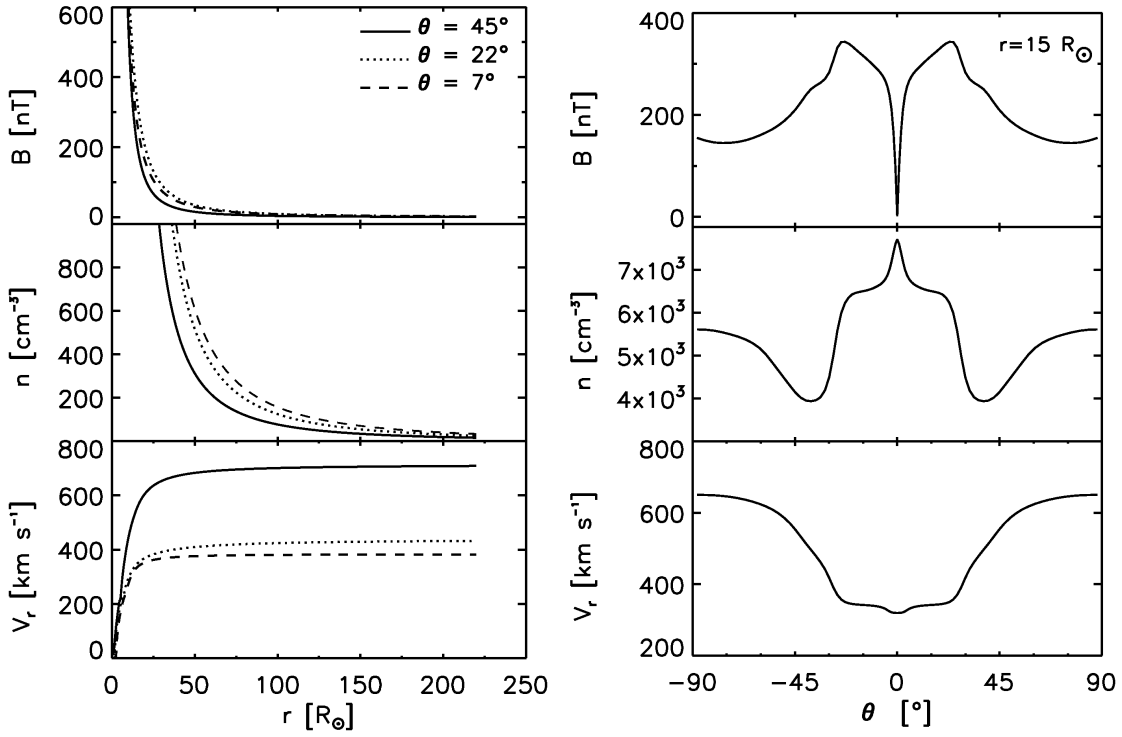

Figure 3.1: Left panels: B, n and v_r radial profiles of the background solar wind for three latitudes, as labelled. Right panels: Same profiles at $r = 15\,\mathrm{R}_\odot$ displayed as a function of the latitude.

Table 3.1: Values of B, n and v_r of the simulated solar wind at 0.4 AU (left) and at 1.0 AU (right), for three latitudes.

		0.4 AU			1.0 AU		
$\theta\,[^\circ]$	7	22	37	7	22	37
$B\,[\mathrm{nT}]$	10.9	11.8	7.2	2.4	2.3	1.2
$n\,[\mathrm{cm}^{-3}]$	209.8	164.3	108.2	34.3	25.3	17.0
$v_r\,[\mathrm{km\,s}^{-1}]$	381	428	638	383	440	651

2002; Manchester et al. 2006, 2008a,b; Colaninno & Vourlidas 2009). The blob is launched in the direction ($\theta_{cme} = 22^\circ, \varphi_{cme} = 180^\circ$). Figure 2.4 shows the profile of the initial radial velocity introduced to simulate the fast shock. To simulate the slow shock, we assume the same scenario and conditions as for the fast shock, but with $v_{cme} = 2000\,\mathrm{km\,s}^{-1}$. This yields the same total mass as for the fast case, and a kinetic energy of $\sim 8.8 \times 10^{32}$ erg.

3.2.3 Location of the observers in space

The evolution of the simulated shocks is followed up to $100\,R_\odot$ from the Sun, with nine observers located at $r = 86\,R_\odot$ (~ 0.4 AU), approximately Mercury's orbit. In a second scenario, we track the evolution of the fast shock up to $220\,R_\odot$ with nine observers located at $215\,R_\odot$ (~ 1.0 AU).

We use the Heliocentric Earth Equatorial (HEE) system of reference[2] (Hapgood 1992; Fränz & Harper 2002) to identify the angular position (longitude and latitude) of the observers. In longitude, we place three observers 45° westward from the nose of the shock, other three observers 30° towards the east, and other three in the same longitude as the shock direction. Thus, according to the HEE system, those observers are placed at W45, E30 and W00[3] in longitude with respect to the solar parent activity, respectively. In latitude, three observers are placed at the same latitude as the shock leading direction, $\theta = 22°$, which are the N22 observers. Other three observers are placed 15° northward of this direction, being the N37 observers ($\theta = 37°$), and three more 15° southward and they are the N07 observers ($\theta = 7°$).

In short, the nine observers are located at N37W45, N22W45, N07W45, N37W00, N22W00, N07W00, N37E30, N22E30 and N07E30, with the shock launched in the N22W00 direction. Figure 3.2 shows three different views of one snapshot of the fast shock simulation 4.95 hours after the launch of the perturbation, as well as the situation of the nine 0.4 AU-observers. Top left and top right panels show a view of the XY and XZ plane, respectively; bottom panel displays a 3D frontal view of the simulation. The dark-grey surface indicates the regions of the CME where the relative radial velocity coincides with the threshold value used to mark the spatial boundary of the front of the expanding interplanetary shock (see next Section). The black line indicates the CME propagation direction. Coloured solid circles indicate the position of the observers, the colour lines their IMF lines and the coloured open circles the location of their corresponding cobpoints. The colour code for the nine observers is as follows: N37W45, brown; N22W45, pink; N07W45, dark-grey; N37W00, red; N22W00, green; N07W00, blue; N37E30, cyan; N22E30, purple; and N07E30, orange.

[2] In the HEE system, the X-axis is the intersection between the solar equator and the central meridian as seen from the Earth, and the Z-axis is the rotation axis of the Sun. The Y-axis is perpendicular to both on them in the equatorial plane, completing the right-handed system.

[3] Note that under this scenario, the W00 observers are central meridian, or CM, observers.

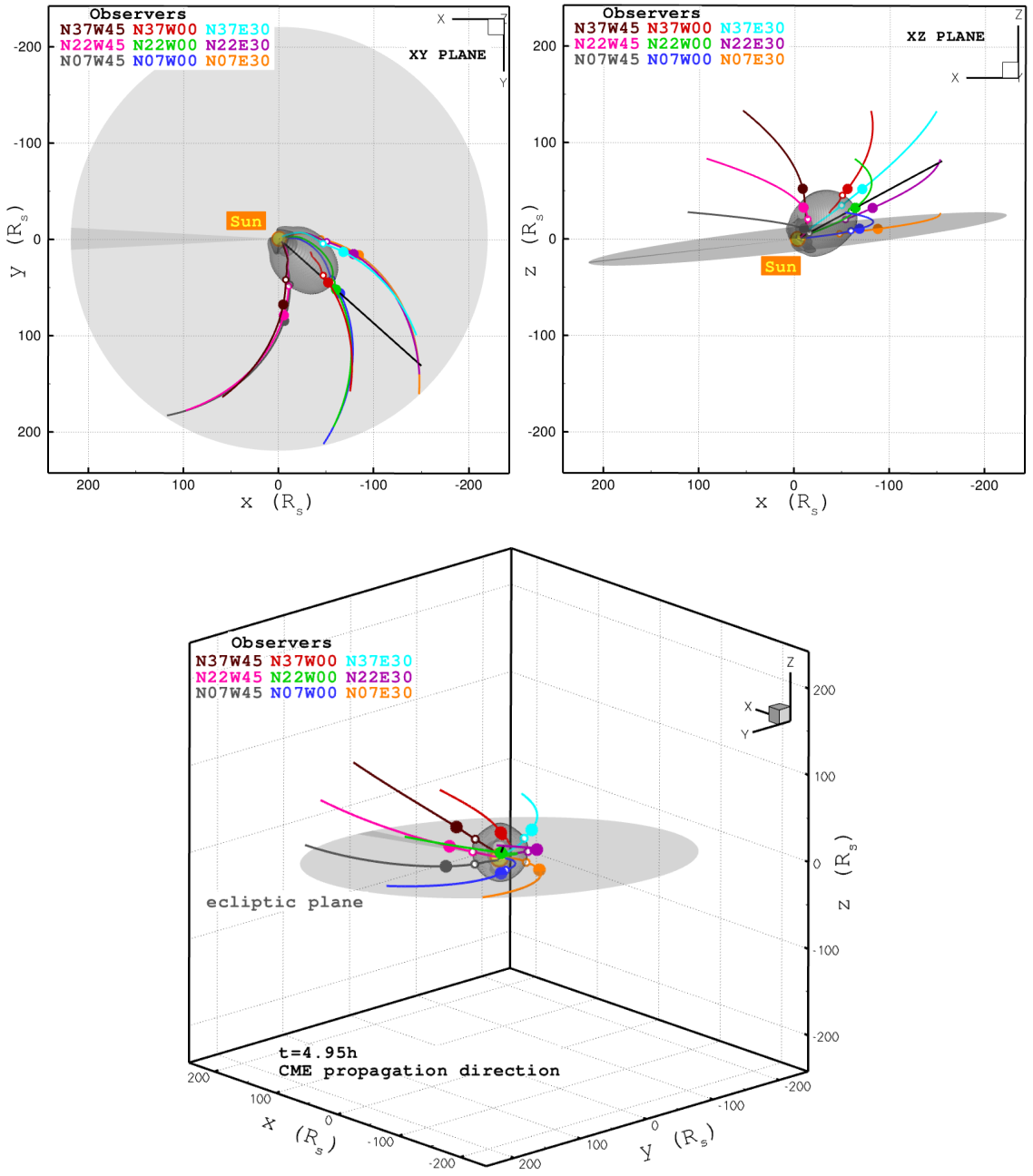

Figure 3.2: Three views of a snapshot of the 3D simulation after t = 4.95 hours. Top left: the XY plane; top right: the XZ plane; bottom: 3D frontal view. The dark-grey isosurface indicates $\xi = 0.01$ (see next Section). The grey slice shows the ecliptic plane, the Sun is located by the yellow point and the black line indicates the CME propagation direction. The colour code for the nine observers, their corresponding IMF lines and cobpoints are as labelled and given in the text.

The shock simulation is performed using a co-rotational 3D MHD model in spherical coordinates (r, θ, φ). Then, the position of a generic observer will be given by $(r, \theta, \varphi - \omega\,\Delta t)$ in a Sun-Earth reference frame, where the Sun rotates with an angular speed ω and Δt is the elapsed time from the beginning of the simulation.

3.3 Shock determination. Procedure

The aim of this section is to describe the main details or elements of the process applied to derive the values of the plasma and magnetic field variables upstream, at the passage and downstream of the shock front, as well as their changes at the vantage position of the observers. A general description of this issue has been presented in Section 2.3.

3.3.1 Determination of the IMF lines and the cobpoint

• The IMF lines

To determine the cobpoint position at the front of the shock, it is necessary to calculate the IMF line connecting the observer with the shock. The position of the observer is the starting coordinates of the IMF line in order to ensure the magnetic connection of the observer with the shock front. From this location, the IMF line is calculated, point by point, towards the Sun and in opposite direction up to the outer grid boundary of the model.

To derive the magnetic field line the values of its components, $(B_r, B_\theta, B_\varphi)$, at each point of the grid are required; these values are provided by the MHD simulation. Then, the computation of each point of the IMF line is done in two steps: a first predictor step and then a corrector step. Assuming that the IMF is a Parker spiral, its components are (Kivelson & Russell 1995):

$$B_r = B_0(\frac{r_0}{r})^2\,;\;\; B_\theta = 0\,;\;\; \text{and}\;\; B_\varphi = -\frac{\Omega\, r\, \sin\theta}{\upsilon_{sw}} B_r, \tag{3.1}$$

where r_0 is an arbitrary heliocentric radial distance (at which the field is assumed to be frozen in the solar wind). Being ψ the angle between the radial and the IMF

line direction, $\tan\psi = \dfrac{\Omega\, r\, \sin\theta}{v_{sw}}$, and then

$$B = B_r\, \sec\psi, \tag{3.2}$$

where $B \equiv |\mathbf{B}|$.

If z is the distance measured along the IMF line, $dr = dz\cos\psi$, one step in the radial direction can be written as

$$\Delta r = r(i+1) - r(i) = \Delta z\, \frac{B_r}{B}; \tag{3.3}$$

and proceeding in a similar way in the azimuthal direction

$$\Delta\varphi = \varphi(k+1) - \varphi(k) = \Delta z\, \frac{B_\varphi}{r\, B\, \sin\theta}, \tag{3.4}$$

where i and k represent the radial and angular positions of the grid. Then, defining a scale factor, S, as

$$S = \pm\frac{1}{2}\,\frac{\Delta r}{2}\,\frac{1}{2}\,\frac{1}{B}, \tag{3.5}$$

the new radial and angular positions are given by

$$r(i+1) \;=\; r(i) \;+\; S\, B_r \tag{3.6}$$

and

$$\varphi(k+1) \;=\; \varphi(k) \;+\; S\,\frac{B_\varphi}{r(i+1)\,\sin\theta}. \tag{3.7}$$

The first $\frac{1}{2}$ in the factor scale appears because the procedure is performed in two steps (predictor-corrector)[4]. The $\Delta z = \frac{1}{2}\,\Delta r$ is a step increase along the IMF line to ensure that the step size is small enough (the minimum possible value is $\Delta z \sim \Delta r$). And the last $\frac{1}{2}$ is introduced since the program stores the calculated IMF points after computing two segments of the line.

For each point of the IMF line, we compute the plasma and magnetic field vari-

[4] The first step (predictor) allows to determine a radial distance different from the initial one in order to calculate a better interpolation for B_φ in the second step (corrector). This method was first elaborated in a 2-D scenario by T. Detman for the first shock-and-particle model (Heras et al. 1992, 1995).

ables, ρ, v_r, v and B, as well as their relative[5] values with respect to the background solar wind. As the points of the IMF line do not necessarily coincide with the grid points, all these values are derived by trilinear interpolation within the 8 neighbouring points of the grid (see Appendix C).

To confirm the goodness of the IMF lines determination we have compared the constructed lines with the streamlines derived using the visualization software Tecplot[6], and with the lines calculated by applying the theoretical expression of Parker (1958). Appendix D gives more details of such comparison. The conclusion of these tests is that we are confident in the procedure performed. Figure 3.2 shows the IMF lines computed for the nine observers and for the snapshot presented; see also Figure D.1 of Appendix D.

• **The cobpoint**

The first step to determine the location of the cobpoint is to search for a candidate[7] point. We start from the position of the observer, moving back toward the Sun along the computed IMF, looking for the first point where the relative radial velocity jumps an 1%[8] over the background solar wind; i.e., $\xi = (v_r - v_{r_{sw}})/v_{r_{sw}} > 0.01$.

The relative ρ can also be used as variable to determine the position of the potential cobpoint, together with the relative v_r. However, the location of the potential cobpoint resulted to be very sensitive, arising situations where the use of both variables produced disparate results. Hence, since the shock-and-particle model focusses on the normalized radial velocity jump, VR, as the variable to quantify the strength of the shock at the cobpoint, we have opted for the use of the relative v_r to identify what we will later consider the front of the shock.

[5] Here, the term 'relative' means $A_{rel} = (A - A_{sw})/A_{sw}$, being A any variable at the investigated point, and A_{sw} the corresponding value of the background solar wind. Thus, they are normalized values.

[6] Tecplot is a software package for data analysis and visualization, well suited for 3D imaging. It can produce very nice plots but the source code is not open; hence, we can not know how exactly it performs and, specially, how precise may it be in complex scenarios. http://www.tecplot.com/

[7] 'Candidate' because there is a chance that the plasma jump, even when large, could be a numerical fluctuation of the simulation.

[8] We have considered other possible thresholds (from 0.01% to 0.5%), concluding that the adopted value is a good choice because the differences found in the identification of the cobpoint candidate position for any of the observers are, in average, smaller than $0.04\,R_\odot$ (and only in one case is $\sim 0.5\,R_\odot$).

We have performed a comparison between several of these cobpoint identifications with those derived from the calculation of the theoretical coronal footpoint, using the mapping-back technique introduced by Nolte & Roelof (1973). Appendix D shows the results of the proves that sustain our approach.

The unitary vector in the radial direction defines the line that connects the Sun and the cobpoint candidate. For each point of the radial line, the program computes the values of the plasma and magnetic field variables, their relative values, as well as the derivatives of the relative density and relative radial velocity in the radial direction, i.e., the radial gradients. To nominate the candidate point as cobpoint, the radial gradients must be larger than the 10% of the maximum gradient value in the radial direction (to avoid small spurious fluctuations). If this criterion is not accomplished, we look for the next cobpoint candidate along the IMF line. The time invested to perform this loop until the appropriate cobpoint is found determines the quality of the cobpoint. Figure 3.2 shows the cobpoints derived for the nine observers presented.

3.3.2 Shock normal and downstream point

Once selected the cobpoint, it is necessary to determine the shock normal direction, $\hat{\mathbf{n}}$, and the "downstream point", to further calculate the plasma jumps across the shock front. To compute $\hat{\mathbf{n}}$ we can figure out that the simulated shock is a real interplanetary shock, with the observer located at the cobpoint when the shock front sweeps its position. Hence, it is necessary to determine a downstream point, where the values of the plasma variables and magnetic field have to be picked up.

As first estimate, we search along the radial line, from the cobpoint moving on toward the Sun: the first point where the radial gradient of the relative radial velocity is still positive and smaller than 20%[9] of the maximum value of this derivative along the radial line, is chosen as downstream point candidate.

[9] We have also tested this threshold both for the position of the cobpoint and the downstream point along the radial line for different values (from 10% to 30%). We have concluded that the adopted value is the one that better matches the whole set of snapshots and observers we are studying, approximately 300 snapshots for each one of the 27 observers.

Note that, near the nose of the shock, the plasma jumps derived directly from observations (radial direction) probably are quite similar to those derived in the shock normal direction. This is most likely not true when the cobpoint is far from the shock nose (either in longitude as in latitude)[10]. Therefore, to obtain a good estimation of the plasma jumps across the shock front, we have to derive the location of the downstream point in the normal direction.

• The shock normal direction

The method developed by Viñas & Scudder (1986) and Szabo (1994)[11] is the most comprehensive method for shock parameters determination from single spacecraft magnetic field and plasma observations (Koval & Szabo 2008). But this technique is currently only applicable to single-point shock measurements, as visual inspection is needed; thus, it is not adapted yet for an automated application to hundreds of points (cobpoints) at the front of a simulated shock. Alternatively, we can use any of the various and well documented existing methods to determine the shock-normal direction (e.g., Viñas & Scudder 1986; Szabo 1994; Berdichevsky et al. 2001; Lin et al. 2006; Koval & Szabo 2008, and references quoted there). We have applied five of them in order to determine the shock normal vector, $\hat{\mathbf{n}}$. These methods are:

– the magnetic field coplanarity method (Colburn & Sonett 1966), MC, which requires that the upstream and downstream magnetic fields and $\hat{\mathbf{n}}$ lie in the same plane, and that the normal components of the magnetic fields are conserved across the shock. Then:

$$\hat{\mathbf{n}} = \frac{(\mathbf{B}_u \times \mathbf{B}_d) \times (\mathbf{B}_u - \mathbf{B}_d)}{|(\mathbf{B}_u \times \mathbf{B}_d) \times (\mathbf{B}_u - \mathbf{B}_d)|}, \tag{3.8}$$

where the subscripts u and d refer to upstream and downstream values, respectively;

– the velocity coplanarity method (Abraham-Shrauner 1972), VC, which uses the

[10] In other words, the observer detects the passage of a region of the shock weaker and/or departed from sphericity. How much? It depends on the angular separation between the observer and the nose of the shock, and on the intrinsic characteristics (e.g., curvature) of the shock itself. So, it could be quite different from event to event.

[11] Appendix H gives a more detailed explanation of the Viñas & Scudder (1986) and Szabo (1994) method.

velocity jump across the shock to obtain $\hat{\mathbf{n}}$:

$$\hat{\mathbf{n}} = \frac{(\boldsymbol{v}_d - \boldsymbol{v}_u)}{|(\boldsymbol{v}_d - \boldsymbol{v}_u)|}; \tag{3.9}$$

and

– the three mixed methods of Abraham-Schrauner (Abraham-Shrauner & Yun 1976), MD, that use a mixture of the plasma velocity coplanarity and the magnetic field coplanarity method to derive $\hat{\mathbf{n}}$:

MD1:

$$\hat{\mathbf{n}} = \frac{(\mathbf{B}_u \times (\boldsymbol{v}_d - \boldsymbol{v}_u)) \times (\mathbf{B}_u - \mathbf{B}_d)}{|(\mathbf{B}_u \times (\boldsymbol{v}_d - \boldsymbol{v}_u)) \times (\mathbf{B}_u - \mathbf{B}_d)|} \tag{3.10}$$

MD2:

$$\hat{\mathbf{n}} = \frac{(\mathbf{B}_d \times (\boldsymbol{v}_d - \boldsymbol{v}_u)) \times (\mathbf{B}_u - \mathbf{B}_d)}{|(\mathbf{B}_d \times (\boldsymbol{v}_d - \boldsymbol{v}_u)) \times (\mathbf{B}_u - \mathbf{B}_d)|} \tag{3.11}$$

MD3:

$$\hat{\mathbf{n}} = \frac{((\mathbf{B}_d - \mathbf{B}_u) \times (\boldsymbol{v}_d - \boldsymbol{v}_u)) \times (\mathbf{B}_u - \mathbf{B}_d)}{|((\mathbf{B}_d - \mathbf{B}_u) \times (\boldsymbol{v}_d - \boldsymbol{v}_u)) \times (\mathbf{B}_u - \mathbf{B}_d)|}. \tag{3.12}$$

Using the location of the cobpoint as upstream[12] point, and the location of the downstream point along the radial direction to the shock, we have applied these five methods to determine the shock normal direction at the cobpoint. From $\hat{\mathbf{n}}$, we calculate the line in the shock normal direction and the plasma and magnetic field variables at each point of this line (by trilinear interpolation).

Figure 3.3 shows the shock normal lines obtained by using these five methods for the N22W00 observer at 0.4 AU (as depicted in Figure 3.2). The top large image is a 2D view of the XY plane, and the colour scale represents v_r-contours for the

[12] The values at the upstream point are those of the background solar wind at the cobpoint position. Without a posteriori 'visual inspection' none of the methods presented can offer 100% guaranteed results. Section D.2 of Appendix D deals with some special situations arisen during the development of the procedure.

slice corresponding to the Z-coordinate of the cobpoint. The bottom large image[13] is a view of the XZ plane with the v_r-contours for the slice corresponding to the Y-coordinate of the cobpoint. The two small figures are zoomed out views of the respective figures to quantify the radial distances involved. Further details about the application of these methods and the tests performed are commented in Appendix D.

We have decided to, basically, rely on the MD3 method to compute $\hat{\mathbf{n}}$, despite all of them are implemented in the procedure. Figure 3.4 shows an example of three computed shock normal lines for the N22W45, N22W00 and N22E30 observers at 0.4 AU (same snapshot and colour code as in Figure 3.2). This figure is a projection in the XY plane of the 3D position of each observer, their computed IMF lines, the location of the cobpoints and the calculated shock normal lines for each observer. The dark-grey isosurface[14] indicates the spatial boundary of the front of the expanding interplanetary shock (i.e., $\xi = 0.01$; see also Figure 3.2). The radial and the normal directions to the shock front are nearly the same when the cobpoint is situated at the nose of the shock, but they largely differ at the wings.

• The downstream point

Once determined the shock normal line, we can look for the definitive downstream point by searching along the normal line, from the cobpoint toward the Sun. We locate the downstream point at the first point where the radial velocity and density start decreasing: there where the derivative of the relative radial velocity in the normal direction (i.e., normal gradient) is the 20%[15] of the maximum value (the same criterion as the one used along the radial line). We have added a second (complementary) criterion for the 1.0 AU-observers: when the shock thickness (see next Section) is larger than a fixed value, 8.0 $R_\odot$, the downstream point is then located where the value of the normal gradient is the 75% of the value at the previous point. This extra condition helps to solve a situation that could appear when the downstream point is located in a flank of the shock. There, the v_r-profiles are very smooth and, hence, the thickness of the shock might be greater than the maximum

[13] This figure is mirrored with respect to the top image in order to better show the computed normals and the observer-Sun line.

[14] Ripples and waves in the surface are graphic artefacts caused by Tecplot's interpolation.

[15] As in former cases, we have considered different values for this threshold (from 10% to 30%), concluding that the adopted value is the better choice for the set of analysed snapshots and observers.

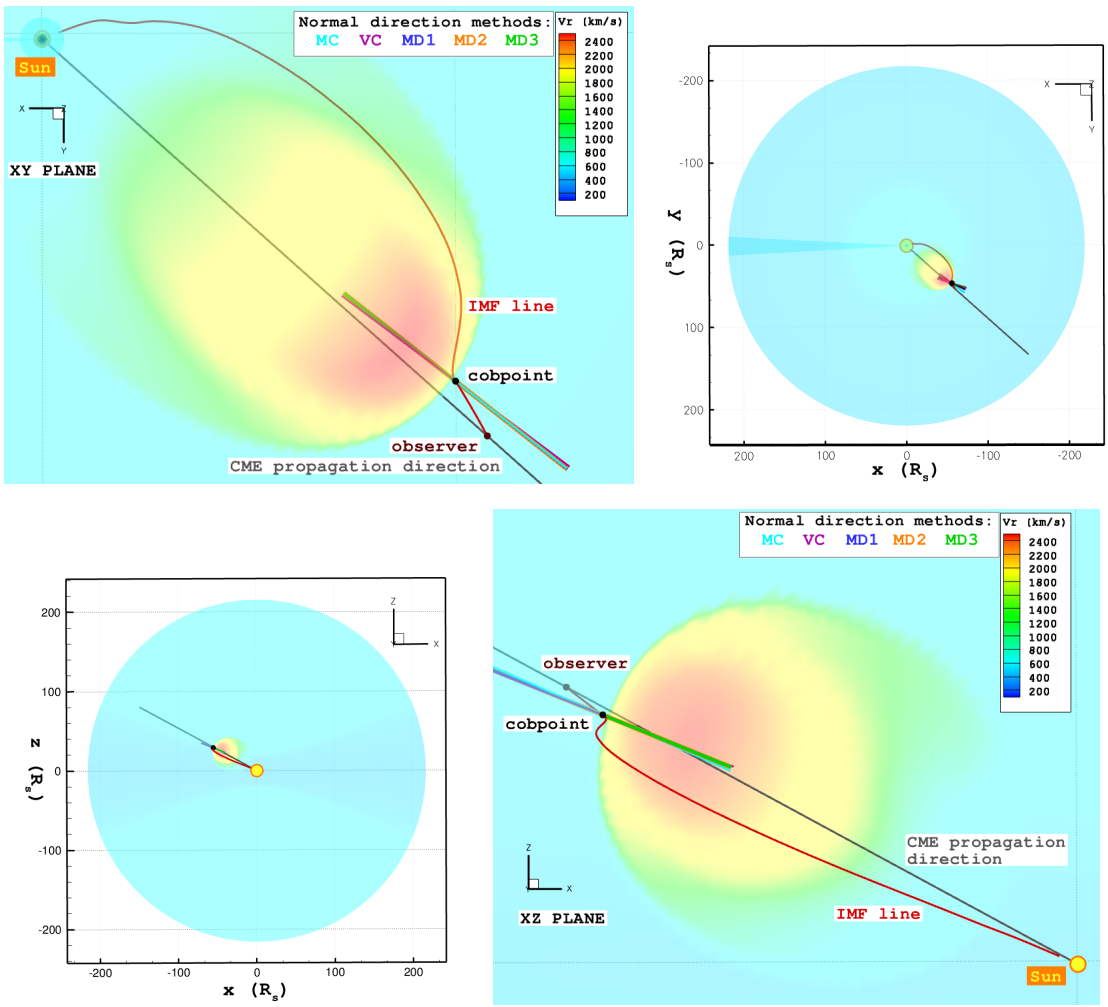

Figure 3.3: Shock normal determinations for the N22W00 observer (two views of the same snapshot as in Figure 3.2) at 0.4 AU. Top: a general (right) and a zoomed (left) view of the XY plane; bottom: the same for the XZ plane. Contours of plasma radial velocity are colour coded (top right bars). The red line is the IMF line that connects the observer with the shock front. The cobpoint is drawn in black. The black line indicates the CME propagation direction. The coloured lines show the different normal directions obtained by applying the methods described in the text (colour identified in the top horizontal inset).

value set for having a "valid" shock (see next Section).

Determining the downstream point in the flank of a shock is a troublesome task (see last point of Section 3.3.3). Luhmann et al. (2010) identify the downstream point as the point where the relative radial speed reaches its maximum value; they state: "*If there are stepped gradients, for example, the shock finder may select the part of the step that includes the compression maximum in the cone model material*

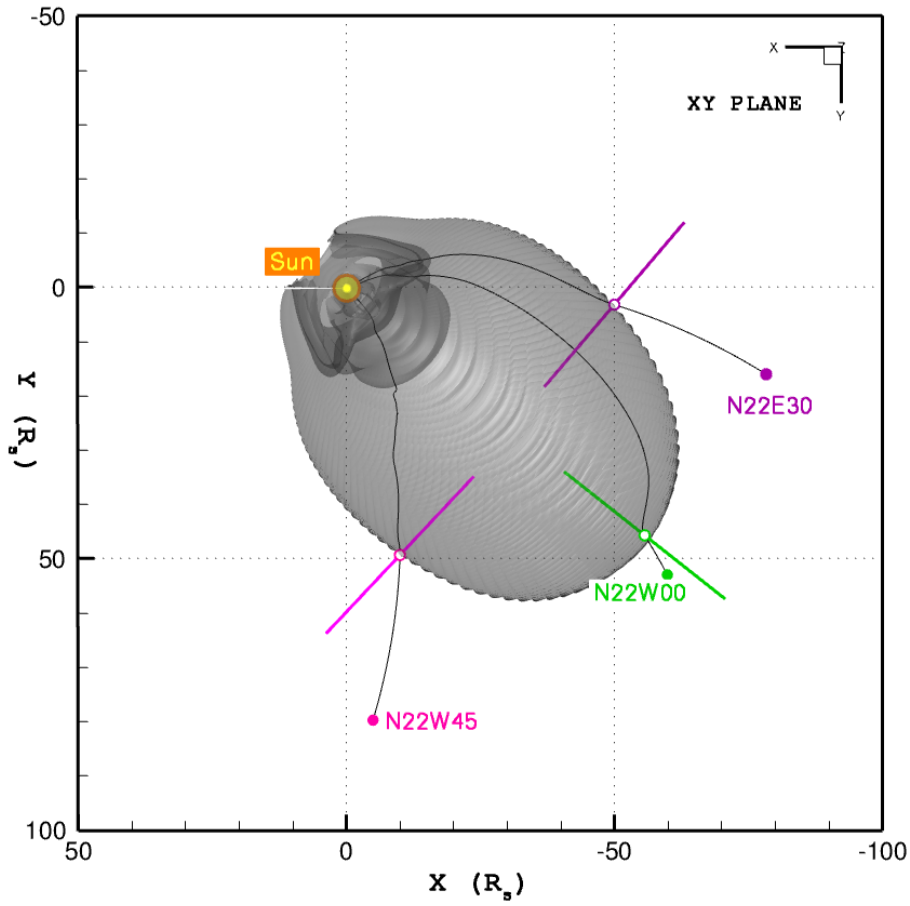

Figure 3.4: XY-plane cut (same snapshot as in Figure 3.2) showing the computed normal direction lines for three 0.4 AU-observers: N22W45 (pink), N22W00 (green) and N22E30 (purple). Coloured solid and open circles indicate the position of the observers and their corresponding cobpoints, respectively. The black lines represent the IMF lines and the coloured traces the shock normal line at each cobpoint position.

as the downstream rather than the shock ahead of it that is not well-separated from the entire sheath-like disturbance".

3.3.3 Characterization of the shock

With the position of the downstream point along the normal direction line determined, we define the thickness of the shock as:

$$d = \hat{\mathbf{n}} \left[\mathbf{r}_d - \mathbf{r}_u \right]. \tag{3.13}$$

In order to determine and characterize the shock, we compute the speed and

magnetic field along the normal direction at the upstream and downstream points; that is:

$$\upsilon_n = \boldsymbol{\upsilon} \cdot \hat{\mathbf{n}} \text{ and } B_n = \mathbf{B} \cdot \hat{\mathbf{n}}, \tag{3.14}$$

where we consider "positive speeds" the ones going from the Sun towards the observer (i.e., in the direction of the plasma flow). Then, the shock speed, υ_{sh}, is:

$$\upsilon_{sh} = \frac{\rho_d \, \upsilon_{n_d} - \rho_u \, \upsilon_{n_u}}{\rho_d - \rho_u}, \tag{3.15}$$

where υ_{n_u} and υ_{n_d} are the upstream and downstream speeds in the normal direction to the shock front at the cobpoint.

If M_f, M_A and M_s are, respectively, the fast, the Alfvén and the slow Mach numbers[16], a MHD shock can be classified (e.g., Kirk et al. 1994; Kallenrode 2004) as: (1) Fast, $M_{f_u} > 1$ and $M_{f_d} < 1$; (2) intermediate, $M_{A_u} > 1$ and $M_{A_d} < 1$; and (3) slow, $M_{s_u} > 1$ and $M_{s_d} < 1$.

We use these criteria to characterize the shock at the cobpoint; when verified, we tag the shock as "valid". If the shock does not fit in any of these conditions, we apply an extra criterion: the plasma variables υ, υ_r, ρ and T at the downstream point must be larger than at the upstream point. We tag the shock as "not valid" when it is not possible to determine the existence of a shock according to any of the above-mention conditions, or when the shock is wider than $8\,\mathrm{R}_\odot$.

Once characterized the shock, the final step is to quantify its strength. As commented in Chapter 2, the efficiency of a shock as a particle-accelerator depends on its strength at the cobpoint and at each moment, as the shock evolves. To quantify its MHD strength at the cobpoint, shock variables such VR, BR, the density compression ratio or θ_{Bn}, determine the efficiency of the acceleration mechanism. It is possible to compute the upstream-to-downstream ratio across the shock front for any plasma variable of the simulation we are interested to study: we particularly focus on calculating VR and BR. Note that, as these quantities are calculated in the shock normal direction at the cobpoint, we are implicitly assuming that the spatial structure of the shock does not change significantly during short periods of time (as accepted for observations with only one spacecraft). The expressions of these

[16] The definitions of M_f, M_A and M_s are shortly reviewed in Appendix A.

quantities are (Equation 2.1):

$$\mathrm{VR} = \frac{v_{r_d} - v_{r_u}}{v_{r_u}}, \tag{3.16}$$

and

$$\mathrm{BR} = \frac{B_d}{B_u}. \tag{3.17}$$

In the next chapter we present part of the results obtained using VR to quantify the strength of the shock at the cobpoint, since it is the variable used in our shock-and-particle models.

• Special situations

Two special situations identified deserve to be commented:

– When $v_{r_d} < v_{r_u}$. This situation might circumstantially appear at the very beginning of the simulation because the plasma variables and magnetic field at the upstream and downstream points are refered to different values of the background solar wind, before it becomes stable (for example, in Figure 3.1, when $v_r \sim 300\,\mathrm{km\,s^{-1}}$). Then, even though the criteria to identify the cobpoint and the downstream point are correctly fulfilled, the fact that $v_{r_d} < v_{r_u}$ can lead to an incorrect determination of the strength of the shock. Under this circumstance, we use as upstream values those of the background solar wind at the downstream point, instead of using their values measured at the cobpoint position. So, we assume that both points have the same background values, being therefore reasonable to compare them to determine the strength of the shock. In fact, this implies to uncomfortably assume that the shock has no thickness. Fortunately, this situation might only appear during the first period of the simulation, when the driven and the shock are too stuck[17].

– When $r_d > r_u$. It can occur when searching for the downstream point along the normal direction line. When determining the distance from a point to a line (in this case, from the Sun to the shocl normal line), there is a point of minimum distance. Then, when moving along the normal line, if the cobpoint is located just ahead of such point of minimum distance, it is feasible that we overpass it and, thus, $r_d > r_u$. This introduces an error in the calculation of the thickness of the shock if we compute

[17] As Luhmann et al. (2010) stress: "*Downstream values are especially problematic because the sheath pileup in the disturbance is often difficult to distinguish from the shock ramp end point.*"

it as the difference of the radial positions of the cobpoint and the downstream point. Therefore, the shock thickness is taken as the difference between the (3D) positions of the cobpoint and the downstream point along the normal direction line.

Chapter 4

Results and conclusions

> La búsqueda de lo excepcional
> obliga a plantearse que lo esencial
> normalmente está oculto.
>
> *Que se levanten los muertos*,
> Fred Vargas

4.1 Introduction

In this chapter we present and discuss the results obtained when applying the shock-and-particle model to derive synthetic flux profiles by using 3D MHD simulations of two interplanetary shocks (fast and slow). The outputs, plasma variables and magnetic field, and particle flux profiles, are presented as if they were real events detected by nine observers located at different longitudes and latitudes, and at two radial distances from the Sun (as described in the previous chapter). The results are not directly compared with observations because it does not exist any specific observed gradual SEP event out of the ecliptic in the inner heliosphere ($r < 1.0\,\mathrm{AU}$) of similar characteristics. We stress the fact that for ongoing or near-future space missions, as Beppi Colombo or Solar Orbiter, these type of 3D models will be necessary to estimate and predict SEP events.

4.2 Fast shock. Flux profiles at 0.4 AU

4.2.1 Solar wind plasma and magnetic field evolution

Figure 4.1 shows the evolution of the solar wind plasma variables and magnetic field as measured for each one of the nine observers located at 0.4 AU (as described in

Section 3.2.3). The vertical panels show, from top to bottom, the evolution of B, n and v_r through the simulation for the observers located at W45, W00 and E30 in longitude (left, middle and right panels, respectively). For each longitude, the profiles corresponding to observers at different latitudes, N37, N22 and N07, are represented by the solid, dotted and dashed lines, respectively. The shock passage occurs between 5 and 13 hours[1] after the launch of the perturbation, depending on the angular position of each observer, and despite that all of them are located at 0.4 AU.

As expected, the background or upstream plasma and magnetic field conditions differ with latitude (see also Figure 3.1). As a consequence of the changes in the solar wind velocity, the longitude of the cobpoint depends on the latitude of the observer, too. The first cobpoint for each observer (i.e., there where the magnetic connection between the observer and the shock is firstly established) can be calculated from the MHD shock simulation following the procedure described in Section 3.3. Table 4.1 and Figure 4.2 show the location of the first cobpoints for the nine 0.4 AU-observers. Differences in the first cobpoint longitude between N07 and N37 observers with the same longitude are of $\sim 7°$, and of $\sim 1.5\,R_\odot$ in radial distance. As the solar wind velocity changes with latitude, the shock itself may travel at different velocities depending on the latitude. This makes the cobpoint position of the different observers varies with time as the shock expands into the interplanetary medium. Furthermore, the cobpoint location also depends on the direction in which the nose of the shock propagates[2], and on the curvature of the front (in latitude and in longitude)[3].

The shock arrives first to the W00 observers, whose cobpoints scan the central region of the shock front: (1) for the case of the N22W00 observer, from approximately 22° to the left part of the shock (as seen from the Sun, Figure 4.2) up to its nose, and (2) from $\sim 23°$ and $\sim 16°$ for the N07W00 and N37W00 observers, respectively (Table 4.1). The shortest shock transit time corresponds to the observer located in the main direction of the shock, N22W00; this is a straightforward result from the fact that this is the perturbation-launch direction (where the maximum initial mo-

[1] Corresponding to transit speeds, from the Sun to 0.4 AU, between 3300 and 1280 $\mathrm{km\,s^{-1}}$.

[2] We will usually refer to the propagation direction of the shock nose as 'the main direction of the shock' or 'the leading edge of the shock'.

[3] In the same way as wide and narrow CMEs exist, it might happen that a shock is narrower in latitude than in longitude (or vice versa).

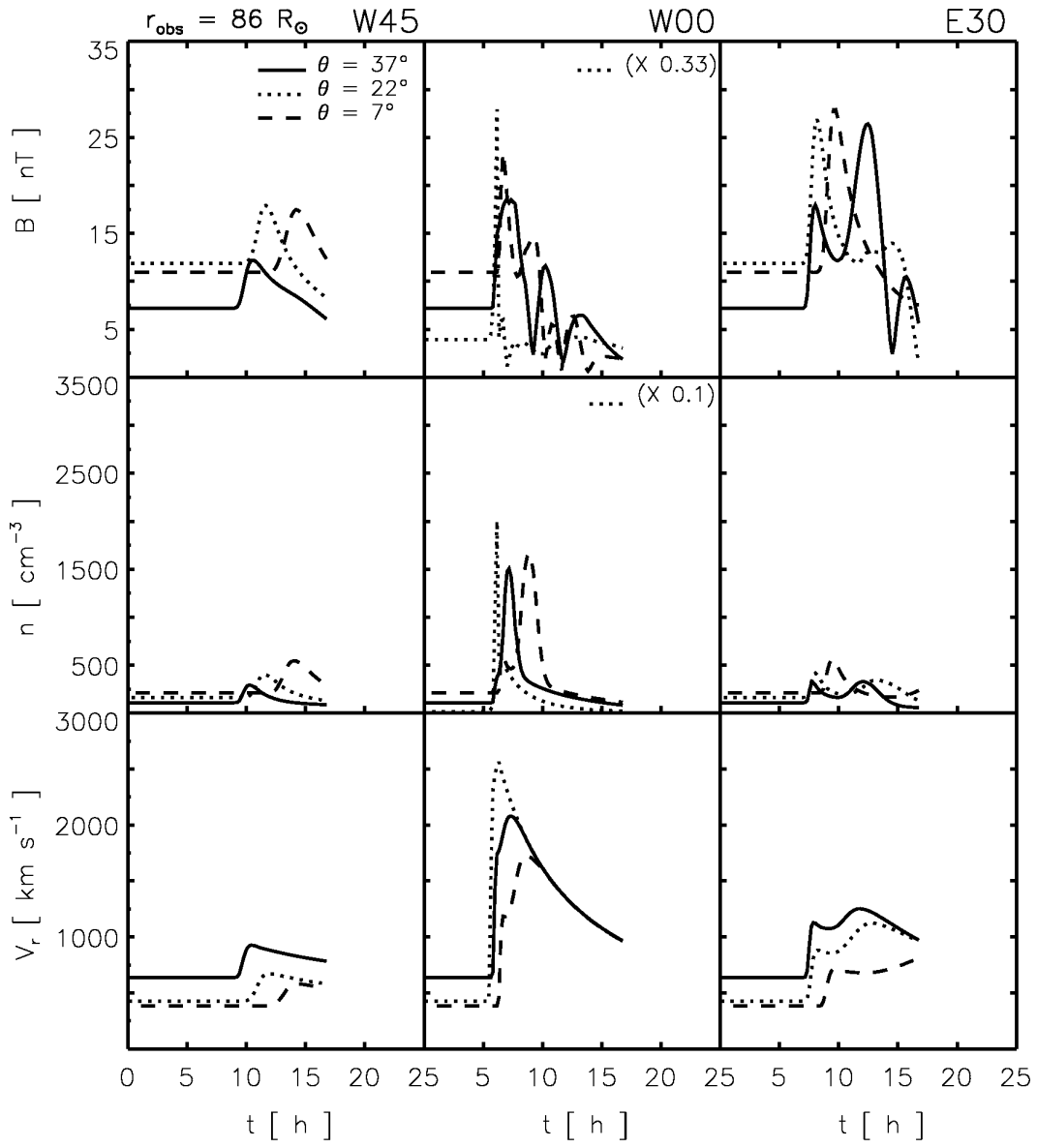

Figure 4.1: Fast shock. From top to bottom: Evolution of B, n and v_r as seen by the nine 0.4 AU-observers. Each column shows the longitude of the observer and each style of line represents its latitude, as labelled. The dotted curves of the two top panels in the middle column had been reduced by the factor specified in each pane.

mentum is directed to), being the central region of the shock front the fastest one. Only 10 minutes later, the shock arrives to the observer with the highest latitude, N37W00, and 40 minutes later to the observer located at N07W00. The reason of these differences is that the background solar wind speeds for these observers are quite different: 626 km s^{-1}, 422 km s^{-1} and 380 km s^{-1} for the N37, N22 and N07

Table 4.1: Fast shock. Location of the first cobpoint for each 0.4 AU-observer.

W45			W00			E30		
$\theta = 7°$	$\theta = 22°$	$\theta = 37°$	$\theta = 7°$	$\theta = 22°$	$\theta = 37°$	$\theta = 7°$	$\theta = 22°$	$\theta = 37°$
N07W22	N22W23	N37W30	N07E23	N22E22	N37E16	N07E53	N22E52	N37E46

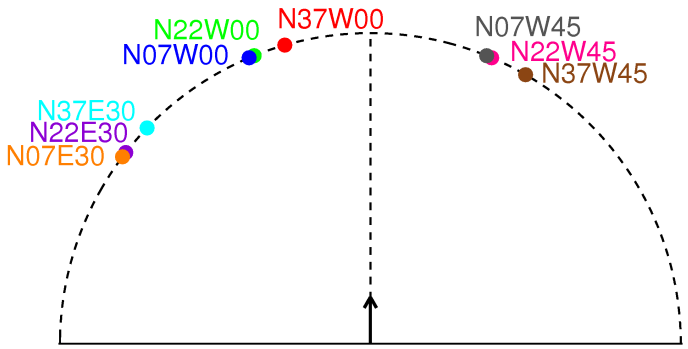

Figure 4.2: Fast shock. Sketch of the first cobpoint location for each 0.4 AU-observer. All the cobpoints are plotted on the same plane to make a direct comparison among their longitudes (differences in radial distance are not drawn). The colour code is the same as in Figure 3.2. The arrow indicates the main direction of the shock.

observers, respectively.

In the case of the W45 observers their cobpoints scan the right wing of the shock as it expands into the interplanetary space: from $\sim 22°$ for the N07W45 observer, and from $\sim 30°$ for the N37W45 observer; in the case of the E30 observers, their cobpoints travel along the left part of the shock front, from $\sim 53°$ and $\sim 46°$, for the N07E30 and N37E30 observers, respectively. For the W45 and E30 observers, the higher is their latitude, the earlier the shock reaches them, because of the higher background speed of the solar wind.

The increase observed in n and v_r at the shock front passage by each spacecraft (i.e., the jump in the plasma variables) is larger for the W00 observers at all latitudes, because the shock strength is higher for the longitudes closer to the shock nose (e.g., Smith & Dryer 1990; Heras et al. 1995; Aran et al. 2005). Nevertheless,

this is not always true for observers with the same longitude but different latitude: for the W45 and E30 observers, the jumps in density at N07 are higher than at N22. The reason is that the upper part of the shock travels faster than the bottom part, compressing the shocked material toward lower latitudes (Manchester et al. 2005).

If we compare the three W00 events, the downstream-to-upstream magnetic field ratio derived for the N37W00 and N07W00 observers are ~ 2.6 and ~ 2.1, respectively. These values are within the range of values reported from Helios observations at 0.4 AU (Volkmer & Neugebauer 1985). The observer placed in the main direction of the shock, N22W00, shows the maximum magnetic field compression, with a downstream value of about 81 nT, which is a reasonable value[4]. However, as commented previously, the background field of the model underestimates the actual background IMF intensity, yielding a magnetic field ratio across the shock of ~ 7.0. The magnetic field jumps across the shock are considerably smaller for the W45 than for the E30 observers, because eastern observers are situated closer to the central part of the shock than western ones.

The central panel of Figure 4.1 shows the particle density recorded at the three W00 observers. The upstream solar wind density varies from $\sim 100\,\mathrm{cm}^{-3}$ for the highest latitude, to $\sim 220\,\mathrm{cm}^{-3}$ near the ecliptic plane. This is a consequence of the assumed high-density and high-velocity initial blob, together with the high density profile for the solar wind model. The difference between the density jumps seen by the N22W00 observer and the N37W00 and N07W00 observers is quite significant (more than a factor 10). And this factor can be larger if we compare the jump of N22W00 with that of the observers located at W45 and E30: the jump falls by a factor 5 for the N07 and N37 observers, and by a factor 40 for the N22 ones.

The bottom panel of the middle column of Figure 4.1 shows the evolution of the radial velocity for the W00 observers. The values measured at the shock arrival are within the range of values expected for a fast interplanetary forward shock[5]. The

[4] For instance, during the shock passage of the event on 7 May 1978, Helios-1 was located at 0.36 AU; the downstream magnetic field value recorded in this event was ~ 72 nT. Another example is the event that occurred on 8 June 1980, when Helios-1 was situated at 0.4 AU at the shock passage and the downstream magnetic field gathered was ~ 67 nT. In the SEP event on 28 April 1978, Helios-1 was at 0.31 AU and measured ~ 108 nT just after the shock crossing.

[5] For example, in the case of the SEP event on 28 October 2003, the solar wind speed reached values close to $2000\,\mathrm{km\,s}^{-1}$ just after the shock passage (Lario et al. 2008).

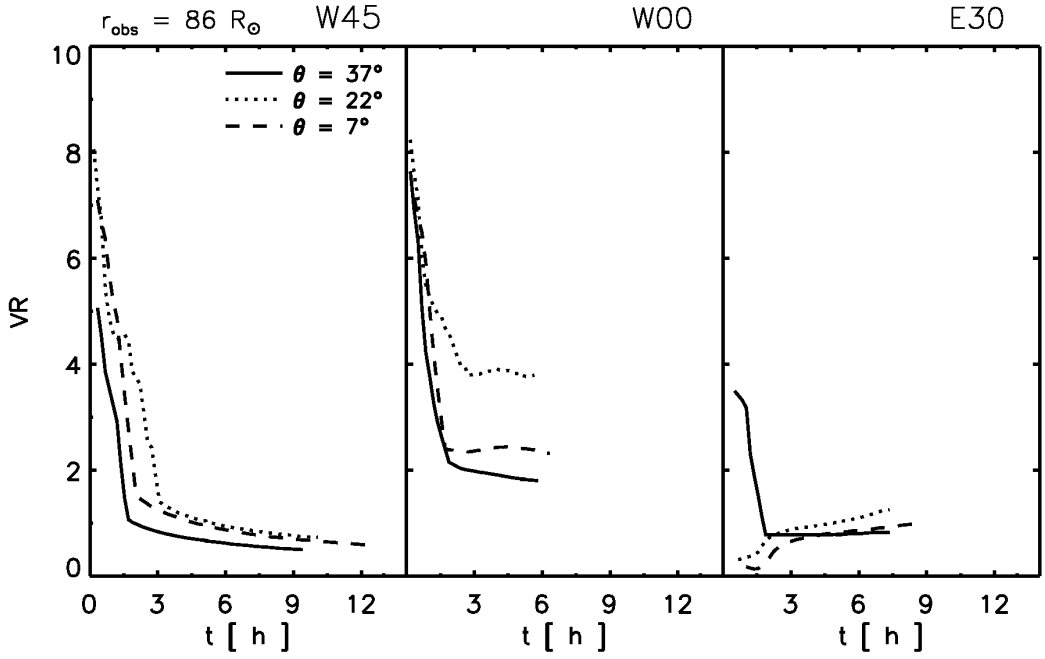

Figure 4.3: Fast shock. Evolution of VR at the cobpoint for the nine 0.4 AU-observers. Each column shows the longitude of the observer and each type of line represents its latitude, as labelled.

normalized radial velocity jump across the shock, VR, for the N22W00 observer is 3.8, and for the N37 and N07 observers are 1.8 and 2.3, respectively (see next section). The small differences when comparing the jumps obtained at different latitudes for the W45 and E30 observers are a consequence of the location of the observers in space (with respect to the main direction of the shock).

4.2.2 Evolution of VR and synthetic flux profiles

Figure 4.3 illustrates the evolution of VR at the cobpoint for the nine observers described, while the shock is expanding up to 0.4 AU. As in Figure 4.1, the three panels show the evolution of VR for the W45 (left), W00 (middle) and E30 (right) observers. The solid, dotted and dashed lines correspond to the N37, N22 and N07 latitudes.

For the W00 observers, the first connection with the shock front occurs very early in the event, at t_c = 30 minutes (t_c is the connecting time, Section 2.4.1); that is, when the shock is close to the Sun, from 4.8 $R_\odot$ for the N37 observer to

6.0 $R_\odot$ for the N07 observer[6], and also close to the shock nose in longitude ($\leq 23°$, Table 4.1). At t_c, the values of VR for the three observers are very high, ranging from 7.1 to 8.2. Then, they rapidly decrease within 2 or 3 hours, when the central part of shock front is at $r \sim 30\,R_\odot$ from the Sun. This implies that the injection rate on shock-accelerated particles at the early phase of the event will be the highest throughout the event, and it will take place near the Sun, as expected for a good connection between the observer and the shock front. Moreover, depending on the latitude, the values of VR can be quite different and, thus, those of the injection rate.

For the W45 observers, the evolution of VR resembles that of the W00 observers. The first magnetic connection for the N07 and N22 observers is established at N07W22 and N22W23, respectively, and the initial values of VR are similar to the ones of the corresponding W00 event. The lower value of VR attained for the N37 observer is a consequence of its first magnetic connection (established at N37W30). Since the cobpoints for the W45 observers scan the right wing of the shock front as the shock reaches them, VR decreases to lower values than for the W00 observers. Such values are ordered in latitudinal distance from the nose of the shock; that is, the closer the observer in latitude with respect to the nose of the shock, the higher the value of VR[7].

For the N07E30 and N22E30 observers VR follows a different evolution from the W45 and W00 observers. For these E30 observers, VR increases with time because their magnetic connection is established far from the shock nose along the left wing; i.e., at E53 and E52. As for the W45 observers, the values of VR are organized with increasing separation in latitude from the shock nose. The N37 observer, instead, is connected to a central region of the shock front and of the downstream region, as suggested by its downstream magnetic field evolution (top right panel of Figure 4.1), which is similar to that one of the W00 observers.

To visualize and quantify the influence of the latitude factor on SEP events through the evolution of VR, we use the particle transport model developed by

[6] Note that this is much closer to the Sun than the inner boundary at 18 $R_\odot$ assumed by many models.

[7] If we measure the coordinates of the observers with respect to a XY plane tilted 22° northward the equatorial plane, i.e., containing the direction of the shock nose, the positions of the N37W45, N22W45 and N07W45 observers are N20W37, N06W41 and S09W45, respectively.

Lario et al. (1998) to produce synthetic flux profiles, as measured by the nine observers formerly described. As we assume the functional dependence $\log Q \propto \mathrm{VR}$, the evolution of VR for different observers (depicted in Figure 4.3) directly translates into an evolution of Q, and, therefore, in a variety of SEP flux profiles (with no other change of any feature or parameter of the model). The values adopted for the description of the interplanetary particle transport are given in Section 2.4.2, and other features of the model can be found in Aran (2007).

Figure 4.4 shows two sets of the synthetic flux profiles derived for the nine 0.4 AU-observers (identified as in Figure 4.3). Blue lines are the derived flux profiles for 1 MeV protons (with $\lambda_{\parallel} = 0.2$ AU, and assuming a foreshock region[8]), and red lines are the flux profiles at 32 MeV (with $\lambda_{\parallel} = 0.2$ AU, and without foreshock). For each observer, we have derived the flux profiles for the ten energy channels and the four transport conditions included in SOLPENCO. The whole set is presented in Appendix F.

The onset of the event shows velocity dispersion for the two energies considered, as expected; there are small time differences at the onset because, depending on the latitude, the first cobpoint occurs at slightly different times and places (Table 4.1). Moreover, the shock passage also varies with the latitude within a few hours. As $\log Q \propto \mathrm{VR}$, small differences in VR can produce important flux variations. For example, the value of VR for the N22W00 and N07W00 observers after three hours is roughly constant but different (~ 4 and ~ 2.4, respectively; Figure 4.3). This translates into an injection rate ~ 6 times higher at the cobpoint for the N22W00 observer than for the N07W00 observer, and, thus, in their respective flux profiles. As a result of the evolution of VR, we can conclude that, for the W00 observers, the closer the latitude of the observer to the shock nose latitude, the larger the attained proton flux; it could be a factor 10 during several hours after the prompt phase of the event (e.g., N22W00 and N37W00 observers).

The left and right panel show the synthetic flux profiles at 1 MeV and 32 MeV, for the W45 and E30 observers, respectively. Both sets measure proton fluxes less intense than the corresponding ones for the W00 observers, mainly as a consequence

[8] A foreshock region that is 0.01 AU wide and active since 20 hours before the shock passage. It is characterized by a $\lambda_{\parallel c} = 0.01$ AU for 0.5 MeV protons (see more details in Aran 2007).

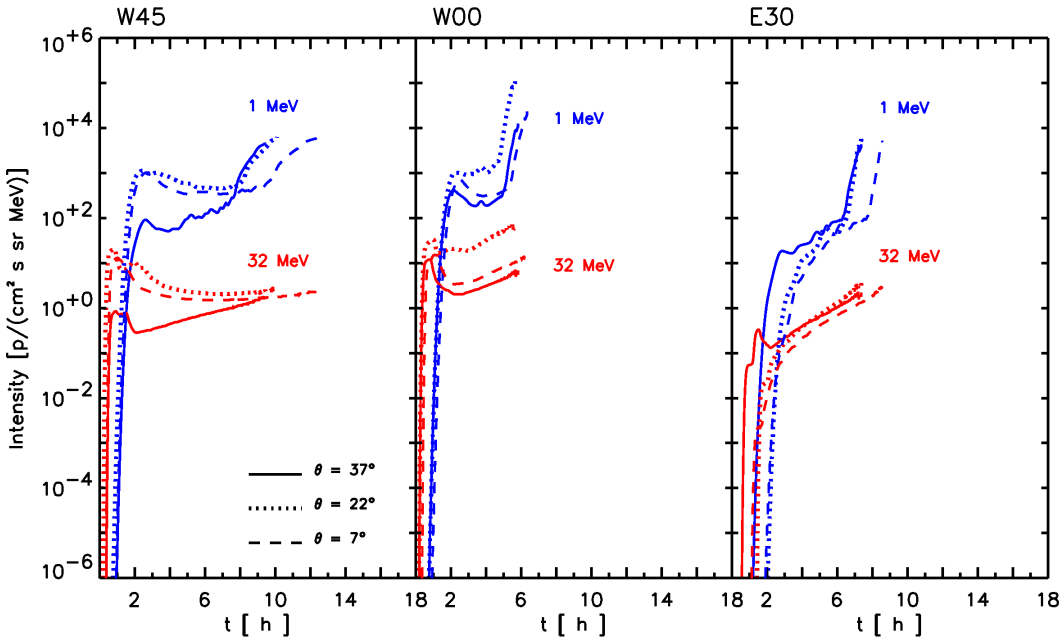

Figure 4.4: Fast shock. Simulated flux profiles derived from the particle transport model for 1 MeV (blue lines) and 32 MeV (red lines) protons, for the nine 0.4 AU-observers. Each column shows the longitude of the observer and each type of line represents its latitude, as labelled.

of the different regions of the front shock scanned by their cobpoints, and, hence, the different evolution of VR. The change with latitude of the position of a W45 observer could lead to a difference in the peak intensity (attained, in this case, at the prompt phase of the event) of one order of magnitude.

4.3 Fast shock. Flux profiles at 1.0 AU

The four figures presented in this section replicate the corresponding ones in Section 4.2, but for the nine observers located at 1.0 AU.

4.3.1 Solar wind plasma and magnetic field evolution

As can be seen in Figure 4.5, in this case the shock passage occurs between 15 and 40 hours[9] after the launch of the perturbation, depending on the position of each observer. The shock arrives first to the W00 observers (middle column), corresponding

[9] Corresponding to transit speeds, from the Sun to 1.0 AU, between 2770 and 1040 km s^{-1}.

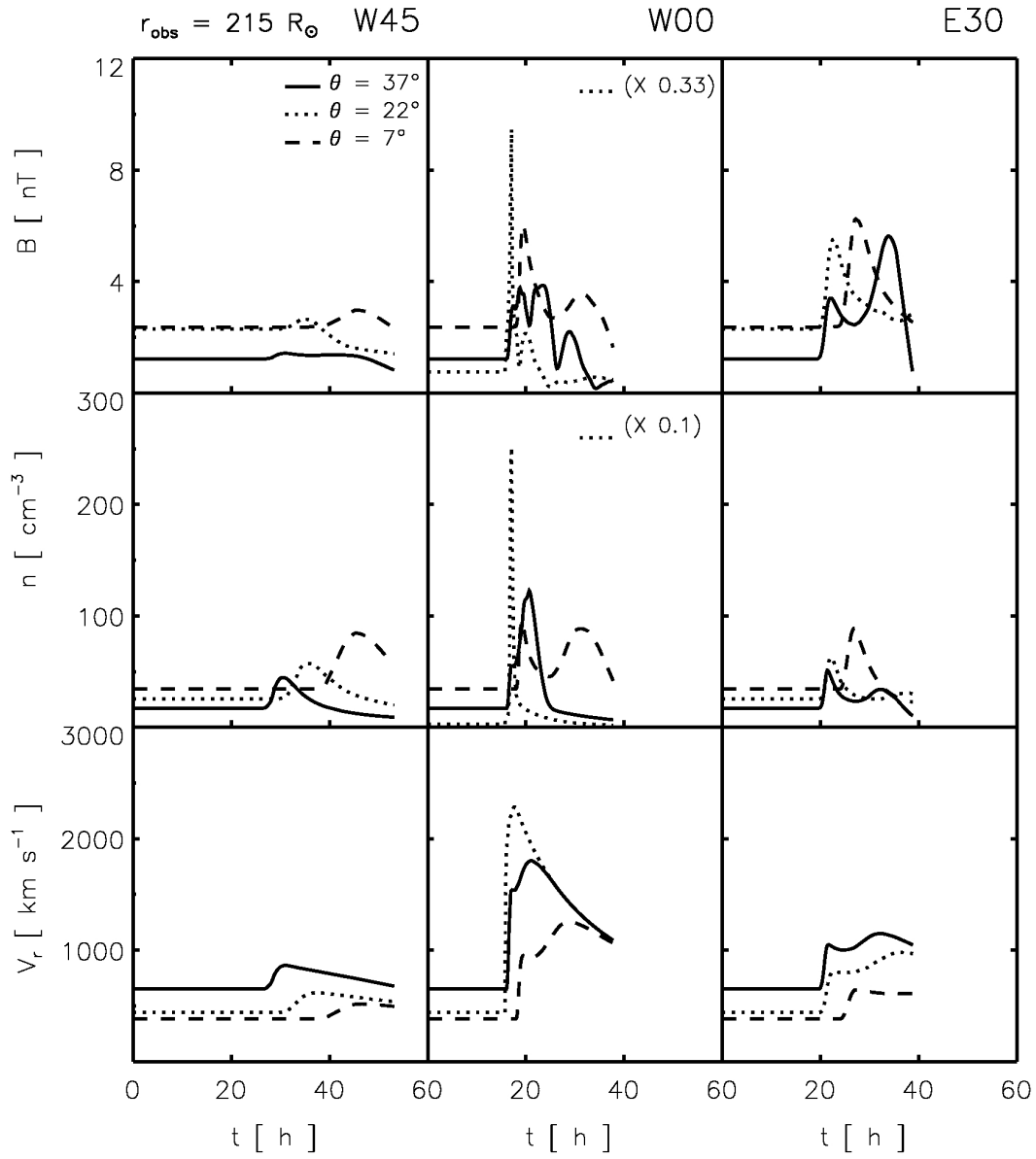

Figure 4.5: Fast shock. From top to bottom: Evolution of B, n and v_r as seen for the nine 1.0 AU-observers. Displayed as in Figure 4.1.

the shortest transit time to the N22W00 observer. It arrives only 20 minutes later to the N37W00 observer, while it takes 2 hours more to pass by the N07W00 one. The reason of these differences in the shock arrival time is the same as commented in Section 4.2.

Table 4.2 and Figure 4.6 display the first cobpoint for each observer. Differences

Table 4.2: Fast shock. Location of the first cobpoint for each 1.0 AU-observer.

W45			W00			E30		
$\theta = 7°$	$\theta = 22°$	$\theta = 37°$	$\theta = 7°$	$\theta = 22°$	$\theta = 37°$	$\theta = 7°$	$\theta = 22°$	$\theta = 37°$
N07E13	N22E07	N37W07	N07E59	N22E53	N37E38	N07E88	N22E84	N37E68

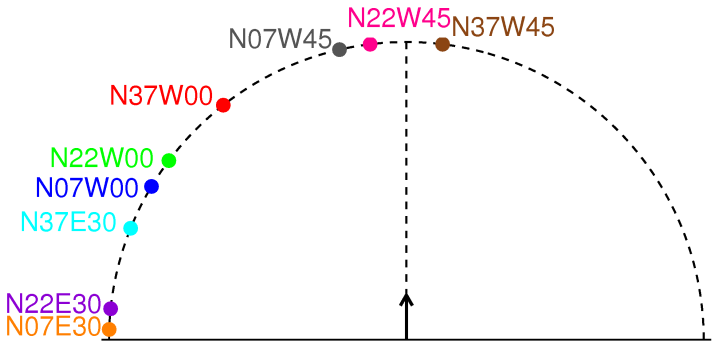

Figure 4.6: Fast shock. Sketch of the location of the first cobpoint for each 1.0 AU-observer. Displayed as in Figure 4.2.

in the first cobpoint for N07 and N37 observers with the same longitude are of $\sim 20°$. The cobpoint for the W00 observers scan the left flank of the shock front: for the N22W00, from $\sim 53°$ to the left up to the nose of the shock, and for the N07W00 and N37W00 observers, from $\sim 59°$ and $\sim 38°$, respectively. The cobpoints for the N07W45 and N2245 observers slide from the left wing, crossing the shock nose up to the position of the observers in the right flank; whereas the cobpoint for the N37W45 observer displaces along the right flank of the shock. The cobpoints for the E30 observers, scan the far left wing of the front of the shock.

From Figure 4.5 it can be seen that the evolution of B, n and v_r and their jumps at the shock passage measured by the nine 1.0 AU-observers follows the same trend as for the corresponding 0.4 AU-observers (Figure 4.1), roughly scaled due to the distance from the Sun. Particularly, the highest plasma and magnetic field jumps at the shock passage are detected by the N22W00 observer; i.e., the closer to the longitude and latitude of the main direction, the stronger and faster the shock. For example, the maximum magnetic field compression is gathered by the N22W00 observer, ~ 12.4, whereas it is only ~ 2.5 for the N07W00 and N37W00 observers.

4.3.2 Evolution of VR and synthetic flux profiles

The first observers to magnetically connect with the shock front are the three W45 observers (left panel of Figure 4.7), being $t_c \leq 20$ minutes. The N22W45 and the N37W45 observers connect at $t_c = 10$ minutes and close to the shock nose, at ~ 5.8 and $5.3\,R_\odot$, respectively (Table 4.2 and Figure 4.6). This is the reason of the high VR values derived at the cobpoint for these observers: 11.4 and 10.8, respectively. Within the following 2.5 hours, the values of VR rapidly decrease; at that time, the nose of the shock has moved outward to $\sim 35\,R_\odot$ from the Sun. Therefore, the highest injection rate of shock-accelerated particles takes place near the Sun, at this early stage of the event.

For the E30 observers (right panel), the values of VR are small (≤ 0.8), but they increase with time because the magnetic connection for these observers are far from the shock nose, from E68 up to E88, in the left wing. As the shock propagates into the interplanetary medium, these cobpoints slide clockwise and the values of VR increase, reaching their maximum at the shock passage.

The evolution of VR for the N37W00 observer follows the same pattern as the one for the W45 observers. Nevertheless, the evolution of VR for the N22W00 and N07W00 observers resembles more to the one for the E30 observers. The reason is the position of their first cobpoints: the N37 observer magnetically connects 38° eastward of the shock nose, at $t_c = 40$ minutes, whereas the N22 and N07 observers establish their connections at E53 and E59, respectively, almost 40 minutes later (i.e., $t_c = 80$ minutes). Hence, the differences on the evolution of VR are due to the latitude of the observer, which modifies the region of the shock front that will be scanned by the corresponding cobpoints.

Two sets[10] of the synthetic flux profiles derived for the nine 1.0 AU-observers are displayed in Figure 4.8. They have been calculated as the profiles shown in Figure 4.4. The only differences are that, in this case, when the shock becomes too weak or it is tagged as "not valid"[11], the injection rate has been ad-hoc exponentially decreased five orders of magnitude[12] (these parts of the flux profiles are drawn

[10] The whole set of the derived synthetic flux profiles is presented in Appendix F.

[11] In Section 3.3.3 we explain the situations when the shock is considered as "not valid".

[12] Appendix D gives more details about when these situations may appear, basically due to the fact that the simulated shock is narrow.

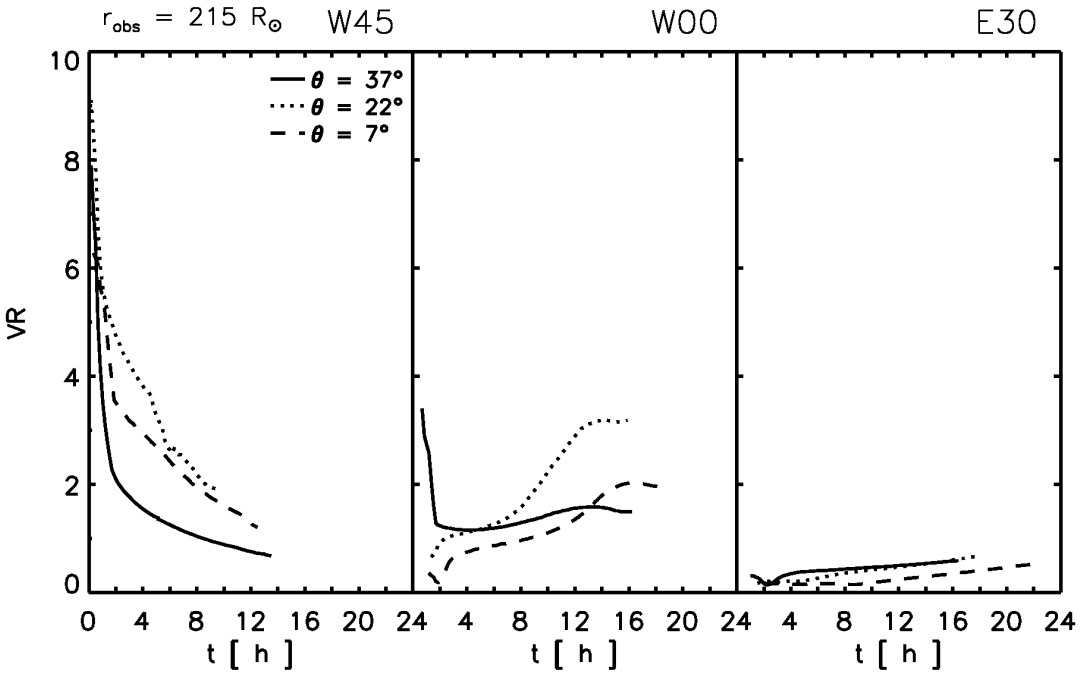

Figure 4.7: Fast shock. Evolution of VR at the cobpoint for the nine 1.0 AU-observers. Displayed as in Figure 4.3.

in black); and that for the W45 and E30 observers, we have not considered any foreshock region.

For a given energy and longitude, the small differences observed in the onset of each event are a direct consequence of the slight differences in the location and connecting time of the corresponding cobpoints (due to the latitude of each observer, Figure 4.6 and Table 4.2). For example, the N37W00 observer has the smallest t_c, and, hence, their proton flux profiles rise earlier. Since for the W00 observers the first cobpoints are at the left wing, their flux profiles grow up as the shock propagates, achieving a maximum value at the shock passage.

The shape of the flux profiles obtained for the W45 and E30 observers is mainly as a consequence of the different regions of the shock front scanned by their cobpoints, and, consequently, of the different evolution of VR that they present. In both cases, the latitude of the observer has influence in the peak intensity and it can be quite relevant. For example, for the W45 observers, the flux profiles peak at the prompt phase of the event, because VR is very high at this stage; the differences in

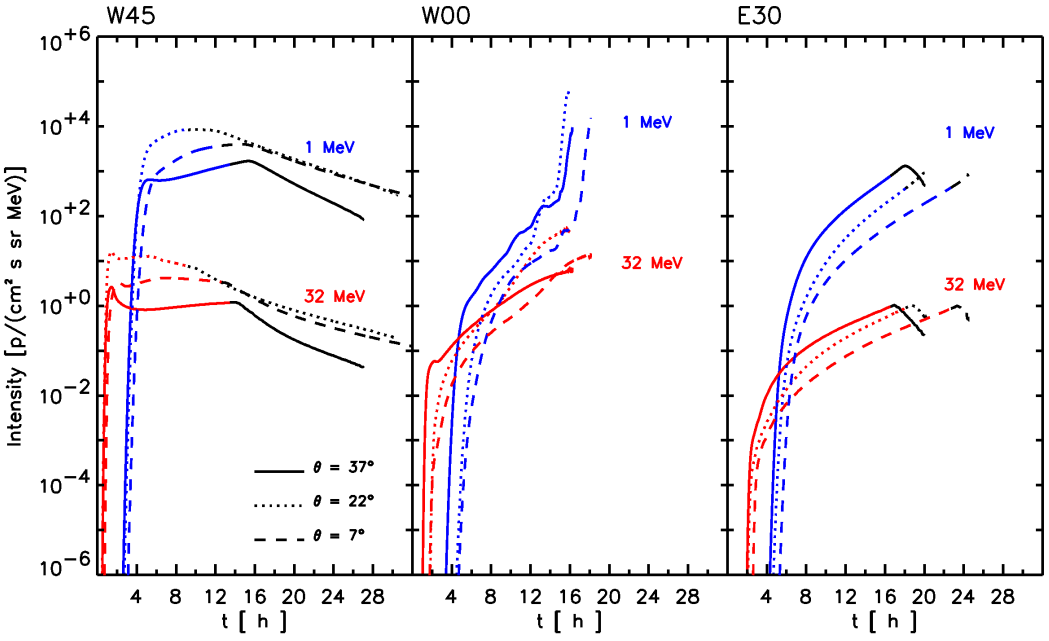

Figure 4.8: Fast shock. Simulated flux profiles derived from the particle transport model for 1 MeV (blue lines) and 32 MeV (red lines) protons, for the nine 1.0 AU-observers. Displayed as in Figure 4.4.

the peak intensity can be as high as one order of magnitude. For the E30 observers, the flux profiles start decreasing shortly before the shock arrival (due to the local weakness of the shock), whereas observations indicate that the peak flux should be at the shock arrival or shortly after (Cane et al. 1988; Lario et al. 1998). This is due to the adopted shape for the initial perturbation, which yields to a fast, but narrow, shock. Therefore, in this scenario, an eastern observer is nearly always connected to a region of weak strength.

We would like to point out that the 32 MeV flux profiles rarely increase after their peak (if there is one) at the prompt phase of the SEP event. After the peak, these profiles tend to monotonically decrease or show a short plateau (see Figures 1.1 and 1.4); sometimes, they may display an ESP component at the shock passage. In our simulations, the high-energy flux profiles result from using the average Q_0 and γ values adopted for SOLPENCO (last paragraph of Section 2.4.2). As discussed in Aran (2007) and Aran et al. (2008), these values are adequate for reproducing low-energy flux profiles but show limitations at high energy. Moreover, the spectral indices adopted at high energy, $\gamma = 3$, can be much harder for individual events (even

Table 4.3: Slow shock. Location of the first cobpoint for each 0.4 AU-observer.

W45			W00			E30		
$\theta = 7°$	$\theta = 22°$	$\theta = 37°$	$\theta = 7°$	$\theta = 22°$	$\theta = 37°$	$\theta = 7°$	$\theta = 22°$	$\theta = 37°$
N07W22	N22W22	N37W29	N07E23	N22E22	N37E16	N07E54	N22E52	N37E46

6 or 7; see, for example, Cane et al. 1988).

4.4 Slow shock. Flux profiles at 0.4 AU

The three figures presented in this section replicate the corresponding ones in Section 4.2, but for the slow shock case.

4.4.1 Solar wind plasma and magnetic field evolution

Depending on the position of each observer, the shock passage occurs between 9 and 17 hours[13] after the onset of the event. The shock arrives first to the N22W00 observer (central panel of Figure 4.9), 10 minutes later to the N37W00, and 50 minutes later to the N07W00. For the W45 and the E30 observers (left and right columns, respectively), the passage of the shock is clearly organized according to the velocity of the solar wind; for these observers, the faster the solar wind, the earlier the shock arrival. Consequently, for the W45 and E30 observers at higher latitudes (N37 and N22), the difference between the shock arrival times is larger than for the corresponding W00. The reason is the 'competition' between the faster solar wind speed at high latitudes (N37) and the maximum velocity of the shock at its central part (N22); this effect is more pronounced as the observer is placed away from the main direction of the shock.

The locations of the first cobpoint for each observer (Table 4.3) are similar to the ones for the fast shock. The differences for observers at the same longitude but different latitude are of $\sim 8°$. The tracks that follow these cobpoints along the front of the expanding shock are also similar.

[13] Corresponding to transit speeds, from the Sun to 0.4 AU, between 1850 and 975 $\mathrm{km\,s^{-1}}$.

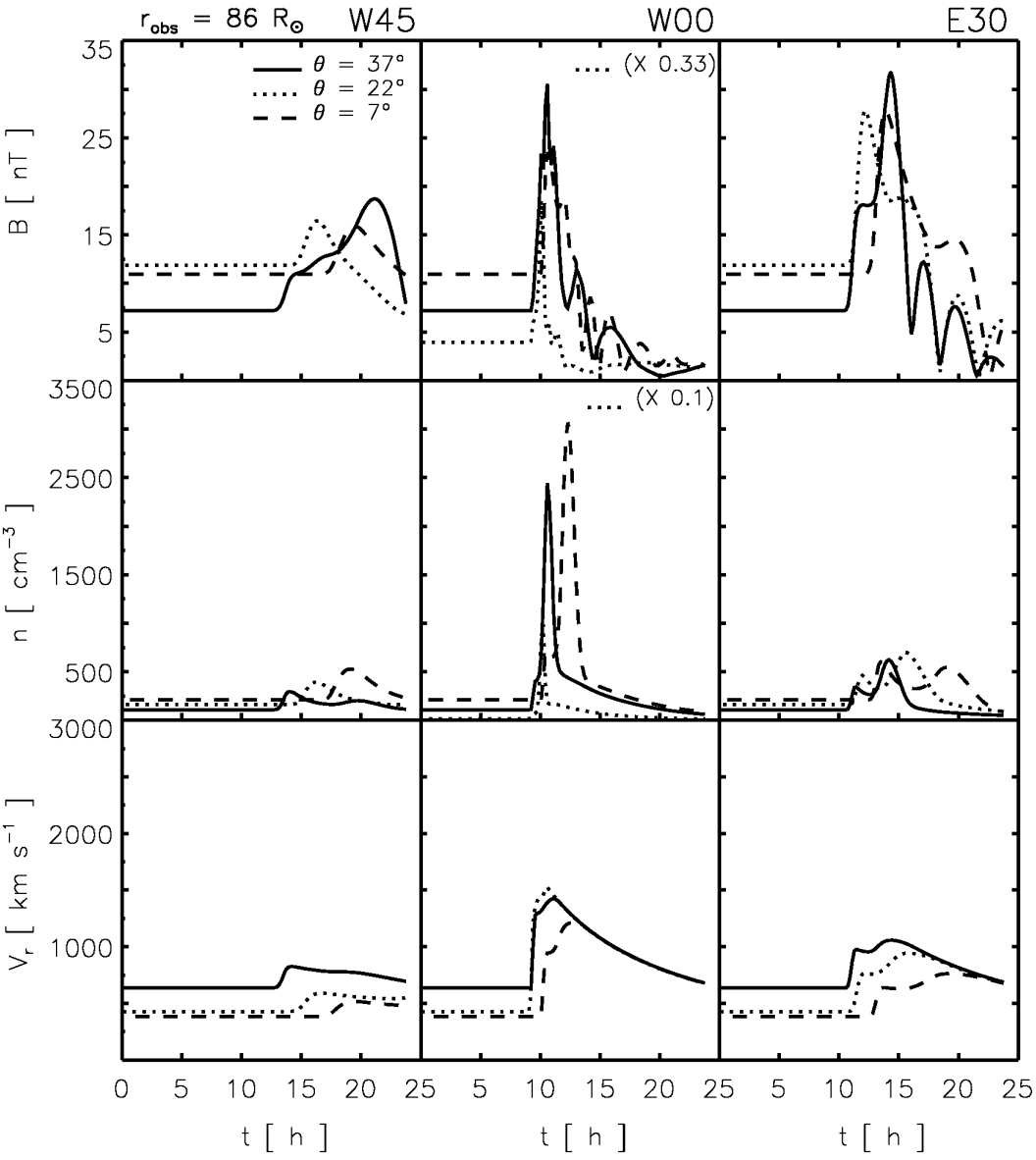

Figure 4.9: Slow shock. From top to bottom: Evolution of B, n and v_r as seen for the nine 0.4 AU-observers. Displayed as in Figure 4.1.

The highest plasma and magnetic field jumps are seen by the N22W00 observer, and they are smaller for the other W00 observers. Away from the shock nose these jumps decrease, being more pronounced in n than in B or v_r. Since the E30 observers are 15° closer to the longitude of the leading shock direction than the W45, the jumps measured by the first are slightly larger than those seen by the second ones.

The highest magnetic field ratio, ~ 4.7, is measured by the N22W00 observer, and it reduces to ~ 3.2 and ~ 2.1 for the N37W00 and N07W00 observers, respectively. For the E30 and W45 observers, these jumps decrease as the observers are placed further away from the main direction of the shock. The evolution of the density and the radial speed is qualitatively similar to the one for the fast shock case. As can be seen, there is a significant difference between the density jump recorded by the N22W00 observer and the one measured by the other eight observers. The slightly larger increase for the N07 observers (regardless of their longitude) is probably due to the compression of the material by the upper part of the shock (see comment on Section 4.2).

4.4.2 Evolution of VR and synthetic flux profiles

The observer located at N37W00 (central panel of Figure 4.10) has VR = 5.8 at the first cobpoint, a value larger than that for the N22W00 observer, VR = 4.9. The reason is the better connection of the N37 observer, since the first cobpoint for both observers takes place at $t_c = 0.1$ hours, when the shock is close to the Sun, $\sim 3.6\,R_\odot$. As VR rapidly decreases after the two and a half hours, the highest injection rate of shock-accelerated particles will occur very early in the event and near the Sun ($< 15\,R_\odot$). The N07W45 and N22W45 observers (left panel) have magnetic connections with similar angular deviations from the shock nose than those for the W00 observers, although in the opposite wing. Then, these W45 observers present also high VR values, which rapidly decrease within the first hours. The E30 observers (right panel) have smaller VR values because their connection with the shock front occur further from its central region (Table 4.3), and later in time ($t_c = 0.5$, 0.6 and 0.8 hours, for the N37W45, N22W45 and N07W45, respectively). Again, the latitude of the observer has influence on the position of the cobpoint and, thus, on the evolution of VR and on where the highest values of Q are reached.

Figure 4.11 shows two sets[14] of the synthetic flux profiles derived for the nine 0.4 AU-observers for the slow shock case. They have been calculated in the same way as for the two previous cases studied.

[14] The whole set of synthetic flux profiles derived is presented in Appendix F.

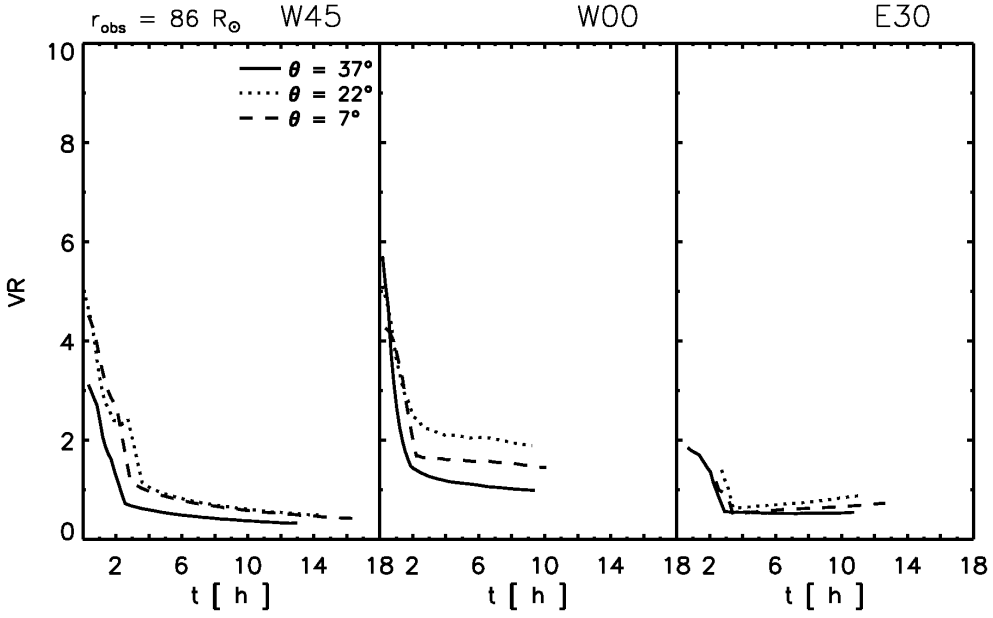

Figure 4.10: Slow shock. Evolution of VR at the cobpoint for the nine 0.4 AU-observers. Displayed as in Figure 4.3.

The shape of the flux profiles for the W00 observers (middle panel) is quite similar to the ones for the fast shock case. The N37 and N22 observers have prompt phases with minor time differences at the onset due to their different connecting times. The prompt phase of the N07 observer, however, is slightly smaller since its magnetic connection occurs a bit further from the shock nose (at E23) and later in time ($t_c = 0.3$ hours). At the shock passage, the time-intensity profiles vary with the latitude according to the evolution of VR.

The flux profiles for the W45 observers (left panel) are similar to the ones derived for the W00 observers, as expected from the evolution of VR. The difference between the flux values at the prompt phase of the N22W00 and N07W00 observers and those of the N37W00 observer, reflects the VR profiles for each observer at this early stage: the higher VR values, the higher the flux values at the prompt phase. The flux profiles for the E30 observers (right panel) show a clear difference between the onset of the prompt phase according to the moment of the magnetic connection: the flux profiles for the N37E30 observer rise earlier than those for the N22E30 and N07E30 observes, due to their different connecting times. For the E30 observers, the flux profiles at the shock passage have similar values, regardless of the latitude

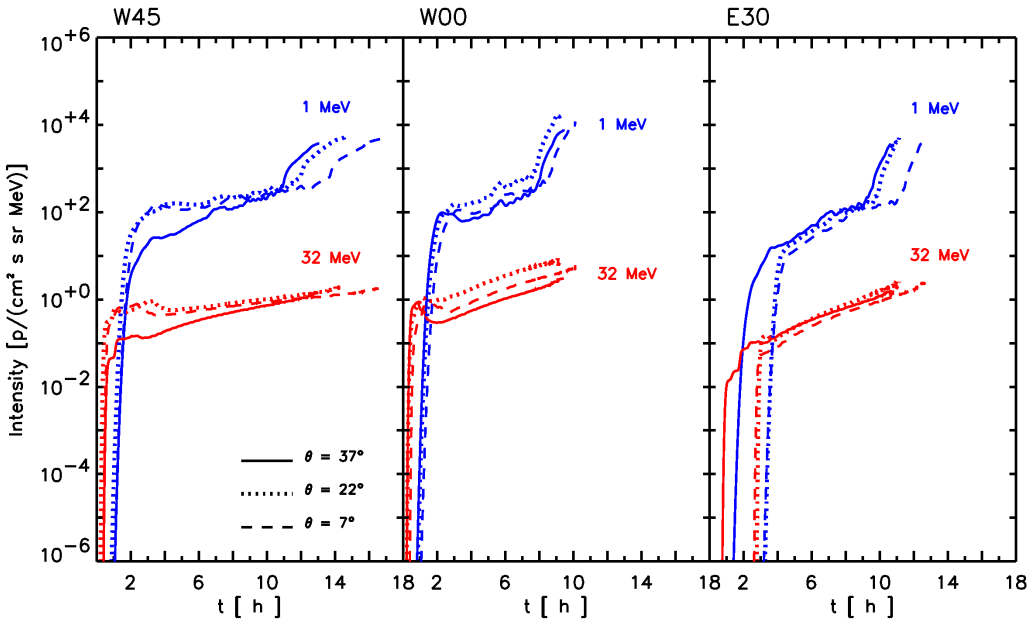

Figure 4.11: Slow shock. Simulated flux profiles derived from the particle transport model for 1 MeV (blue lines) and 32 MeV (red lines) protons, for the nine 0.4 AU-observers. Displayed as in Figure 4.4.

of the observer.

4.5 Comparing flux profiles

4.5.1 Fast shock: 0.4 AU-observers versus 1.0 AU-observers

If we compare the solar wind plasma and magnetic field evolution for the fast shock seen by the 0.4 AU-observers and the 1.0 AU-observers (Figure 4.1 and Figure 4.5), we can see that the jumps are smaller at 1.0 AU than at 0.4 AU, because the shock becomes weaker as it expands into the interplanetary medium, and that the highest plasma jumps are those detected by the N22W00 observer. The time of the shock passage, t_s, by the position of each 0.4 AU- and 1.0 AU-observers is listed in the left part of Table 4.4. There is a noticeable delay between the 0.4 AU-observers (up to 7 hours) and the 1.0 AU-observers (up to 20 hours), depending on the position of each observer. For observers with the same longitude, the faster the background solar wind, the earlier the shock arrives to the observer, at both radial distances. For observers with the same latitude, the larger the separation between the nose of

Table 4.4: Comparative between the shock passage time and the location of the first cobpoint for the 0.4 AU-observers (left) and the 1.0 AU-observers (right).

		t_s* [h]		First cobpoint	
		0.4 AU	1.0 AU	0.4 AU	1.0 AU
W45	$\theta = 7°$	12.3	*37.0*	N07W22	N07E13
	$\theta = 22°$	10.1	*29.0*	N22W23	N22E07
	$\theta = 37°$	9.4	*26.3*	N37W30	N37W07
W00	$\theta = 7°$	7.0	18.1	N07E23	N07E59
	$\theta = 22°$	5.6	15.9	N22E22	N22E53
	$\theta = 37°$	5.8	16.2	N37E16	N37E38
E30	$\theta = 7°$	8.5	*24.2*	N07E53	N07E88
	$\theta = 22°$	7.3	*19.9*	N22E52	N22E84
	$\theta = 37°$	7.3	*19.8*	N37E46	N37E68

(* For the 1.0 AU-observers, the time given in italic refers to the passage of the perturbation, since the discontinuity is too weak to be considered as a shock.)

the shock and the observer, the later the passage of the shock.

Figure 4.12 shows a comparison between the location of the first cobpoint for the 0.4 AU- and the 1.0 AU-observers, as well as their fiducial IMF lines. The right part of Table 4.4 lists the position of these first cobpoints. The differences in the cobpoint location between observers located at the same longitude and latitude are due to the fact that the observers are located at different radial distances, as well as to the variation of the solar wind speed with latitude. For example, the N22W00 1.0 AU-observer lies on almost the same IMF line than the N22E30 0.4 AU-observer, but this is not true for the other two latitudes.

A consequence of these magnetic connections is that, for observers with the same longitude and latitude but different radial distance, the evolution of VR does not behave in the same way (Figures 4.3 and 4.7), because their respective cobpoints scan different regions of the shock front. For the 0.4 AU-observers, the highest VR value is reached by the N22W00 observer, whereas for the 1.0 AU-observers by the N22W45. These observers are the ones connected closest to the shock nose at the beginning of the event, at N22E22 and at N22E07, respectively. Since this later connection is closer to the shock nose, the N22W45 1.0 AU-observer measures the

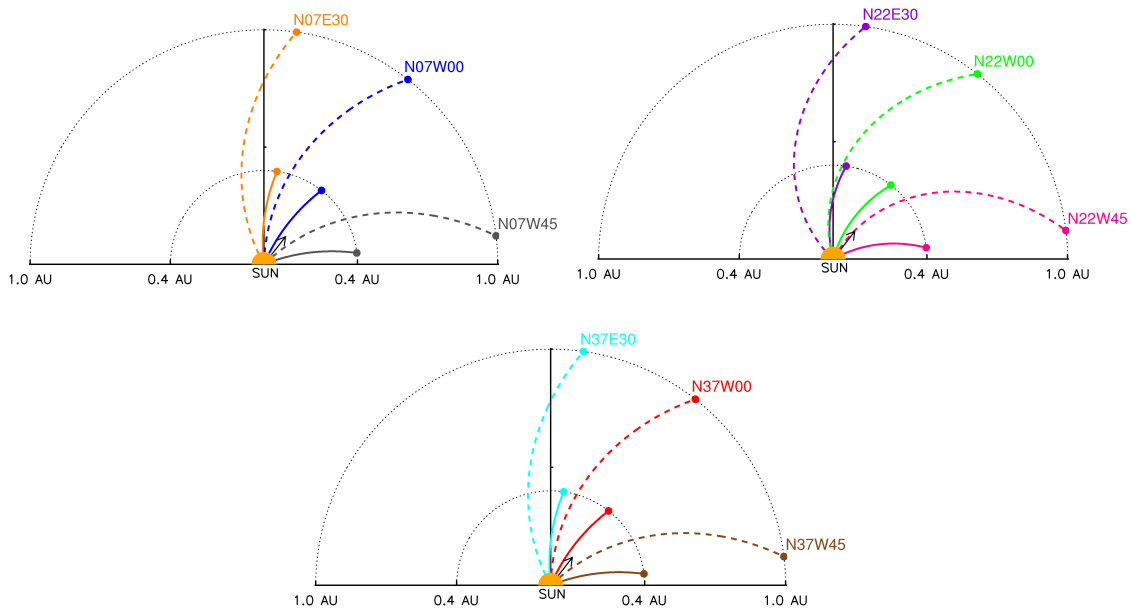

Figure 4.12: Comparative between the location of the first cobpoint for the 0.4 AU- and the 1.0 AU-observers. Top left: $\theta = 7°$; top right: $\theta = 22°$; and bottom: $\theta = 37°$. Each panel displays the position of the 0.4 AU- and 1.0 AU-observers and their corresponding IMF lines (solid and dashed lines, respectively). Observers are colour-coded according to Figure 3.2. The arrow indicates the main direction of the shock.

greatest value of VR, in spite of its radial distance.

In the magnetically well-connected cases, there is a rapid decrease of the values of VR within, approximately, the first two hours of the simulation; this indicates that the first shock-accelerated particles are injected when the shock is still very close to the Sun. This is the case, for example, of the N22W00 observer at 0.4 AU: it is well-connected from the beginning of the event (N22E22), and so the high values of VR for $t < 3$ hours; but in spite of the movement of its cobpoint toward the nose of the shock, VR decreases down to a constant value, due to the deceleration of the simulated shock. In contrast, the same observer at 1.0 AU magnetically connects to 31° farther away from the nose of the shock (N22E53), and, hence, its cobpoint scans the left wing of the front, moving toward more central positions. This is the reason of the low values of VR at the beginning of the event, which increase monotonically with time. These values are smaller than for the 0.4 AU-observer because the 1.0 AU-observer is connected to the weak wing of the shock when it is still strong (i.e., close to the Sun), and because its cobpoint only reaches the central region

when the shock has travelled a longer distance. Except for one 0.4 AU-observer, the E30 observers connect to the eastern wing of the shock, which weakens as it expands; consequently, their VR evolution is practically constant and smaller than in the other cases.

The derived synthetic proton flux profiles (Figure 4.4 and Figure 4.8) are a consequence of the continuous injection of shock-accelerated particles (controlled by VR), plus the conditions of the particle transport along the IMF lines, and the fact that the shock injects more particles during its travel up to 1.0 AU than up to 0.4 AU. The maximum intensity is measured by the N22W00 observer in any scenario considered. The shape of the proton flux profiles for corresponding observers at different radial distances might considerably differ. For example, at 1 MeV, for the W00 0.4 AU-observers, there is a sudden increase of the intensity at the prompt phase, followed by a further significant increase at the shock passage (due to the foreshock region); for the W00 1.0 AU-observers, however, the flux profiles evolve more slowly. The increase at the shock passage (ESP component) does not appear for the W45 and E30 observers because the shock becomes too weak. As expected, the prompt phase in the case of the W00 and E30 observers at 0.4 AU is more intense than in the case of the corresponding 1.0 AU-observers; the reason is, once more, their respective magnetic connections (Table 4.4).

The presence of a foreshock that confines low-energy particles might have a significant effect on the shape of the flux profiles. With an active foreshock at 1 MeV, for example, the maximum intensity at the prompt phase is frequently exceeded by the intensity value at the shock passage. But this depends both on the radial distance of the observer and on its angular (longitude and latitude) position with respect to the leading edge of the shock. For the 0.4 AU-observers (Figure 4.4), the intensity peaks at the shock passage, and it is higher as closer is the position of the observer to the main shock direction. On the other hand, for the 1.0 AU-observers (Figure 4.8), we only see an ESP component for the W00 events. This is because, for the W45 and E30 observers at 1.0 AU, the shock weakens and disappears prior to its arrival to these observers, and, hence it is too weak to confine particles in front of its wings; consequently, we have not simulated the effects of a foreshock region.

In conclusion, the variation of the effects of the foreshock region with the ra-

dial distance depends mainly on the characteristics of the modelled shock, and on the way we simulate this foreshock. Nevertheless, it is risky to extend the conclusions afforded about the influence of the foreshock only from the analysis of these simulations. In other scenarios (a wider shock, for example), the 1 MeV-intensity profile for the W45 1 AU-observers could display the peak intensity at the shock passage. It is worth to remind that it does not exist yet a consistent interplanetary shock-foreshock model contrasted with observations (at different radial and angular distances)[15].

Comparing the peak intensity values obtained at 0.4 AU and at 1.0 AU, we can derive a radial index, α, assuming that the peak intensity, P, varies with the radial distance as $P \propto r^{\alpha}$ (as in Aran 2007). Figure 4.13 presents the peak intensity values at 0.4 AU and at 1.0 AU, as well as the radial indices derived. Allowing for small variations, the general tendency of the radial dependence is the same for both energies for a given longitude (i.e., the tendency is similar in latitude), but it largely changes for observers at different longitudes. We obtain that the peak intensity decreases with radial distance, except for the case of the W45 observers at high energy. The reason is that the W45 observers at 1.0 AU have the best connection with the shock at the beginning of the event (see Figure 4.12). This also applies for the N22W45 observer at low energy, because the peak intensity is achieved at the prompt phase of the event. For the N07W45 and N37W45 observers, the radial indices both at low and high energy show similar values; hence, they are organized with respect to the latitudinal distance to the nose of the shock. For the W00 and E30 observers we do not find this trend: the radial index varies differently with the longitude and the latitude. These results are a consequence of the way each observer is connected to the front of this narrow shock.

Since we are using the same Q(VR) relation as in SOLPENCO (Aran et al. 2006) and the radial distances studied there are the same as in this work, the comparison of the obtained radial indices is straightforward. In the case of the W00 and E30 events, where the peak intensities are attained at the shock arrival, the radial indices that we derive are in agreement with those ones obtained in SOLPENCO: $-1 < \alpha < 0$ for 1 MeV, and $-0.8 < \alpha < 0.1$ for 32 MeV. In the case of the W45 observers, although

[15] In plain words, foreshock simulations contain ill-defined ad hoc parameters, mainly derived from isolate observations at 1 AU (see, for example, Vainio & Laitinen 2007).

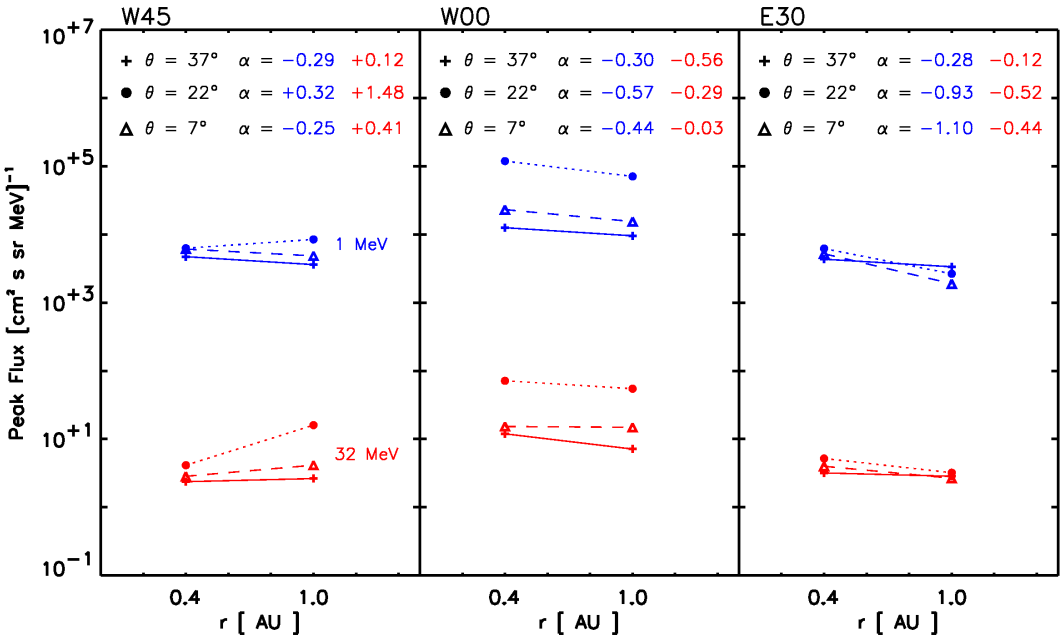

Figure 4.13: Radial variations of 1 MeV (blue) and 32 MeV (red) proton peak intensities for the 0.4 AU- and the 1.0 AU-observers. The values of α are given in the inset for each latitude and energy.

the radial indices are similar to those obtained in SOLPENCO (-0.5 < α < 0.3 both for 1 MeV and 32 MeV), we instead obtain the highest energy peak intensities at the prompt phase of the event, in agreement with observations.

From the analysis of Helios-1, Helios-2 and IMP-8 data, Lario et al. (2006) find that α = -1.95 ± 0.25 for 27 - 37 MeV protons. This value is steeper than the values we obtain, but it must be pointed out that the radial position of Helios varies from 0.3 AU to 0.98 AU, and, therefore, this average value can not be univocally compared with the values derived from our 32 MeV-protons profiles.

Simulations assuming an extended continuous contribution of shock-accelerated particles (Aran et al. 2005; Vainio et al. 2007) derive radial dependences for peak intensities (and fluences) that depend both on the particle energy and on the parameters featuring the model. They conclude that the longitudinal angular separation between the observer and the solar parent activity is the fundamental parameter that controls the radial variation of the proton peak intensity.

In a recent study, Aran et al. (2009) consider two sets of spacecraft located at 0.4 AU, 0.7 AU, 1.0 AU (W00 and W60 observers) and 1.6 AU, sharing the same Archimedian IMF line. Then, they use the SaP10 model to derive the dependences of the peak intensity on the radial distance. Simulations 1 and 2 of Aran et al. (2009), allow us a partial or approximate comparison with our simulations[16]: the values of α derived from Aran's simulations varies between -0.69 and -1.89 at 2 MeV, and it is practically constant, $\alpha \sim$ -1.46, at 32 MeV. At low energy, these values are in agreement with those depicted in Figure 4.13, but at high energy they considerably differ. Apart from the influence of the latitude, the most probable reason for such difference is that the 3D shock we have simulated is much narrower than the 2D shock simulated by Aran et al. (2009); thus, despite the fact that the shock strength might be similar (and hence, also the injection rate of particles), the region of the front to which the observer of our simulation connects, weakens much faster than in Aran's simulations (thus, Q decreases more rapidly).

4.5.2 0.4 AU-observers: Fast shock versus Slow shock

A generalized perception of what an interplanetary shock is naturally derives from the analysis of many of them, frequently from solar wind and magnetic field measurements performed by one spacecraft at $\sim$1 AU. It is then implicitly assumed that the analysis of a large set of such shocks should yield an average picture of which is the spatial structure of an interplanetary shock at 1 AU. But SEP modelling needs to know how the shock is, from near to the Sun and all the way while it is propagating, because, to take into account the particle acceleration processes, it is necessary to have some knoweldge of the plasma conditions at the cobpoint location.

However, the shock transit time up to a certain radial distance could vary depending on the angular (longitude and latitude) distance of the observer with respect to the main direction of the shock. For example, for a 0.4 AU-observer, a shock transit time of $\sim$ 10 hours could correspond to the slow shock simulation for a W00 observer (S-W00 case, Figure 4.9) or to the fast shock simulation for a W45 observer (F-W45

[16] We just say 'partial or approximate comparison' because, for example, whereas Aran's simulations have shock transit times up to 1.0 AU of 25.4 hours and 49.5 hours (simulations 1 and 2, and W00 and W60 observers, respectively), in our simulation the shock transit time spans between 15 hours and 40 hours, depending on the longitude and the latitude of the observer. Hence, the differences between these shock transit times correspond to different features of the simulations; i.e., shock type versus observer's position.

case, Figure 4.1), even without considering the influence of the latitude. But, in spite of having similar shock transit times, the intensity profiles and the peak intensities derived for these two cases (S-W00 case, Figure 4.11; F-W45 case, Figure 4.4) are quite different. The reason is, again, that the injection rate of shock-accelerated particles changes as the cobpoint scans different regions of the shock front.

The highest plasma and magnetic field jumps are detected by the N22W00 observer for both shock scenarios (Figure 4.1 and Figure 4.9), with a drastic decrease of their values for observers placed away from the nose of the shock, both in longitude and in latitude. As expected, for corresponding observers the jumps are larger for the fast shock than for the slow shock.

The shocks maintain their order of arrival according to the longitude and latitude of the observer in both simulations. Nevertheless, the delay between the first and the last shock passage in each case is different, being 5 hours for the case of the fast shock (the fastest shock passage occurs at $t = 8$ hours, and the slowest one at $t = 13$ hours), whereas for the slow shock is 6.5 hours. The reason is that the slow shock decelerates more rapidly than the fast shock, while expanding in interplanetary space.

For the fast shock case, the highest VR value is observed by the N22W00 observer (Figure 4.3), whereas for the slow shock (Figure 4.10) the observer located at N37W00 has a slightly higher value due to its better connection in longitude (Table 4.1 and Table 4.3). In both cases, the first cobpoint for the N22W00 observers happens at the same time, but the strength of the fast shock is much larger than the one of the slow shock. In the magnetically well-connected cases, there is a rapid decrease of the VR values within the first three hours of the simulation.

In both scenarios, the N22W00 observer sees the largest intensity (Figure 4.4 and Figure 4.11), but there is a difference of one order of magnitude between them. The peak intensities for corresponding observers are comparable, being larger those for the fast shock. The prompt phase of the fast shock is more intense than that of the slow shock, up to one order of magnitude, depending on the longitude and latitude of the observer; also the differences due to the latitude of the observer are more pronounced in the fast shock scenario.

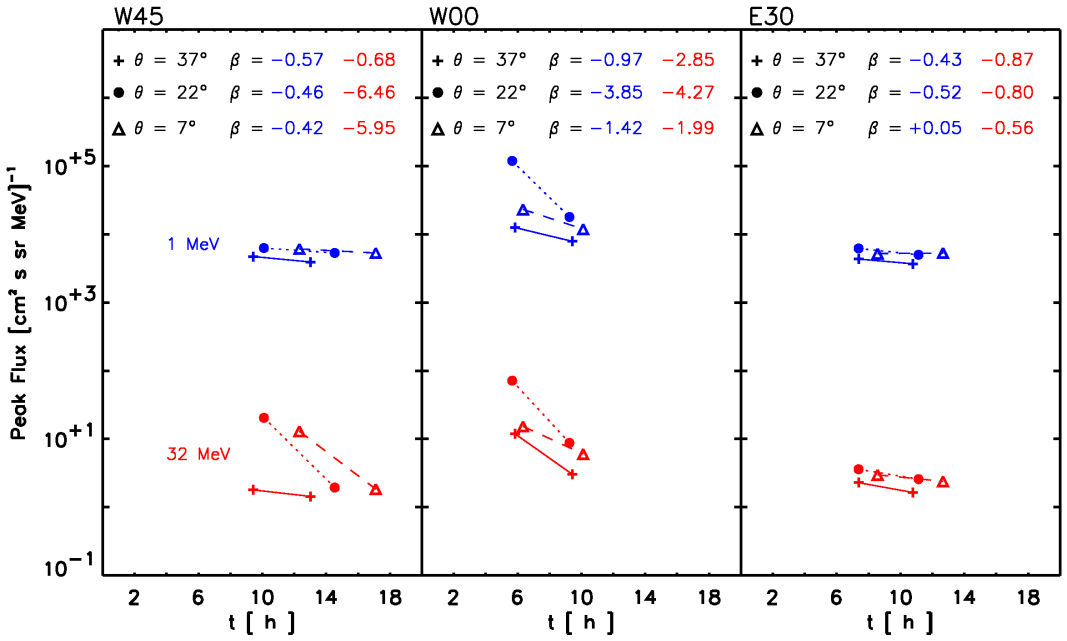

Figure 4.14: Peak intensity dependence of 1 MeV (blue) and 32 MeV (red) protons on their time-occurrence for observers at 0.4 AU. Panels, lines and symbols have the same meaning as in Figure 4.13. The first point of each pair corresponds to the fast shock, and the second point to the slow shock (lines are a visual aid).

With the aim to find a dependence between the velocity of the shock and the peak intensity, we have adjusted a power law to the values derived for the fast and slow scenarios, for the 0.4 AU-observers. Assuming $P \propto t^{\beta}$, in Figure 4.14 we show the peak intensity values as function of their time-occurrence, as well as the β-values derived. This dependence is hold for the W00 and E30 observers for the two energies considered; but it changes for the W45 observers. The reason of this discrepancy is the moment at which the peak intensity is achieved. At low energy, the intensities peak at the shock arrival, whereas at high energy it depends on the shock scenario and the position of the observer. In the fast shock case, for the N22W45 and the N07W45 observers, the intensity peaks at the prompt phase, whereas for the N37W45 observer it occurs at the shock passage; in the slow shock case, instead, all the W45 observers measure the maximum intensity at the shock passage.

4.6 Conclusions

We have developed a procedure to automatically determine the location of the cob-point, the corresponding shock normal and the downstream point, for 3D simulations. We have applied this procedure to several observers located at 0.4 AU and at 1.0 AU, and at different heliocentric longitudes and latitudes, which gives a total of nine positions for each radial distance. We have used a 3D MHD model to simulate the propagation of a fast and a slow CME-driven shocks.

We have analysed the evolution of the magnetic field intensity, number density and radial velocity for these observers and these scenarios, discussing the relevance of the latitude of the observer. We have found that the highest plasma jumps at the shock passage are detected by the N22W00 observer at both distances and for both shocks. We have also seen that there is a considerable reduction in the plasma values as the observer is placed far apart from the nose of the shock, both in longitude and in latitude. We have checked that the general behaviour of the plasma and magnetic field jumps are qualitatively the same at 0.4 AU and at 1.0 AU, being the jumps smaller at 1.0 AU. Also for both scenarios, the plasma and magnetic field jumps show the same behaviour, with higher jumps for the fast shock case than for the slow one.

As a consequence of the variations in the solar wind speed with latitude, we have corroborated that the shock itself travels at different speeds, depending on the background velocity over which the shock expands; consequently, the velocity of propagation of the shock also depends on the latitude. This translates into the fact that, for observers with the same longitude, the shock arrives earlier to those observers that are located at higher latitudes (i.e., with a faster background solar wind). For observers with the same latitude, the shock arrives later as larger is the separation between the position of the observer and the nose of the shock.

Based on the method used to characterize the shock strength in former shock-and-particle models, we have studied the evolution of the normalized radial velocity jump, VR, for these set of observers and scenarios. We have shown that: (1) MHD simulations of shocks have to include the evolution of the plasma variables and magnetic field close to the Sun (i.e., below 18 $R_\odot$), since the strength of the shock may rapidly decrease with radial distance, and hence, the efficiency of the shock

as particle accelerator, which is especially important at high energies; and (2) VR also varies with the latitude, not only with the longitude. The highest values of VR correspond to those observers with the cobpoints nearer to the shock nose, depending their location on the radial position of the observer and on its latitude. Therefore, combined models of shock propagation and particle acceleration, injection and transport, should take into account the influence of the variations of the plasma variables at the shock front with latitude.

We have derived the synthetic flux profiles for the cases presented throughout the chapter, within the frame of our shock-and-particle model, and we have presented examples illustrating the relevance of the latitude of the observer. We have shown that, in both shock simulations and for the two energies studied, the N22W00 observer gathers the maximum intensity. Within the same shock simulation, the flux profiles can differ up to one order of magnitude for observers with the same longitude but different latitudes, for both the 0.4 AU and the 1.0 AU-observers. These differences imply a large variation in the efficiency of the shock in the injection of accelerated particles, being larger for the fast shock than for the slow shock, and for the 0.4 AU-observers than for the 1.0 AU ones.

We have been able to reproduce the prompt phase of gradual well connected SEP events; the injection of the high energy particles near the Sun can be consistently simulated because the cobpoint is traced back closer to the Sun than in former shock models. We find that the intensities attained at the prompt phase depend on the magnetic connection of the observer with the shock front (which in turns depends on the latitude), in such a way that the better the observer is connected to the shock at the beginning of the event, the more intense is the prompt phase of the SEP event. We have also corroborated that, in general, the prompt phase is more intense for the 0.4 AU-observers than for the 1.0 AU ones, as well as for the fast shock case than for the slow shock case.

We have analysed the peak intensities in each case showing that, in all scenarios, the N22W00 observer attains the maximum intensity. We find that the peak intensities largely change, even up to one order of magnitude, for observers at any distance or longitude, depending on their latitude. For the fast shock, the peak intensity of the associated proton event is higher than for the slow shock, being the difference

larger at high energy than at low energy.

We have noted that the presence of a foreshock can largely modify the shape of the flux profiles and, so, the peak intensity values and their time-occurrence. At high energy, the peak usually appears at the prompt phase; but at low energy, it could be exceeded by the value at the shock passage. For those peaks that occur at the prompt phase of the event, the better the magnetic connection between the observer and the front shock, the higher the peak; while for the cases when the peak intensity occurs at the shock passage, the peak is larger as closer of the shock nose is the observer. The peak intensity values also depend on the velocity of the shock; this is especially important for magnetically well-connected events generated by fast shocks, where the peak intensity varies considerably with the longitude and the latitude of the observer. For each observer, we obtain that the peak intensity increases with the speed of the shock, with the exception of the N07E30 observer at low-energy, where the attained peaks are very similar. In this case, the slow shock is injecting particles for a longer period of time than the fast shock, and this counterbalances the effect of the slightly higher values of VR obtained in the fast shock when the shocks arrive to the observer.

We have analysed the radial dependence of the peak intensity for observers at 0.4 AU and 1.0 AU, located at the same longitude and latitude. We obtain that the peak intensity decreases with radial distance, except for the case of the W45 observers at high energy. The reason is that the W45 observers at 1.0 AU have the best connection with the shock at the beginning of the event. This also applies at low energy for the N22W45 observer, because the peak intensity is achieved at the prompt phase of the event. For the W45N07 and W45N37 observers, the radial indices both at low and high energy show similar values; hence, they are organized with respect to the latitudinal distance to the nose of the shock. For the W00 and E30 observers, we can not define a general trend of the radial index either with the latitude or the longitude of the observers: the radial index shows a high variability as a function of the longitude and latitude. These results are a consequence of the way each observer is connected to the front of this narrow shock.

The main conclusion of this study is the relevance of the latitude of the observer with respect to the leading direction of the shock. This is a factor scarcely

commented and quantitatively not formerly addressed in numerical simulations of SEP events. At present, practically all efforts have been focused on the longitude of the observer, mainly because: (1) the main body of observations comes from spacecraft located near 1.0 AU close to the ecliptic plane; and (2) 3D modeling of SEP events is a complex and computer demanding task hardly affordable, even nowadays.

We sustain that the inclusion of the latitude is relevant for space weather purposes and, therefore, it deserves much further attention. Needless to say that many more simulations (as other radial distances, latitudes, shock velocities and shapes, etc.) are required to draw definitive conclusions.

Part II

2D modelling of proton gradual events: the 1 March 1979 event

Chapter 5

Multi-spacecraft observations and shock simulation

I a vegades ens en sortim.
I a vegades una carambola de sobte
ens demostra que ens en sortim.
I a vegades, contra tot pronòstic,
una gran bestiesa capgira allò
que crèiem lògic tot fent evident
que, per un moment, ens en sortim.

Captatio benevolontiae, MANEL

5.1 Introduction

Multi-spacecraft observations of gradual SEP events in the ecliptic plane show that the particle intensity-time profiles measured by each spacecraft may display different shapes, even when they are located at similar distances from the Sun. In spite of their interest, due to the constraints that observations from separate vantage points impose, only a bunch of these events have been analysed and interpreted in terms of the particle shock-acceleration paradigm. At present, the modelling of a multi-spacecraft SEP event, jointly considering their shock and particle features, has been only undertaken in two cases: the 24 April 1979 event[1], with Helios-2 and ISEE-3 (Lario et al. 1998), and the 6 March 1989 event[2], with IMP-8 and Phobos-2 (Aran

[1] Helios-2 was located at 0.41 AU, W00, and ISEE-3 at 0.99 AU, W00. The flux profiles fitted are one energy channel of each spacecraft, at $\sim$100 keV (see also Heras et al. 1992). Helios-1, Pioneer-Venus and Venera 11 did not detect any shock or particle event at that time (see Sanahuja et al. 1983), which implies a gradual SEP event generated by a narrow interplanetary shock.

[2] See Figure 2.6. The flux profiles fitted are six energy channels between 0.5 MeV and 48 MeV of IMP-8, and four channels between 0.9 MeV and 19 MeV of Phobos-2.

et al. 2007).

The main reason of this scarce number of attempts is that modelling of gradual SEP events requires a set of a priori conditions[3] which gives reasonable guarantees that the assumptions adopted when developing the MHD model for shock simulations and the transport model for energetic particle simulations are fulfilled at their best. In the case of multi-spacecraft SEP events, these conditions have to be fulfilled by the event measured by each spacecraft and, hence, it reduces the number of events suitable for modelling. In addition, it is also necessary to take into account the relative radial and angular separation among the spacecraft and with respect to the solar origin of the event[4]. Finally, the existing number of such observed multi-spacecraft interplanetary SEP events in inner space is quite limited. Here (this chapter and the next one), we would like to evaluate the performance of the 2D model by simulating one multi-spacecraft SEP event.

From the list of 72 multi-spacecraft SEP events compiled by Lario et al. (2006), we have selected among those observed by Helios-1, Helios-2 and IMP-8, five candidates that we consider the most appropriate for modelling with the SaP10 model (see Appendix G) and, from them, we have chosen the 1 March 1979 SEP event. At the time of the event, the three spacecraft were located at similar radial distances from the Sun but showing a significant spread in longitude. The simulation of the shock propagation has been performed by fitting the shock arrival time and plasma jumps observed by each spacecraft, and the transport model reproduces the proton flux profiles measured in the upstream region, for different energy channels. We quantify the efficiency of the shock as particle injector in its way toward each observer and we draw conclusions on the influence of the relative position of the observer on the derived injection rate, as well as on the particle transport conditions found.

[3] As for example, the stability of the upstream solar wind and interplanetary magnetic field; no contamination of proton energy channels and overlapping of flux profiles with the downstream part of a former event; a clear identification of the solar origin of the event; for a 2D model, observations in the ecliptic plane or near by; etc. (see Chapters 1 and 2).

[4] Spacecraft too separate in longitude and radial distance require a denser or more extended numerical grid formulations (thus, computing time demanding).

5.2 Description of the event

At 1019 UT on 1 March 1979 (doy 60) took place the maximum of a 3N H_α-flare located at S23E58 (Kahler 1982; Lario et al. 2006, and references therein). At that time, Helios-1 was located at 0.95 AU and 66.7° eastward of the Earth-Sun line (E66.7). Helios-2 was at 0.93 AU, E26.6, whereas IMP-8 was at 0.99 AU, W00. Therefore, the relative longitude of these spacecraft with respect to the heliolongitude of the flare is: W08.7 for Helios-1, E31.4 for Helios-2 and E58 for IMP-8.

Almost two days after the occurrence of this solar activity, an interplanetary shock reached Helios-1 at 0202 UT and Helios-2 at 0934 UT, on 3 March (doy 62) (Volkmer & Neugebauer 1985; Daibog et al. 2000). At that time, IMP-8 was inside the magnetosphere, but ISEE-3 observed a sudden increase in the solar wind and magnetic field parameters at 0439 UT on 4 March (doy 63), which has been taken as the shock passage time[5] (see, for example, Figure 4 of Reames et al. 1997) by IMP-8/ISSE-3[6] (see Appendix G for more details about these spacecraft and data presented here).

When the interplanetary shock swept the two Helios spacecraft on 3 March, they have already slightly moved with respect to their positions on 1 March: 0.01 AU closer to the Sun and 2° westward, approximately[7]. Figure 5.1 shows the average position for each spacecraft during these two days: Helios-1 is at 0.945 AU, W08.5 (shortly speaking, W08), and Helios-2 is at 0.925 AU, E32.2 (shortly, E32). This figure also displays their nominal magnetic connection[8] to the Sun. The assumption of these two-day average locations might affect the position of the footpoint or the cobpoint, which is relevant for the transport model (because it assumes that the observer is connected to the cobpoint by an unique flux tube; see Section 2.4.1). But its potential effects are much smaller than other assumptions formerly adopted

[5] Reames et al. (1997) quote Reames et al. (1996) as the source of the identification of the shock passage, and there they refer to J. Gosling (private communication).

[6] From now on, otherwise indicated, we will not differentiate between these two spacecraft, despite ISEE-3 was orbiting L1 at 0.99 AU and IMP-8 was orbiting Earth. To our purposes, this small difference in distance is not relevant due to the spatial and temporal scales involved in our simulations. Solar wind plasma and magnetic field observations come from ISEE-3, and proton flux intensities are from IMP-8.

[7] These changes are smaller than the size of the dots pointing the location of each spacecraft in Figure 5.1.

[8] Considering, for each spacecraft, the solar wind speed given in Table 5.1.

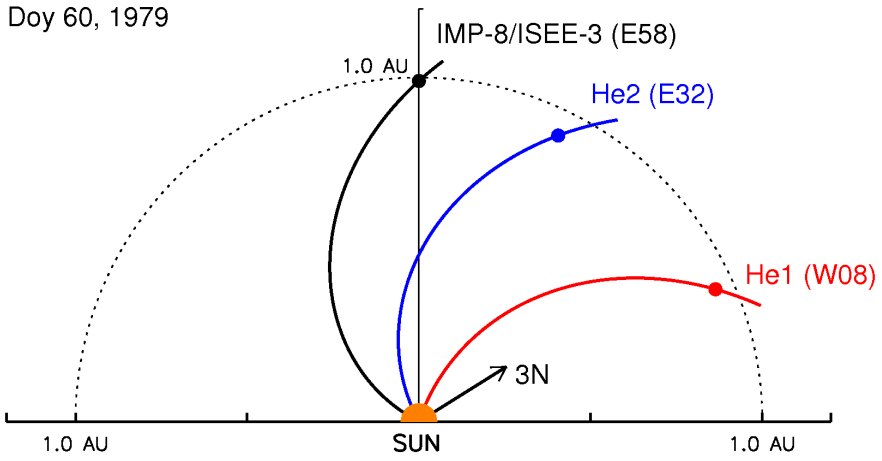

Figure 5.1: 1 March 1979 SEP event. Location of the three spacecraft and their initial IMF connection to the Sun, as assumed in our simulation.

in the model (like ignoring the corotation effect or the influence of the latitude, for example). For modelling purposes, hereafter we identify the angular location of each spacecraft by its relative longitude with respect to the 3N-flare (not with respect to the Sun-Earth line); therefore, Helios-1 is assumed to be at W08, Helios-2 at E32 and IMP-8 at E58, as labelled in Figure 5.1.

Top panels of Figure 5.2 and 5.3 show the proton flux profiles for the four energy channels (between 3.77 MeV and 50.7 MeV) of Helios-1 and Helios-2 that we model[9]. The following panels display, from top to bottom: the solar wind velocity, density and temperature, as well as the magnetic field strength, latitude and azimuth. The dashed vertical lines indicate the time of the solar activity and the solid vertical lines the passage of the aforementioned shocks. Figure 5.4 also shows, as in the two previous figures, the proton flux profiles of the simulated fourteen energy channels (between 5.9 MeV and 81.0 MeV) of IMP-8, and the solar wind plasma and magnetic field data from ISEE-3.

Lario et al. (2006) find that peak intensities and fluences are much better organized in terms of the longitude than in terms of the radial position (bottom panels of Figures 2 and 3 of Lario et al. 2006). Although the radial distances of the three

[9] We do not consider the 1.28 - 3.77 MeV proton channel because the pre-event intensities were high due to a previous event, and because it is most probably contaminated from high-energy protons or electrons in the case of Helios-1.

spacecraft were similar, the peak intensities varied by two orders of magnitude and were well ordered with the increasing angular distance between the footpoint[10] and the flare site (Figure 1c of Lario et al. 2006, or Figure 5.1 of this work).

Prior to the shock arrival at Helios-1, all three spacecraft appear to be in the same magnetic sector and detect similar solar wind speeds (see Figure 5 of Reames et al. 1996). Reames et al. (1996) analyse the intensity-time profiles of 3 - 6 MeV and 30 - 45 MeV protons observed by the three spacecraft, focussing in their respective downstream regions which show common features[11]. They describe this event as generated by a CME-driven shock that is assumed to be the main source of accelerated particles, describing the shapes of the intensity-time profiles in terms of the shock-accelerated particles paradigm. Since Helios-1 sees the event as near CM, it is poorly connected when the shock is close to the Sun. At low energy, the early rise phase is relatively slow, appearing the characteristic flat profile (~ 100 protons $[\mathrm{cm}^2\,\mathrm{sr}\,\mathrm{s}\,\mathrm{MeV}]^{-1}$) and peaking at the shock passage, approximately. At Helios-2, the onset of the proton high energy (>12 MeV) component shows a ~ 4 hours delay. Lower energy proton intensities slowly increase from the background because the cobpoint scans the east flank toward the leading edge part (stronger) of the shock. The intensity peaks about one hour after the shock passage (a time delay frequently observed in large eastern events; Sanahuja & Domingo 1987), attaining a value similar to that observed by Helios-1. For IMP-8, this is a far eastern proton event and, hence, the cobpoint samples the shock even farther from the nose than Helios-2, measuring much lower intensities and a slower rise. From the qualitative description of this SEP event, Reames et al. (1997) conclude that this shock *"must have a steep gradient in intensity with longitude around the nose"*.

This E58 SEP event seen by IMP-8 on 1 March 1979, resembles the SEP event of the 6 March 1989 also observed by IMP-8 (Aran et al. 2007). Both are associated with flares at similar heliolongitudes (E58 and E69, respectively), have large transit

[10] The footpoint of each spacecraft on the Sun is computed by assuming a Parker spiral for the IMF with a constant solar wind speed of $450\,\mathrm{km\,s^{-1}}$.

[11] Reames et al. (1996) and Reames et al. (1997) describe the region of the spectral invariance identified in the downstream part of this (and others) SEP event. Well behind the shock passage, the $3 < \mathrm{E} < 56$ MeV proton intensities observed by the three spacecraft join (within a factor of two) and track each other, and decrease continuously over several days. The authors estimate the time decay of the proton intensities in this downstream spectral invariant region. Nevertheless, apart from a short description of the complex and different time intensity profiles observed in this region, there is no attempt to model such intensity profiles and shock passages.

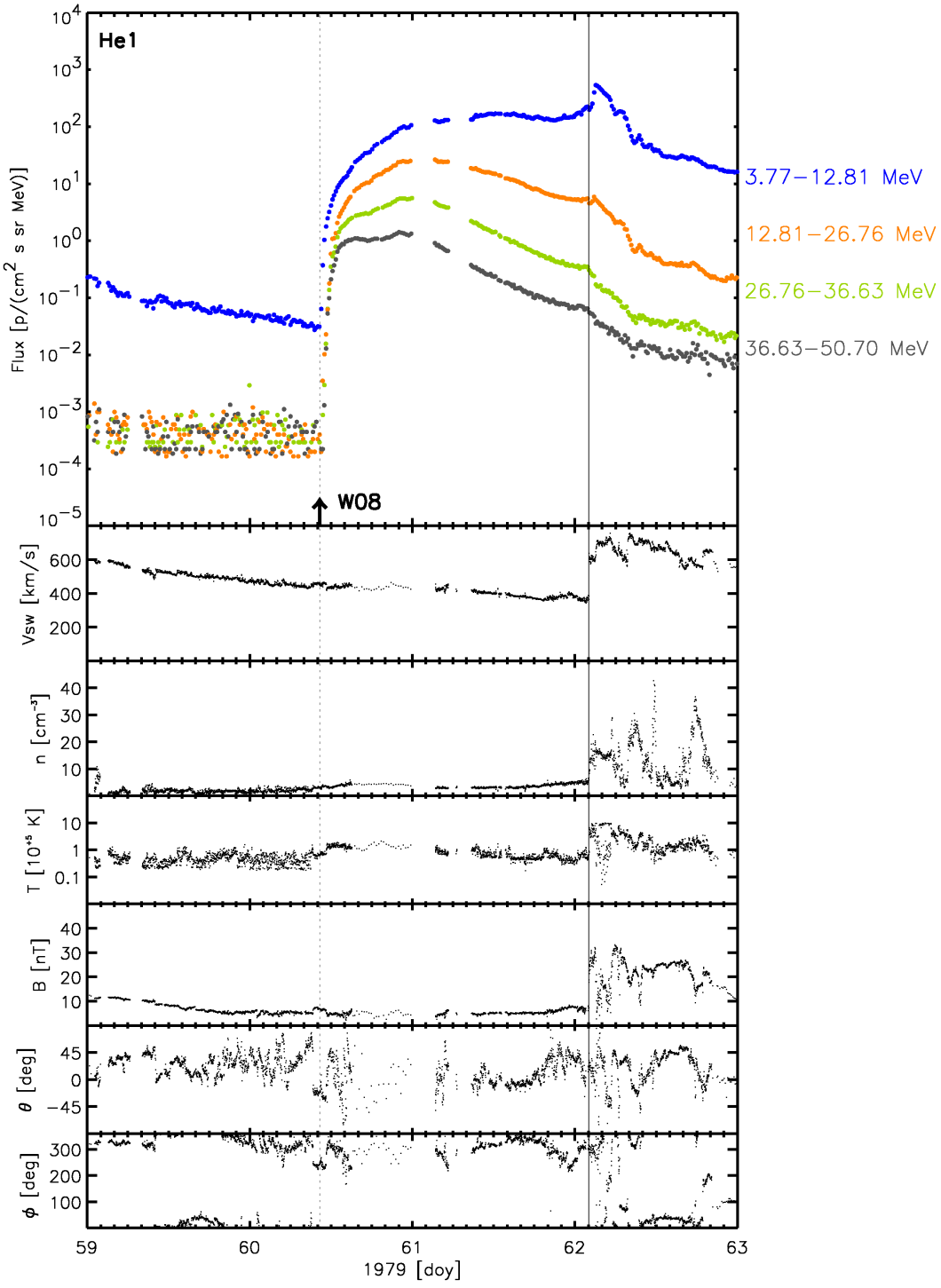

Figure 5.2: 1 March 1979 event. Helios-1: Evolution of the proton flux profiles for four energy channels (as labelled), and solar wind plasma and magnetic field variables. The vertical line marks the shock passage and the arrow and dashed line the time of the solar activity.

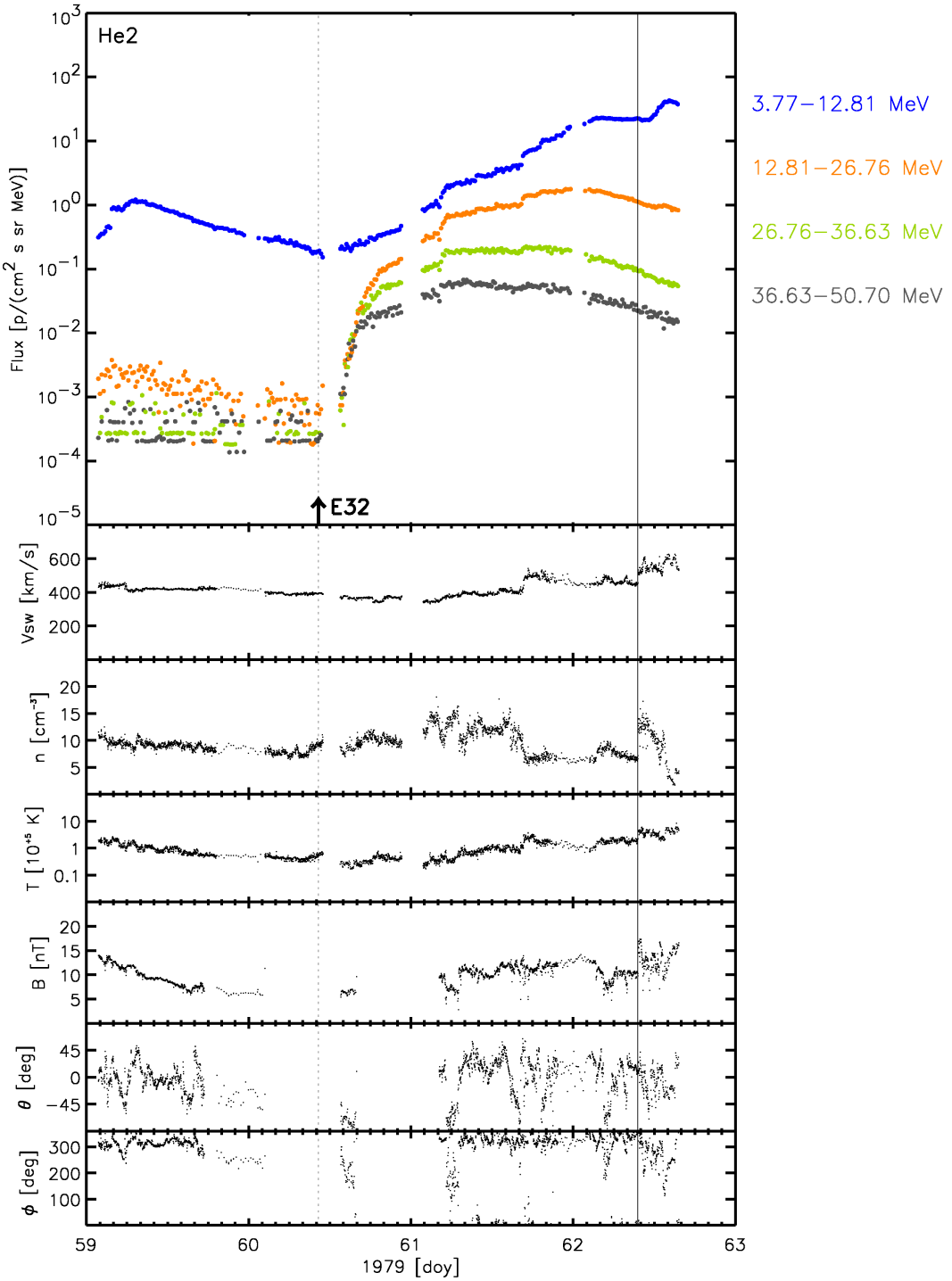

Figure 5.3: 1 March 1979 event. Helios-2: Displayed as in Figure 5.2.

times to Earth (66.3 hours, Table 5.2, and 52.1 hours, respectively), and their flux profiles reach similar maximum values for comparable energy channels (those in Fig-

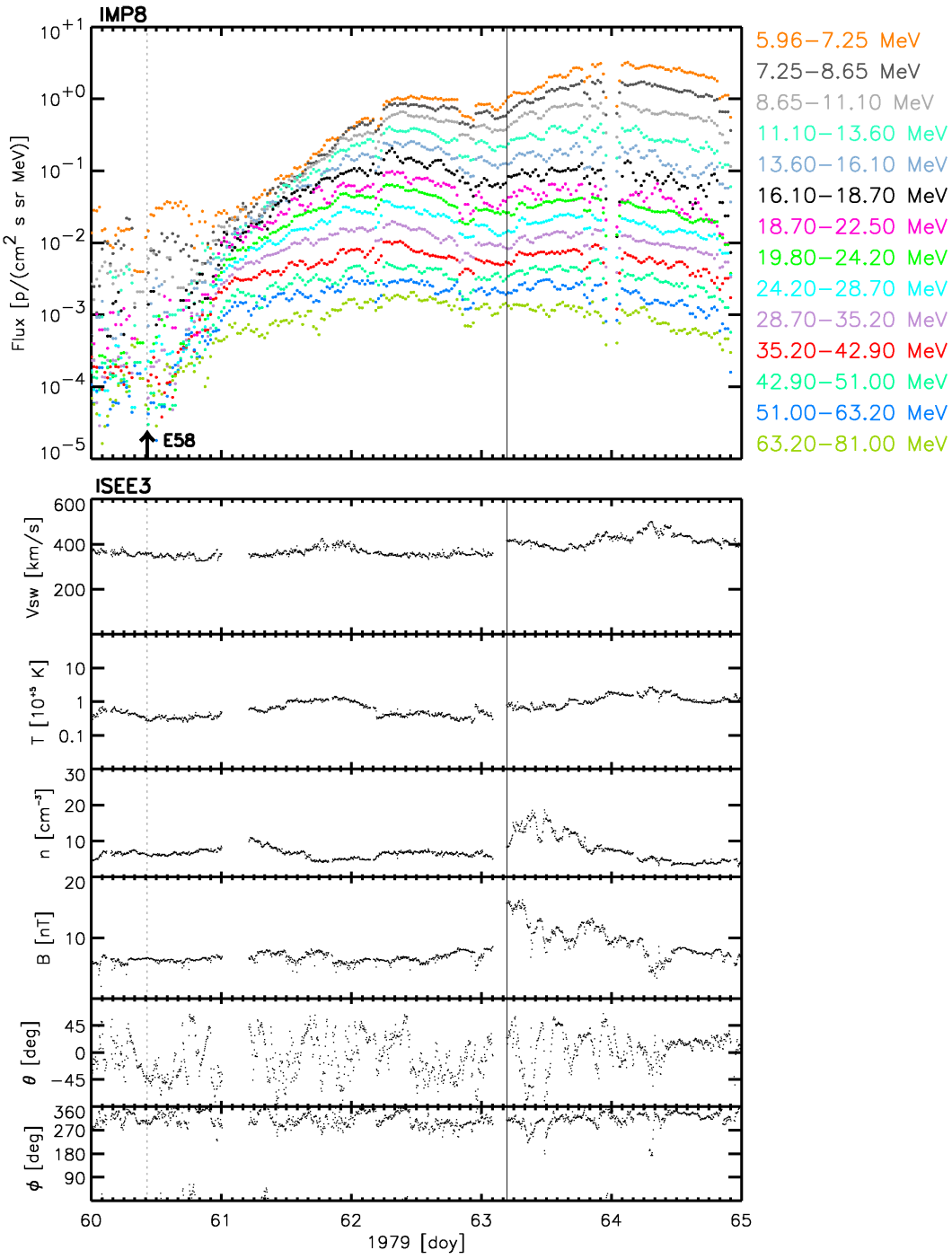

Figure 5.4: 1 March 1979 event. IMP-8 and ISEE-3: Displayed as in Figure 5.2.

ure 5.4 compared to those in Figure 4 of Aran et al. 2007, excluding the ESP peak at the shock passage). Nevertheless, there are two significant differences between

them: (1) the high energy proton flux in the 6 March 1989 event starts rising from the background > 14 hours after the maximum of the assumed solar parent activity, whereas in the 1 March 1979 this delay is only of ~ 4 hours; and (2) the flux at high energy increases more slowly in the 1989 event that in the 1979 one, showing in this latter event particle enhancements up to 80 MeV. This represents a too early onset for an E58 event, and also a too rapid increase of the flux with respect to what would be expected for a 'standard' $>$ E55 event (within the shock-accelerated-particle paradigm).

Three examples of such 'standard' behaviour for eastern events with heliolongitudes smaller than 45° ($<$ E45) can be found in one of the insets of Figure 1.4, or among those of Figure 2.4 of Aran (2007) or Figure 2 of Reames et al. (1996). But in the case of the 1 March 1979 event, the associated solar activity occurred eastward (as seen by IMP-8) of the events previously mentioned, and hence, the initial magnetic connection[12] of the SEP event measured by IMP-8 should be delayed with respect to the qualitatively magnetic connection cartooned in these figures (whenever it happens). In this direction, we would also like to remark that the fast rise of the high energy flux profile observed by Helios-2 is not a typical feature of an E32 event; the upstream profile evolution resembles more to a W00 event, like the E01 event presented in Figure 2 of Reames et al. (1996) or the W09 event in Figure 2.4 of Aran et al. (2007).

5.3 MHD modelling

5.3.1 Background solar wind

To simulate the pre-event background solar wind we use the model described in Section 2.2.2. At the solar surface, the polytropic index is set to $\gamma_0 = 1.05$, varying smoothly from its coronal value to its interplanetary value, $\gamma_1 = 1.4$, within the first $50\,R_\odot$. These values, as well as $K_{1AU} = 4 \times 10^{22}\,\mathrm{N\,m^{3\,\alpha-2}}$, allow us to better reproduce the observed plasma variables. Figure 5.5 presents the magnetic field, number density, speed and temperature profiles of the solar wind from $1\,R_\odot$ to $350\,R_\odot$.

Table 5.1 summarizes the comparison between the observed and simulated solar

[12] We will return to the first magnetic connection in Section 5.4.2.

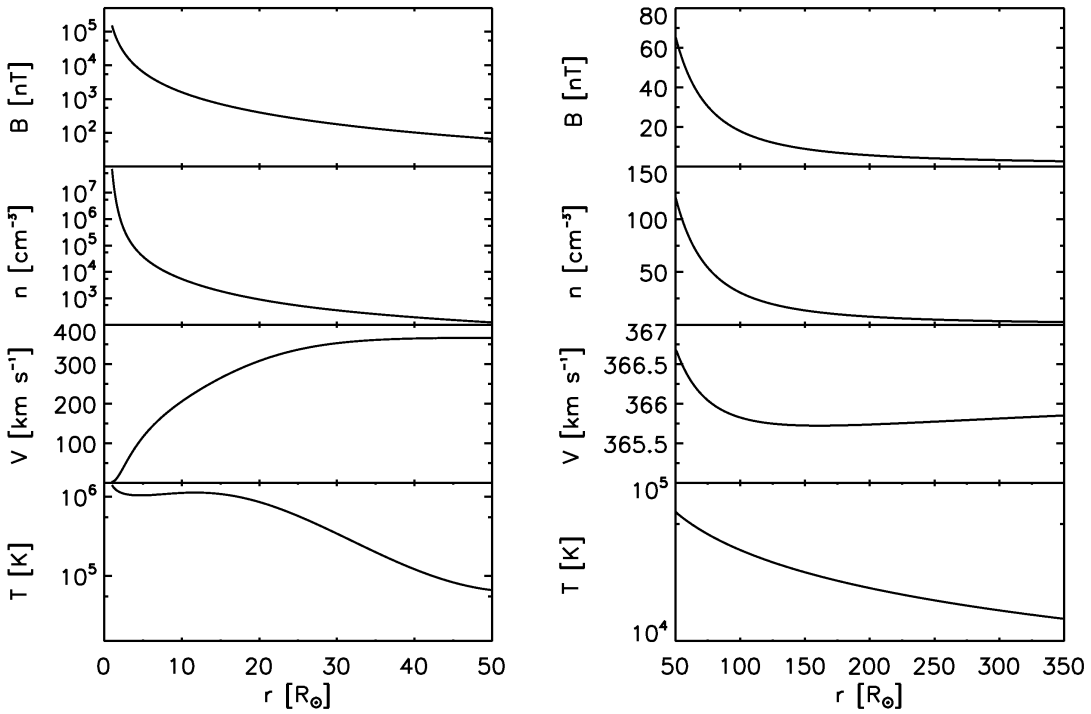

Figure 5.5: Left panels: magnetic field strength (B), number density (n), speed (v) and temperature (T) profiles for the background solar wind as a function of the radial position until $50\,\mathrm{R}_\odot$. Right panels: Same profiles as in the left panels but displayed for the radial positions between $50\,\mathrm{R}_\odot$ and $350\,\mathrm{R}_\odot$.

wind plasma and magnetic field variables at each spacecraft. The values match well for Helios-2[13] and ISEE-3, but there is a small disagreement for Helios-1, because the solar wind was slightly perturbed[14] prior to the onset of the event due to the arrival of an interplanetary shock and an ICME early on the 27 February (doy 58, not shown in Figure 5.2). Owing to the observed long and highly perturbed sheath after the shock passage on doy 58, it is plausible that a high speed stream interacted with the ICME driving this shock (as discussed in Rodriguez et al. 2009, for the case of the April 2000 SEP event). The increase on the solar wind speed (up to $\sim 500\,\mathrm{km\,s^{-1}}$) observed by Helios-2 at 1700 UT on doy 61 coincides with the passage of such high speed stream. This faster solar wind speed observed prior to the shock arrival at Helios-2 slightly affects the measured particle intensities as clearly seen in

[13] We have ignored the short increase in the solar wind velocity detected by this spacecraft around 17.5 hours before the shock passage.

[14] At the onset of the SEP event, the solar wind velocity detected by Helios-1 was $448\,\mathrm{km\,s^{-1}}$ whereas at the shock arrival is slightly slower, $384\,\mathrm{km\,s^{-1}}$.

Table 5.1: Observed and simulated values of the solar wind plasma and magnetic field variables at the position of the three spacecraft.

	Helios-1		Helios-2		ISEE-3	
	Obs.	Model	Obs.	Model	Obs.	Model
$v\,[\mathrm{km\,s^{-1}}]$	448	366	369	366	362	366
$n\,[\mathrm{cm^{-3}}]$	2.8	7.3	8.2	7.6	5.7	6.7
$T\,[10^5 \times \mathrm{K}]$	0.70	0.21	0.31	0.22	0.28	0.21
$B\,[\mathrm{nT}]$	6.8	5.5	5.4	5.6	6.5	5.2

Figure 5.3. On the other hand, the temperature is systematically underestimated by the model (as frequently happens in polytropic solar wind models).

5.3.2 Shock simulation

Applying the model described in Section 2.2.2 to simulate the shock, we place the initial plasma perturbation at $1.75\,\mathrm{R_\odot}$ and we launch it in $\varphi_{cme} = 180°$ direction[15]. We also assume[16] $d_{cme} = 0.5\,\mathrm{R_\odot}$, $A = 15$, $\Delta\Phi = 0.5$ and $a_{cme} = 160°$. The initial density and velocity of the perturbation have been taken as $n_{cme} = 0.5 \times 10^8\,\mathrm{cm^{-3}}$ and $v_{cme} = 1900\,\mathrm{km\,s^{-1}}$. Figure 2.3 presents the initial profile of the radial velocity used for this simulation.

The observed and simulated solar wind profiles obtained from the MHD model are shown in Figures 5.6, 5.7 and 5.8, for Helios-1, Helios-2 and ISEE-3, respectively. As can be seen, the simulated shock reproduces the jump in velocity at the shock arrival for the three spacecraft and the jumps in magnetic field and also density for ISEE-3. The simulated shock overestimates the jumps in density and magnetic field for Helios-1 and Helios-2, and underestimates the jumps in temperature. Table 5.2 compares the shock transit times and speeds[17] obtained from the observations and from the simulation, for the three spacecraft. The model perfectly and simultane-

[15] It is worth to remind that the CME is not necessarily centred on the flare location and that an error of $\sim 20°$ could easily occur in this presumed direction (e.g., Reames et al. 1996).

[16] These values are the same ones adopted in the construction of SOLPENCO2 database, within the SEPEM project.

[17] The transit time of the shock is defined as the time interval passed from the onset of the flare to the shock arrival at a given spacecraft; and the transit speed as the Sun-spacecraft distance divided by the transit time.

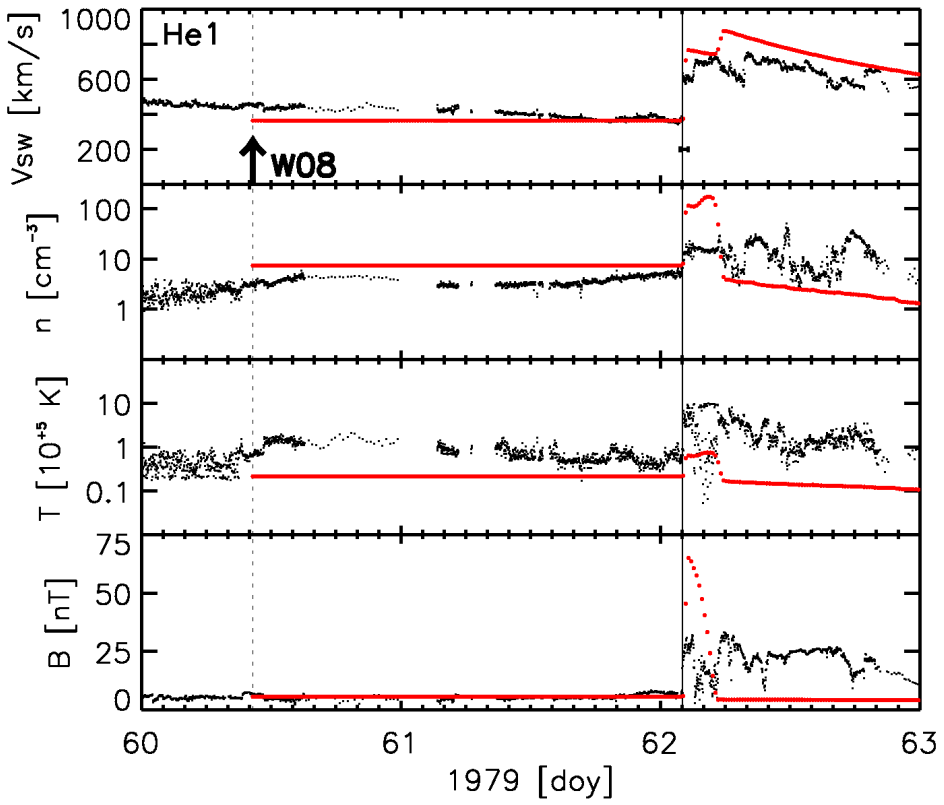

Figure 5.6: Interplanetary shock at Helios-1. Observations in black and simulations in red. From top to bottom: v, n, T and B. The arrow and the dashed line indicate the onset of the event, and the solid line the shock passage. The error bars for the simulated transit time are marked at the shock arrival line.

Table 5.2: Observed and simulated shock transit times and speeds.

	Helios-1		Helios-2		ISEE-3	
	Obs.	Model	Obs.	Model	Obs.	Model
Transit time [h]	39.72	39.79	47.25	47.04	66.33	66.56
Transit speed [km s^{-1}]	988	987	813	817	620	618

ously reproduces the three shock arrival times, with a maximum difference in speed of 4 km s^{-1}. In short, the MHD simulation of the shock reproduces well the transit speed and the jump in velocity at the three spacecraft, which are the main inputs for the particle model.

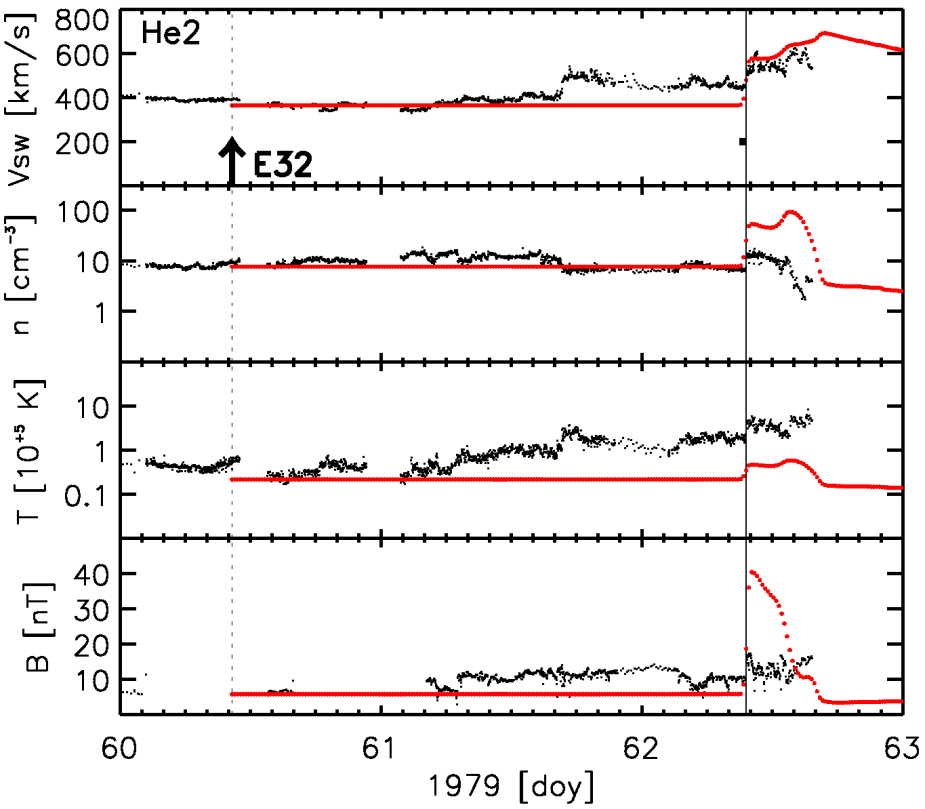

Figure 5.7: Interplanetary shock at Helios-2. Displayed as in Figure 5.6.

It must be pointed out that these small differences between the observed and the simulated transit times and speeds should be taken within the assumed accuracy for the scenario depicted, since Helios spacecraft slightly change their radial and angular positions throughout the event (as commented in the previous section). Taking the location of both spacecraft at the respective shock passage moments instead of at the average locations adopted for the simulation, the transit times derived are 39.54 hours for Helios-1 and 47.03 hours for Helios-2. For Helios-2, this value coincides with the one derived from the average position. The reason is that, although this spacecraft is closer to the Sun, it is swept by a region of the shock front which is $\sim 2°$ further from the nose (with respect to the case where the spacecraft had a constant position); thus, the shock moves slower and this compensates its proximity to the Sun. For Helios-1, at W08, these two factors add instead of counterbalance each other, so the larger difference. These differences are plotted in the corresponding top panels of Figures 5.6 and 5.7 as error bars at the shock passage; anyway, they are not relevant within this simulation.

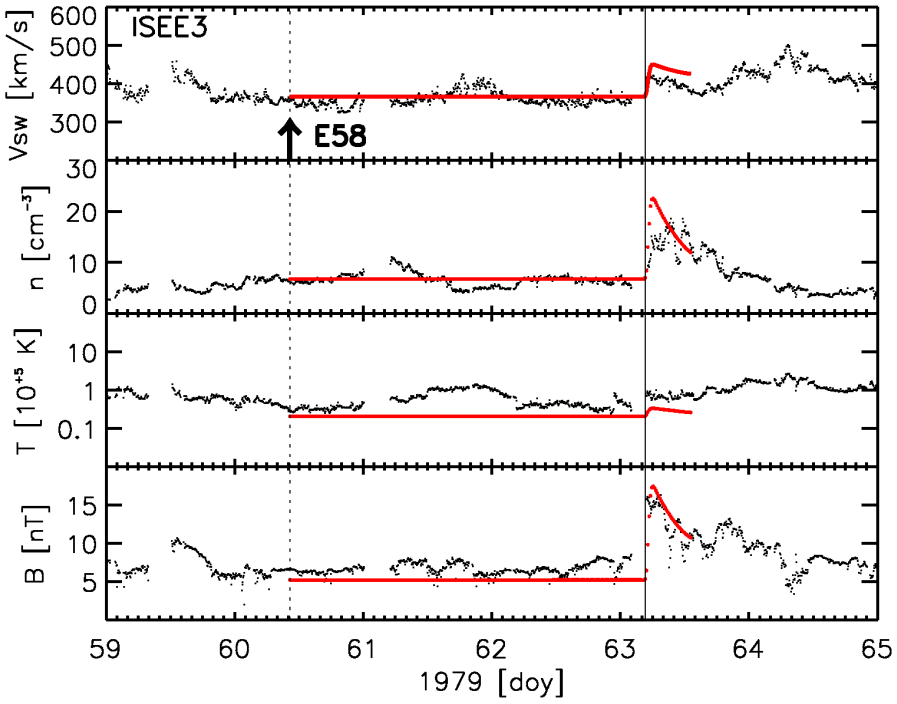

Figure 5.8: Interplanetary shock at ISEE-3. Displayed as in Figure 5.6.

Figure 5.9 shows four snapshots of the shock simulation corresponding, from top to bottom and from left to right, to 2.25, 6.20, 16.02 and 37.29 hours after the launch of the perturbation, respectively. In each panel, the contours illustrate the radial velocity v_r. The Sun is located at the $(X, Y) = (0, 0)$ point and the main direction of the shock is toward the negative X-values. The last panel of this figure also displays the position of Helios-1, Helios-2 and IMP-8. The black circle marks the position of the cobpoint for Helios-1 and the orange circle its downstream point at each corresponding time (in the following section we describe how the front shock and these points are determined). In this figure, the colour code used for the v_r-contours, from red at the shock nose to green-bluish at the wings, allows a rapid visual identification of the expanding perturbation from near the Sun to ~ 1 AU (shortly before the shock passage by Helios-1 in the last panel). As the dynamic range of the colour code is the same for the four snapshots, it is easy to distinguish the compact region between the shock front and the compressing (ICME) driver, as well as how the strength of the shock decays as it outwardly expands.

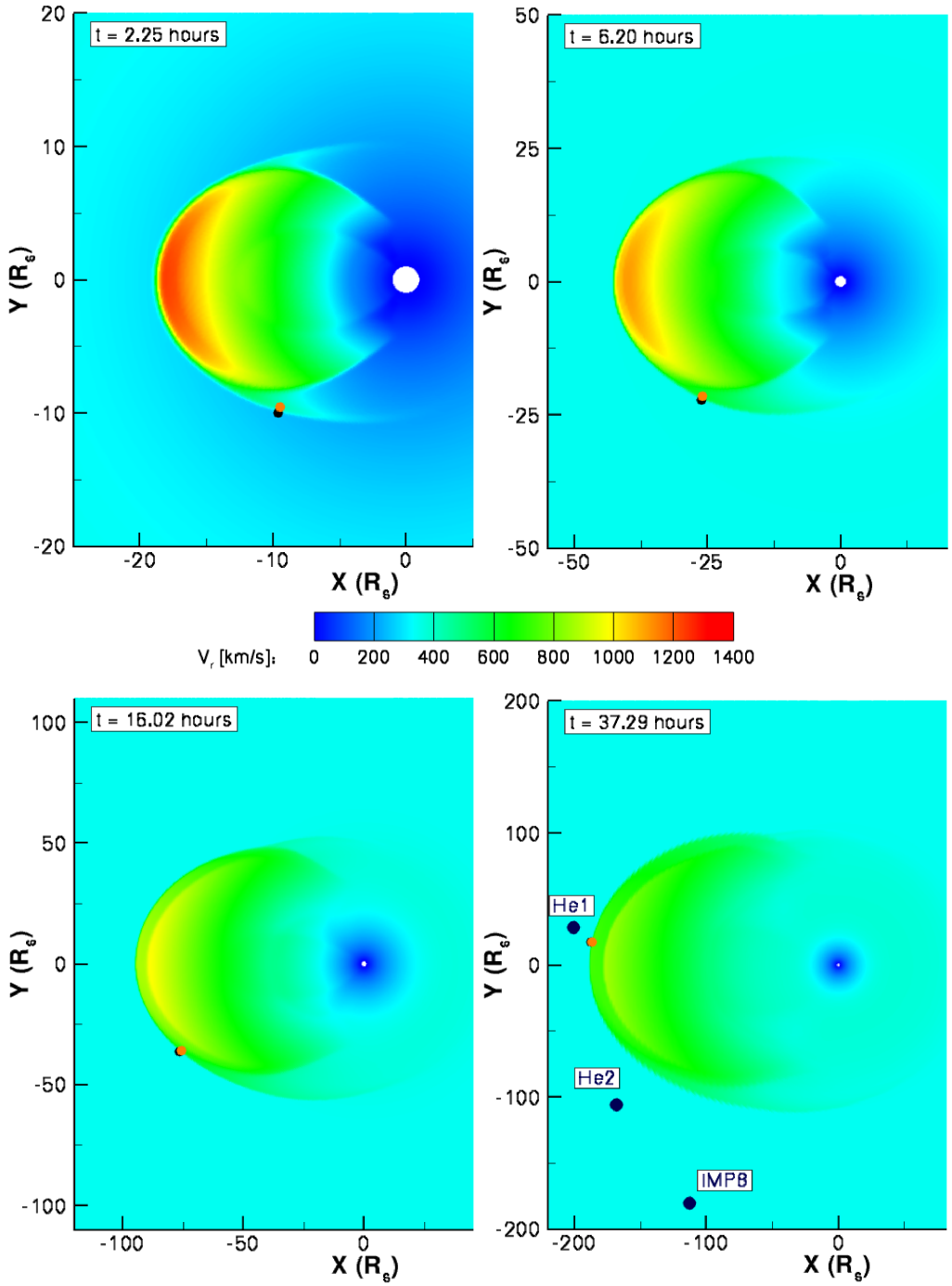

Figure 5.9: Four snapshots of the shock simulation at $t = 2.25$ (top left), 6.20 (top right), 16.02 (bottom left) and 37.29 hours (bottom right). The colour code represents the v_r-contours. The black and orange circles mark the position of the cobpoint and the downstream for Helios-1 (to be commented in the next section). Last panel shows also the position of Helios-1, Helios-2 and IMP-8.

5.4 Shock determination

In this section we describe the details of the procedure applied to derive the values of the plasma and magnetic field variables upstream, at the passage and downstream of the shock front, as well as their changes at the position of the spacecraft.

5.4.1 Cobpoint and shock finder

For each snapshot of the 2D MHD simulation, we calculate in an automated manner[18] the position of the cobpoint and the plasma variable jumps across the shock front for each observer/spacecraft. For a given observer, we trace back to the Sun the IMF line using the same procedure described in Section 3.3.1. Moving along the field line, from the outer boundary of the domain towards the Sun, we determine the location of a cobpoint candidate where the relative[19] density or radial velocity exceed a certain threshold value (10% for the density and 5% for the radial velocity).

Then, we compute the normal direction to the shock front at the cobpoint candidate location by means of the density and radial velocity gradients: the shock normal direction is assumed to be the average of both gradients and directed sunward (hence, in the opposite sense of the plasma flow). To check that at the cobpoint candidate's position there is a steep increase in density and velocity, the derivatives of the relative variables are calculated along the normal direction. To nominate the candidate point as cobpoint, we require that one of the two derivatives must be the 75% of its respective maximum value. If this condition is not satisfied, the cobpoint-candidate search procedure is repeated; in this way, the procedure is able to exclude small fluctuations and smooth disturbances not steepened enough to be considered as a shock.

Afterwards, it is necessary to verify that the disturbance found at the cobpoint is really a shock. Therefore, we have to identify the downstream point by setting conditions on the derivatives of the relative plasma variables:
− the downstream point is the point where the first order difference for each relative variable becomes smaller than the 75% of the difference in the previous point;

[18] The procedure described in this subsection has been developed by C. Jacobs and A. Aran within the SEPEM project.
[19] As in previous chapters, the term 'relative' means with respect to the background solar wind.

− if the downstream points determined by considering the relative density or the relative radial velocity do not coincide, we take as downstream point the one which is closer to the cobpoint;
− if the downstream point is located farther than $5\,R_\odot$ apart from the cobpoint, the detected disturbance is not classified as a shock.

Finally, we compute the upstream and downstream Mach numbers (see Appendix A), to check what kind of shock we are dealing with; thus, it may be classified as fast, intermediate or slow shock, or even not shock at all. This later possibility occurs from time to time, since the determination of the Mach numbers is sensitive[20] to the location of the downstream point.

Once verified that there is a shock at the cobpoint, we look for the downstream point in the radial direction (pointing towards the Sun). The criterion applied is similar to the criterion used to determine it in the normal direction: we locate the downstream point where the differences in the relative plasma variables become smaller than the 20% of the maximum difference value[21]. The final step is to take the values of the solar wind plasma and magnetic field variables at the cobpoint and at the downstream point, and to calculate VR and BR (although we mainly focus on VR, Equation 2.1, as commented in Section 2.1).

5.4.2 Evolution of the cobpoint and VR

Figure 5.10 displays a snapshot of the shock simulation at $t = 36.04$ hours, showing the position of the three spacecraft, their corresponding cobpoints (purple circles) and the computed IMF lines.

The cobpoint of Helios-1 is marked in the four panels of Figure 5.9 (whereas the position of the spacecraft only appears in the last panel). As can be seen, the cobpoint moves from the left flank of the shock (as seen from the Sun) towards its nose, as the shock expands. This evolution and the corresponding for Helios-2 and IMP-8

[20] It might happen (rarely, but it does), for example in locally weak shocks, that the automated procedure oddly diagnoses 'no shock detection' after a 'fast shock' diagnose in the preceding snapshot.

[21] This recipe for automated determinations does not always work properly. For example, when the shock normal direction is nearly perpendicular to the radial direction, the change of the plasma variables in the radial direction can be very smooth.

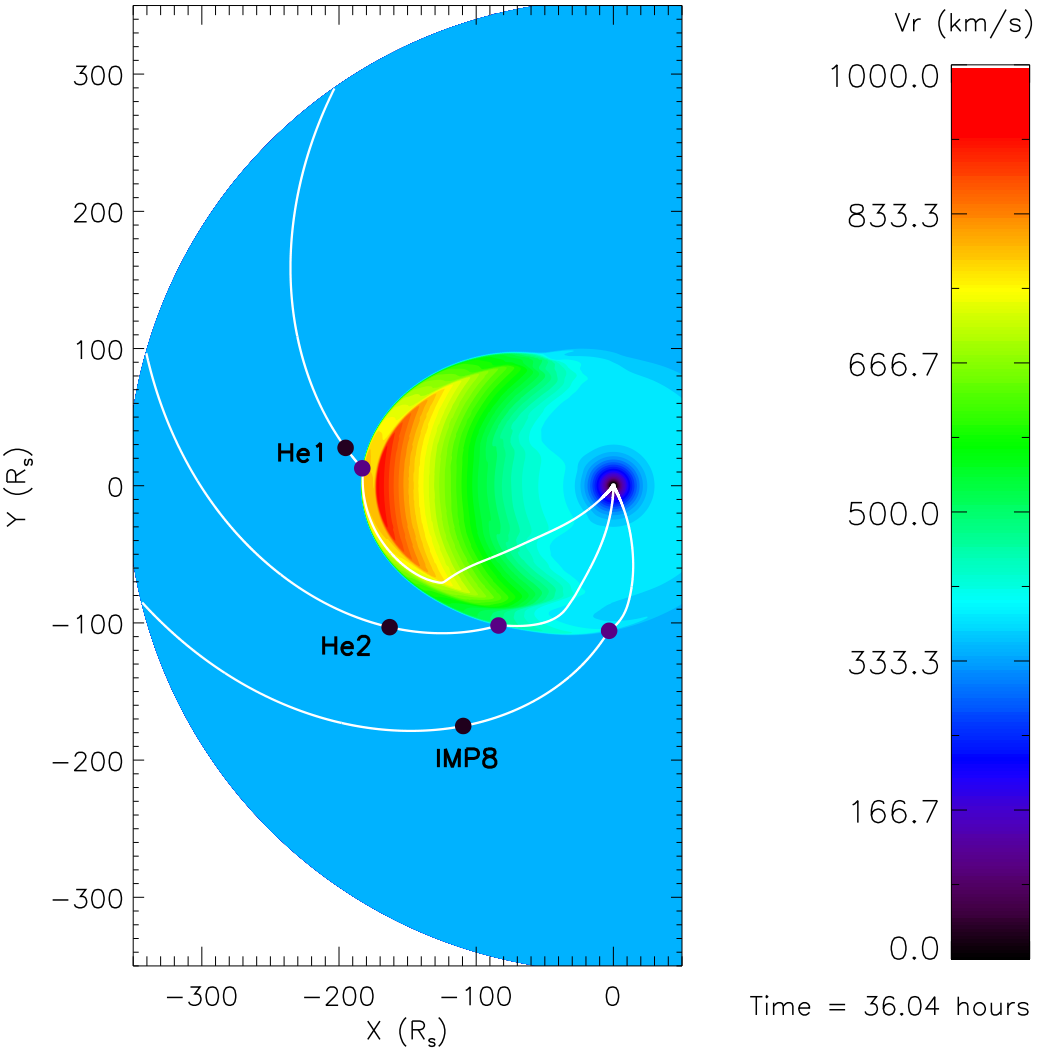

Figure 5.10: Snapshot of the shock simulation at $t = 36.04$ hours. The colour code represents the v_r-contours. The black circles mark the positions of Helios-1, Helios-2 and IMP-8 spacecraft (as labelled), the purple circles their corresponding cobpoints and the white lines the connecting IMF lines.

are better tracked in Figure 5.11. It shows, from top to bottom, the evolution of the radial and angular position[22] of the cobpoint, as well as the evolution of VR and BR at the cobpoint for the three spacecraft. The vertical arrows mark the onset of the simulation, the colour vertical lines the shock arrival time at each spacecraft (as labelled) and the dotted line flags $r = 1$ AU. The evolution of Helios-1 is the shortest

[22] Positive values mean the right wing of the shock, whereas negative values the left one (as seen from the Sun).

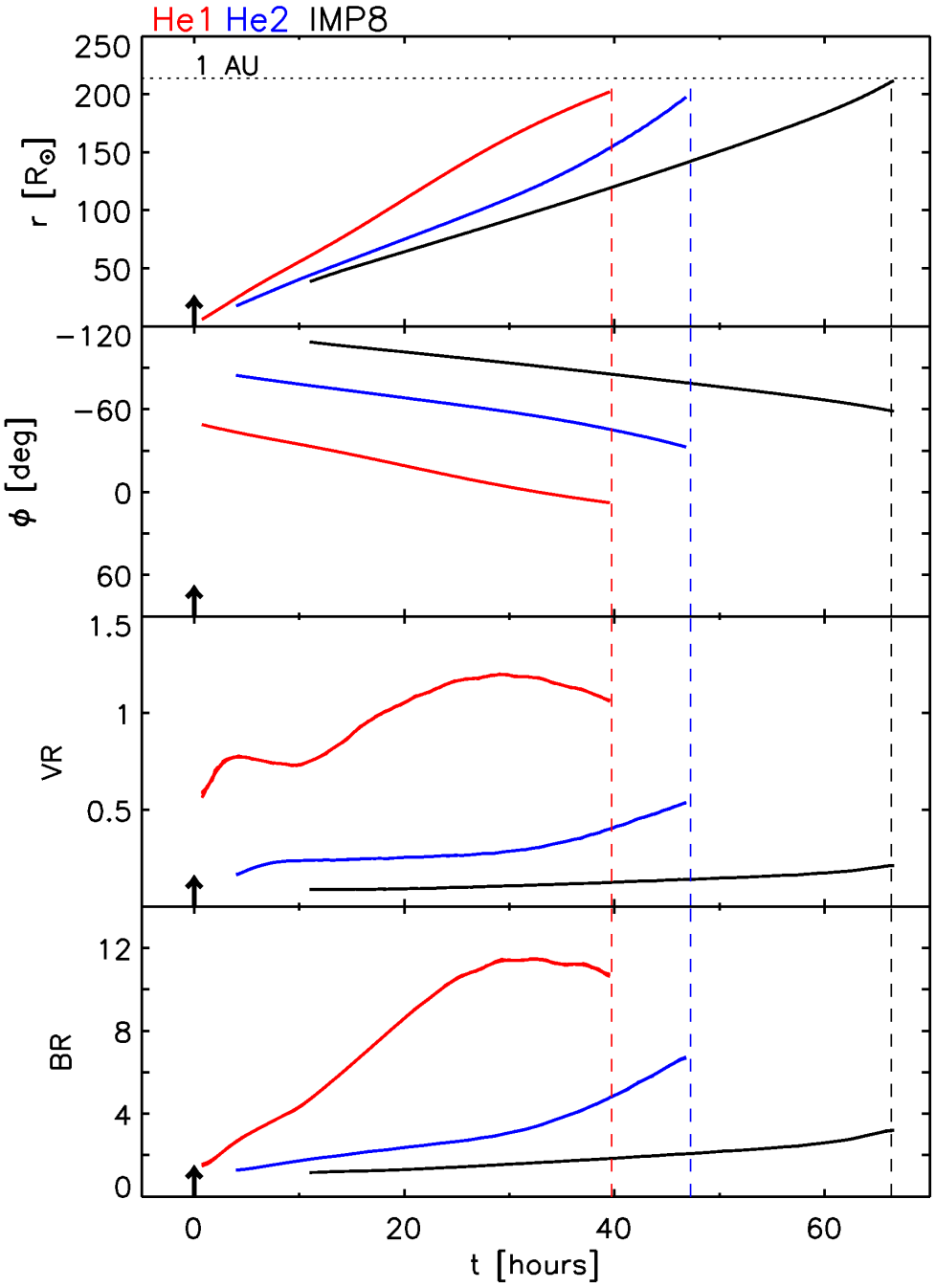

Figure 5.11: From top to bottom: evolution of the radial and angular position of the cobpoint, VR and BR at the cobpoint for the three spacecraft. The vertical arrows indicate the onset of the simulation, the coloured lines the shock arrival time at each spacecraft (as labelled) and the horizontal dotted line marks $r = 1$ AU. $\phi = 0°$ corresponds to the leading direction of the shock (W00).

of the three displayed because of its smaller transit time (Table 5.2). Moreover, this is the first spacecraft to establish the magnetic connection with the shock front (because it is the closest to the solar parent activity longitude): $t_c = 2.25$ hours, at $14.3\,R_\odot$. The further the longitude of the spacecraft, the later the connection; for Helios-2, $t_c = 4.0$ hours, at $17.6\,R_\odot$, whereas for IMP-8 the magnetic connection is established when $t_c = 11.0$ hours, at $38.5\,R_\odot$. The first cobpoint of Helios-1, is located 50° in the left flank of the shock (E50), then it slides counterclockwise toward the nose of the shock (W00) until it reaches the position of the spacecraft (W08) on the right flank of the shock at its passage. The cobpoint of Helios-2 scans from E84 to E32, and that of IMP-8 from E109 to E58; therefore, they remain in the left wing of the shock and do not reach its nose before the shock passage.

As a consequence of the different regions along the shock front scanned by the cobpoints of the three spacecraft, the evolution of their respective VR and BR are quite different. The shapes of VR and BR for Helios-2 and IMP-8 correspond to those expected for an eastern observer (see, for example, Figure 3.4 of Lario 1997): the curves monotonically increase as the cobpoint slides toward the central part of the shock front. Since Helios-2 is nearer in longitude to the main direction of the shock, VR and BR show higher values than those obtained for IMP-8. In the case of Helios-1, the shape of the evolution of BR is similar to that obtained for the 13 December 2006 SEP event[23] (Aran et al. 2010), except for the decrease at the shock arrival and the values of the jump, which are similar to those obtained for the W66 4 April 2000 SEP event[24] (Aran et al. 2011).

As suggested by the observed prompt phase of the high energy protons seen in the particle intensities measured by Helios-1 (Figure 5.6), this particle event would be classified as a well-connected central meridian (W08) event. However, the derived evolution of VR does not follow the profile expected for a typical western well-connected event: a first rapid decrease of VR early in the event, when the shock is close to the Sun and the observer magnetically connects to its nose, and a softer decrease later on, when the cobpoint slides along the right wing of the shock front and the shock is travelling far from the Sun (as in the case of the 13 December 2006 event, Aran et al. 2010). Instead, for Helios-1, we obtain that VR

[23] Flare at W23 in heliolongitude; shock transit speed of $1155\,km\,s^{-1}$

[24] This event runs on top of the same background solar wind as the March 1979 event we study here.

increases with time (except for a period from 4 hours to 10 hours, Figure 5.11), to later decrease when the shock approaches the observer. This behaviour reflects the fact that the observer is connected far in the left wing of the shock front at the beginning of the event. Then, the cobpoint moves toward the nose, passes it and moves shortly along the right wing, where VR starts decreasing again (Figure 5.9). In terms of the shock transit time and heliolongitude of the parent activity, up to now, the modelled event closest to the event seen by Helios-1 is the 13 December 2006 event; but the simulated shock was wide and run on top a fast solar wind. Hence, the results of both simulations do not allow for a direct comparison, because of the different widths of the shocks and because the modelled solar wind conditions are very different when the shock is near the Sun.

We suspect that the reason for this atypical behaviour of the evolution of VR is the early magnetic connection established to the left wing of the shock, that yields the identification of a rather weak shock, precursor of the 'actual' shock that may be seen by the high energy particle component (i.e., the central round part of the simulated disturbance, top left panel of Figure 5.9). The simulation of a narrow shock travelling on a slow solar wind background is a scenario never used before to model a SEP with the SaP10 model, and this unexpected result, not specially significant in terms of the shock propagation modelling, might have consequences as what concerns to particle modelling. In the next section we further investigate this by checking the performance of the finder procedure.

5.4.3 Checking the finder procedure

To determine the cobpoint and the downstream point we have used the automated procedure previously described, which contains several parameters whose values have been fixed after many numerical tests (while keeping in mind the theoretical conditions to characterize an interplanetary shock). The values finally selected are robust in the sense that the shock features and the results obtained by applying this procedure do not vary significantly when different values of these parameters (within a reasonable range) are taken. To illustrate this statement, we will show how v_r-values change at the downstream point (a basic issue to determine VR), from the onset of the event to the shock passage by Helios-1, when several choices are considered.

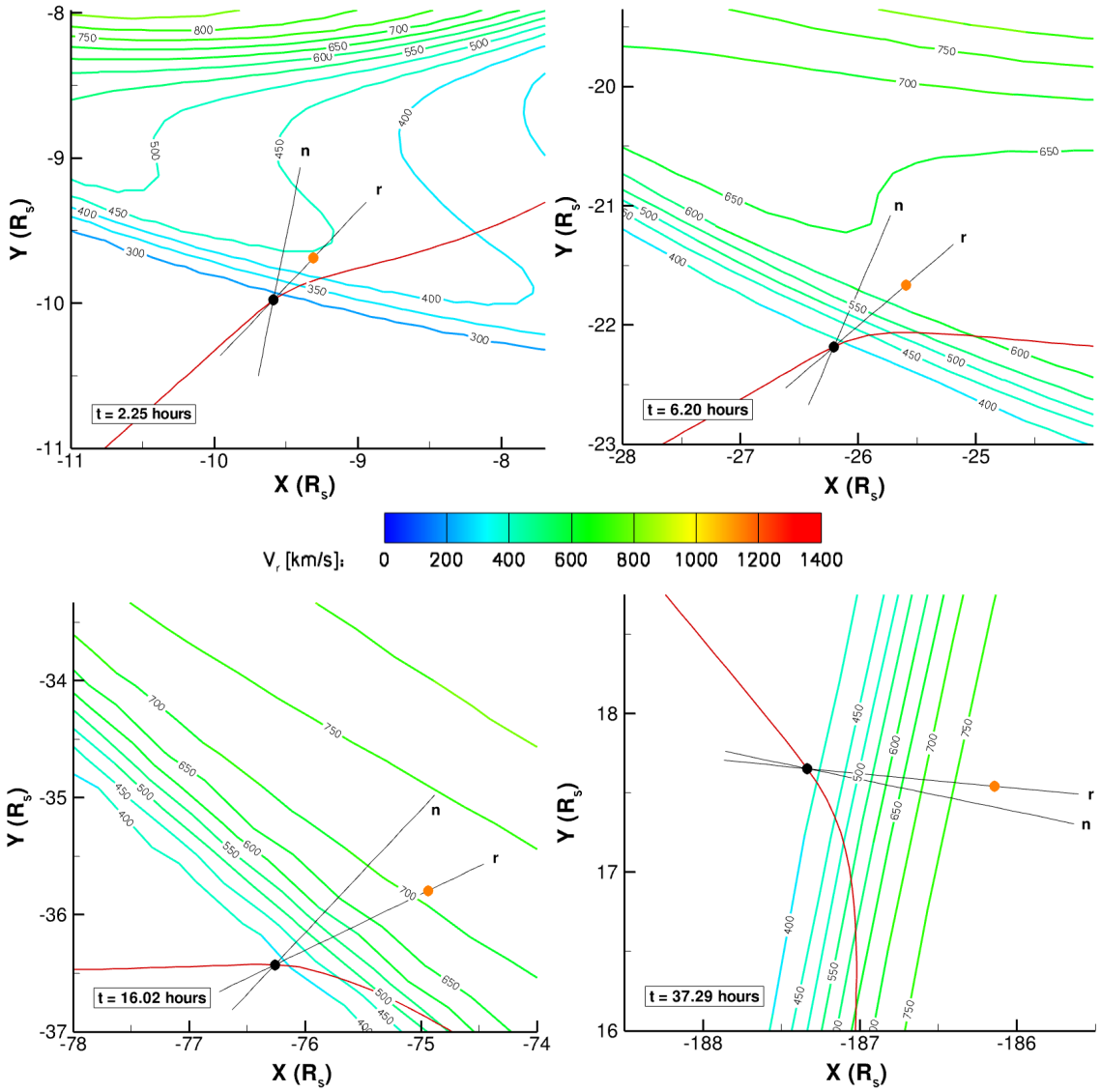

Figure 5.12: Iso-contours of v_r for the same four snapshots as displayed in Figure 5.9. The black and orange circles mark the position of the cobpoint and the downstream for Helios-1. The black lines indicate the radial, r, and normal, n, direction to the shock front at the cobpoint (as labelled), and the red trace the IMF line.

Figure 5.12 displays the iso-contours of v_r for the same four snapshots shown in Figure 5.9, but zoomed in $1\,R_\odot$-resolution around the location of the cobpoint (black) and downstream point (orange) for Helios-1. The red line marks the IMF line passing by the cobpoint position (note the bending of the line in the downstream region). The thin line connecting the cobpoint and the downstream point (labelled as 'r') indicates the radial direction, and the other black line (labelled as

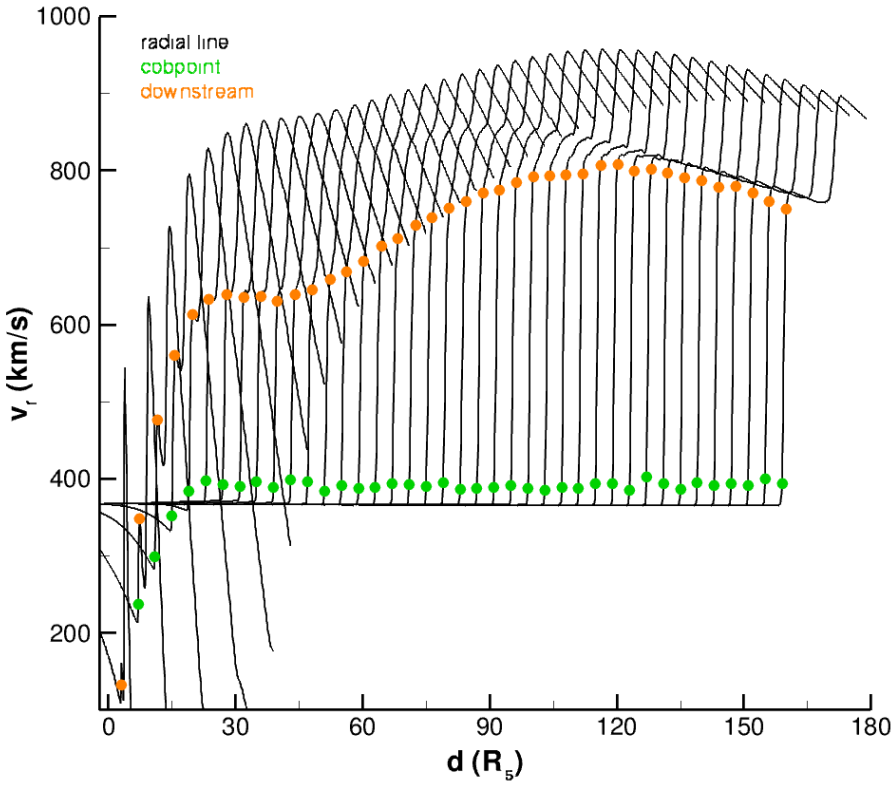

Figure 5.13: Profile of v_r seen by Helios-1 along the radial direction for every four snapshots of the simulation (see text).

'n') the normal direction of the shock front at the cobpoint. As can be seen, the distance between the cobpoint and the downstream point (the 'thickness' of the shock) is $\sim 1.5\,R_\odot$ or smaller. When the shock is still close to the Sun (two top panels), Helios-1's cobpoint is at the wing of the shock[25], far from its nose; there, the shock front is well differentiated from the compressing following driver. Later on, as the cobpoint moves toward the shock nose (left bottom panel), it scans regions where the driver is strongly compressing the sheath region behind the shock front. Thus, we find stronger gradients that imply larger VR-values. When the cobpoint reaches the nose of the shock, VR attains its maximum value, and then it decreases as the cobpoint moves away toward the opposite flank of the shock (bottom right panel[26]).

Figure 5.13 shows how the values of v_r at the cobpoint and at the downstream

[25] It is worth to point out that in the first panel ($t = 2.25$ hours) the background solar wind has not reached the stationary state yet.

[26] Note that in this last panel the radial and normal directions are similar since the cobpoint is near to the nose of the shock.

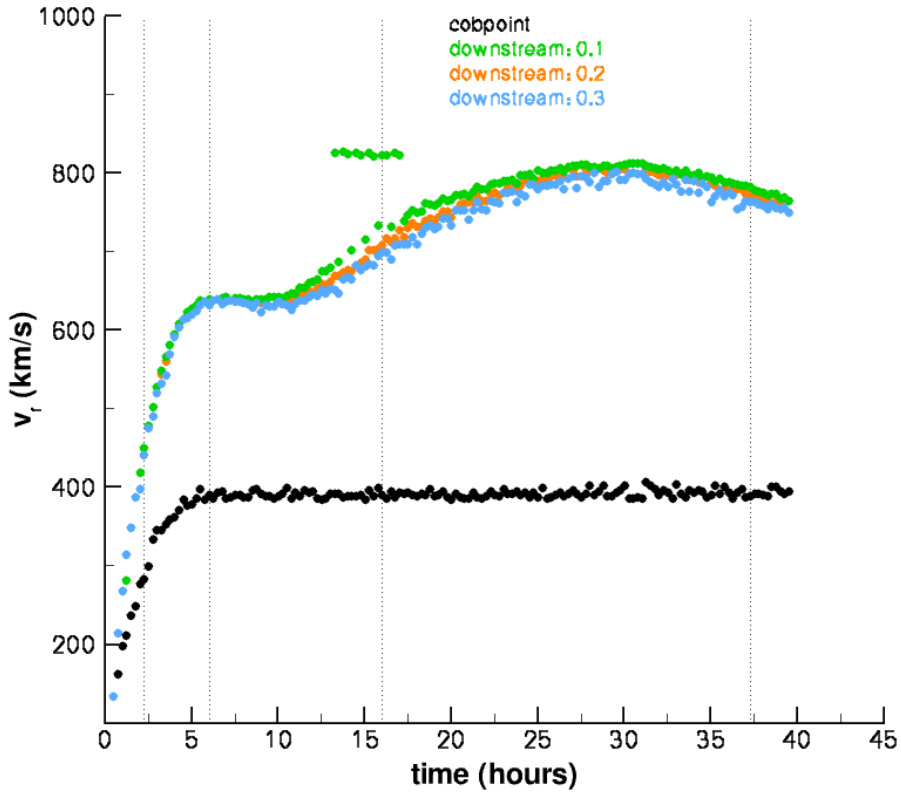

Figure 5.14: Evolution of v_r as seen by Helios-1 when considering different values (as labelled) of the factor used to determine the downstream point. The cobpoint is marked in black and the four dotted lines correspond to the snapshot times presented in Figure 5.12.

point change along the radial line[27], every four snapshots of the simulation (to make the figure clear). Looking at the behaviour of these profiles it seems that the identification of the downstream point is correct (or, at least, coherent). As can be seen, at the onset of the event ($r < 20\,R_\odot$) a local maximum of v_r appears due to the separation between the downstream sheath following the front and the driver. This produces the unexpected behaviour of VR described in Figure 5.11[28].

In the preceding discussion, we have assumed that the factor used to determine the position of the downstream point along the radial direction is 0.2[29]. Figure 5.14

[27] The profile of v_r is given as function of the points that form the radial line, that is: 300 points within $40\,R_\odot$, $20\,R_\odot$ of them ahead of the cobpoint and the other $20\,R_\odot$ behind. So, in the snapshots, the cobpoint is situated at the central position of the line (i.e., $0\,R_\odot$). We have shifted the position of these points according to the respective snapshot number in order to be able to distinguish among the several curves.

[28] Another matter is to understand the origin of this v_r-profile. This relates to the adopted assumptions when modelling the shock or defining the shock finder procedure.

[29] According to Section 5.4.1, this value, 0.2, means that the downstream point is at the position

depicts the evolution of v_r when considering other choices: green for 0.1, orange for 0.2 and blue for 0.3. The black circles mark the location of the cobpoint and the vertical dotted lines indicate the snapshot times reproduced in Figure 5.12. We can see that the trend and values of v_r are maintained regardless of the value for the downstream point location used, with the exception of a few deviations in one case (green). Hence, we conclude that the automated shock finder procedure developed performs well, and that the evolution of VR at the onset of the event for Helios-1 does not seem to be related with the finder procedure.

where the derivatives of the relative variables become smaller than the 20% of the maximum derivative value along the radial line.

Chapter 6

SEP modelling. Results and conclusions

El "sentido" y la "esencia"
no se hallan en algún lugar
tras de las cosas,
sino en ellas mismas, en todo.

Siddhartha, Hermann Hesse

6.1 Introduction

The source term in Equation 2.19 is the injection rate of shock-accelerated particles, Q, that evolves in time and space as the shock expands in the interplanetary medium and the cobpoint scans different regions of the shock front. To derive this injection rate, we have fit the particle intensities observed by Helios-1, Helios-2 and IMP-8, following the procedure described by Lario et al. (1998): we assume that shock-accelerated particles are injected from the cobpoint onto the IMF line that connects the shock front with each spacecraft. The influence of the magnetic field on the particle population during its journey along the IMF lines is modelled by means of a transport equation that considers the effects of streaming, scattering, convection and adiabatic deceleration (Section 2.4.1).

The three basic parameters of the particle transport model are: the injection rate of shock-accelerated particles at the cobpoint, $Q(E,t)$, the mean free path of the protons, $\lambda_{||}$, and the spectral index, γ. To simulate the proton flux profiles we first fit the intensity for a given energy channel, E_0, deriving the evolution of the in-

jection rate, $Q(E_0, t)$, and the value of $\lambda_{||0}$. To fit the remaining energy channels, we assume for Q a power law dependence on the energy, $Q(E,t) = Q(E_0,t)(E/E_0)^{-\gamma}$, being the spectral index γ a free parameter to determine. We also assume that $\lambda_{||} = \lambda_{||0}(R/R_0)^{2-q}$, where R is the rigidity and q the power index of the magnetic field fluctuations spectrum (Equation 2.18) taken as constant.

Table 6.1 summarizes the energy channels (4 for Helios-1 and Helios-2, and 14 for IMP-8) considered for the simulation of this event. The mean value of each energy channel is $< E > = \sqrt{E_1 \cdot E_2}$, with E_1 and E_2 being the minimum and the maximum energy of the channel, respectively, and its relative width is $\Delta_E = (E_2 - E_1)/ < E >$. As can be seen from the last column, the energy channels of IMP-8 are much narrower than those of the Helios spacecraft. The 3.77 - 12.81 MeV-channel ($< E > = 6.95$ MeV) of Helios has a window of 9.04 MeV, while similar energy channels of IMP-8 (the 6.57 MeV, or the following, the 7.92 MeV-channel) have smaller energy windows (< 1.40 MeV). A similar situation appears with the 12.81 - 26.76 MeV-channel, and, to a less extent, with the two higher energy channels of Helios. This fact can have consequences when comparing injection rates deduced from the fits to the observed fluxes for similar energies from different spacecraft. For example, when modelling the flux profiles of the first energy channel of IMP-8 we are implicitly assuming that the 5.96 MeV- and the 7.25 MeV-protons undergo the same kind of scattering processes during its journey in interplanetary space, which is a reasonable approximation. But such assumption is not acceptable for the 3.77 MeV-protons with respect to the 12.81 MeV-protons of the first energy channel of Helios. In fact, when modelling such a wide energy channel, we are forcing the shock to be more efficient at accelerating the high-energy protons of the channel than it really is (see discussion in Aran et al. 2007, when comparing IMP-8 and Phobos-2 energy channels).

6.2 Fitting the proton flux profiles

Figure 6.1 shows the observed proton flux data (black dots) for the four energy channels (from 3.77 MeV to 50.70 MeV; Table 6.1) of Helios-1 (four top panels) and Helios-2 (four bottom panels), in comparison with the flux profiles fitted by using the transport model (red curves), as well as the profile of the computed first-order parallel anisotropies, A_1/A_0. For these spacecraft, the reference energy taken is the

Table 6.1: Energy range, average value and width of each channel of Helios and IMP-8 spacecraft considered for the simulation of 1 March 1979 SEP event.

Spacecraft	E [MeV]	$< E >$ [MeV]	Δ_E
Helios-1 & Helios-2	3.77 - 12.81	6.95	1.30
	12.81 - 26.76	18.51	0.75
	26.76 - 36.63	31.31	0.31
	36.63 - 50.70	43.09	0.32
IMP-8	5.96 - 7.25	6.57	0.19
	7.25 - 8.65	7.92	0.17
	8.65 - 11.10	9.80	0.25
	11.10 - 13.60	12.29	0.20
	13.60 - 16.10	14.80	0.16
	16.10 - 18.70	17.35	0.14
	18.70 - 22.50	20.51	0.18
	19.80 - 24.20	21.88	0.20
	24.20 - 28.70	26.35	0.17
	28.70 - 35.20	31.78	0.20
	35.20 - 42.90	38.86	0.19
	42.90 - 51.00	46.77	0.17
	51.00 - 63.20	56.77	0.21
	63.20 - 81.00	71.54	0.25

average value of the third energy channel, $E_0 = 31.31$ MeV ($R_0 = 244.41$ MV). In the same way, Figures 6.2 and 6.3 show the flux profiles for the fourteen energy channels (from 5.96 MeV to 81.00 MeV) of IMP-8, together with the flux fits and the computed first-order parallel anisotropies. The energy of reference taken for IMP-8 is the average value of the tenth energy channel, $E_0 = 31.78$ MeV ($R_0 = 246.26$ MV).

At low energy (< 12.81 MeV), Helios-1 detects a smooth increase of the particle flux up to the shock arrival, followed by a sudden increase (ESP component) that peaks just after the passage of the shock. Above 12.81 MeV, after a rapid flux increase at the onset of the event, the intensity keeps slightly increasing (plateau on doy 61),and then decreases until the shock arrival. Helios-2 observations show at the beginning of the event a smooth increase of the flux profiles. For $E < 12.81$ MeV, this increase is more rapid and lasts until the shock arrival, whereas at higher en-

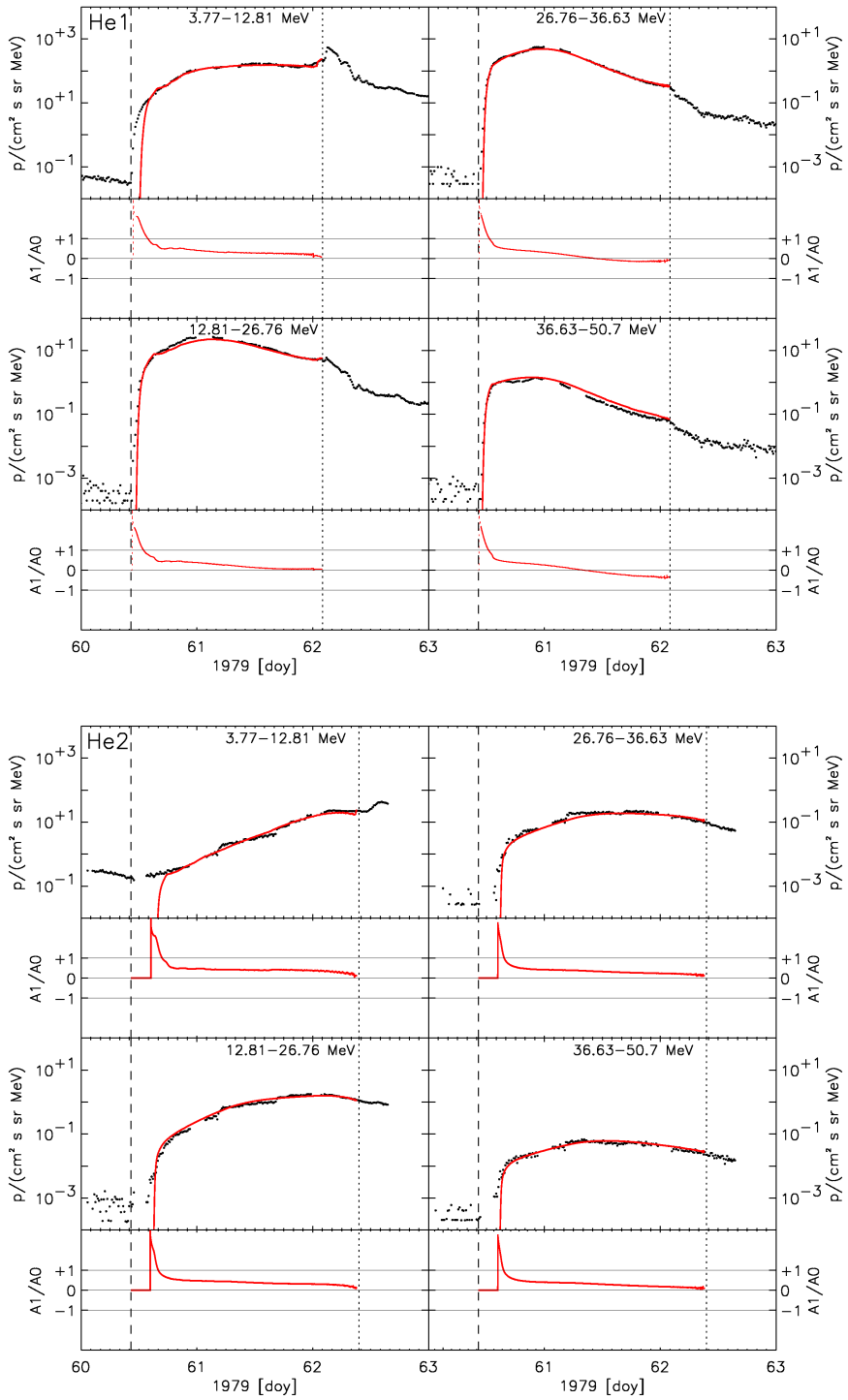

Figure 6.1: Helios-1 (four top panels) and Helios-2 (four bottom panels). Fitting of the proton flux and calculated anisotropy profiles for 4 energy channels (from 3.77 MeV to 50.70 MeV). Black: observations. Red: fits. The dashed line indicates the onset of the event and the dotted line the shock passage.

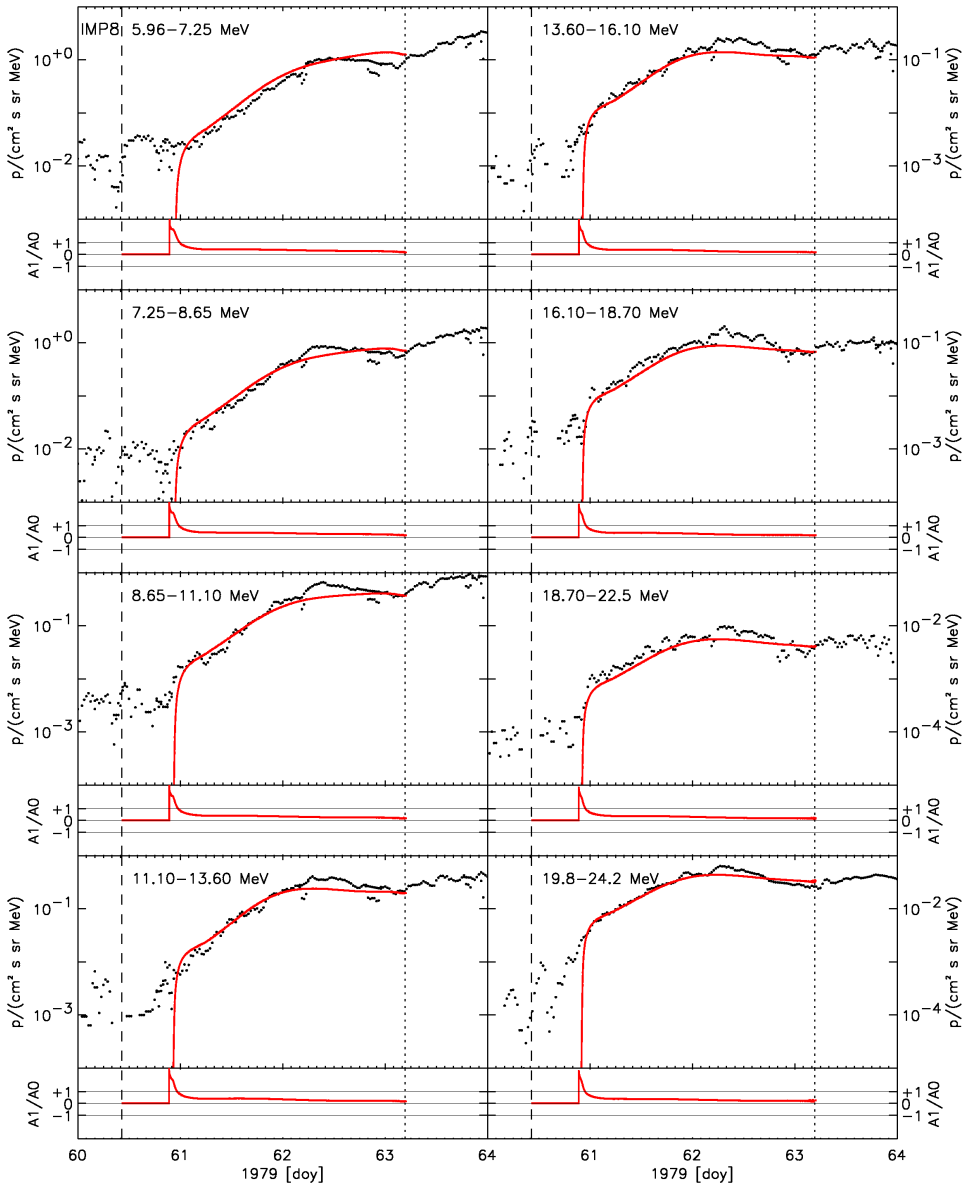

Figure 6.2: IMP-8. Displayed as in Figure 6.1.

ergies the flux profiles start to smoothly decrease prior to the shock arrival. In both cases, the intensities attained at the shock decrease with increasing the proton energy. This behaviour reflects the decrease of the efficiency of the shock as a particle accelerator with increasing energy when the shock is arriving at ~ 1 AU; this is what we quantify after modelling by means of the injection rate of particles, Q.

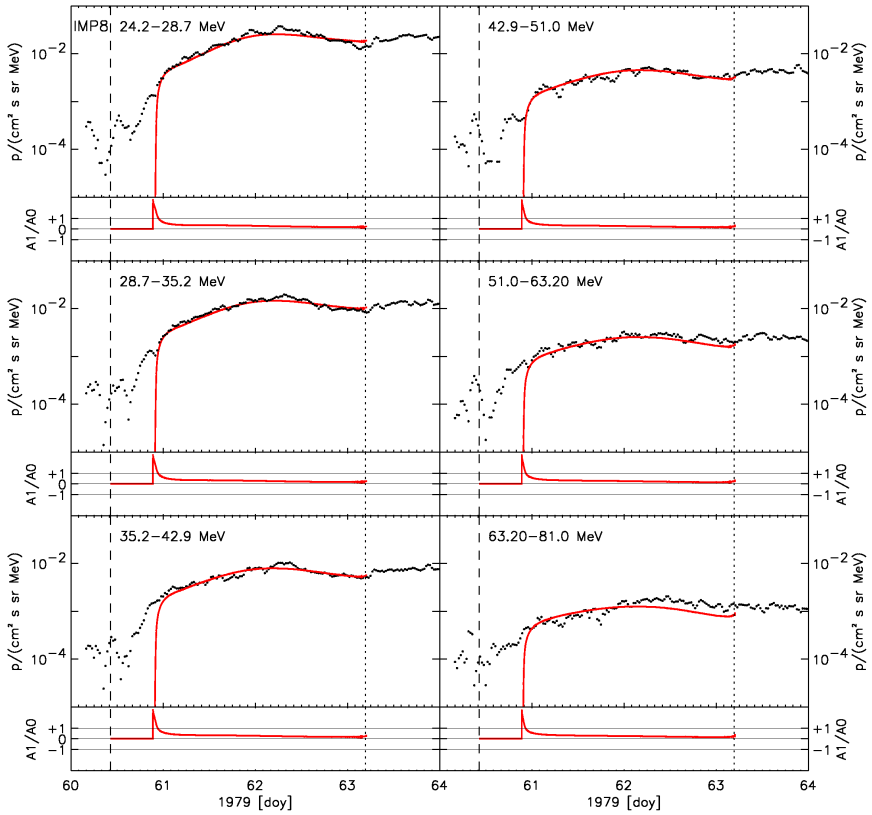

Figure 6.3: IMP-8. Continued of Figure 6.2.

At Helios-1, the onset[1] of the proton intensities occurs about two hours before the connecting time, t_c. To simulate this early energetic particle contribution, we have assumed a Reid-Axford profile, with $\beta = 3$ hours and $\tau = 8$ hours (footnote 2, Chapter 2). This is a useful way to represent an impulsive injection of particles accelerated at the flaring region or at the coronal shock at distances smaller than $4\,R_\odot$; within the context of the SaP10 model we can not discern the exact nature of such contribution because of the inner boundary of the MHD model. The effects of such initial injection are frequently invoked; for example, when defining 'CME/eruptive flares' and to explain the SEP hybrid or two-component events (e.g., Cliver & Cane 1996; Klein & Posner 2005; Cane et al. 2010, and references quoted there).

The flux profiles measured by IMP-8 resemble those ones of Helios-2. For

[1] For both Helios spacecraft, the low energy channels show a background population which makes difficult to precisely determine the onset of the event (see Figures 5.2 and 5.3). For IMP-8, this incertitude extends to energies as high as ~ 20 MeV.

$E < 11$ MeV, they smoothly increase up to the shock passage, and for $E > 11$ MeV the flux profiles show a small decrease just before the passage of the shock. The intensities attained at the shock arrival decrease with increasing the proton energy.

6.2.1 Mean free path and spectral indices

For both Helios spacecraft, the mean free path derived from the fitting of the flux profiles at 31.31 MeV is $\lambda_{\parallel 0} = 0.36$ AU. We assume a turbulent foreshock at low energy (< 19 MeV for Helios-1, and < 7 MeV for Helios-2) to simulate the small flux ramp at the shock passage observed at these energies. This foreshock region is 0.05 AU wide, active after 6.0 hours and characterized by a mean free path $\lambda_{\parallel c} = \lambda_{\parallel c0}(R/R_0)^{0.3}$, with $\lambda_{\parallel c0} = 0.01$ AU. This represents an additional parameter of the model, necessary to simulate the flux (and anisotropy) profiles[2].

The particle injection rate function, G, scales with the energy as a power law, $G(E) \propto E^{-\gamma}$. The values derived for the spectral index γ are the following:
at Helios-1,
– if $E < 13$ MeV: $\gamma = 2.5$ for $t \leq 4$ hours, $\gamma = 3.5$ for $4 < t \leq 16$ hours, $\gamma = 4.7$ for $16 < t \leq 26$ hours and $\gamma = 5.0$ for $t > 26$ hours;
– if $E \geq 13$ MeV: $\gamma = 3.6$ for $t \leq 6$ hours, $\gamma = 5.0$ for $6 < t \leq 16$ hours and $\gamma = 6.0$ for $t > 16$ hours;

and at Helios-2,
– if $E < 13$ MeV: $\gamma = 2.7$ for $t \leq 12$ hours, $\gamma = 3.2$ for $12 \leq t \leq 30$ hours and $\gamma = 4.2$ for $t > 30$ hours;
– if $E \geq 13$ MeV: $\gamma = 2.8$ for $t \leq 12$ hours, $\gamma = 4.0$ for $12 \leq t \leq 30$ hours and $\gamma = 5.0$ for $t > 30$ hours.

For IMP-8, the mean free path derived from the fitting at 31.78 MeV is $\lambda_{\parallel 0} = 0.36$ AU; and the values of γ are:
– if $E < 11$ MeV: $\gamma = 2.3$ for $t < 24$ hours, $\gamma = 3.0$ for $24 \leq t < 44$ hours and $\gamma = 3.6$ for $t \geq 44$ hours;
– if $11 \leq E \leq 32$ MeV: $\gamma = 2.5$ for $t < 24$ hours, $\gamma = 3.5$ for $24 \leq t < 44$ hours and $\gamma = 3.7$ for $t \geq 44$ hours;

[2] Its significance is commented in Section 2.4, and in Beeck & Sanderson (1989) and Heras et al. (1992).

– if $E > 32\,\mathrm{MeV}$: $\gamma = 3.0$ for $\mathrm{t} < 24\,\mathrm{hours}$, $\gamma = 3.6$ for $24 \leq \mathrm{t} < 44\,\mathrm{hours}$ and $\gamma = 3.7$ for $\mathrm{t} \geq 44\,\mathrm{hours}$.

In summary, the spectrum of the injection rate hardens (larger negative γ-values) with time and with increasing energies.

6.2.2 The injection rate Q

Figure 6.4 shows the evolution of Q at the cobpoint for Helios-1, Helios-2 and IMP-8, for the energy channels listed in Table 6.1. These values are derived directly from the transport equation after fitting the corresponding particle fluxes. Time $t = 0$ is the onset of the H_α-flare; then, the first point of each curve is the injection rate derived for the first cobpoint at the connecting time, t_c, as indicated in each panel, and the last point is the value of Q just before the shock passage. The undulating appearance of these curves is as a consequence of the polynomial fit applied to the discrete nature of the initial values of the G function obtained when performing the fits to the flux profiles.

For the same (or similar) energy channels, the injection rate derived for Helios-1 is higher than for Helios-2 and IMP-8, and for Helios-2 is higher than for IMP-8, as expected from the intensities measured by each spacecraft. The evolution of Q in each case results from two factors: (1) the time when the magnetic connection between the spacecraft and the shock front is established. The smaller the longitudinal separation of the footpoint of the IMF line passing through the observer and the nose of the shock, the smaller the time of connection and, hence, the better connection in terms of the strength of the shock. And (2) the region of the shock front scanned by the cobpoint throughout the event. The cobpoint of Helios-1 moves along the shock front from the left wing up to the shock nose, whereas the respective cobpoints of Helios-2 and IMP-8 remain located at the left flank (see Section 5.4.2 and second panel of Figure 5.11).

In the case of Helios-1, the injection rate at high energy ($> 26\,\mathrm{MeV}$) decreases rapidly: two orders of magnitude during the first 8 hours, and it continues decreasing another two orders more up to the shock passage. Thus, there is a strong injection of high energy shock-accelerated particles when the shock is still close to the Sun, followed by a rapid decrease of its effectiveness when the shock expands away toward

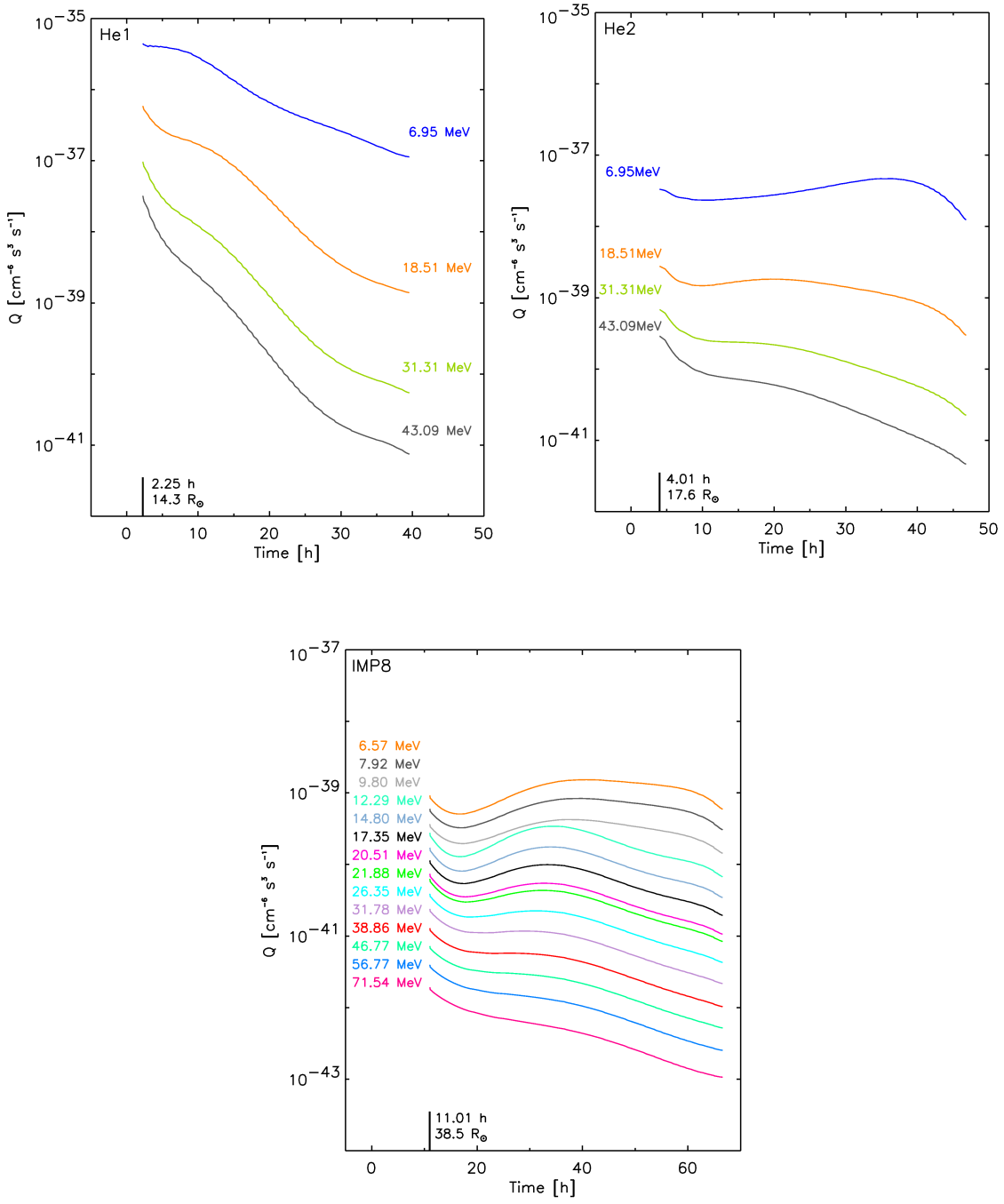

Figure 6.4: Helios-1, Helios-2 and IMP-8. Evolution of Q for the set of energy channels simulated. The thick mark in each panel indicates the connecting time and the radial distance of the first cobpoint.

the observer. The values of Q for Helios-2 and IMP-8 are smaller with respect to those ones for Helios-1, up to $\sim$1.5 orders of magnitude smaller at high energy. In addition, the evolution of Q for these two spacecraft is softer than in the case of Helios-1. The reason is that the left wing of the shock, to which these observers are magnetically connected, is less effective at accelerating particles[3].

To our understanding, the evolution of Q for Helios-1 does not resemble to what it would be expected for a 'normal' central meridian event; instead, it is more similar to that of a western magnetically well-connected event. As commented at the end of Section 5.2, the flux profiles observed by Helios-1 should show a slightly larger connecting time and, specially, a not so abrupt flux increase at the onset of the event. Moreover, the flux profiles measured by Helios-2 resemble more as those corresponding to a western/central meridian event (e.g., W08) than an E32 event. Actually, the evolution of Q for Helios-2 and IMP-8 are also peculiar because, even being an E32 and E58 event (with their first cobpoints at E84 and E109) respectively, they display a rather strong injection of high energy particles at the onset of the event. In short, the derived evolution of the three Q functions displayed in Figure 6.4 just translates the analysis of their flux profiles described in Section 5.2 (i.e., the 1 March 1979 event can not be considered a 'standard' SEP event).

A clue for an explanation to the flux profiles observed by Helios-1 and Helios-2 is the existence of a high background of low-energy (3.77 - 12.81 MeV-channel) protons on doys 58, 59 and 60, prior to the onset of the SEP event (see footnote 1). This seed population filling the magnetic field tubes to be swept by the travelling shock would allow it to accelerate a higher amount of particles and to higher energies than expected. There is strong evidence that such suprathermal population can serve as source material for large SEP events (Mason et al. 1999; Desai et al. 2006). The model of Tylka et al. (2005) assumes acceleration of these suprathermal particles at quasi-perpendicular shocks (for a discussion of the physical process see Desai & Burgess 2008). Cane et al. (2003, 2006), instead, propose another explanation interpreting that these large SEP events can be a mixture of flare- and shock-accelerated populations, and that their relative contribution depends on the properties of the flare, the strength of the shock and the observer's magnetic connection to the flare site.

[3] As it would be expected in the case of a "slower shock".

Both explanations, seed population or flare contribution, could explicate the flux profiles measured during the 1 March 1979 event, keeping in mind the solar-interplanetary scenario depicted in Figure 5.1: Helios-1 is well connected to the flare site, being the reason of the assumed short impulsive initial injection of flare-accelerated particles before t_c, and both Helios flux profiles rise over a large background population. However, we have not explored such possibilities because, even with the present data available, it is difficult to determine the characteristics of the seed particle population and to distinguish between the various acceleration processes occurring at the Sun on the basis of near-Earth data. We could, for example, consider an extended/strong injection of flare-accelerated particles when fitting the flux profiles observed by Helios-1 (taking larger values for the β and τ parameters of the Reid-Axford profile), but we do not have arguments that justify this[4].

On the other hand, we have assumed that the propagation direction of the nose of the interplanetary shock takes place in the direction (longitude) of the flare (Section 5.2), which may be not necessarily true. For example, if the leading edge associated with the CME (in case it existed) driving the shock was moved 20° or 30° counterclockwise with respect to the heliolongitude of the 3N H_α-flare, the flux profiles would be more 'conceptually according' to the scenario. But it seems not to be solar proxy data that gives indications in this (or any other) sense.

Moreover, the presence of a high speed stream (Section 5.2) could modify the local curvature of the IMF lines, and thus, it would change the position of the cobpoint once it had swept Helios-2 and IMP-8; but the difference in the solar wind speed implied within this possible scenario, will not yield to any significant change in the derivation of Q. It could also happen that the magnetic connections between the observers and the shock front near the corona, although consistently modelled within the simulation, were not the actual connections (for example, due to the complex magnetic field structure of the corona); this may be the case since the first cobpoint of Helios-1 is at $\sim 14\,R_\odot$ (top left panel of Figure 6.4), and further away for the other two spacecraft.

[4] Others than to obtain a better evolution of Q.

Another possibility is that the shape of the modelled shock does not reflect its real structure, understanding by 'real structure' not the output of the MHD simulation but what shock-accelerated particles would find or experiment when crossing the front shock. Shock simulations can adequately reproduce the conditions at the shock front, where the shock is strong enough to be well featured, but most probably this is not the case in the far regions of the flanks, where there must be a transition from the shock to the solar wind discontinuity. It is worthwhile to remind that the injection rate Q depends not only on the movement of the cobpoint but also on the MHD conditions for the shock acceleration at this point; problems arise if these conditions are not well defined. Weak shocks or weak flanks of strong shocks do not efficiently accelerated particles; then, how can be quantified a transition from a 'not efficient' to an 'efficient' accelerator? In this SEP event, the first cobpoints are in the eastern flank of the shock; it could occur that the set up conditions for the flanks of the initial perturbation,or even for the solar wind, were not well enough characterized by the approximations considered. These two factors may modify substantially the structure of the CME-driven shock near the Sun, which would affect the efficiency of the shock as particle accelerator, especially at high energy.

Quoting Aran et al. (2007): *"A local pre-existing seed particle population could make the injection rate Q more efficient at the early stages of the shock propagation from a quasi-perpendicular geometry (Tylka et al. 2005)."*. Nevertheless, our shock simulation does not yield a quasi-perpendicular configuration at the first connections because of the narrow wing developed (as can be seen in the top left panel of Figure 5.12). We would like to stress the fact that the MHD simulation performed requires to consider a narrow shock to fit the Helios-1, Helios-2 and IMP-8 plasma and magnetic field observations, which largely constrain the initial parameters of the perturbation. This renders a too early weak connection for Helios-1, and a non-perpendicular geometry at the cobpoint in the eastern flank of the shock, near the Sun. It is worth to mention that the only existing cases of multi-spacecraft events where the shock features can be fitted by three spacecraft (the 24 April 1979 event in Lario et al. 1998, and the one presented here), result in narrow CME-driven shocks, while we usually assume wide shocks within the present paradigm.

6.3 Correlation between Q and VR

Once the evolutions of Q and VR have been derived (Figures 6.4 and 5.11), it is possible to study any correlation between Q and VR of the type given by Equation 2.2. Proceeding in a similar way as described in Section 2.4.2 and applying the same methodological approach as Aran et al. (2011)[5], we have studied the correlation between Q and VR. The modelled solar wind includes the region where it is accelerated; the solar wind speed is increasing during the first $50\,R_\odot$, and beyond $100\,R_\odot$ this speed remains almost constant with increasing the radial distance (see Chapter 2 and 5). Accordingly, the approach of Aran et al. (2011) considers two different regions where to evaluate the potential dependence between Q and VR for each spacecraft: the first region comprises from the moment of the first cobpoint (t_c) up to when the shock front is at $50\,R_\odot$; and the second region extends from $100\,R_\odot$ up to the shock passage by the spacecraft. Both regions are linked through a transition region where the Q(VR) relation is a straight line joining the values at $50\,R_\odot$ with those at $100\,R_\odot$.

The three panels of Figure 6.5 show the correlation between Q and VR derived for Helios-1, Helios-2 and IMP-8. Each point in these panels represents a time step of the numerical integration at which the position of the cobpoint has been calculated; this is, when the particle shock-injection occurs. In the panels of Helios-2 and IMP-8 time runs from left to right, being the first point to the left the time of the first cobpoint, t_c, and the last point to the right the moment of the shock arrival. For Helios-1, this is also true except for the lower part of the curves, after the maximum of VR (reached at the shock nose). The solid lines in Figure 6.5 are the linear fits performed for each energy channel[6]; the dashed lines separate the three regions.

By looking at the correlation between Q and VR for the three spacecraft (dotted traces) two results are deduced: (1) in the case of Helios-1, the correlation between $\log Q$ and VR is not linear either in the first or in the second region. Therefore, we do not expect, in this case, to derive a Q(VR) relation as found in other SEP events. And (2) all Q(VR) relations found will have a negative slope (i.e., a negative value

[5] Aran et al. (2011) study the correlation between Q and VR for the 4 April 2000 SEP event, in the frame of the SEPEM project.

[6] The six fits plotted for IMP-8 correspond to the energy channels more similar to the energy channels of Helios.

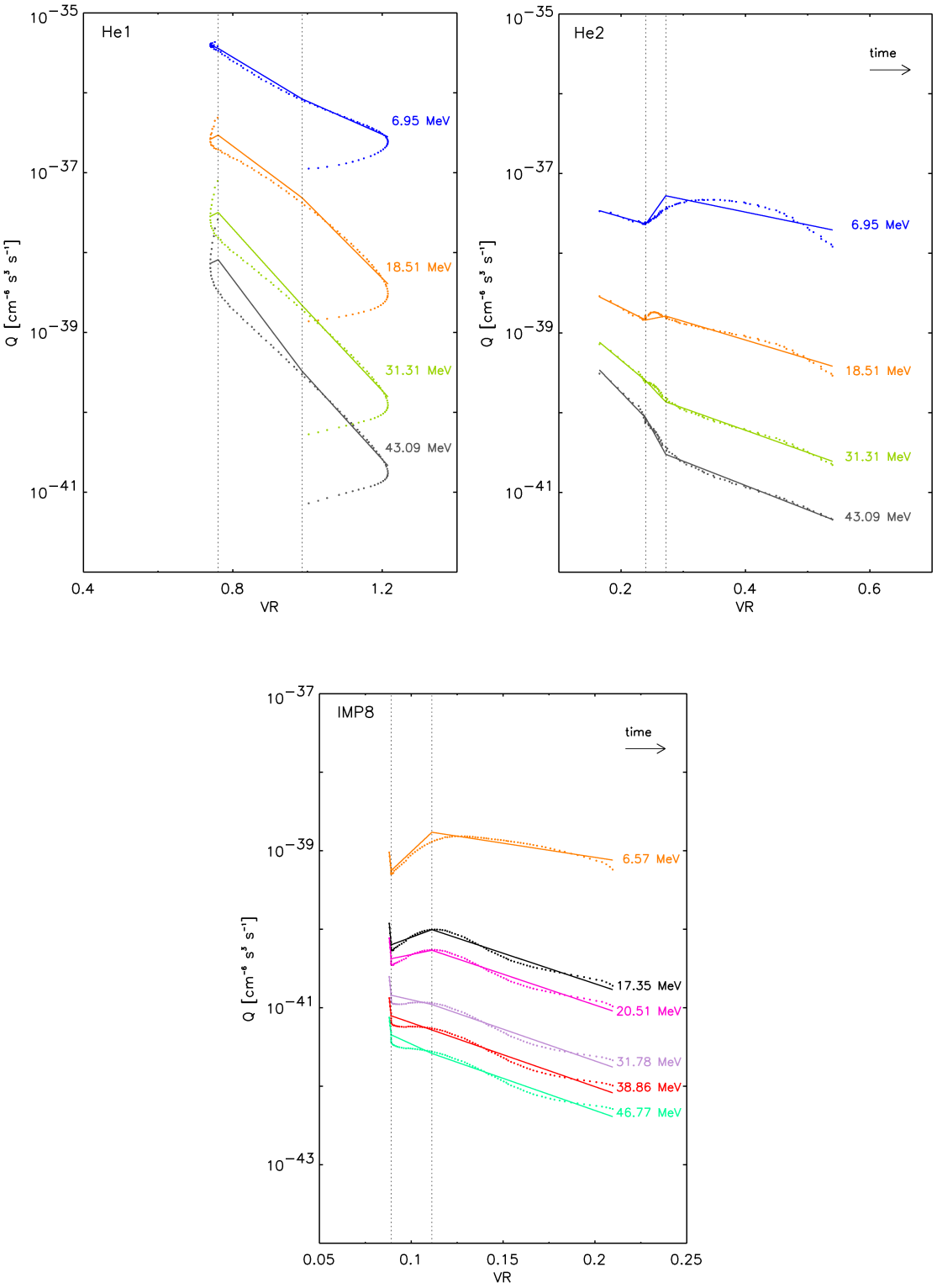

Figure 6.5: Helios-1, Helios-2 and IMP-8. Correlation between Q and VR for the energy channels modelled. For clarity, for IMP-8 only the energy channels similar to those ones of Helios have been plotted.

Table 6.2: Q_0 and k coefficients derived from the linear fits $\log Q$ - VR shown in Figure 6.4. Left values: first region. Right values: second region.

Spacecraft	$< E >$	Q_0	k	Q_0	k
Helios-1	6.95	1.42×10^{-34}	-2.10	9.09×10^{-35}	-2.06
	18.51	3.75×10^{-39}	2.49	2.06×10^{-33}	-4.70
	31.31	5.28×10^{-40}	2.34	1.76×10^{-34}	-4.98
	43.09	1.59×10^{-40}	2.25	3.91×10^{-35}	-5.15
Helios-2	6.95	8.05×10^{-38}	-2.25	1.43×10^{-37}	-1.60
	18.51	1.25×10^{-38}	-3.89	7.10×10^{-39}	-2.35
	31.31	9.10×10^{-39}	-6.49	7.83×10^{-40}	-2.78
	43.09	7.50×10^{-39}	-8.09	2.04×10^{-40}	-3.05
IMP-8	6.57	6.80×10^{-20}	-225.44	4.33×10^{-39}	-3.60
	17.35	4.20×10^{-17}	-267.36	7.23×10^{-40}	-7.76
	20.51	3.19×10^{-18}	-256.78	4.04×10^{-40}	-7.85
	31.78	3.66×10^{-21}	-228.99	8.78×10^{-41}	-8.10
	38.86	3.69×10^{-22}	-220.75	4.20×10^{-41}	-8.14
	46.77	4.43×10^{-23}	-213.13	2.13×10^{-41}	-8.17

($< E >$ [MeV]; Q_0 [$\mathrm{cm^{-6}\,s^3\,s^{-1}}$])

of k). We further discuss these two points below.

The intercept and slope values, Q_0 and k respectively, of the Q(VR) relations shown in Figure 6.5 are listed in Table 6.2: columns 3 and 4 for the first region, and columns 5 and 6 for the second region. To perform the linear fits of Helios-1 we have only considered the values up to the moment that the cobpoint sweeps the shock nose. The values of the regression coefficient, ξ, are higher than 0.95, except for the first energy channel of Helios-2 and IMP-8 in region 2 ($\xi = 0.81$ and $\xi = 0.91$, respectively), and for the four energy channels of Helios-1 in region 1 ($\xi < 0.5$). This poor correlation in the first region of Helios-1 results from the fact that Q rapidly decreases, whereas VR[7] notably oscillates in a narrow range of values ($0.71 < \mathrm{VR} < 0.78$). For Helios-2 and IMP-8, these deviations are much smaller than those for Helios-1; they are due to the wavy shape of Q at low-energy derived from the fit performed (see comments in Section 6.2.2).

[7] For Helios-1, we have adjusted a third degree fit to the VR-curve, in order to skip the small bump that appears (commented in the previous chapter).

In principle, the values derived from these linear regressions have to be applied in the range of values of VR derived, and Q_0 should be understood as the injection rate of shock-accelerated particles assumed when the shock-acceleration processes start (in terms of the shock efficiency; i.e., $\mathrm{VR} \geq 0.09$)[8]. But the correlations found here yield negative values of k, which have no physical sense because the larger the value of VR (i.e., the stronger the shock and hence the more efficient at accelerating particles) the smaller the proton injection rate[9]. This result is mainly as a consequence of the evolution of Q derived from the fitting of the observed flux profiles.

In the case of Helios-1 (top left panel in Figure 6.5), the initial bump and the low values derived for VR within the first ~ 15 hours (Figure 5.11) cause the bended and near-vertical decrease of Q; the final loop is due to the overcome of the cobpoint by the nose of the shock (then, the values of VR start decreasing because the shock is narrow). It would be possible to produce a better fit for the correlation between Q and VR in the transition region, but we prefer to continue by considering the recipe developed by Aran et al. (2011), as the aim is not to use such correlation to produce predictions. For the same reason, we have applied the linear regression to the longer portion of linear-like dependence between Q and VR in the second region, although we may find a linear fit with a positive k in the short interval where the cobpoint has slid past the shock nose. For Helios-2, the fits in both regions are quite good, but k is negative. The same is true for the second region of IMP-8; for this spacecraft, the fits in the first region have a doubtful sense because VR is practically constant and just at the efficiency threshold (i.e., $\mathrm{VR} \approx 0.09$ within this region). The values of Q are always very small as consequence of the weak SEP event observed by IMP-8.

Thus, in which concerns to determine an empirical $Q(\mathrm{VR})$ relation for this multi-spacecraft SEP event, the conclusion is that we can not define it as in previous SEP events. The basic cause is twofold: the flux profiles do not agree with the solar interplanetary scenario resulting from the available solar activity proxy indicators; and the precise fit resulting from the MHD model lead to identify magnetic connections at the shock front near the Sun that, most probably, are not accurate enough

[8] Lario et al. (1998) established the limit of $\mathrm{VR} \geq 0.1$ as the lower limit from which the shock-acceleration is active. We have slightly relaxed this limit to accommodate the whole range of values given by the MHD model for the events studied here.

[9] This result prevents us from doing any forecasting with this event, except as an academic exercise.

(both, because information in this region is scarce and because MHD models for CME-driven shocks should be improved, as discussed in Section 6.2). In addition, it remains as a future task to investigate whether the available Helios sectored data have enough statistics at the studied energies to shed some light on the particle transport conditions and on other particle injections different from the associated shock. We would like to point out that, to determine the range of applicability of the Q(VR) relation, more multi-spacecraft SEP events need to be modelled, and that other dependences of Q on shock characteristics should be further investigated as soon as MHD models allow it.

6.4 Conclusions

We have simulated a multi-spacecraft SEP event by using a new 2D shock-and-particle model, the SaP10 model. The 1 March 1979 SEP event was observed by Helios-1, Helios-2 and IMP-8/ISEE-3 spacecraft. These spacecraft were located at similar radial distances from the Sun, from 0.925 to 0.99 AU, but showing a significant spread in longitude, from E58 to W08. With the new 2D MHD model we are able to simulate the travelling interplanetary shock from $4\,R_\odot$, which in turn allows us to determine the injection rate of shock-accelerated particles from close to the Sun, up to 1.6 AU (in the case that a spacecraft were located at such a distance).

From the simulation of the propagation of the shock, we have been able to reproduce, simultaneously, the time of the shock arrival, the shock transit speed and the most relevant plasma jumps across the shock as observed at the three spacecraft. This is the first case of interplanetary shock modelling using full plasma and magnetic field data from three different spacecraft.

We have developed a new automated procedure to localize the cobpoint and the downstream point, and we have applied it for each snapshot and each spacecraft, determining the shock front and the normal direction to it. We have derived the evolution of VR (and other plasma jumps) at the cobpoint for each spacecraft. We have checked the robustness of the procedure and we have discussed its limitations.

Using the SaP10 model we have simulated the upstream proton intensities observed in 4 energy channels by Helios-1 and Helios-2, and in 14 energy channels by

IMP-8, within the 3.77 - 81 MeV range. The intensities achieved at the shock passage are lower as the proton energy increases, meaning that the efficiency of the shock as particle accelerator decreases with increasing the energy. We have also derived the average transport conditions of the protons from the flux profiles measured by each spacecraft.

We have quantified the efficiency of the shock at injecting particles in its way toward each observer. We have drawn conclusions on the influence of the relative position of the observer (with respect to the main direction of the nose shock) on the determination of the injection rate of shock-accelerated particles, Q. For similar energies, the injection rate derived at Helios-1 is higher than at Helios-2, and this latter one higher than at IMP-8. The rapid decrease of Q derived for Helios-1 implies a strong injection of high energy particles close to the Sun, followed by a rapid decrease of the effectiveness of the shock as it approaches the observer. The injection rate derived for Helios-2 and IMP-8 presents the same trend but with a softer evolution than in the case of Helios-1. This different behaviour reflects the fact that their respective cobpoints scan different regions of the shock front. For Helios-1, the cobpoint scans a region that extends from the left wing up to the shock nose, since it is a W08 event. For Helios-2 and IMP-8 the event is an eastern event (E32 and E38, respectively), with their cobpoints remained along the left flank of the shock. We have interpreted the evolution of Q in terms of the solar-interplanetary scenario depicted, concluding that the 1 March 1979 SEP event can not be considered a typical central meridian (as seen by Helios-1) or eastern (as seen by Helios-2) SEP event.

We have studied the correlation between Q and VR at the three spacecraft. Although the correlation found is high (the regression coefficients are, in general, larger than 0.95), the evolution of Q and VR does not allow us to derive a Q(VR) relation for these spacecraft. This confirms ourselves the necessity to model a much large set of SEP events (multi-spacecraft events, whenever possible) in order to refine such empirical relation.

We have discussed the factors that SaP10 is still not able to take into account and that might play an important role, being the most relevant the existence of a seed particle population, the possible contribution to the flux of flare-accelerated particles, and the shape of the shock when it is still close to the Sun.

Chapter 7

Summary and future perspectives

...I el que facin els altres tant se val, la feina ben feta no té fronteres, ni té rivals.

7.1 Summary

Gradual SEP events is one of the greatest hazards in space environment, particularly for the launch and operation of spacecraft and for manned exploration. Predictions of their occurrence and their intensity are essential to ensure the proper operation of technical and scientific instruments. However, nowadays there is a large gap between observations and models these events that can lead to predictions. This work focuses on the modelling of SEP events, particularly, on the influence of the relative position of the observer and of the shock strength, on the simulated SEP flux profiles. The following paragraphs summarize the main conclusions of this work; the detailed conclusions have been already given in Section 4.6 for Part I and in Section 6.4 for Part II.

Part I of the thesis, '3D modelling of proton gradual events', deals with 3D MHD simulations of interplanetary shocks. We have studied the potential relevance of the latitude of the observer on the evolution of the strength of the shock and its influence on the injection rate of shock-accelerated particles; thus, on the resulting flux profiles. It is the first time that such dependence on the latitude is quantified from the modelling of SEP events, because most of the codes used so far to simulate interplanetary shocks are not 3D codes or they have been applied to near-ecliptic

events.

To study the influence of the latitude of the observer and the strength of the shock in the SEP flux profiles, we have simulated the propagation of two shocks (slow and fast) up to several observers placed at different positions with respect to the nose of the shock. We have calculated the evolution of the plasma and magnetic field variables at the cobpoint, and we have derived the injection rate of shock-accelerated particles and the resulting proton flux profiles to be measured by each observer. We have discussed how observers located at different positions in space measure different SEP profiles, showing that variations on the latitude may result in intensity changes of up to one order of magnitude. Therefore, for space weather purposes the inclusion of the latitude of the observer deserves as much attention as the longitude, when modelling SEP events.

In Part II of the thesis, '2D modelling of proton gradual events: the 1 March 1979 event', we have used the SaP10 to simulate this SEP event that was observed by Helios-1, Helios-2 and IMP-8/ISEE-3. These spacecraft were positioned at similar radial distances but at significantly different angular positions, with respect to the associated solar source location. This particular scenario allows us to test the capability of the shock-and-particle model to study the relevance of longitudinal variations in the shape of the intensity flux profiles, and to derive the injection rate of shock-accelerated particles. Despite the interest of multi-spacecraft events and due to the restrictions that they impose (observations from different points), this is just the second multi-spacecraft scenario for which their shock-particle characteristics have been modelled so far.

For the first time, a simulation of a propagation of an interplanetary shock starting at $4\,R_\odot$ has simultaneously reproduced the time shock arrival and the relevant plasma jumps across the shock at three spacecraft located between 0.95 and 0.99 AU. We have fitted the proton intensities at the three spacecraft for different energy channels, and we have derived the particle transport conditions in space. We have quantified the efficiency of the shock at injecting particles in its way toward each observer, and we have discussed the influence of the relative position of the observer on the injection rate of shock-accelerated particles. We have concluded that in this specific event the evolution of the injection rate can not be completely

explained in terms of the normalized velocity jump.

The work performed during this thesis shows that the injection rate of shock-accelerated particles and their resulting flux profiles depend both on the latitude and on the longitude of the observer. This implies that more SEP events have to be modelled in order to quantify this conclusion on firm ground.

7.2 Future perspectives

As commented along this report, many (if not all!) relevant issues about simulations, CMEs, shocks and particles remain open. A few of them, concerning directly to our interest, are: the development of improved MHD models able to better reproduce the evolution of interplanetary shocks for specific SEP events; the improvement of the algorithms used to determine the location of the front shock and the plasma parameters at the cobpoint; the application of the shock-and-particle model to a large number of SEP events (whenever possible considering multi-spacecraft configurations), both to derive and analyse the evolution of Q, $\lambda_{||}$ and γ under different conditions and scenarios; the study of the variation of the fluence and peak fluxes as a function of the radial, longitudinal and latitudinal (when using 3D models) distances; etc. This wishing list can extend ad infinitum; here, we would like to point out just some topics already mentioned, in which we have started to work or we plan to do so at short term.

• The SREM project and the SPACECAST project

We are collaborating in the 'SREM[1] Solar Particle Event Scientific Analysis' project[2]; its main aim is to produce comparative and optimization studies of the SVD-based[3] unfolding method of SREM data and the creation of an application for automated calculation. Our specific contribution to this project consists in perform-

[1] SREM: Standard Radiation Environment Monitor (http://srem.web.psi.ch). The SREM unit belongs to a programme of instruments established by ESA/ESTEC to provide a minimum intrusive particle radiation detectors on ESA's spacecraft, for particle radiation alerts and other space weather applications. At present, SREM units are flying as piggyback payload on board PROBA-I, INTEGRAL, Rosetta, Herschel, Planck and Giove-B spacecraft.

[2] Leaded by Prof. I. Daglis from the Institute for Space Applications and Remote Sensing (National Observatory Athens, Greece). This project is an extension of ESA/ESTEC Contract no. 21480/08/NL/NR.

[3] SVD: Singular Value Decomposition Technique (Sandberg et al. 2010).

ing direct comparisons of individual SEP events from the SREM database with the synthetic flux profiles generated by using the database of SOLPENCO2, for similar solar-interplanetary scenarios. Therefore, we have to prepare a list of selected SEP events (a subset from the SREM database of events), to choose the identified solar-interplanetary features most adequate as inputs for SOLPENCO2, and finally to use this database to produce the required synthetic flux profiles for comparison. Such comparison will allow us to check the capability of SOLPENCO2 to reproduce SEP events, as well as to identify updates and improvements applicable to the SaP10 model (thus, to SOLPENCO2). It might be also useful for the data production process from SREM units counts.

We will also participate in the modelling of new SEP events, using SaP10, within the frame of the three-years 'SPACECAST'[4] project[5]. The STP/SPW group is responsible for one of its workpackages, whose aim is to model several SEP events to gain insights in the relation between the source term of shock-accelerated particles and the plasma jumps across the shock.

• 2D and 3D simulations of SEP events

We will continue the collaboration (started some years ago) with researchers from the CPA/KUL. With their expertise on 2D and 3D MHD modelling of coronal/interplanetary shocks, it will be possible to better reproduce the initial conditions near the solar corona (using observational data, for example), as well as a more realistic conditions for the CME-initiation mechanism, which would yield a better description of the features of the shock front. The final main aim is to model more SEP fluxes and anisotropies profiles at different energies, in different scenarios, in order to better characterize the evolution and the dependence of Q on VR at the front of the shock, and to check the possibility of extending it to other plasma variables (BR, θ_{Bn}, Mach number, etc.).

On the other hand, last year we started a collaboration with researchers from the State Key Laboratory of Space Weather[6] to simulate the 4 - 6 April 2000 halo-

[4] SPACECAST is a project of the 7th Framework Programme (FP7-Space-2010-1: 'Protecting space assets from high particles by developing European dynamic modelling and forecasting capabilities'). It is leaded by Prof. R. Horne from the British Antarctic Survey (Cambridge, UK).

[5] In collaboration, among others, with researchers from the CPA/KUL.

[6] Center for Space Science and Applied Research, Chinese Academy of Science, Beijing, China.

CME SEP event. They use a 3D MHD code with the asynchronous and parallel time-marching method to simulate CME-driven interplanetary shocks (Shen et al. 2007, 2010). The solar wind background is based on observations of the solar magnetic field and K-coronal brightness; the structures on the source surface can be established with the help of the MHD equations at $2.5\,R_\odot$ according to the global distribution of coronal mass outputs flux (Wei et al. 2003). The CME is simulated by means of a simple flux rope model based on Chané et al. (2008).

In a first round, we worked on the computation of the plasma features at the shock front and we realized that the grid resolution of the MHD code was too coarse to catch them with the required resolution to be used as input for the particle transport code. The next step, and our specific contribution, should be to study the evolution of the plasma conditions at the cobpoint and to calculate the proton flux profiles to be compared with those ones measured by ACE. After that, we will be able to derive conclusions about the role of the latitude after simulating a real SEP event.

• Improving the determination of the shock normal

We would like to evaluate the possibility of improving the automated determination of the shock normal direction at the cobpoint by implementing the Viñas-Scudder method (Viñas & Scudder 1986; Szabo 1994) into the procedure presented in Section 3.3. This is an accurate and fast iterative method to resolve the geometrical properties, propagation velocity and characteristics of shock waves from simple conservation principles. The technique uses the in-situ space magnetic field and plasma measurements, and it is well conditioned and reliable at all θ_{Bn} angles regardless of the shock strength or geometry. The Shock and Discontinuities Analysis Tool, SDAT (Viñas & Holland 2005), is an analysis/visualization tool based in the Viñas-Scudder method which allows an easy and friendly use of this procedure to study shocks and other discontinuities from observations of plasma and magnetic field data. A first approach of its use is shown in Appendix H, for several observers and several snapshots of the 3D fast shock presented in Chapter 3; we have basically checked the concordance between our method to determine the shock normal and those implemented in SDAT.

http://www.spaceweather.ac.cn/english/englishindex.htm

Appendix A

MHD equations, R-H conditions and Mach numbers

A.1 The (ideal) MHD equations

The ideal MHD equations[1] for the conservation of physics quantities relative to the plasma fluid approximation, can be written in conservative form as (Goedbloed & Poedts 2004; Jacobs 2007):

$$\frac{\partial \rho}{\partial t} + \boldsymbol{\nabla} \cdot (\rho \boldsymbol{v}) = 0, \tag{A.1}$$

$$\frac{\partial \rho \boldsymbol{v}}{\partial t} + \boldsymbol{\nabla} \cdot \left[\rho \boldsymbol{v}\boldsymbol{v} + (p + \frac{B^2}{2})\mathbb{I} - \mathbf{B}\mathbf{B} \right] = \rho \mathbf{g}, \tag{A.2}$$

$$\frac{\partial e}{\partial t} + \boldsymbol{\nabla} \cdot \left[(e + p + \frac{B^2}{2})\boldsymbol{v} - (\boldsymbol{v} \cdot \mathbf{B})\mathbf{B} \right] = \rho \boldsymbol{v} \cdot \mathbf{g}, \tag{A.3}$$

$$\frac{\partial \mathbf{B}}{\partial t} + \boldsymbol{\nabla} \cdot [\boldsymbol{v}\mathbf{B} - \mathbf{B}\boldsymbol{v}] = 0, \tag{A.4}$$

where

$$e = \frac{p}{\gamma - 1} + \frac{\rho}{2}\boldsymbol{v}^2 + \frac{\mathbf{B}^2}{2}, \tag{A.5}$$

is the total energy density and $\mathbb{I}$ corresponds to the unity matrix. The meaning of the rest of the symbols is the typical: ρ is the mass density; $\boldsymbol{v}$ denotes the mass-flow velocity vector; $\mathbf{B}$ is the magnetic field vector; T is the temperature; p is the total

[1] For convenience, the constant μ_0 has been dropped. To restore mks units one should make the replacement $\boldsymbol{B} \rightarrow \boldsymbol{B}/\sqrt{\mu_0}$.

gas pressure (accounting for equal electron and proton contributions via Dalton's Law); e is the sum of the internal, kinetic and magnetic energy; and γ the specific heat ratio. Equation A.1 gives the continuity for the conservation of mass, while Equations A.2 - A.4 refer to the momentum, energy-conservation and magnetic field (induction), respectively. The constraint $\boldsymbol{\nabla}\cdot B = 0$ is used in order to obtain the conservative formulation of the momentum equation.

A.2 Rankine-Hugoniot conditions in MHD shocks

An interplanetary shock is characterized by a sudden variation of the typical variables characterizing a plasma (Kallenrode 2004). Conservation laws establish the relationship between the two sets of variables characterizing the plasma in the upstream and downstream region of the shock. The Rankine-Hugoniot (R-H) conditions is a set of six equations for ρ, υ_n, $\boldsymbol{\upsilon_t}$, p, B_n and $\boldsymbol{B_t}$, that describes the conservation of mass, momentum and energy through the shock front. These equations are applied to simple shocks in space plasmas, when the distribution functions are isotropic and Maxwellian, and the IMF is roughly parallel to the flow; the shock is assumed to be an infinitesimally thin[2] discontinuity.

If $[[A]] = A_u - A_d$ is the difference of a quantity A in the upstream and downstream media, $\hat{\mathbf{n}}$ the unit vector along the shock normal and taking the fluid velocities refered to the shock frame, the R-H relations are (Goedbloed & Poedts 2004):

– mass,

$$[[\rho\upsilon_n]] = 0 \tag{A.6}$$

– normal momentum,

$$[[\rho\upsilon_n^2 + p + \frac{1}{2}B_t^2]] = 0 \tag{A.7}$$

– tangential momentum,

$$\rho\upsilon_n[[\boldsymbol{\upsilon_t}]] = B_n[[\mathbf{B_t}]] \tag{A.8}$$

– energy,

$$\rho\upsilon_n\left[\left[\frac{1}{2}\left(\upsilon_n^2 + \upsilon_t^2\right) + \frac{1}{\rho}\left(\frac{\gamma}{\gamma-1}p + B_t^2\right)\right]\right] = B_n[[\boldsymbol{\upsilon_t}\cdot\mathbf{B_t}]] \tag{A.9}$$

[2] In MHD, a boundary is considered thin with respect to the scale length of the fluid parameters but thick with respect to the Debye length and the ion gyro-radius (Goossens 2003).

– normal flux,

$$[[B_n]] = 0 \tag{A.10}$$

– tangential flux,

$$\rho v_n \left[\left[\frac{\mathbf{B_t}}{\rho}\right]\right] = B_n[[\boldsymbol{v_t}]]. \tag{A.11}$$

This set of equations, hence, allows the calculation of the downstream plasma parameters from the knowledge of the upstream parameters of a MHD shock.

A.3 Mach numbers

The characteristic speeds of the MHD waves are defined as:

– fast speed,

$$v_f^2 = \frac{1}{2}[c_s^2 + v_A^2 + \{(c_s^2 + v_A^2)^2 - 4\, c_s^2\, v_A^2\, \cos^2\theta_{Bn}\}^{\frac{1}{2}}] \tag{A.12}$$

– Alfvén speed (in the normal direction),

$$v_{A_n}^2 = v_A^2 \cos^2\theta_{Bn} \tag{A.13}$$

– slow speed,

$$v_s^2 = \frac{1}{2}[c_s^2 + v_A^2 - \{(c_s^2 + v_A^2)^2 - 4\, c_s^2\, v_A^2\, \cos^2\theta_{Bn}\}^{\frac{1}{2}}], \tag{A.14}$$

where θ_{Bn} is the angle between the upstream magnetic field, B_u, and the shock normal, $\hat{\mathbf{n}}$; v_A is the Alfvén speed; and c_s is the sound speed[3] (Kallenrode 2004).

Being $v_{b_n} = v_n - v_{sh}$ the normal bulk speed in the shock frame reference, with v_n the speed along the normal direction and v_{sh} the shock speed, three different types of Mach numbers can be defined[4]:

[3] Alfvén speed: $v_A = \dfrac{B}{\sqrt{\rho}}$; sound speed: $c_s = \sqrt{\dfrac{\gamma\, p}{\rho}}$.

[4] See, for example, Bazer & Ericson (1959); Wu et al. (1996a,b); Vourlidas et al. (2003), and other references quoted there.

– fast Mach number,

$$M_f = \frac{v_{b_n}}{v_f} \tag{A.15}$$

– Alfvén Mach number,

$$M_A = \frac{v_{b_n}}{v_{A_n}} \tag{A.16}$$

– slow Mach number,

$$M_s = \frac{v_{b_n}}{v_s}. \tag{A.17}$$

Appendix B

Calibration factor

This appendix is based on Appendix D of Lario (1997) and on Section A1 of Appendix A of Aran (2007). The transport model gives the particles distribution function along the flux tube and integrated for all the pitch angle cosines. That is, for a given time t, radial distance r and momentum p,

$$F(t,r,p) = \int_{-1}^{+1} F(t,r,\mu,p)\, d\mu. \tag{B-1}$$

This axisymmetric distribution function is related to the distribution function in the phase space, $f(t,r,\mu,p)$, by

$$F(t,r,p) = A(r)\, f(t,r,\mu,p), \tag{B-2}$$

where $A(r)$ is the flux tube section at the distance r and it is calculated assuming that the magnetic field follows a Parker spiral with a constant solar wind radial speed.

The differential omnidirectional intensity of the particles, $I(t,r,p)$, is given by

$$I(t,r,p) = \frac{1}{2}\int_{-1}^{+1} f(t,r,\mu,p)\, d\mu, \tag{B-3}$$

and hence,

$$F(t,r,p) = 2\, A(r)\, I(t,r,p). \tag{B-4}$$

But the observable is the differential flux intensity, $J(t,r,p)$, which is related to

the omnidirectional intensity by

$$J(t, r, p) = p^2\, I(t, r, p), \tag{B-5}$$

and so, in terms of the transport code outputs,

$$J(t, r, p) \;=\; \frac{p^2}{2\, A(r)}\, F(t, r, p). \tag{B-6}$$

B.1. Calibrating $J(t, r, p)$

Since the model proportionates $F(t, r, p)$ in arbitrary units, it is necessary to convert it into differential flux with physical units to be able to compare the results of the model with the observations. Being $J^{arbi}(t, r, p)$[1] the differential flux in arbitrary units derived from the transport model at an observer position r, for a given momentum p and time t, the transformation can be done by

$$J^{phys}(t, r, p) = \frac{J^{obs}(t_0, r_0, p_0)}{J^{arbi}(t_0, r_0, p_0)}\, J^{arbi}(t, r, p), \tag{B-7}$$

where $J^{obs}(t_0, r_0, p_0)$ is the value of the observed flux at t_0, r_0 and p_0, and $J^{arbi}(t_0, r_0, p_0)$ is the differential flux derived from the model at the same point (t_0,r_0,p_0). The time t_0 is taken where the observed flux profile is approximately constant during a reasonable time interval, in order to ensure that the particles intensity does not vary sharply.

Using Equation B-6 we have

$$J^{phys}(t, r, p) = \frac{J^{obs}(t_0, r_0, p_0)}{\dfrac{p_0^2}{2\, A(r_0)}\, F^{arbi}(t_0, r_0, p_0)}\, \frac{p^2}{2\, A(r)}\, F^{arbi}(t, r, p), \tag{B-8}$$

and, hence, the expression of the normalization constant reads as

$$K = \frac{J^{obs}(t_0, r_0, p_0)}{\dfrac{p_0^2}{2\, A(r_0)}\, F^{arbi}(t_0, r_0, p_0)}, \tag{B-9}$$

[1] The super-index *phys* indicates physical units whereas *arbi* indicates arbitrary units.

where we assume that K is constant $\forall\, t, r$ and p. In this equation, $A(r_0)$ is the transverse section of the flux tube at the distance r_0 where we obtain the omnidirectional distribution function $F^{arbi}(t_0, r_0, p_0)$; p_0 is the proton moment of the reference energy channel with main energy E_0; and t_0 and r_0 are, respectively, the reference time and distance where the observed differential flux, $J^{obs}(t_0, r_0, p_0)$, and the value of $F^{arbi}(t_0, r_0, p_0)$ are compared to convert from arbitrary magnitudes to physical ones. So, we can define a scale factor:

$$S = \frac{J^{obs}(t_0, r_0, p_0)}{F^{arbi}(t_0, r_0, p_0)}. \tag{B-10}$$

This way, we can write the Equation B-9 as

$$K = S\,\frac{2\,A(r_0)}{p_0^2}, \tag{B-11}$$

and, hence, we have

$$J^{phys}(t, r, p) = K\,\frac{p^2}{2\,A(r)}\,F^{arbi}(t, r, p), \tag{B-12}$$

or, shortly,

$$J^{phys}(t, r, p) = K\,J^{arbi}(t, r, p). \tag{B-13}$$

B.2. Fitting flux profiles at r_1 from fits at r_0

If we want to obtain proton differential flux profiles at a given radial distance r_1 from the fit of proton differential flux profiles derived from the same event (i.e., accelerated and injected by the same interplanetary shock) at a distance r_0, the procedure to be applied is the following:

1. Fitting, with the transport model, the proton differential flux[2] profile observed at r_0. From the fit we can get the calibration constant K (Equation B-9).

2. From the fit of the event at r_0 we obtain the axisymmetric injection rate[3] $G(t, r_0, p)$

[2] Here the common name 'flux' used is an abuse of language since what it is usually fitted is the differential intensity of the particles integrated for all pitch angles cosines, μ, instead of $\int_{-1}^{+1} \mu\, F(t, r, \mu, p)\, d\mu$.

[3] In fact, the model gives $G(t, r, \mu, p)$ as a development of orthogonal Legendre polynomials, P_μ

in arbitrary units. Then,

$$G(t, r_0, p) \;=\; K\, G^{arbi}(t, r_0, p). \tag{B-16}$$

As $Q(t, r, p) \;=\; \dfrac{G(t, r, p)}{A(r)}$ (Equation 2.20), from Equation B-16 we can calculate the injection rate of shock accelerated protons at the cobpoint position, $Q(t, r_{0c}, p)$, where $r_{0c} \equiv r_{0c}(t)$; and, then, the injection rate at each energy channel i is given by

$$Q(t, r_{0c}, p_i) = \frac{K}{A(r_{0c})}\, G^{arbi}(t, r_{0c}, p_i). \tag{B-17}$$

3. Once the injection rate at each energy channel i, $Q(t, r_{0c}, p_i)$, is known, we can calculate the Q(VR) relation for each energy channel of the detector. So,

$$\log\, Q(t, r_{0c}, p_i) = \log\, Q_0(p_i) \;+\; k(p_i)\, \mathrm{VR}(t, r_{0c}). \tag{B-18}$$

Thus, from the i-Equations B-18 we can derive the values at r_1 taking into account that:

- It can happen that the detector at r_1 has different energy channels, identified here as p_j. Then, $Q_0(p_j)$ can be calculated from the fit of $Q_0(p_i) \;=\; C\, E_i^{-\gamma}$.

- For a specific channel p_j we assume that $k(p_j) \;=\; k(p_i)$, where p_i is the energy channel closer to p_j.

- The values of $\mathrm{VR}(t, r_{1c})$ must be derived from the shock simulation, since the position of the cobpoint of the detector at r_1 is now $r_{1c} \equiv r_{1c}(t)$.

Then, the injection rate $Q(t, r_{1c}, p_j)$ will be:

$$\log\, Q(t, r_{1c}, p_j) = \log\, Q_0(p_j) \;+\; k(p_j)\, \mathrm{VR}(t, r_{1c}). \tag{B-19}$$

(up to the fifth order), and with a dependence on the energy that follows a potential law with p:

$$G(t, r, \mu, p) = (G_0 + G_1\mu + G_2\frac{1}{2}(2\mu^2 - 1) + ...)\, \left(\frac{p}{p_0}\right)^{-\gamma}, \tag{B-14}$$

where γ often takes a pair of different values according to the time interval; this way, G can be expressed by using two or three different gamma indices. In all cases, $G_0 = G_0(t, r)$, where their values are derived when fitting the reference channel. Then,

$$G^{arbi}(t, r, p) = \frac{1}{2} \int_{-1}^{+1} G(t, r, \mu, p)\, d\mu = G_0(t, r)\, \left(\frac{p}{p_0}\right)^{-\gamma}. \tag{B-15}$$

4. Once we know $Q(t, r_{1c}, p_j)$, we must calculate the value of G^{arbi} to introduce it to the transport model and calculate the proton intensity profiles at r_1. In this way, for each j-Equations B-19 we have that the injection rate along the flux tube is given by

$$G^{arbi}(t, r_{1c}, p_j) = Q(t, r_{1c}, p_j)\,\frac{A(r_{1c})}{K}, \tag{B-20}$$

where the constant that translates from physical units to arbitrary units is the one obtained from the fit at r_0.

5. Then, when running the transport model, we get the values of $F^{arbi}(t, r_1, p_j)$. To compare them with the measures of the differential flux at r_1 we must apply Equation B-13, with K defined by Equation B-9.

All this procedure implicitly assumes that: (1) K keeps constant, i.e., it does not depend on the solar wind velocity (which may vary at different latitudes or very close to the Sun); and (2) the factor scale, S, does not depend on the position of the spacecraft. This latter point can be a source of error due to intrinsic (as the absorbent boundary) or extrinsic factors (as the calibration of the instruments of measure).

B.3. SOLPENCO case

In SOLPENCO, the calibration constant, K, depends on the particle energy since the scale factor, S, was taken constant. That is,

$$K(p) = S\,\frac{2\,A(r_0)}{p^2}. \tag{B-21}$$

Hence, the flux in physical units at a given radial distance r_0 is obtained as

$$J^{phys}(t, r_0, p) = K(p)\,\frac{p^2}{2\,A(r_0)}\,F^{arbi}(t, r_0, p) = S\,F^{arbi}(t, r_0, p); \tag{B-22}$$

and at any other radial distance r_1 as

$$J^{phys}(t, r_1, p) = K(p)\,\frac{p^2}{2\,A\,(r_1)}\,F^{arbi}(t, r_1, p) = S\,\frac{A(r_0)}{A(r_1)}\,F^{arbi}(t, r_1, p). \tag{B-23}$$

Appendix C

Trilinear interpolation

Trilinear interpolation is a method of multivariate interpolation on a 3D regular grid of discretely sampled data. It approximates the value of an intermediate point (x, y, z) within the local axial rectangular prism linearly, using data on the lattice points.

Starting with bilinear interpolation (an extension of linear interpolation) for interpolating functions of two variables on a bidimensional regular grid, the key idea is to perform linear interpolation first in one direction, and then in the other direction. To find the value of the unknown function f at the point $P = (x, y)$, where $x_1 < x < x_2$ and $y_1 < y < y_2$, it is necessary to know the value of f at the four surrounding points: $Q11 = (x_1, y_1)$, $Q12 = (x_1, y_2)$, $Q21 = (x_2, y_1)$, and $Q22 = (x_2, y_2)$. Then, linear interpolation in the X-direction yields

$$f(R_1) \approx \frac{x_2 - x}{x_2 - x_1} f(Q_{11}) + \frac{x - x_1}{x_2 - x_1} f(Q_{21}) \quad \text{where} \quad R_1 = (x, y_1), \tag{C-1}$$

$$f(R_2) \approx \frac{x_2 - x}{x_2 - x_1} f(Q_{12}) + \frac{x - x_1}{x_2 - x_1} f(Q_{22}) \quad \text{where} \quad R_2 = (x, y_2). \tag{C-2}$$

And the interpolation in the Y-direction,

$$f(P) \approx \frac{y_2 - y}{y_2 - y_1} f(R_1) + \frac{y - y_1}{y_2 - y_1} f(R_2), \tag{C-3}$$

gives the desired estimate of $f(x, y)$

$$\begin{aligned} f(x,y) \approx & \frac{f(Q_{11})}{(x_2-x_1)(y_2-y_1)}(x_2-x)(y_2-y) \\ & + \frac{f(Q_{21})}{(x_2-x_1)(y_2-y_1)}(x-x_1)(y_2-y) \\ & + \frac{f(Q_{12})}{(x_2-x_1)(y_2-y_1)}(x_2-x)(y-y_1) \\ & + \frac{f(Q_{22})}{(x_2-x_1)(y_2-y_1)}(x-x_1)(y-y_1) \end{aligned} \tag{C-4}$$

The result of bilinear interpolation is independent of the order of interpolation: if performing first the linear interpolation in the Y-direction and then in the X-direction, the resulting approximation would be equivalent (to first order).

To perform a trilinear interpolation the 8 adjacent pre-defined values surrounding the interpolation point are required. That is, it is necessary to know the value of f at the eight surrounding points: $Q111 = (x_1, y_1, z_1)$, $Q211 = (x_2, y_1, z_1)$, $Q121 = (x_1, y_2, z_1)$, $Q221 = (x_2, y_2, z_1)$, $Q112 = (x_1, y_1, z_2)$, $Q212 = (x_2, y_2, z_2)$, $Q112 = (x_1, y_1, z_2)$ and $Q222 = (x_2, y_2, z_2)$, where $x_1 < x < x_2$, $y_1 < y < y_2$ and $z_1 < z < z_2$. Proceeding in a similar way as for the bilinear interpolation case, it is finally obtained

$$\begin{aligned} f(x,y) \approx & \frac{f(Q_{111})}{(x_2-x_1)(y_2-y_1)(z_2-z_1)}(x_2-x)(y_2-y)(z_2-z) \\ & + \frac{f(Q_{211})}{(x_2-x_1)(y_2-y_1)(z_2-z_1)}(x-x_1)(y_2-y)(z_2-z) \\ & + \frac{f(Q_{121})}{(x_2-x_1)(y_2-y_1)(z_2-z_1)}(x_2-x)(y-y_1)(z_2-z) \\ & + \frac{f(Q_{221})}{(x_2-x_1)(y_2-y_1)(z_2-z_1)}(x-x_1)(y-y_1)(z_2-z) \\ & + \frac{f(Q_{112})}{(x_2-x_1)(y_2-y_1)(z_2-z_1)}(x_2-x)(y_2-y)(z-z_1) \\ & + \frac{f(Q_{212})}{(x_2-x_1)(y_2-y_1)(z_2-z_1)}(x-x_1)(y_2-y)(z-z_1) \\ & + \frac{f(Q_{122})}{(x_2-x_1)(y_2-y_1)(z_2-z_1)}(x_2-x)(y-y_1)(z-z_1) \\ & + \frac{f(Q_{222})}{(x_2-x_1)(y_2-y_1)(z_2-z_1)}(x-x_1)(y-y_1)(z-z_1) \end{aligned} \tag{C-5}$$

Appendix D

Testing the procedure

• IMF lines

To ensure the goodness of the IMF lines computation, we compared the IMF lines calculated by using the procedure presented in Section 3.3 with the streamlines derived from the magnetic field vector by means of the visualization software Tecplot and the lines calculated by applying the theoretical formula given by Parker (1958):

$$\varphi = \varphi_0 + \omega \, \frac{(r - r_0)}{v_{sw}}, \tag{G-1}$$

where r_0 and φ_0 are the radial and longitudinal positions of a given point in space (e.g, that of the observer). Figure D.1 depicts an example of such comparison. The plots show three views of the computed IMF lines (XY, XZ and YZ planes). As can be seen, the three lines practically coincide.

• First magnetic connection point

We checked the procedure to compute the cobpoint when this point can be identified with coronal footpoint of the IMF line connecting with the observer (this is, without considering any shock). We compare the results derived by applying the backmapping technique (Nolte & Roelof 1973). This method starts at the location of the spacecraft and uses the measured solar wind speed to calculate the archimedian spiral back to the Sun[1]. Table D.1 presents the values of the first magnetic connec-

[1] To extrapolate from the critical coronal transition point back to the surface of the Sun, Nolte & Roelof (1973) assumes that the solar wind flows radially with a constant velocity. They find that, for $v_{sw} = 400\,\mathrm{km\,s^{-1}}$ and $r = 1.0\,\mathrm{AU}$, the uncertainty in this method is $\sim 10°$. This error may result from the deviation of the IMF line from the fiducial archimedian spiral.

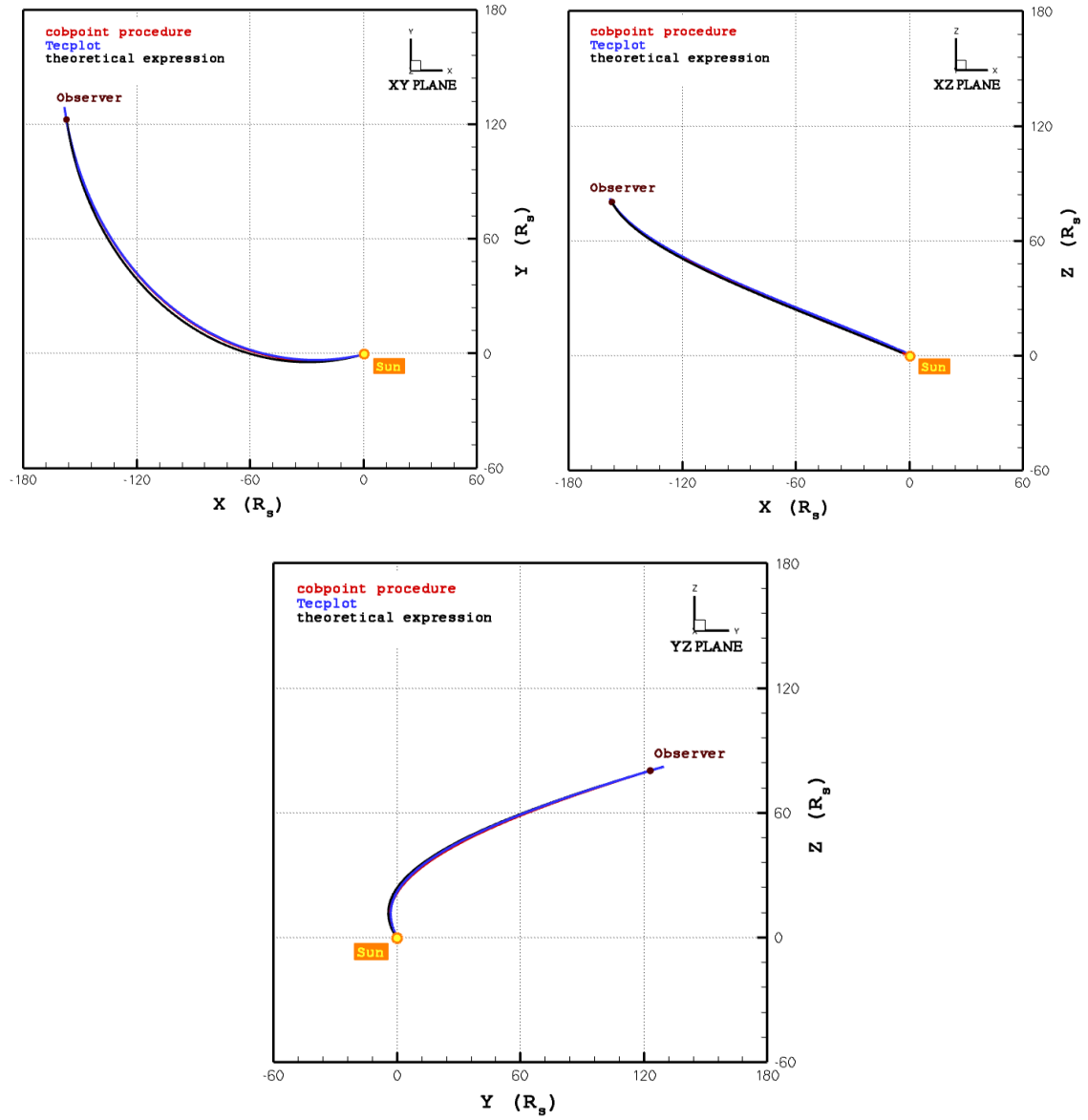

Figure D.1: Comparison between the IMF lines calculated by applying our cobpoint procedure (red), the visualization software Tecplot (blue) and Parker's expression (black). Brown circle: location of the observer; yellow point: the Sun.

tion with the shock front for the 0.4 AU-observers (left) and the 1.0 AU-observers (right) derived when applying the cobpoint procedure (φ') and derived with Nolte's expression (φ), as well as the differences among them ($\delta\,\varphi$). These differences are much smaller than the estimated errors of this approximation.

Table D.1: Comparative between the computed (φ') and the theoretical (φ) heliolongitudinal location of the first magnetic connection of each observer with the shock front, and their differences ($\delta\,\varphi$).

		0.4 AU			1.0 AU		
		φ'	φ	$\delta\,\varphi$ [°]	φ'	φ	$\delta\,\varphi$ [°]
$\theta = 7°$	W45	W22.4	W19.9	2.5	E13.1	E17.1	4.0
	W00	E22.6	E25.0	2.4	E58.5	E62.1	3.6
	E30	E53.2	E55.0	1.8	E88.3	E92.1	3.8
$\theta = 22°$	W45	W23.0	W22.7	0.3	E07.5	E09.2	1.7
	W00	E21.8	E22.2	0.4	E52.9	E54.2	1.3
	E30	E52.5	E52.2	0.3	E83.6	E84.2	0.6
$\theta = 37°$	W45	W29.5	W30.0	0.5	W06.8	W08.3	1.5
	W00	E15.8	E14.9	0.9	E38.0	E36.6	1.4
	E30	E46.4	E44.9	1.5	E68.6	E66.6	2.0

• Shock normal line

The MC and VC methods show limitations due to the adopted simplifying assumptions, while the MD methods fail when the shock is perpendicular and give disparate results for quasi-perpendicular shocks (see more information about the limitations of these methods in, for example, Koval & Szabo 2008). For several numerical test using the nine observers located at 0.4 AU, we realized that the maximum deviation between any of these five normals is smaller than 2°, and smaller than 0.1° within the normals calculated using the MD methods. This behaviour holds for eight of the observers, being the maximum angular difference between two of these normals smaller than 1.2° at a given cobpoint for the N22W45 observer. The conclusion is that the MD3 method gives the more stable values.

• Downstream point

In order to look for the appropriate downstream point, we considered several methods. These methods assume that the downstream point is located where: (1) the normal gradient is the 20% of the maximum value of the normal gradient; (2) the cobpoint will be 10 minutes later, p_d, with $p_d = r_c\,v_{sh}\,t$, where r_c is the radial position of the cobpoint and v_{sh} the value of the shock speed (calculated by means

of any other method); (3) the thickness of the shock is a given fixed value (in this case, $1.6\,\mathrm{R}_{\odot}$); and (4) the relative radial speed reaches its maximum value. After checking the results of the downstream point location when applying all these methods, we concluded that method (1) is the most suitable for the set of observers and snapshots we are analysing.

• Iterating downstream

Once determined the downstream point, it is possible to improve its location (as well as the determination of the shock normal direction) by iterating the procedure, taking as new initial point the value previously computed. We checked this possibility by applying the method (1) to eight observers. Figure D.2 shows the differences in the radial position of the downstream point, $\delta\, r$, derived when applying the method (1) once and after performing 5 (top panel) and 20 (bottom panel) iterations. Three observers are located at $86\,\mathrm{R}_{\odot}$ ($\sim 0.4\,\mathrm{AU}$), and five at $215\,\mathrm{R}_{\odot}$ ($\sim 1.0\,\mathrm{AU}$). As can be seen, the determination of the downstream point improves substantially for a few snapshots of some observers after iterations. This issue requires further work to meliorate the determination of $\hat{\mathbf{n}}$ and the downstream point.

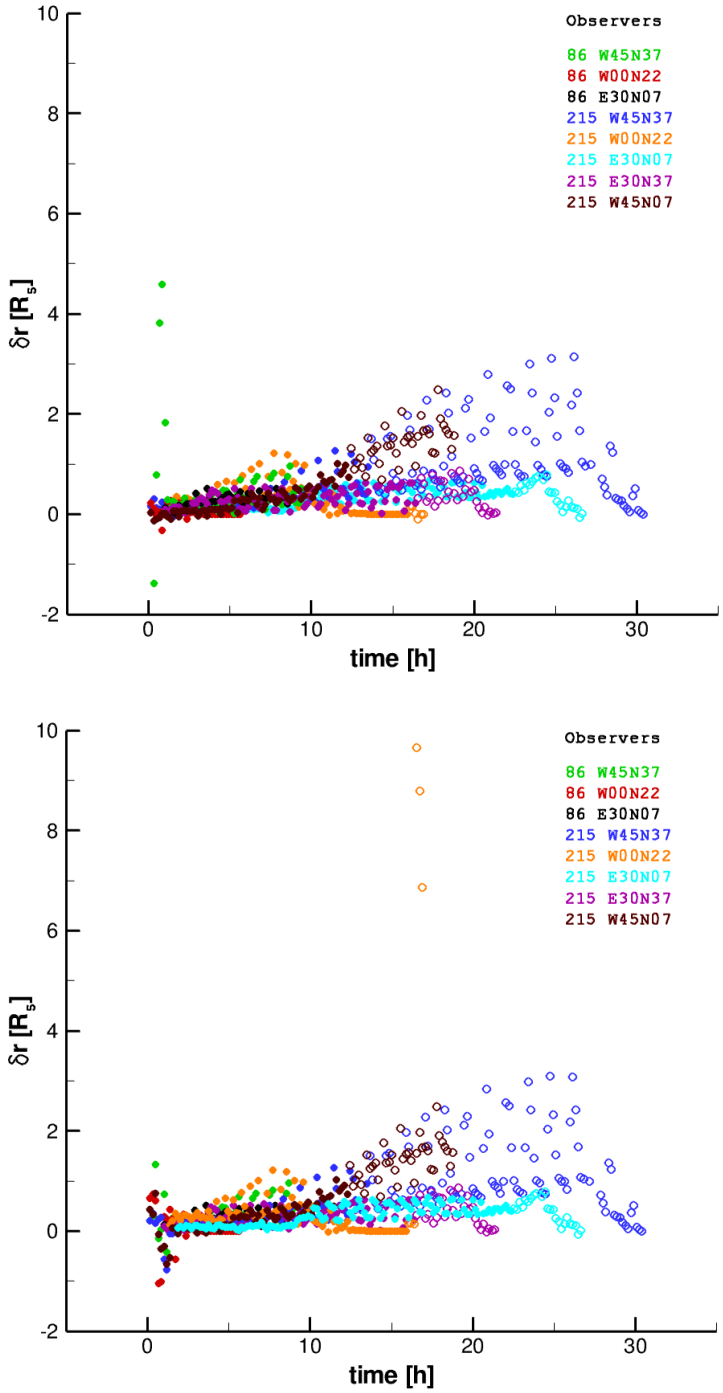

Figure D.2: Differences in the radial position of the downstream point when using the iterative method (see text) for the 8 observers as labelled, 3 located at 86 $R_\odot$ and 5 at 215 $R_\odot$. Solid circles: shock identified; open circles: no-shock found. Top panel: after 5 iterations. Bottom panel: after 20 iterations.

Appendix E

Network of spacecraft: determination of the shock front

A main difference between the treatment of observed and simulated shocks is that observed shocks are analysed as function of time, usually for a given location in space, while simulated shocks are analysed as function of space, at a given time (i.e., snapshot). The basic reason is the huge amount of simulated data to be examined automatically (and visually in odd or special situations) to determine the potential shock front. This approach implicitly assumes that the structure of the shock front does not change significantly between two consecutive snapshots. It is possible to determine the shock front assuming a virtual armada of spacecraft located at 215 $R_\odot$ and at different latitudes and longitudes, and then applying the procedure described in Chapter 3 to identify the cobpoint and the downstream point of each observer. Spacecraft of this armada are located at latitudes 7°, 22° and 37° over the equator, and at longitudes from W45 to E30 of the parent activity, with an angular separation of 5°. Each panel of Figures D-1 to D-3 displays, from top to bottom, the radial position, latitude and longitude of the cobpoint (black) and downstream point (red), and VR at the cobpoint, as function of the longitude of the spacecraft (with respect to the main direction of the shock). We present a set of 6 snapshots, corresponding to 1 hour interval[1] of the simulation. As can be seen, the structure of the shock front is maintained -even when the shock continues evolving-, corroborating our idea that analysing the spatial evolution of the simulated shock instead of its temporal evolution does not introduce a significant bias or error.

[1] In the MHD simulation of the shock propagation, the outputs are stored every 10 minutes; that means, about 300 snapshots of 1.6 Gb each one.

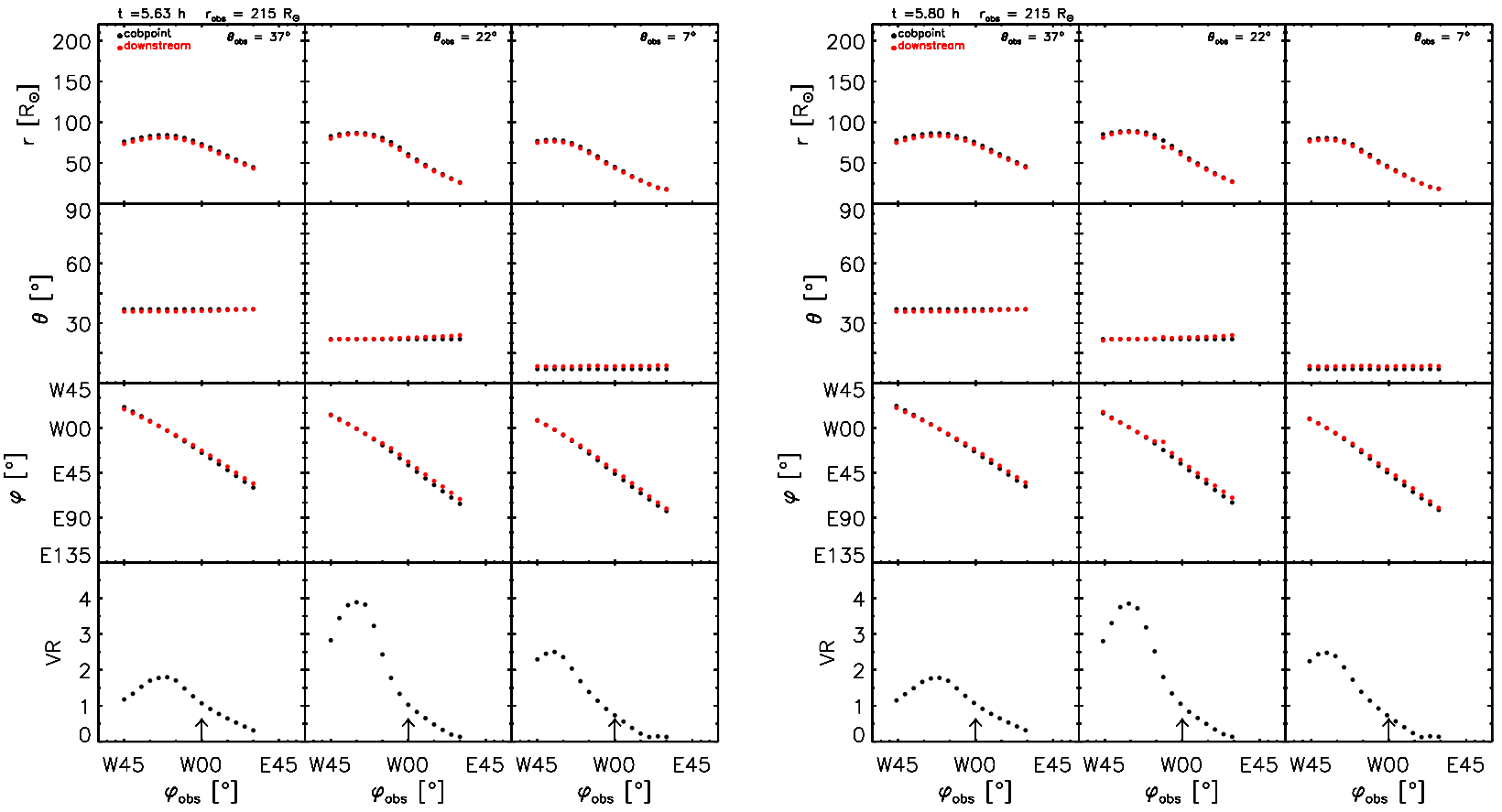

Figure D-1: From top to bottom: radial position, longitude and latitude of the cobpoint (black) and downstream point (red), and VR at the cobpoint, of a network of spacecraft situated from W45 to E30, for two consecutive snapshots: at $t = 5.63$ hours (left) and at $t = 5.80$ hours (right). The arrow marks the main direction of the shock.

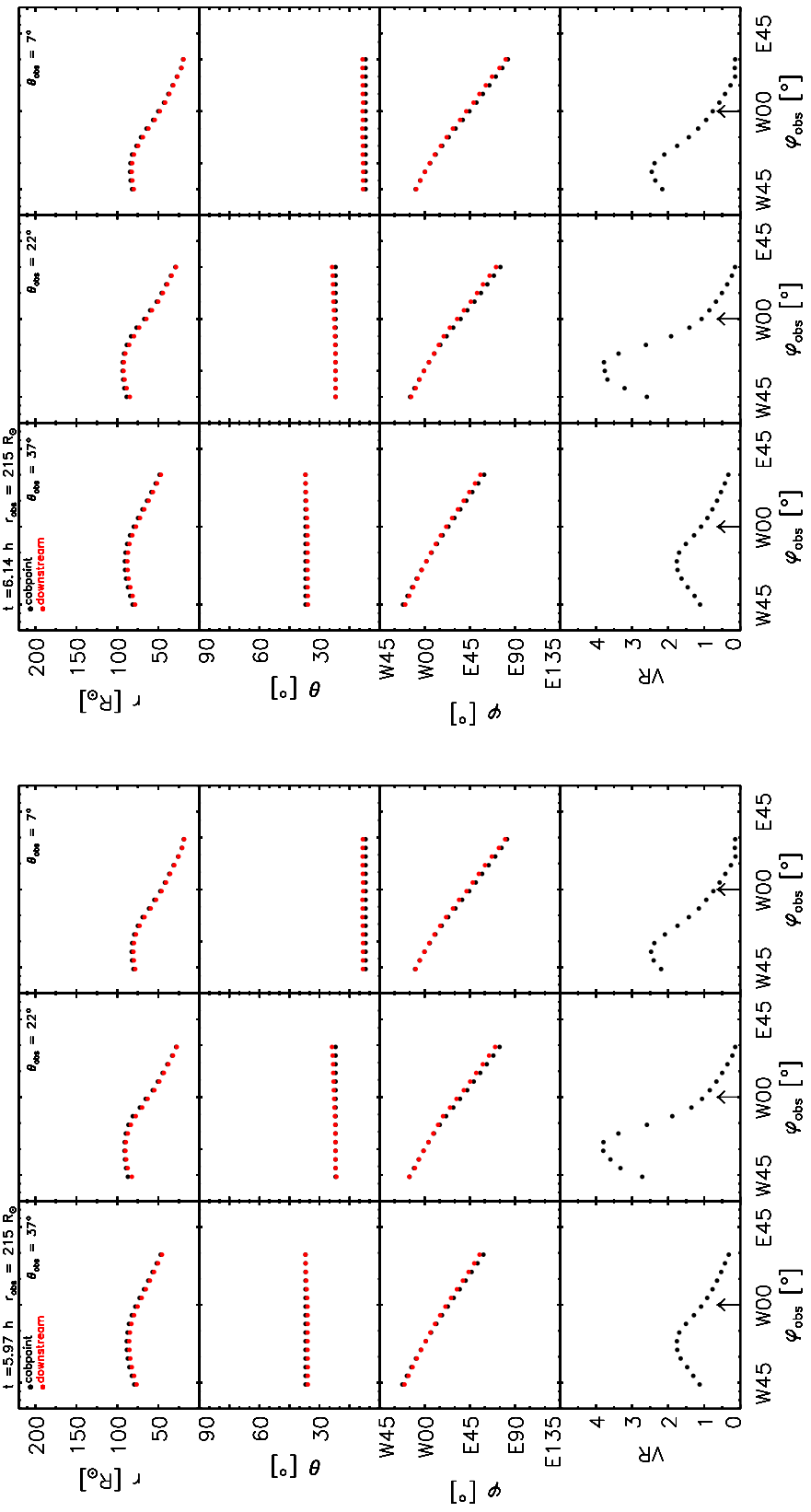

Figure D-2: Displayed as in Figure D-1, but for snapshots at $t = 5.97$ hours (left) and at $t = 6.14$ hours (right).

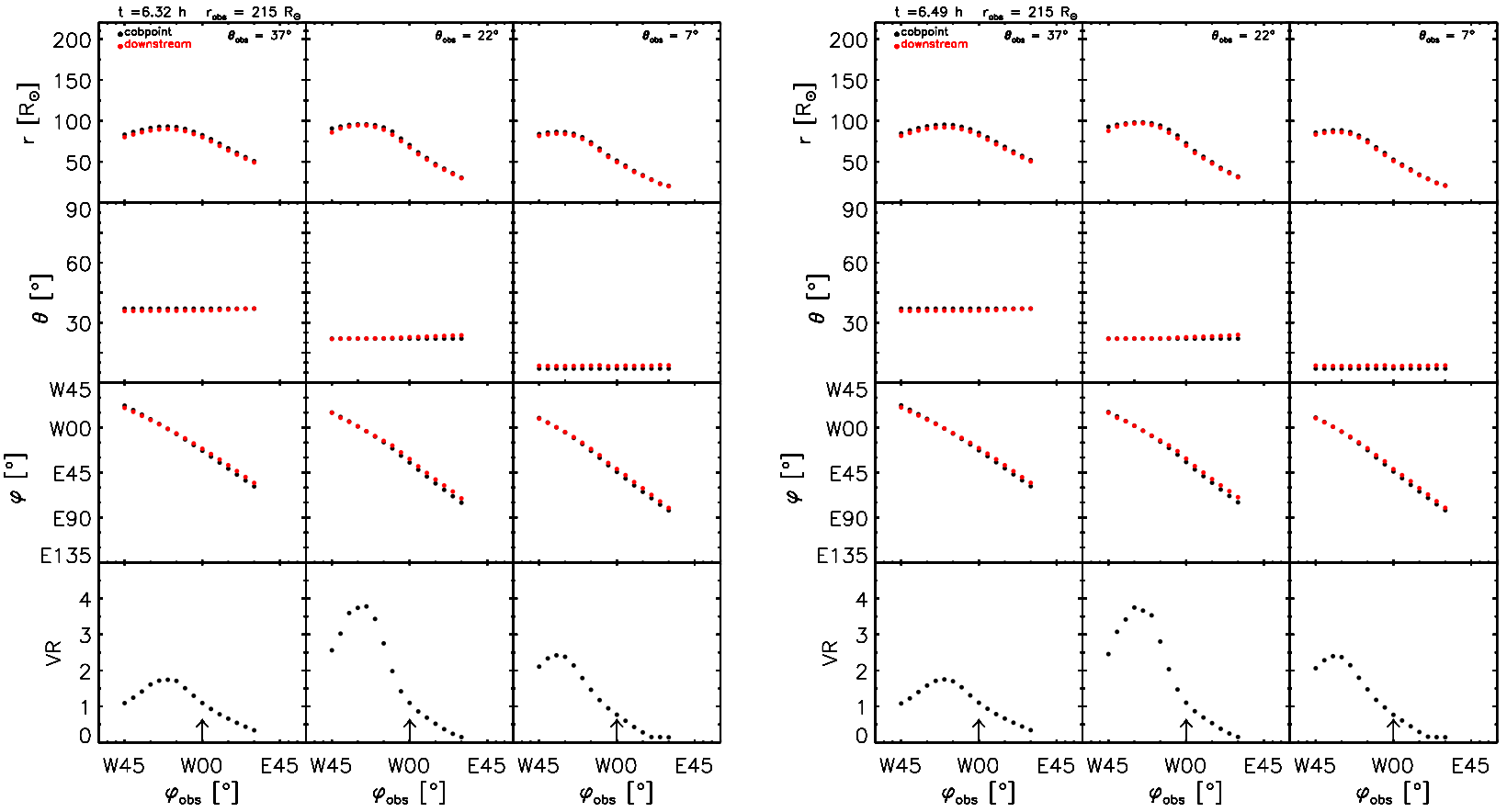

Figure D-3: Displayed as in Figure D-1, but for snapshots at $t = 6.32$ hours (left) and at $t = 6.49$ hours (right).

Appendix F

Simulated proton flux profiles

In this appendix we present the synthetic proton flux profiles derived for the set of shocks and observers described in Chapter 3. Each simulation has been performed for ten energy channels, from 0.125 up to 64 MeV (as labelled), and for four different transport conditions: assuming a $\lambda_{||0} = 0.2$ AU (top panels) without and with a foreshock region ahead of the shock (left and right, labelled I02TN and I02TY respectively), and considering a $\lambda_{||0} = 0.8$ AU (bottom panels) without and with foreshock region (left and right, labelled I08TN and I08TY respectively). The foreshock region is assumed to be 0.01 AU width and active from 20 hours before the shock passage. Figures D-1 to D-3 display the flux profiles for the nine 0.4 AU-observers in the case of the fast shock. Figures D-4 to D-6 show the equivalent flux profiles for the 1.0 AU-observers. When the shock is too weak or is not detected (in the sense commented in Section 3.3.3), the corresponding part of the profile is not depicted. Figures D-7 to D-9 show the flux profiles derived for the nine 0.4 AU-observers in the case of the slow shock.

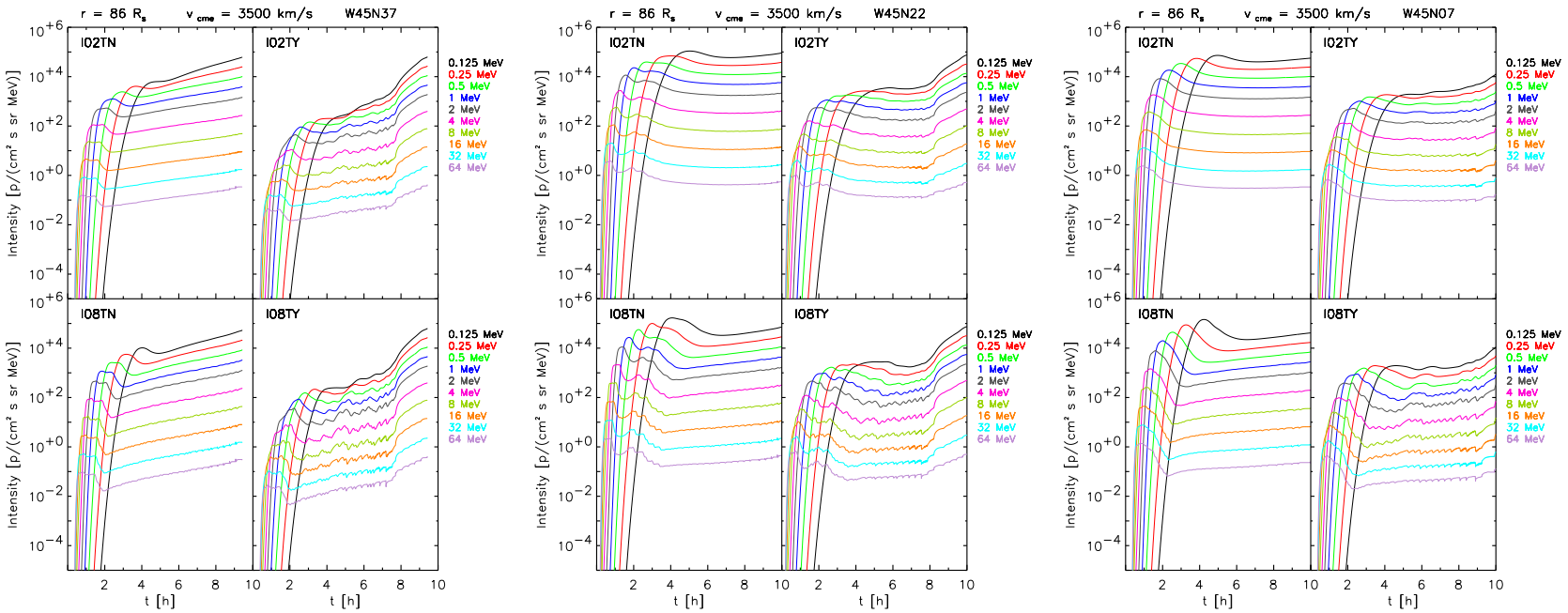

Figure D-1: Fast shock. Simulated proton flux profiles for the W45N37, W45N22 and W45N07 0.4 AU-observers, for $0.125 < E < 64\,\mathrm{MeV}$ (as labelled). Top panels: $\lambda_{||0} = 0.2\,\mathrm{AU}$ without (left) and with (right) the presence of foreshock. Bottom panels: the same as top panels but for $\lambda_{||0} = 0.8\,\mathrm{AU}$.

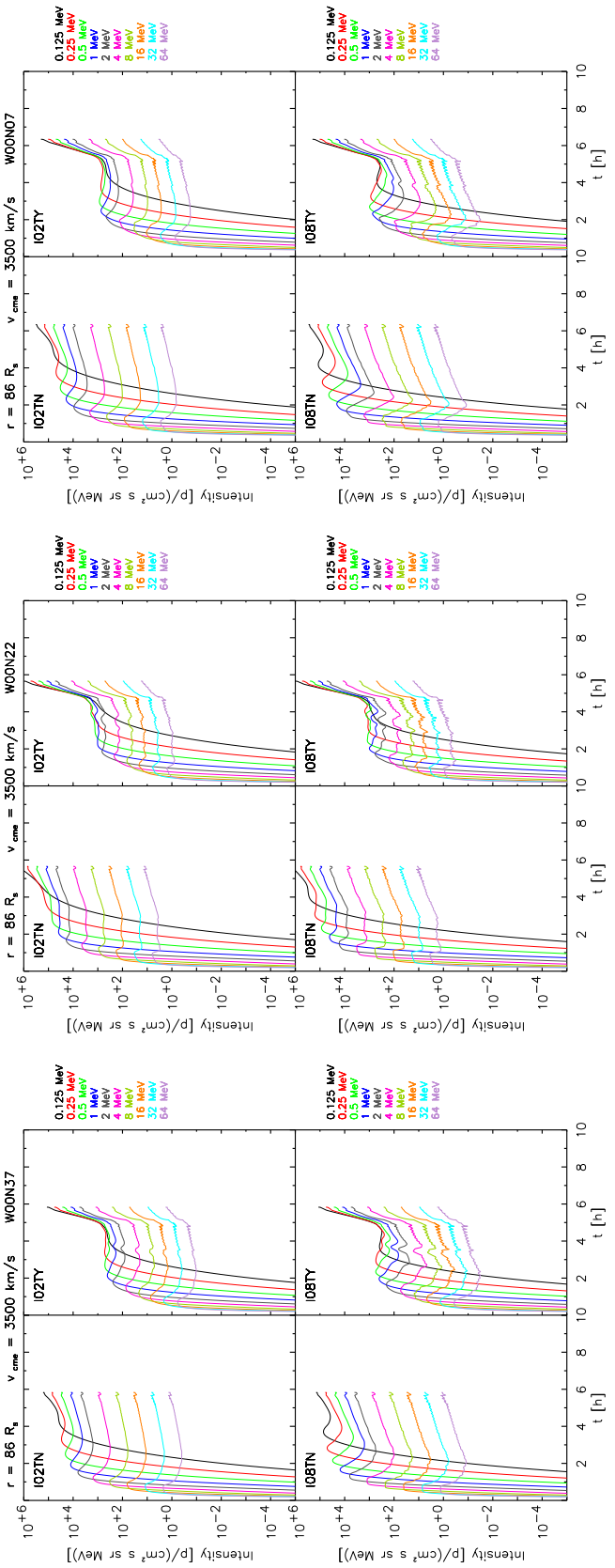

Figure D-2: Fast shock. Displayed as in Figure D-1, but for the W00N37, W00N22 and W00N07 0.4 AU-observers.

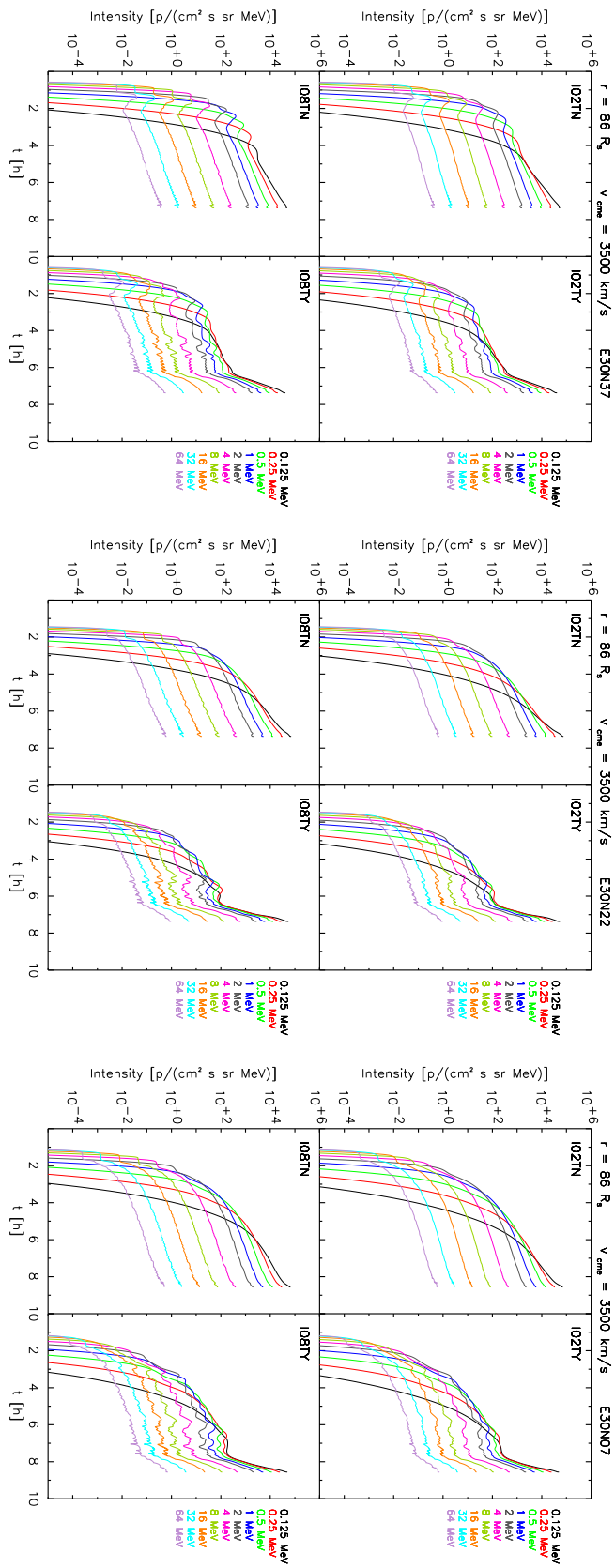

Figure D-3: Fast shock. Displayed as in Figure D-1, but for the E30N37, E30N22 and E30N07 0.4 AU-observers.

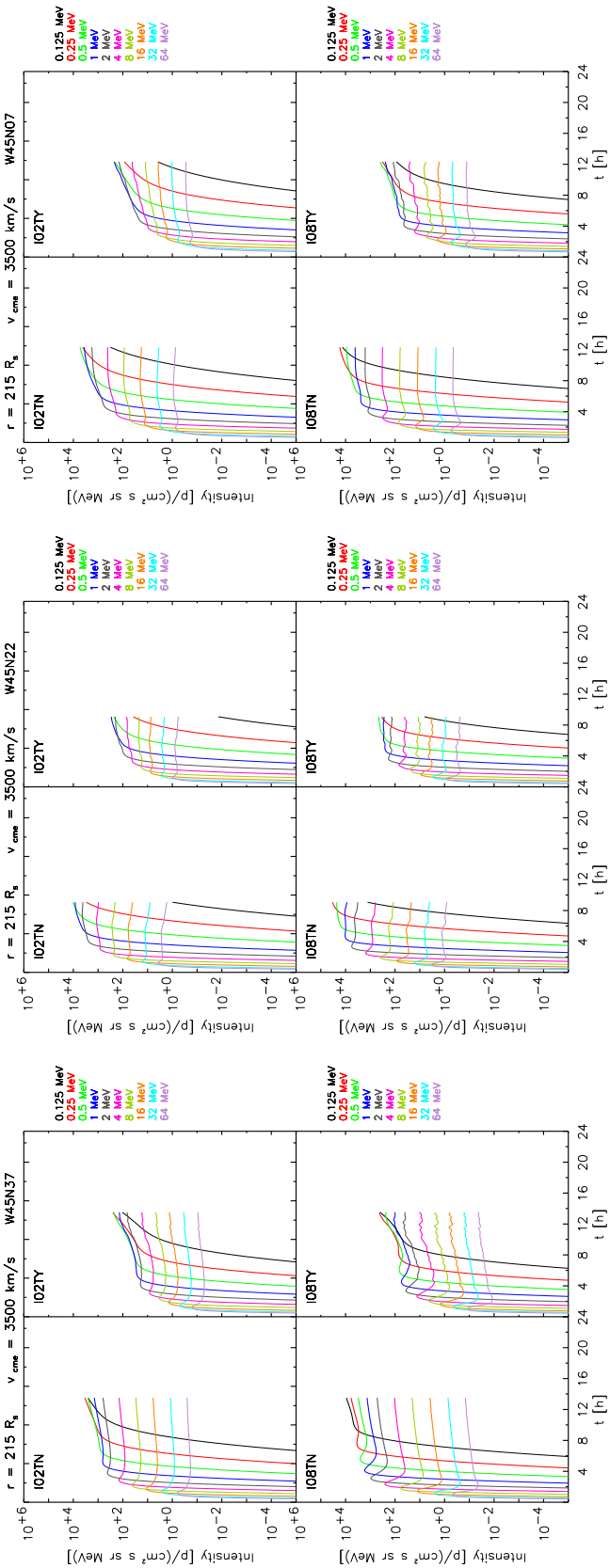

Figure D-4: Fast shock. Displayed as in Figure D-1, but for the W45N37, W45N22 and W45N07 1.0 AU-observers.

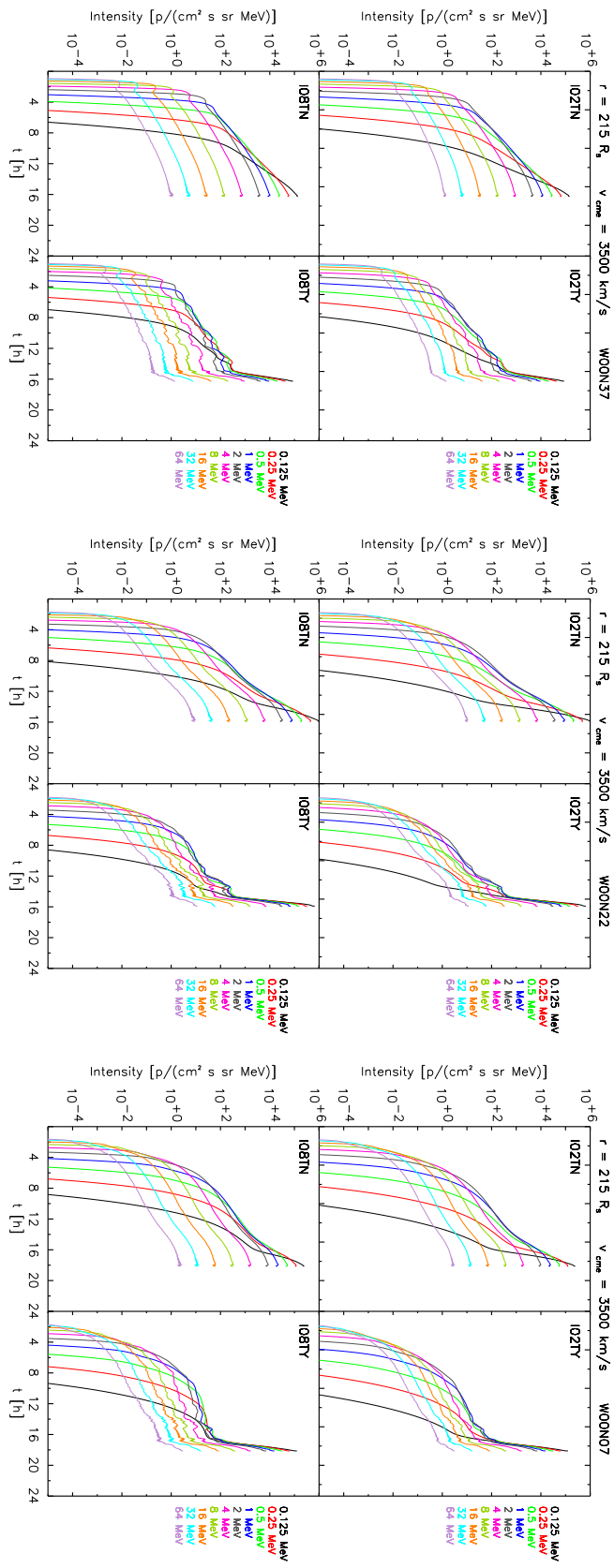

Figure D-5: Fast shock. Displayed as in Figure D-1, but for the W00N37, W00N22 and W00N07 1.0 AU-observers.

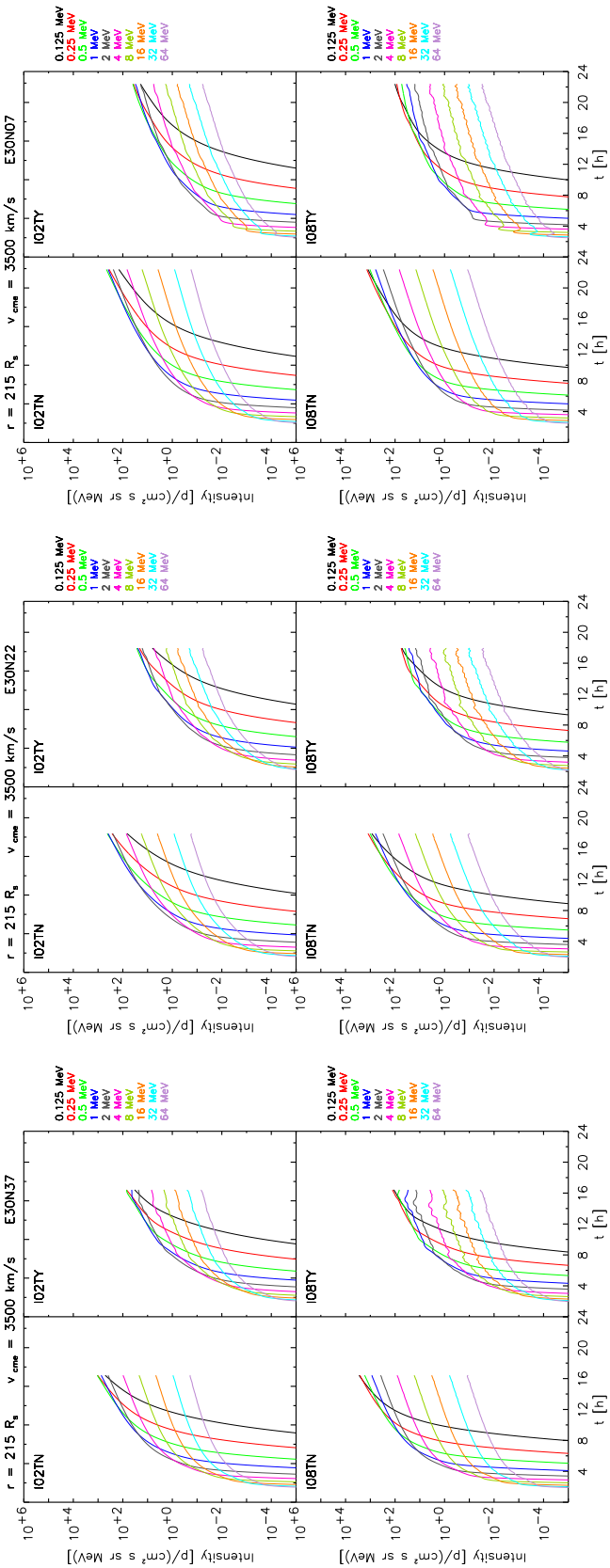

Figure D-6: Fast shock. Displayed as in Figure D-1, but for the E30N37, E30N22 and E30N07 1.0 AU-observers.

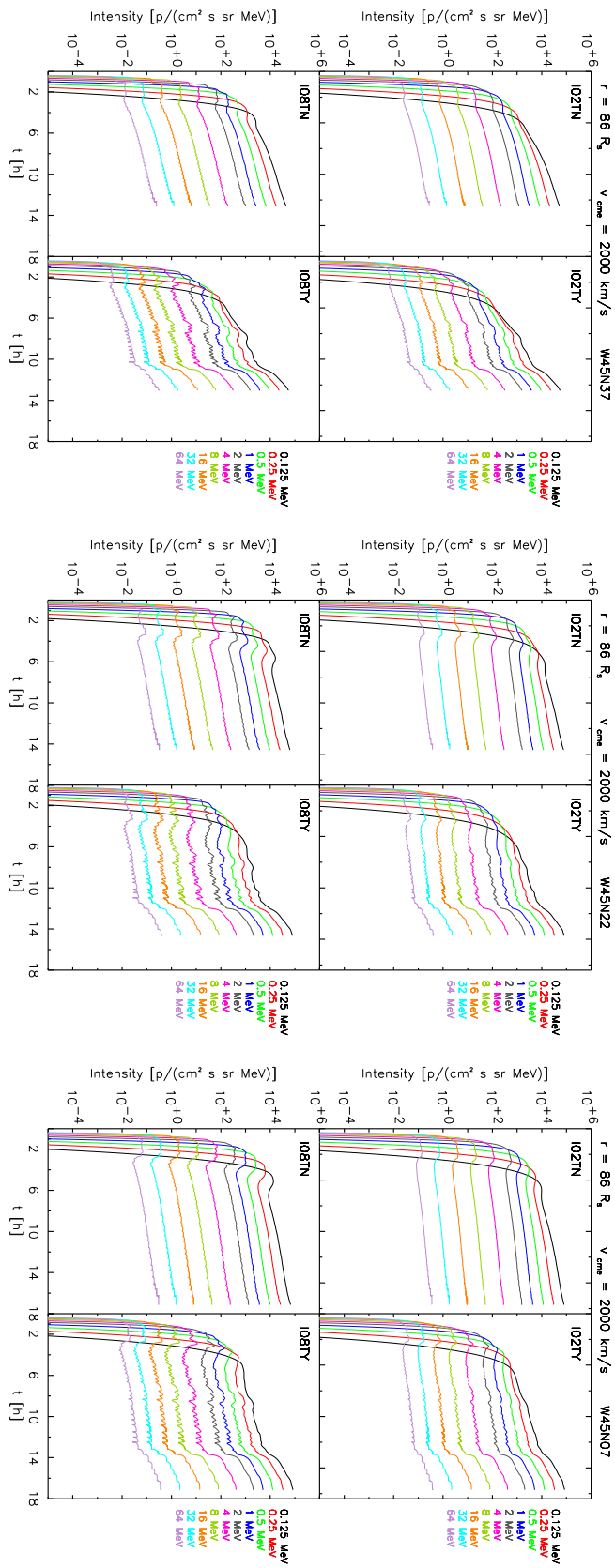

Figure D-7: Slow shock. Displayed as in Figure D-1, but for for the W45N37, W45N22 and W45N07 0.4 AU-observers.

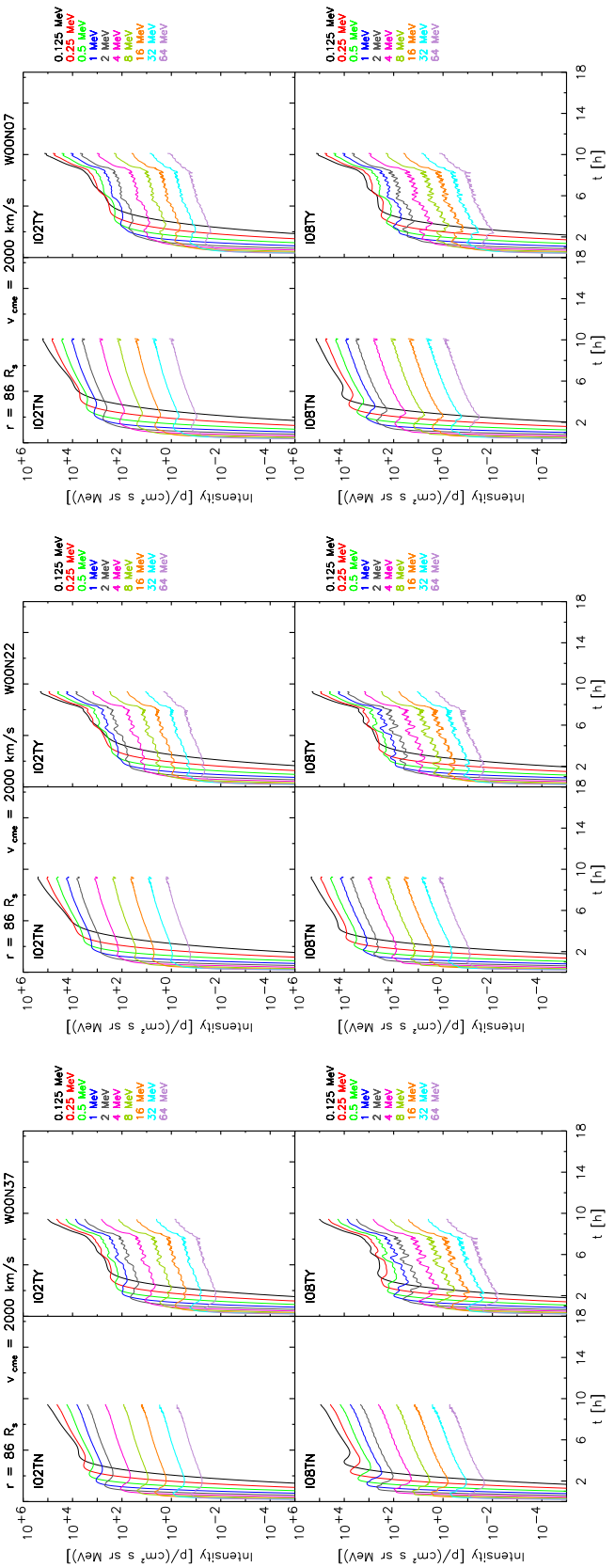

Figure D-8: Slow shock. Displayed as in Figure D-1, but for for the W00N37, W00N22 and W00N07 0.4 AU-observers.

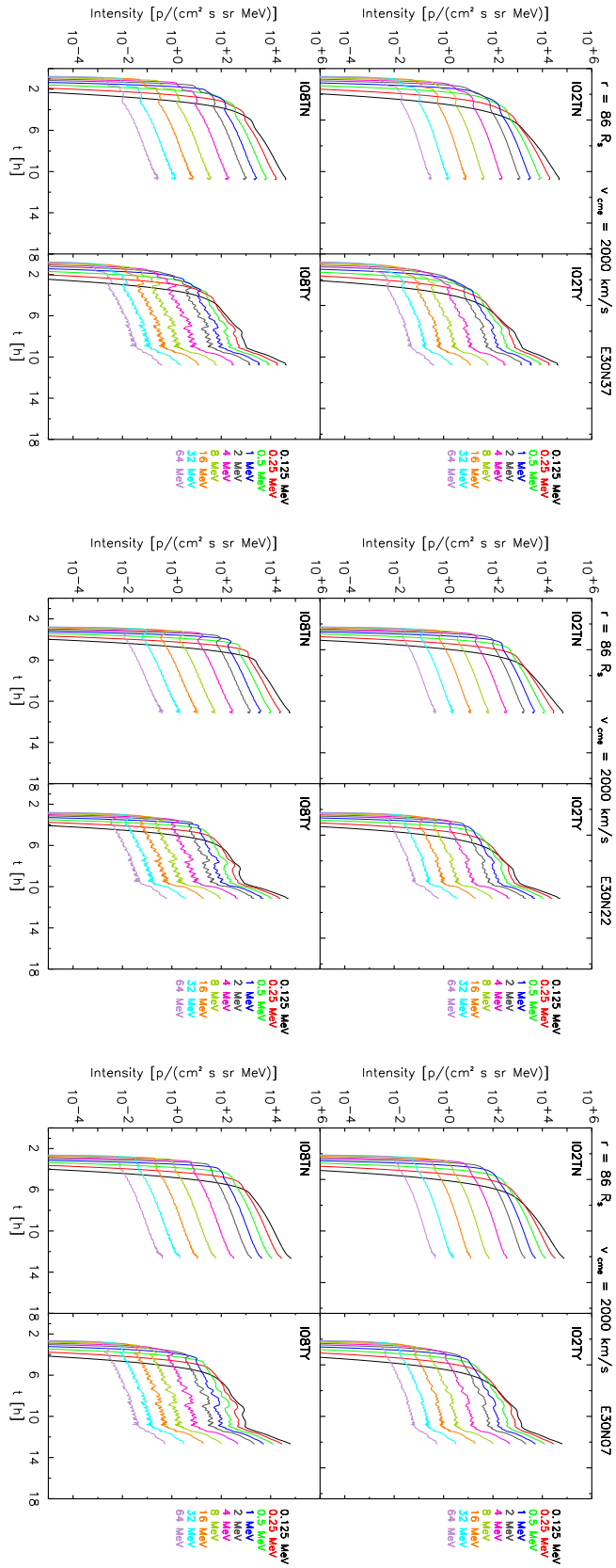

Figure D-9: Slow shock. Displayed as in Figure D-1, but for for the E30N37, E30N22 and E30N07 0.4 AU-observers.

Appendix G

The Helios-1 and -2, IMP-8 and ISEE-3 spacecraft. Candidate SEP events

G.1 The Helios spacecraft

The Helios spacecraft were a pair of deep space probes developed by the Federal Republic of Germany (FRG) in a cooperative program with NASA. Helios-1 was active from December 1974 to March 1986, and Helios-2 from February 1976 to March 1980. Both spacecraft were in highly eccentric orbits around the Sun with distances ranging between 0.3 and 0.98 AU, and small variable inclinations (of up to $\sim 7^{\circ}$ with respect to the ecliptic plane). Their orbits made them an ideal platform for making long baseline time-of-arrival measurements to obtain source directions[1].

The high resolution particle data used within this work were measured by the University of Kiel E6 Cosmic Ray Experiment[2] on board both Helios spacecraft (time resolution of 15 minutes and, in some cases, of 1 minute; courtesy of Prof. R. Müller-Mellin, private communication). We also use the high resolution complete merged data set[3] of the plasma experiment E1 and magnetometer experiment E2 on board both Helios spacecraft (time resolution of ~ 3 minutes; courtesy of Prof. R. Schwenn

[1] More information in http://www.mps.mpg.de/en/projekte/helios/

[2] For a detailed description of the two identical instruments, we refer to Kunow et al. (1977).

[3] Selected parameters are available on a CD-ROM provided by the Max Planck Institute for Solar System Research: http://www.mps.mpg.de/dokumente/projekte/helios/helioscd.html

and Dr. A. de Lucas, private communication).

G.2 The IMP-8 spacecraft

The IMP-8 spacecraft was launched on 26 October 1973 to measure the magnetic fields, plasmas, and energetic particles of the Earth's magnetotail and magnetosheath, and of the near-Earth solar wind. It had a $\sim 35\,R_E$ geocentric orbit with a period of 12 days, of which ~ 7 days were spent in the solar wind upstream of Earth's bow shock. The mission officially terminated in October 2001, but data continued to be collected up to 2006 to provide an ongoing 1.0 AU baseline for the Voyager and Ulysses missions. This spacecraft accumulated a long-time series database useful in understanding long-term solar processes[4].

For the event studied in Chapter 5 we use the high resolution particle data recorded by the Goddard Medium Energy (GME) Experiment instrument[5] (time resolution of 30 minutes). The particle data for the events presented in this Appendix comes from the Charged Particle Measurement Experiment (CPME) instrument[6] (time resolution of ~ 5.5 minutes). We use the Field-Plasma-Merged 1-min IMP-8 Data Set[7], created at GSFC/SECAA[8] in 2005. No plasma parameters are available when the spacecraft is in the magnetosphere.

G.3 The ISEE-3 spacecraft

ISEE-3 was the third satellite of the International Sun-Earth Explorer (ISEE) program, designed to make fields, plasma, waves and particle measurements in the near-Earth environment. Launched on 12 August 1978, it had an orbit about the L1, $\sim 240\,R_E$ upstream the Earth. In June 1982, ISEE-3 was renamed ICE (International Cometary Explorer), starting the magnetotail and comet encounter phases of its mission. It will return to the vicinity of the Earth-Moon system in August 2014[9].

[4] More information in http://spdf.gsfc.nasa.gov/imp8/project.html
[5] GME: http://spfd.gsfc.nasa.gov/imp8_GME/GME_home.html
[6] CPME: http://sd-www.jhuapl.edu/IMP/imp_cpme_info.html
[7] This data comes from: http://nssdcftp.gsfc.nasa.gov/spacecraft_data/imp/imp8/merged/
[8] GSFC/SECAA, NASA: http://spdf.gsfc.nasa.gov/spdf-secaa_usage.html
[9] More information in http://heasarc.gsfc.nasa.gov/docs/heasarc/missions/isee3.html

We use the data[10] from the solar plasma wind instrument[11] and Vector Helium Magnetometer[12] (time resolution of 5 minutes).

G.4 Candidate SEP events

• The 24 September 1977 event

The onset of the main radio event occured at 0554 UT on 24 September 1977 (doy 267) associated with an active region locate at N10W120 (C82, L06)[13]. An interplanetary shock reached Helios-1 at 0241 UT on September 25 (doy 268), that some hours later, at 1251 UT, also hit Helios-2 (V85). Helios-1 was located at 0.58 AU and $\sim 25\,^{\circ}$ eastward of the solar parent activity, while Helios-2 was at 0.64 AU and at E49 (K97, D00, L06). IMP-8, situated at 1.0 AU, saw the particle event as an W120 event (L06). Figure F-1 displays the proton flux profiles measured by Helios-1, Helios-2 and IMP-8 (respectively), in several energy channels, as well as the evolution of the solar wind plasma and magnetic field variables. In each panel, the dotted line and the small arrow indicate the time of the solar activity, whereas the solid line marks the shock passage by the corresponding spacecraft.

• The 13 February 1978 event

At 0254 UT on 13 February 1978 (doy 44) the maximum in soft X-rays of a 1N/M7 flare at N16W20 was observed (KH82, K92, L06). On February 15 (doy 46), an interplanetary shock reached Helios-1 at 0130 UT; at 0153 UT it also arrived at Helios-2 (V85, K97). Helios-1 was at 0.95 AU and $\sim 73\,^{\circ}$ westward of the flare location, while Helios-2 was at 0.95 AU and saw the event as a W40 event (K97, D00, L06). IMP-8 was situated at 0.99 AU[14] and at W20 (L06). The proton flux profiles and the evolution of the solar wind plasma and magnetic field intensity measurements from these spacecraft are shown in Figure F-2.

[10] This data comes from: http://sprg.ssl.berkeley.edu/impact/data_browser_helios.html‡popup
[11] http://nssdc.gsfc.nasa.gov/nmc/experimentDisplay.do?id=1978-079A-01
[12] http://nssdc.gsfc.nasa.gov/nmc/experimentDisplay.do?id=1978-079A-02
[13] In this section, references have been shortened as follows: Cliver et al. (1982) as C82; Kahler (1982) as KH82; Volkmer & Neugebauer (1985) as V85; Kallenrode et al. (1992) as K92; Kallenrode (1997) as K97; Daibog et al. (2000) as D00; and Lario et al. (2006) as L06.
[14] In the magnetosphere. It did not measure interplanetary solar wind nor magnetic field variables.

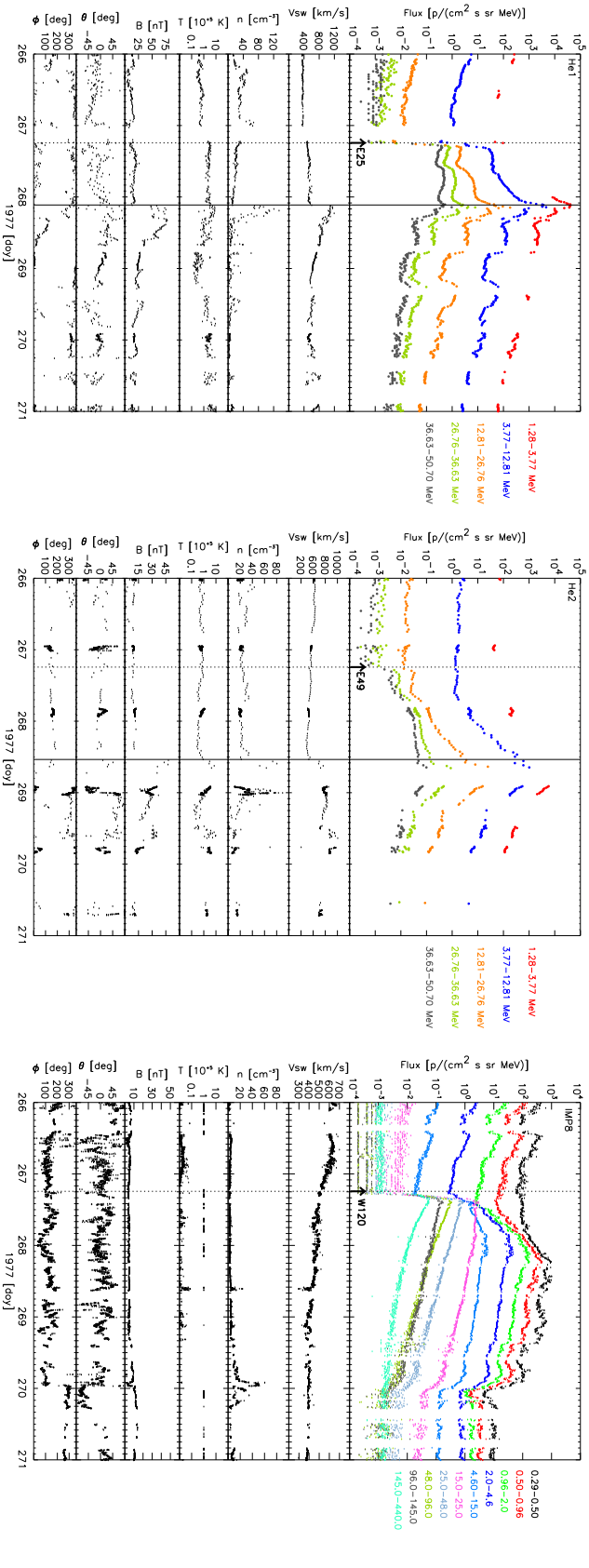

Figure F-1: The 24 September 1978 event. Proton flux profiles measured by several energy channels (as labelled), and evolution of the solar wind plasma and IMF variables.

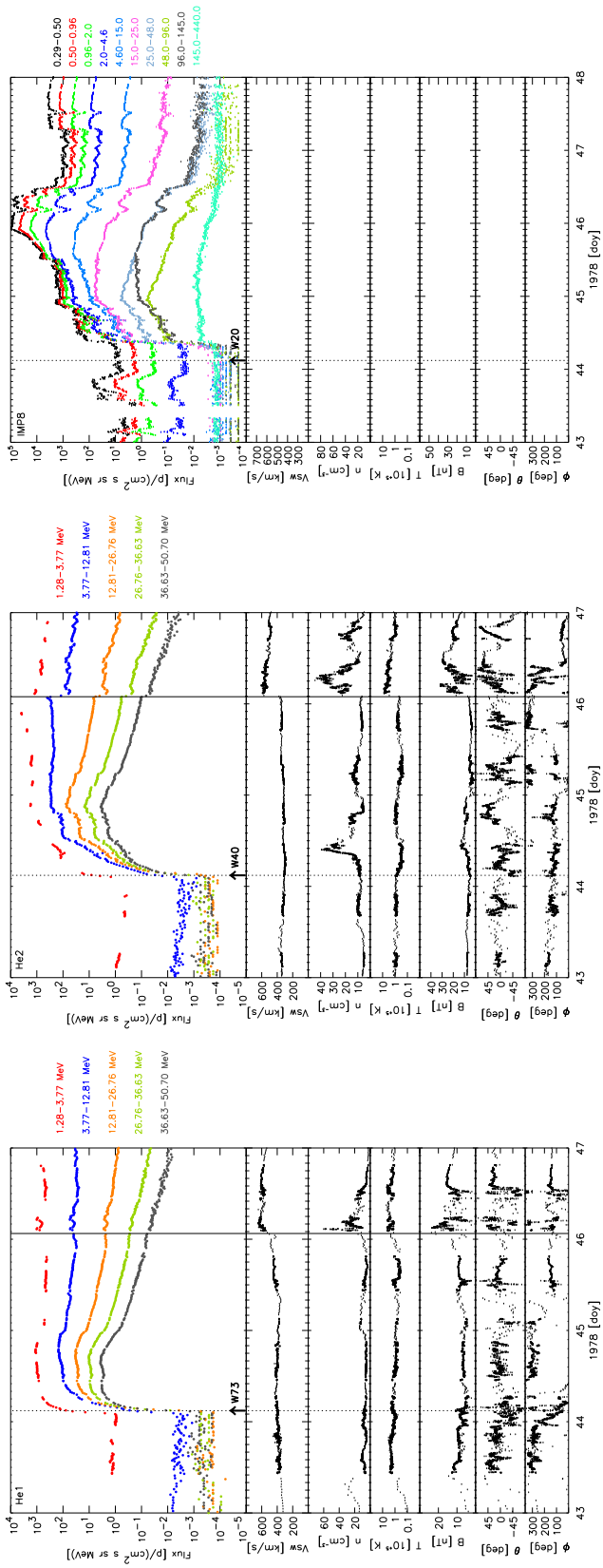

Figure F-2: The 13 February 1978 event. Displayed as in Figure F-1.

• The 8 April 1978 event

At 0239 UT on 8 April 1978 (doy 98) the maximum in soft X-rays of a 2B/X1 flare took place at N19W11 (KH82 ,K92, L06). On April 9 (doy 119), an interplanetary shock reached Helios-2 at 0716 UT; at 0718 UT it also hit Helios-1 (V85, D00, L06). Helios-1 was at 0.50 AU and $\sim 49\,^{\circ}$ westward of the flare location, while Helios-2 was at 0.51 AU and at W20 (V85, D00, L06). IMP-8 was situated at 1.0 AU[15] and at W11 (L06). The proton flux profiles and the evolution of the solar wind plasma and magnetic field intensity measurements from these spacecraft are shown in Figure F-3.

• The 11 December 1978 event

At 1945 UT on 11 December 1978 (doy 345) the maximum of a 1B/X1 flare at S15E14 in soft X-rays took place (K92, L06). Helios-1 did not record any shock, while Helios-2 was hit by two interplanetary shocks: at 0247 UT and at 1247 UT on December 13 (doy 347) (V85, D00). Helios-1 was at 0.70 AU and saw the particle event as a W39 event, while Helios-2 was at 0.75 AU and $\sim 5\,^{\circ}$ eastward of the flare location (V85, D00, L06). IMP-8 was situated at 0.98 AU[16] and at E14. The proton flux profiles and the evolution of the solar wind plasma and magnetic field intensity measurements from these spacecraft are shown in Figure F-4. It must be pointed out that all the authors that quote this particle event relate it with the flare indicated, but K92 report a second 2N/M3 flare at 0003 UT on the same day (S13E29), being possible that one of the shocks that reached Helios-2 might be associated with this event.

[15] As footnote 14.

[16] There is not plasma and magnetic field data recorded by IMP-8 in this case. But, fortunately, ISEE-3 does provide in-situ measurements for this period of time.

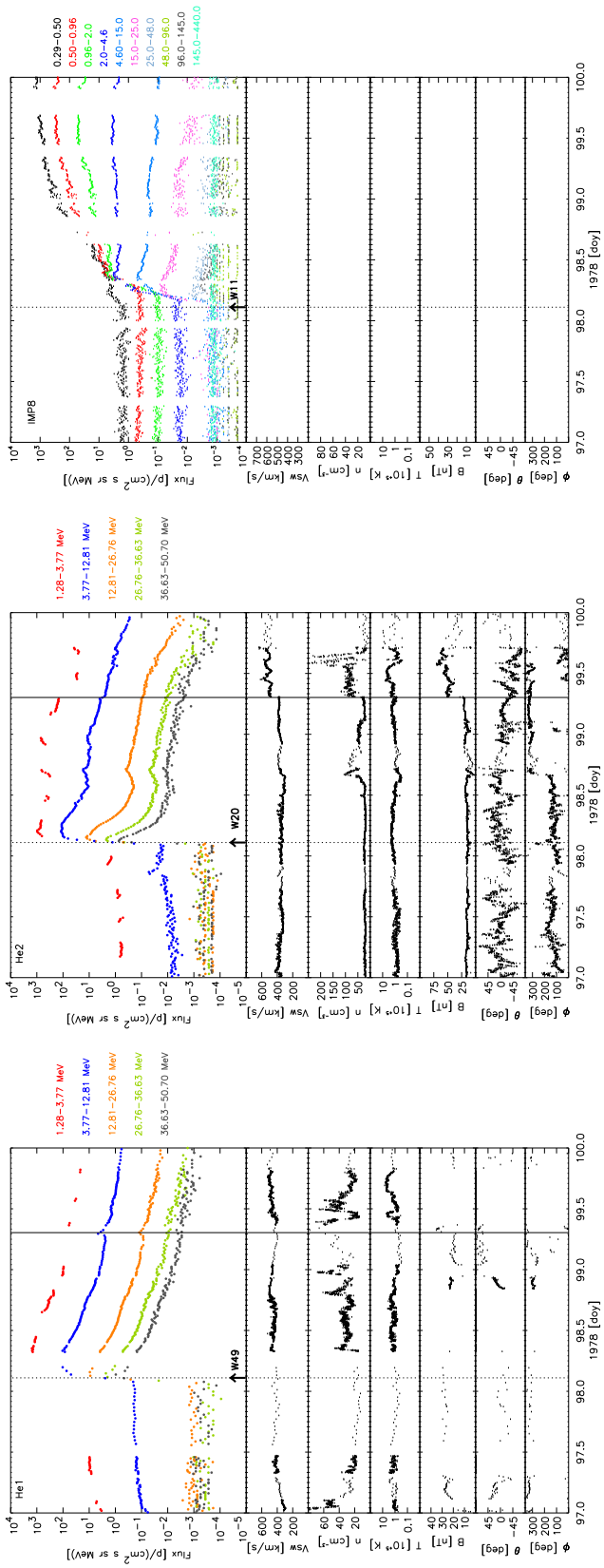

Figure F-3: The 8 April 1978 event. Displayed as in Figure F-1.

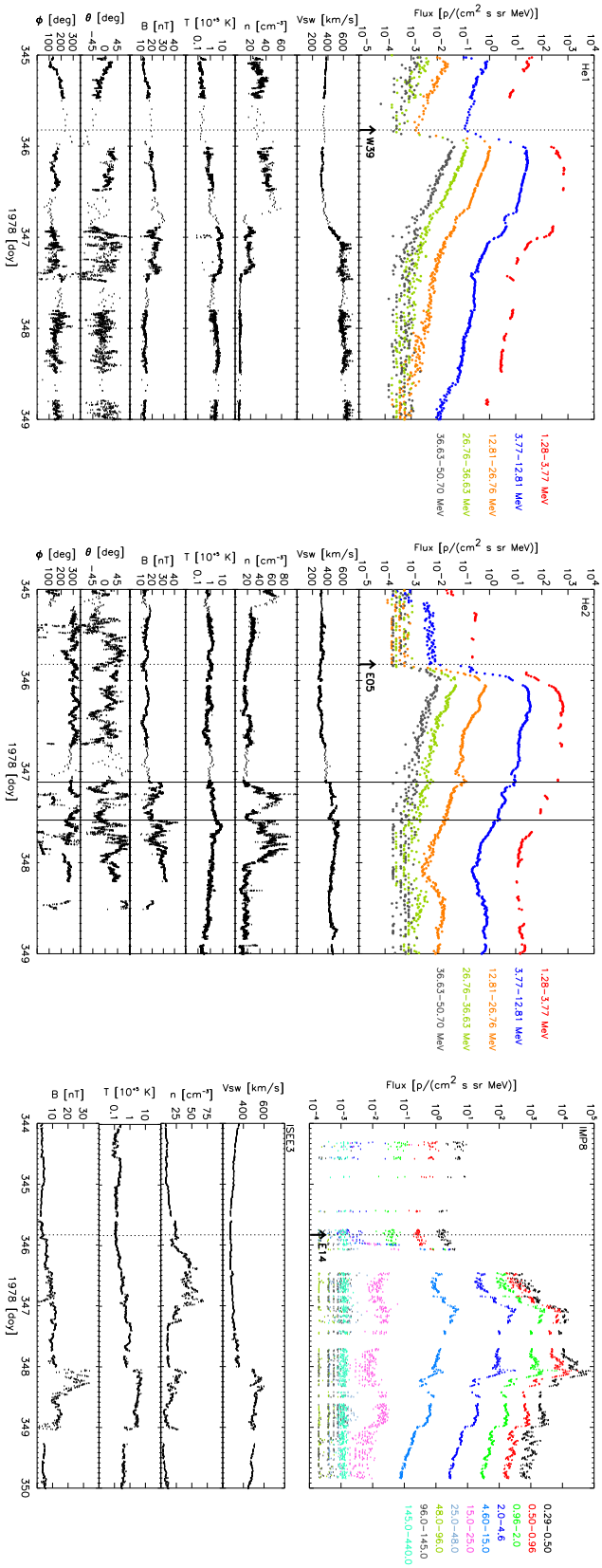

Figure F-4: The 11 December 1978 event. Displayed as in Figure F-1.

Appendix H

The Viñas-Scudder method and the SDAT tool

The Viñas-Scudder method consists of determining the shock normal polar angles (ϕ, θ) and the shock speed, v_{sh}, using the R-H equations and the plasma and magnetic field (time series) data on both sides of the shock, by applying a nonlinear least squares method. Once the optimal shock normal angles and speed have been determined, their values are used in conjunction with the data to uniquely define the conservation constants: the mass flux, the normal component of the magnetic field, the tangential components of the momentum flux and the tangential components of the electric field in the frame of the observations. Finally, the procedure uses the determined shock normal, speed and conservation constants in conjunction with the data back in the R-H equations to predict the self-consistent asymptotic states of the magnetofluid in the upstream and downstream sides of the shock.

To render the use of this method easy and friendly, an extension was implemented in SDAT[1] (Viñas & Holland 2005). This is an analysis/visualization tool to study shocks and other discontinuities from observations of plasma and magnetic field data. It is developed fully in IDL and reads ASCII files as input data, which can be in any coordinate system and at their own native resolution because the tool allows for data zooming in time. SDAT provides shock parameters such as θ_{Bn}, $\hat{\mathbf{n}}$, v_{sh} or Mach numbers, as well as the solution of the shock normal by several methods, as the method of Abraham-Shrauner (AS), Magnetic Coplanarity (MC), Velocity Coplanarity (VC), Minimum Variance analysis in the magnetic field (MB)

[1] SDAT: Shock and Discontinuities Analysis Tool.

and Minimum Variance analysis in the mass flux (MF). These solutions can be used as initial guess for the Viñas-Scudder (VS) iterative scheme. Finally, the tool estimates the error bounds and the region of confidence for the shock parameters, too. All data displays and graphics generated are written in Postscript and a summary of the analysis is generated as an ASCII file.

However, the actual version of this tool requires the visual inspection of the shock in order to select the upstream and the downstream regions, which renders it rather useless for the purposes of our research (i.e., applying it to MHD shock simulations). Hence, as a first guess we have applied SDAT to several observers, for several snapshots of the 3D fast shock presented in Chapter 3 and 4, to check the concordance between the chosen method to determine the shock normal (MD3 method, Section 3.3) with the different techniques implemented in the tool. For simplicity, we have applied it to three snapshots for each one of a few observers: at the moment of the first magnetic connection; approximately when the shock front is at half of its way to the observer's position; and at the shock passage time[2]. For each snapshot (time instant), we have computed the radial position and longitude of the cobpoint[3], and we have compared the θ_{Bn} calculated by applying our procedure with the angle computed with SDAT. It must be pointed out that the shock normal used as initial guess for the Viñas-Scudder iterative scheme is calculated by applying the AS method, to render θ_{Bn} as much comparable as possible. The results are summarized in Table H.1, where successive columns show (1) the position of the observer, (2) the snapshot time, (3) and (4) the radial and angular position of the cobpoint, (5) the θ_{Bn} calculated by means of our procedure, and from (6) to (9) the θ_{Bn} obtained when applying SDAT.

It must be pointed out that SDAT is thought to be applied to (temporal) evolution of the plasma variables and magnetic field, while we are applying it to spatial variations (i.e., along the radial direction to the shock front). And that SDAT requires of visual inspection to determine the location of the shock as well as to select the upstream and the downstream regions; hence, the selection of the upstream and downstream points (mainly this later one) has been performed as similar as possible

[2] For the cases of the 1.0 AU-observers, when the shock is taged as "no valid", we have used the last snapshot for which the shock was still determined.

[3] The longitude of the cobpoint is given with respect to the main direction of the shock; that is, positive angles mean towards the West, while negative angles mean toward the East.

Table H.1: Comparison between the θ_{Bn} values obtained applying our procedure with those calculated using SDAT (see text).

Observer		time [h]	r_c [$R_\odot$]	φ_c [°]	θ_{Bn}-MD3 [°]	θ_{Bn}-SDAT [°]			
						AS	MC	VC	VS
0.4 AU	N37W45	0.3	5.5	29.5	87.7	88	88	88	68
		4.4	49.8	38.7	43.2	44	40	28	88
		9.4	86.0	45.0	37.7	32	32	24	64
	N22W00	0.2	4.9	-21.8	81.8	80	72	40	84
		2.6	42.4	-10.9	33.5	44	44	44	44
		5.6	86.0	0.0	15.8	20	20	20	68
	N07E30	1.0	4.7	-53.2	83.4	80	76	104	12
		3.6	31.1	-45.0	68.1	64	64	60	96
		8.5	86.0	-30.0	72.6	72	64	60	28
1.0 AU	N07W45	0.3	7.3	-12.0	36.3	60	60	28	84
		5.6	76.8	7.6	38.8	40	40	36	120
		12.3	129.9	22.0	36.1	40	36	32	88
	N22W00	1.4	11.2	-50.6	85.2	84	84	104	80
		7.0	79.9	-32.6	70.0	68	68	56	104
		15.9	215.0	0.0	35.5	36	36	36	60
	N37E30	1.0	4.3	-68.7	80.3	84	76	112	168
		7.3	59.6	-57.3	61.7	60	60	56	144
		16.4	157.6	-40.1	69.5	72	68	60	64

to that one that our automatic procedure yields. We think that this may be one of the main reasons of the discord among the different determinations of θ_{Bn}. Despite this, the values obtained by means of the AS method implemented in SDAT are in good agreement with those ones calculated with the MD3 method we implemented. The MC and VC method have limitations due to their own formulations, which may fail for quasi-perpendicular shocks (MC) or for quasi-parallel shocks (VC), for example. The disagreements with the VS method need to be studied in more detail, in order to ensure its applicability within the procedure that we have developed to determine the shock front.

Bibliography

Abraham-Shrauner, B. 1972, J. Geophys. Res., 77, 736

Abraham-Shrauner, B. & Yun, S. H. 1976, J. Geophys. Res., 81, 2097

Agueda, N., Vainio, R., Lario, D., & Sanahuja, B. 2008, ApJ, 675, 1601

Aguilar-Rodriguez, E., Blanco-Cano, X., Russell, C. T., et al. 2010, Twelfth International Solar Wind Conference, 1216, 467

Anderson, J. D. J. 1995, Computational Fluid Dynamics (McGraw-Hill International Editions)

Aran, A. 2007, PhD thesis, Universitat de Barcelona, Barcelona, Spain

Aran, A., Agueda, N., Jacobs, C., et al. 2010, American Geophysical Union, Fall Meeting, San Francisco, California, USA, Poster. Abstract num. SH33A

Aran, A., Jacobs, C., Lario, D., Sanahuja, B., & Poedts, S. 2009, Sixth European Space Weather Week, Brugges, Belgium, Poster

Aran, A., Jacobs, C., Sanahuja, B., et al. 2011, A&A (to be submitted)

Aran, A., Lario, D., Sanahuja, B., et al. 2007, A&A, 469, 1123

Aran, A., Sanahuja, B., & Lario, D. 2004, An engineering model for solar energetic particles in interplanetay space. Final Report, Tech. rep., ESA/ESTEC Contract 14098/99/NL/MM

Aran, A., Sanahuja, B., & Lario, D. 2005, Ann. Geophys., 23, 3047

Aran, A., Sanahuja, B., & Lario, D. 2006, Adv. Space Res., 37, 1240

Aran, A., Sanahuja, B., & Lario, D. 2008, Adv. Space Res., 42, 1492

Arge, C. N., Luhmann, J. G., Odstrčil, D., Schrijver, C. J., & Li, Y. 2004, Journal of Atmospheric and Solar-Terrestrial Physics, 66, 1295

Armstrong, T. P., Chen, G., Sarris, E. T., & Krimigis, S. M. 1977, in Astrophysics and Space Science Library, Vol. 71, Study of Travelling Interplanetary Phenomena, ed. M. A. Shea, D. F. Smart, & S. T. Wu, 367–388

Aschwanden, M. 2006, Pyhsics of the Solar Corona: An Introduction with Problems and Solutions, ed. Springer

Bazer, J. & Ericson, W. B. 1959, ApJ, 129, 758

Beeck, J. & Sanderson, T. R. 1989, J. Geophys. Res., 94, 8769

Berdichevsky, D. B., Szabo, A., Lepping, R. P., Viñas, A. F., & Mariani, F. 2001, J. Geophys. Res., 106, 25133

Bieber, J. W., Eroshenko, E., Evenson, P., Flückiger, E. O., & Kallenbach, R. 2000, Space Sci. Rev., 93, 1

Brackbill, J. U. & Barnes, D. C. 1980, J. Comp. Phys., 35, 426

Bryant, D. A., Cline, T. L., Desai, U. D., & McDonald, F. B. 1962, J. Geophys. Res., 67, 4983

Campeanu, A. & Schlickeiser, R. 1992, A&A, 263, 413

Cane, H. V. & Erickson, W. C. 2005, ApJ, 623, 1180

Cane, H. V., Erickson, W. C., & Prestage, N. P. 2002, J. Geophys. Res. (Space Physics), 107, 1315

Cane, H. V. & Lario, D. 2006, Space Sci. Rev., 123, 45

Cane, H. V., McGuire, R. E., & von Rosenvinge, T. T. 1986, ApJ, 301, 448

Cane, H. V., Mewaldt, R. A., Cohen, C. M. S., & von Rosenvinge, T. T. 2006, J. Geophys. Res. (Space Physics), 111

Cane, H. V., Reames, D. V., & von Rosenvinge, T. T. 1988, J. Geophys. Res., 93, 9555

Cane, H. V., Richardson, I. G., & von Rosenvinge, T. T. 2010, J. Geophys. Res. (Space Physics), 115, 8101

Cane, H. V., von Rosenvinge, T. T., Cohen, C. M. S., & Mewaldt, R. A. 2003, Geophys. Res. Lett., 30, 120000

Chané, E., Jacobs, C., van der Holst, B., Poedts, S., & Kimpe, D. 2005, A&A, 432, 331

Chané, E., Poedts, S., & van der Holst, B. 2008, A&A, 492, L29

Chané, E., van der Holst, B., Jacobs, C., Poedts, S., & Kimpe, D. 2006, A&A, 447, 727

Chao, J. K. & Hsieh, K. C. 1984, Planet. Space Sci., 32, 641

Cliver, E. W. 1996, in American Institute of Physics Conference Series, Vol. 374, American Institute of Physics Conference Series, ed. R. Ramaty, N. Mandzhavidze, & X.-M. Hua, 45–60

Cliver, E. W. & Cane, H. V. 1996, J. Geophys. Res., 101, 15533

Cliver, E. W. & Cane, H. V. 2002, EOS Transactions, 83, 61

Cliver, E. W., Kahler, S. W., & et al. 1995, in International Cosmic Ray Conference, Vol. 4, International Cosmic Ray Conference, 257

Cliver, E. W., Kahler, S. W., Shea, M. A., & Smart, D. F. 1982, ApJ, 260, 362

Cliver, E. W. & Ling, A. G. 2007, ApJ, 658, 1349

Colaninno, R. C. & Vourlidas, A. 2009, ApJ, 698, 852

Colburn, D. S. & Sonett, C. P. 1966, Space Sci. Rev., 5, 439

Courant, R., Friedrichs, K., & Lewy, H. 1967, IBM Journal (English translation of the 1928 German original), 215

Courant, R. & Friedrichs, K. O. 1948, Supersonic flow and shock waves, ed. Courant, R. & Friedrichs, K. O.

Daibog, E. I., Stolpovskii, V. G., Svertilov, S. I., et al. 2000, Adv. Space Res., 26, 871

Dayeh, M. A., Desai, M. I., Kozarev, K., et al. 2010, Space Weather, 8

De Hoffmann, F. & Teller, E. 1950, Phys. Rev., 80, 692

Desai, M. I. & Burgess, D. 2008, J. Geophys. Res., 113, A00B06

Desai, M. I., Mason, G. M., Gold, R. E., et al. 2006, ApJ, 649, 470

Domingo, V., Sanahuja, B., & Heras, A. M. 1989, Adv. Space Res., 9, 191

Evans, C. R. & Hawley, J. F. 1988, ApJ, 332, 659

Falkenberg, T. V., Vršnak, B., Taktakishvili, A., et al. 2010, Space Weather, 8, 6004

Feng, H. Q., Lin, C. C., Chao, J. K., et al. 2007, J. Geophys. Res., 112, 10104

Feynman, J. & Gabriel, S., eds. 1988, Interplanetary Particle Environment. Proceedings of a Conference

Fisk, L. A., Jokipii, J. R., Simnett, G. M., von Steiger, R., & Wenzel, K. 1998, Space Sci. Rev., 83

Forbes, T. G., Linker, J. A., Chen, J., et al. 2006, Space Science Reviews, 123, 251

Forbush, S. E. 1946, Physical Review, 70, 771

Fränz, M. & Harper, D. 2002, Planet. Space Sci., 50, 217

Gibson, S. E. & Low, B. C. 1998, ApJ, 493, 460

Goedbloed, J. P., Keppens, R., & Poedts, S. 2010, Advanced Magnetohydrodynamics: with applications to laboratory and astrophysical plasmas, ed. J. P. (Hans) Goedbloed, R. Keppens and S. Poedts (Cambridge, UK: Cambridge University Press)

Goedbloed, J. P. & Poedts, S. 2004, Principles of Magnetohydrodynamics: with applications to laboratory and astrophysical plasmas, ed. J. P. (Hans) Goedbloed, R. Keppens and S. Poedts (Cambridge, UK: Cambridge University Press)

Golightly, M., Barth, J., Bieber, J., et al. 2005, Radiation Working Group Report, Tech. rep., NASA Sun-Solar System Connection, Greenbelt, MD

Gombosi, T. I., Toth, G., Volberg, O., et al. 2004, AGU Spring Meeting Abstracts, A2

Goossens, M., ed. 2003, Astrophysics and Space Science Library, Vol. 294, An introduction to plasma astrophysics and magnetohydrodynamics

Gopalswamy, N., Lara, A., Kaiser, M. L., & Bougeret, J. 2001, J. Geophys. Res., 106, 25261

Gopalswamy, N., Yashiro, S., Michałek, G., et al. 2002, ApJ Lett., 572, L103

Gopalswamy, N., Yashiro, S., Stenborg, G., & Howard, R. A. 2003, in International Cosmic Ray Conference, Vol. 6, International Cosmic Ray Conference, 3549–3552

Gosling, J. T. 1993, J. Geophys. Res., 98, 18937

Groth, C. P. T., de Zeeuw, D. L., Gombosi, T. I., & Powell, K. G. 2000, Adv. Space Res., 26, 793

Hamilton, C. D., Mason, M. G., & McDonald, B. F. 1990, in International Cosmic Ray Conference, Vol. 5, International Cosmic Ray Conference, 237

Hamilton, D. C. 1988, in Interplanetary Particle Environment, ed. J. Feynman and S. Gabriel, 86–90

Hapgood, M. A. 1992, Planet. Space Sci., 40, 711

Hasselmann, K. & Wibberenz, G. 1970, ApJ, 162, 1049

Heras, A. M., Sanahuja, B., Lario, D., et al. 1995, ApJ, 445, 497

Heras, A. M., Sanahuja, B., Sanderson, T. R., Marsden, R. G., & Wenzel, K. 1994, J. Geophys. Res., 99, 43

Heras, A. M., Sanahuja, B., Smith, Z. K., Detman, T., & Dryer, M. 1992, ApJ, 391, 359

Hsieh, K. C. & Richter, A. K. 1986, J. Geophys. Res., 91, 4157

Hudson, H. 2010, Observations of solar and stellar eruptions, flares and jets, ed. Schrijver, C. J. and Siscoe, G. L. (Cambridge University Press), 123–158

Hudson, H. S., Bougeret, J., & Burkepile, J. 2006, Space Sci. Rev., 123, 13

Jacobs, C. 2007, PhD thesis, Katholieke Universiteit Leuven, Leuven, Belgium

Jacobs, C., Poedts, S., & van der Holst, B. 2006a, in ESA Special Publication, Vol. 617, SOHO-17. 10 Years of SOHO and Beyond

Jacobs, C., Poedts, S., & van der Holst, B. 2006b, A&A, 450, 793

Jacobs, C., Poedts, S., Van der Holst, B., & Chané, E. 2005, A&A, 430, 1099

Jacobs, C., van der Holst, B., & Poedts, S. 2007, A&A, 470, 359

Jokipii, J. R. 1966, ApJ, 146, 480

Jokipii, J. R. 1982, ApJ, 255, 716

Kahler, S. W. 1982, J. Geophys. Res., 87, 3439

Kahler, S. W. 1992, ARA&A, 30, 113

Kahler, S. W. 2001, J. Geophys. Res., 106, 20947

Kallenrode, M. 1997, J. Geophys. Res., 102, 22335

Kallenrode, M. 2001, J. Geophys. Res., 106, 24989

Kallenrode, M. 2002, J. Atmos. Terr. Phys., 64, 1973

Kallenrode, M. 2004, Space physics: an introduction to plasmas and particles in the heliosphere and magnetospheres, ed. Kallenrode, M. B. (Berlin: Springer)

Kallenrode, M., Cliver, E. W., & Wibberenz, G. 1992, ApJ, 391, 370

Kallenrode, M. & Wibberenz, G. 1997a, J. Geophys. Res., 102, 22311

Kallenrode, M. & Wibberenz, G. 1997b, J. Geophys. Res., 102, 22311

Keppens, R., Baty, H., Bergmans, J., & Casse, F. 2004, Ap&SS, 293, 217

Keppens, R., Nool, M., Tóth, G., & Goedbloed, J. P. 2003, Comput. Phys. Commun., 153, 317

Kirk, J. G., Melrose, D. B., & Priest, E. R. 1994, Plasma Astrophysics, ed. Benz, A. O. and Courvoisier, T. J.-L. (Berlin: Springer)

Kivelson, M. G. & Russell, C. T. 1995, Introduction to Space Physics, ed. Kivelson, M. G. and Russell, C. T. (Cambridge, UK: Cambridge University Press)

Klecker, B., Kunow, H., Cane, H. V., et al. 2006, Space Sci. Rev., 123, 217

Klein, K. & Posner, A. 2005, A&A, 438, 1029

Klimchuk, J. A. 2001, Space Weather (Geophysical Monograph 125), Washington: Am. Geophys. Un., 125, 143

Kocharov, L., Pizzo, V. J., Odstrčil, D., & Zwickl, R. D. 2009, J. Geophys. Res. (Space Physics), 114, 5102

Kóta, J., Manchester, W. B., & Gombosi, T. 2005, in International Cosmic Ray Conference, Vol. 1, International Cosmic Ray Conference, 125–128

Kota, J., Manchester, W. B., Jokipii, J. R., de Zeeuw, D. L., & Gombosi, T. I. 2004, in COSPAR, Plenary Meeting, Vol. 35, 35th COSPAR Scientific Assembly, 3851

Koval, A. & Szabo, A. 2008, J. Geophys. Res., 113, 10110

Kozarev, K., Schwadron, N. A., Dayeh, M. A., et al. 2010, Space Weather, 8

Kunow, H., Wibberenz, G., Green, G., Müller-Mellin, R., & Kallenrode, M. 1991, Energetic Particles in the Inner Solar System, ed. Schwenn, R. and Marsch, E., 243–342

Kunow, H., Witte, M., Wibberenz, G., et al. 1977, J. Geophys. Res., 42, 615

Lario, D. 1997, PhD thesis, Universitat de Barcelona, Barcelona, Spain

Lario, D., Aran, A., Agueda, N., & Sanahuja, B. 2007, Adv. Space Res., 40, 289

Lario, D., Aran, A., & Decker, R. B. 2008, Space Weather, 6, 12001

Lario, D. & Decker, R. B. 2001, AGU Fall Meeting Abstracts, B754

Lario, D., Decker, R. B., Ho, G. C., et al. 2005, in American Institute of Physics Conference Series, Vol. 781, The Physics of Collisionless Shocks: 4th Annual IGPP International Astrophysics Conference, ed. G. Li, G. P. Zank and C. T. Russell, 180–184

Lario, D., Kallenrode, M., Decker, R. B., et al. 2006, ApJ, 653, 1531

Lario, D., Roelof, E. C., Decker, R. B., & Reisenfeld, D. B. 2003, Adv. Space Res., 32, 579

Lario, D., Sanahuja, B., & Heras, A. M. 1997, Adv. Space Res., 20, 115

Lario, D., Sanahuja, B., & Heras, A. M. 1998, ApJ, 509, 415

Lario, D. & Simnett, G. M. 2004, in Washington DC American Geophysical Union Geophysical Monograph Series, Vol. 141, Solar Variability and its Effects on Climate, ed. J. M. Pap, P. Fox, C. Frohlich, H. S. Hudson, J. Kuhn, J. McCormack, G. North, W. Sprigg and S. T. Wu, 195

Lario, D., Vandas, M., & Sanahuja, B. 1999, in American Institute of Physics Conference Series, ed. S. R. Habbal, R. Esser, J. V. Hollweg, & P. A. Isenberg, Vol. 471, 741–744

Lee, C. O., Luhmann, J. G., Odstrčil, D., et al. 2009, Sol. Phys., 254, 155

Lee, M. A. 1982, J. Geophys. Res., 87, 5063

Lee, M. A. 1983, J. Geophys. Res., 88, 6109

Lee, M. A. 1997, in Geophysical Monograph Series, Vol. 99, Coronal Mass Ejections, ed. Crooker, N. U., Joselyn, J. A. and Feynman, J. (American Geophysical Union), 227–234

Lee, M. A. 2005, ApJS, 158, 38

Lee, M. A. & Fisk, L. A. 1982, Space Sci. Rev., 32, 205

Lepping, R. P. & Argentiero, P. D. 1971, J. Geophys. Res., 76, 4349

Leske, R. A., Mewaldt, R. A., Cohen, C. M., et al. 2008, AGU Fall Meeting Abstracts, A7

Li, G., Zank, G. P., , M. I., Mason, G. M., & Rice, W. K. M. 2005a, in Particle Acceleration in Astrophysical Plasmas: Geospace and Beyond, ed. Gallagher, D. L., Horwitz, J. L., Perez, J. D., Preece, R. D. and Quenby, J. J. (Geophysical Monograph 156 (AGU: Washington)), 51–58

Li, G., Zank, G. P., & Rice, W. K. M. 2003, J. Geophys. Res. (Space Physics), 108, 1082

Li, G., Zank, G. P., & Rice, W. K. M. 2005b, J. Geophys. Res. (Space Physics), 110, 6104

Lin, C. C., Chao, J. K., Lee, L. C., Lyu, L. H., & Wu, D. J. 2006, J. Geophys. Res., 111, 9104

Lin, C. C., Feng, H. Q., Chao, J. K., et al. 2008, J. Geophys. Res. (Space Physics), 113, 1101

Lindsay, G. M., Russell, C. T., Luhmann, J. G., & Gazis, P. 1994, J. Geophys. Res., 99, 11

Linker, J. A. & Mikić, Z. 1995, ApJ Lett., 438, L45

Linker, J. A., Mikić, Z., Biesecker, D. A., et al. 1999, J. Geophys. Res., 104, 9809

Lugaz, N., Manchester, IV, W. B., & Gombosi, T. I. 2005a, ApJ, 634, 651

Lugaz, N., Manchester, IV, W. B., & Gombosi, T. I. 2005b, ApJ, 627, 1019

Lugaz, N., Manchester, IV, W. B., Roussev, I. I., Tóth, G., & Gombosi, T. I. 2007, ApJ, 659, 788

Lugaz, N., Vourlidas, A., Roussev, I. I., & Morgan, H. 2009, Sol. Phys., 256, 269

Luhmann, J. G., Ledvina, S. A., Odstrčil, D., et al. 2010, Adv. Space Res., 46, 1

Luhmann, J. G. & Mann, A. 2007, Adv. Space Res., 39, 1882

Luhmann, J. G., Solomon, S. C., Linker, J. A., et al. 2004, Journal of Atmospheric and Solar-Terrestrial Physics, 66, 1243

Manchester, W. B., Gombosi, T. I., Roussev, I., et al. 2004a, J. Geophys. Res., 109, 1102

Manchester, W. B., Gombosi, T. I., Roussev, I., et al. 2004b, J. Geophys. Res., 109, 2107

Manchester, W. B., Ridley, A. J., Gombosi, T. I., & Dezeeuw, D. L. 2006, Advances in Space Research, 38, 253

Manchester, W. B., Vourlidas, A., Jai, Y., et al. 2008a, AGU Fall Meeting Abstracts, A7

Manchester, IV, W. B., Gombosi, T. I., De Zeeuw, D. L., et al. 2005, ApJ, 622, 1225

Manchester, IV, W. B., Vourlidas, A., Tóth, G., et al. 2008b, ApJ, 684, 1448

Mann, G., Klassen, A., Aurass, H., & Classen, H. 2003, A&A, 400, 329

Mariani, F. & Neubauer, F. M. 1990, The Interplanetary Magnetic Field, ed. Schwenn, R. and Marsch, E., 183

Mason, G. M., Mazur, J. E., & Dwyer, J. R. 1999, ApJ Lett., 525, L133

Mason, G. M., Wiedenbeck, M. E., Miller, J. A., et al. 2002, ApJ, 574, 1039

Meliani, Z., Keppens, R., & Casse, F. 2006, in SF2A-2006: Semaine de l'Astrophysique Francaise, ed. D. Barret, F. Casoli, G. Lagache, A. Lecavelier and L. Pagani, 167

Mewaldt, R. A., Cohen, C. M. S., & Mason, G. M. 2006, AGU Geophysical Monograph, 165, 115

Mikić, Z. & Lee, M. A. 2006, Space Science Reviews, 123, 57

Mikić, Z. & Linker, J. A. 1994, ApJ, 430, 898

Mikić, Z., Linker, J. A., Schnack, D. D., Lionello, R., & Tarditi, A. 1999, Physics of Plasmas, 6, 2217

Miller, J. A. & Viñas, A. F. 1993, ApJ, 412, 386

NASA/TM-2006-214137. 2006, Solar Sentinels: Report of the Science and Technology Definition Team, Tech. rep., Goddard Space Flight CEnter

Ng, C. K. 2007, in American Institute of Physics Conference Series, Vol. 932, Turbulence and Nonlinear Processes in Astrophysical Plasmas, ed. D. Shaikh and G. P. Zank, 271–276

Ng, C. K., Reames, D. V., & Tylka, A. J. 1999, Geophys. Res. Lett., 26, 2145

Ng, C. K., Reames, D. V., & Tylka, A. J. 2001, in International Cosmic Ray Conference, Vol. 8, International Cosmic Ray Conference, 3140–3143

Ng, C. K., Reames, D. V., & Tylka, A. J. 2003, ApJ, 591, 461

Ng, C. K. & Wong, K. 1979, in International Cosmic Ray Conference, Vol. 5, International Cosmic Ray Conference, 252–257

Nolte, J. T. & Roelof, E. C. 1973, Sol. Phys., 33, 241

Odstrčil, D., Pizzo, V. J., Linker, J. A., et al. 2004, Journal of Atmospheric and Solar-Terrestrial Physics, 66, 1311

Odstrčil, D. 2003, Adv. Space Res., 32, 497

Odstrčil, D., Linker, J. A., Lionello, R., et al. 2002a, in ESA Special Publication, Vol. 506, Solar Variability: From Core to Outer Frontiers, ed. A. Wilson, 95–98

Odstrčil, D., Linker, J. A., Lionello, R., et al. 2002b, J. Geophys. Res. (Space Physics), 107, 1493

Odstrčil, D. & Pizzo, V. J. 1999, J. Geophys. Res., 104, 483

Odstrčil, D., Pizzo, V. J., & Arge, C. N. 2005, J. Geophys. Res. (Space Physics), 110, 2106

Odstrčil, D., Riley, P., & Zhao, X. P. 2004, J. Geophys. Res. (Space Physics), 109, 2116

Parker, E. N. 1958, ApJ, 128, 664

Parker, E. N. 1965, Planet. Space Sci., 13, 9

Poedts, S. & Arge, C.-N. 2007, in Commission 49: Interplanetary Plasma and Heliosphere, Reports on Astronomy 2002-2005, ed. Engvold, O., 116–120

Powell, K. G., Roe, P. L., Linde, T. J., Gombosi, T. I., & de Zeeuw, D. L. 1999, J. Comp. Phys., 154, 284

Prölss, G. W. & Bird, M. K. 2004, Physics of the Earth's Space Environment: an introduction, ed. Prölss, G. W. and Bird, M. K. (Springer-Verlag Berlin Heidelberg)

Reames, D. V. 1990, ApJ Lett., 358, L63

Reames, D. V. 1999, Space Science Reviews, 90, 413

Reames, D. V. 2000, in American Institute of Physics Conference Series, Vol. 516, 26th International Cosmic Ray Conference, ICRC XXVI, ed. B. L. Dingus, D. B. Kieda and M. H. Salamon, 289–300

Reames, D. V., Barbier, L. M., & Ng, C. K. 1996, ApJ, 466, 473

Reames, D. V., Kahler, S. W., & Ng, C. K. 1997, ApJ, 491, 414

Reid, G. C. 1964, J. Geophys. Res., 69, 2659

Reinard, A. A. & Andrews, M. A. 2006, Adv. Space Res., 38, 480

Rice, W. K. M. & Zank, G. P. 2003, Adv. Space Res., 31, 901

Rice, W. K. M., Zank, G. P., & Li, G. 2003, J. Geophys. Res. (Space Physics), 108, 1369

Richardson, I. G. 1985, Planet. Space Sci., 33, 557

Richardson, I. G., Cane, H. V., & von Rosenvinge, T. T. 1991, J. Geophys. Res., 96, 7853

Richter, A. K., Hsieh, K. C., Luttrell, A. H., Marsch, E., & Schwenn, R. 1985, Washington DC American Geophysical Union Geophysical Monograph Series, 35, 33

Riley, P., Linker, J. A., & Mikić, Z. 2001, J. Geophys. Res., 106, 15889

Riley, P., Linker, J. A., Mikić, Z., et al. 2003, J. Geophys. Res. (Space Physics), 108, 1272

Rodriguez, L., Zhukov, A. N., Cid, C., et al. 2009, Space Weather, 7, S06003

Rodríguez-Gasén, R., Aran, A., Sanahuja, B., Jacobs, C., & Poedts, S. 2011, Adv. Space Res., in press

Roelof, E. C. 1969, in Lectures in High-Energy Astrophysics, ed. H. Ögelman & J. R. Wayland, 111

Roth, I. & Temerin, M. 1997, ApJ, 477, 940

Roussev, I. I., Forbes, T. G., Gombosi, T. I., et al. 2003a, ApJ Lett., 588, L45

Roussev, I. I., Gombosi, T. I., Sokolov, I. V., et al. 2003b, ApJ Lett., 595, L57

Roussev, I. I. & Sokolov, I. V. 2006, Washington DC American Geophysical Union Geophysical Monograph Series, 165, 89

Roussev, I. I., Sokolov, I. V., Forbes, T. G., et al. 2004, ApJ Lett., 605, L73

Ruffolo, D. 1995, ApJ, 442, 861

Ruffolo, D. 2002, Adv. Space Res., 30, 45

Russell, C. T. 1988, Adv. Space Res., 8, 147

Russell, C. T., Jian, L. K., Blanco-Cano, X., & Luhmann, J. G. 2009, Geophys. Res. Lett., 36, 3106

Sanahuja, B. & Domingo, V. 1987, J. Geophys. Res., 92, 7280

Sanahuja, B., Domingo, V., Wenzel, K., Joselyn, J. A., & Keppler, E. 1983, Sol. Phys., 84, 321

Sanahuja, B. & Lario, D. 1998, in in 19th European Cosmic Ray Symposium (Acalá University Editions, 129–139

Sandberg, I., Daglis, I. A., Anastasiadis, A., et al. 2010, in Astronomical Society of the Pacific Conference Series, Vol. 424, 9th International Conference of the Hellenic Astronomical Society, ed. K. Tsinganos, D. Hatzidimitriou and T. Matsakos, 43–46

Sanderson, T. R., Reinhard, R., van Nes, P., & Wenzel, K. P. 1985, J. Geophys. Res., 90, 19

Schwadron, N. A., Townsend, L., Kozarev, K., et al. 2010, Space Weather, 8

Severe Space Weather Events–Understanding Societal and Economic Impacts: A Workshop Report. 2008, Tech. rep., Committee On The Societal & Economic Impacts Of Severe Space Weather Events. The National Research Council of the National Academies. US National Academy of Sciences, National Academy Press. ISBN: 978-0-309-12769-1

Shea, M. A. & Smart, D. F. 1990, Sol. Phys., 127, 297

Shen, F., Feng, X., Wu, S. T., & Xiang, C. 2007, J. Geophys. Res. (Space Physics), 112, 6109

Shen, F., Feng, X., Xiang, C., & Song, W. 2010, Journal of Atmospheric and Solar-Terrestrial Physics, 72, 1008

Smith, Z. & Dryer, M. 1990, Sol. Phys., 129, 387

Soenen, A., Zuccarello, F. P., Jacobs, C., et al. 2009, A&A, 501, 1123

Sokolov, I., Roussev, I., & Liu, Y. 2006a, AGU Fall Meeting Abstracts, A5

Sokolov, I. V., Roussev, I. I., Fisk, L. A., et al. 2006b, ApJ Lett., 642, L81

Sokolov, I. V., Roussev, I. I., Gombosi, T. I., et al. 2004, ApJ Lett., 616, L171

Sokolov, I. V., Roussev, I. I., Skender, M., Gombosi, T. I., & Usmanov, A. V. 2009, ApJ, 696, 261

Space Radiation Hazards and the Vision for Space Exploration: Report of a Workshop. 2006, Tech. rep., The National Research Council of the National Academies. US National Academy of Sciences, National Academy Press. ISBN: 0-309-66291-5

St. Cyr, O. C., Howard, R. A., Simnett, G. M., et al. 1997, in ESA Special Publication, Vol. 415, Correlated Phenomena at the Sun, in the Heliosphere and in Geospace, ed. A. Wilson, 103–110

Szabo, A. 1994, J. Geophys. Res., 99, 14737

Tan, L. C., Mason, G. M., Lee, M. A., Klecker, B., & Ipavich, F. M. 1992, J. Geophys. Res., 97, 1597

Temmer, M., Veronig, A. M., Gopalswamy, N., & Yashiro, S. 2011, Solar Physics (accepted)

Torsti, J., Kocharov, L. G., Vainio, R., Anttila, A., & Kovaltsov, G. A. 1996, Sol. Phys., 166, 135

Tóth, G. 1996, Astrophys. Lett. Commun., 34, 245

Tóth, G. 1997, J. Comp. Phys., 138, 981

Tóth, G., Sokolov, I. V., Gombosi, T. I., et al. 2005, J. Geophys. Res. (Space Physics), 110, 12226

Totten, T. L., Freeman, J. W., & Arya, S. 1995, J. Geophys. Res., 100, 13

Tsurutani, B., Wu, S. T., Zhang, T. X., & Dryer, M. 2003, A&A, 412, 293

Tsurutani, B. T. & Lin, R. P. 1985, J. Geophys. Res., 90, 1

Tsurutani, B. T., Smith, E. J., & Jones, D. E. 1983, J. Geophys. Res., 88, 5645

Tylka, A. J., Boberg, P. R., McGuire, R. E., Ng, C. K., & Reames, D. V. 2000, in American Institute of Physics Conference Series, Vol. 528, Acceleration and Transport of Energetic Particles Observed in the Heliosphere, ed. R. A. Mewaldt, J. R. Jokipii, M. A. Lee, E. Möbius and T. H. Zurbuchen, 147–152

Tylka, A. J., Cohen, C. M. S., Dietrich, W. F., et al. 2005, ApJ, 625, 474

Tylka, A. J. & Lee, M. A. 2006, ApJ, 646, 1319

Vainio, R., Agueda, N., Aran, A., & Lario, D. 2007, in Astrophysics and Space Science Library, Vol. 344, Space Weather: Research Towards Applications in Europe 2nd European Space Weather Week (ESWW2), ed. J. Lilensten, 27

Vainio, R., Desorgher, L., Heynderickx, D., et al. 2009, Space Science Reviews, 147, 187

Vainio, R. & Laitinen, T. 2007, ApJ, 658, 622

Vainio, R. & Schlickeiser, R. 1999, A&A, 343, 303

van Nes, P., Reinhard, R., Sanderson, T. R., Wenzel, K., & Zwickl, R. D. 1984, J. Geophys. Res., 89, 2122

Vandas, M., Odstrčil, D., & Watari, S. 2002, J. Geophys. Res. (Space Physics), 107, 1236

Verkhoglyadova, O. P., Li, G., Zank, G. P., et al. 2010, J. Geophys. Res., 115, 12103

Verkhoglyadova, O. P., Li, G., Zank, G. P., Hu, Q., & Mewaldt, R. A. 2009, ApJ, 693, 894

Viñas, A. F. & Holland, M. P. 2005, AGU Spring Meeting Abstracts, B10

Viñas, A. F. & Scudder, J. D. 1986, J. Geophys. Res., 91, 39

Volkmer, P. M. & Neugebauer, F. M. 1985, Ann. Geophys., 3, 1

von Rosenvinge, T. T., Cohen, C. M. S., Christian, E. R., et al. 2001, in American Institute of Physics Conference Series, Vol. 598, Joint SOHO/ACE workshop "Solar and Galactic Composition", ed. R. F. Wimmer-Schweingruber, 343–348

Vourlidas, A., Buzasi, D., Howard, R. A., & Esfandiari, E. 2002, in ESA Special Publication, Vol. 506, Solar Variability: From Core to Outer Frontiers, ed. Kuijpers, J., 91–94

Vourlidas, A., Wu, S. T., Wang, A. H., Subramanian, P., & Howard, R. A. 2003, ApJ, 598, 1392

Wang, Y. & Sheeley, Jr., N. R. 1990, ApJ, 355, 726

Watermann, J., Wintoft, P., Sanahuja, B., et al. 2009, Space Science Reviews, 147, 233

Weber, E. J. & Davis, Jr., L. 1967, ApJ, 148, 217

Wei, F., Feng, X., Cai, H., & Zhou, Q. 2003, J. Geophys. Res. (Space Physics), 108, 1238

Williamson, S. P., Babcock, M. R., & Bonadonna, M. F. 2010, Space Weather, 8, 12001

Wu, C., Feng, X. S., Wu, S. T., Dryer, M., & Fry, C. D. 2006, J. Geophys. Res. (Space Physics), 111, 12104

Wu, C., Wu, S. T., & Dryer, M. 1996a, Annales de Geophysique, 14, 375

Wu, C., Wu, S. T., Dryer, M., et al. 2005a, J. Geophys. Res. (Space Physics), 110

Wu, C. C., Chao, J. K., Wu, S. T., & Dryer, M. 1996b, Sol. Phys., 165, 377

Wu, S. T., Dryer, M., & Han, S. M. 1983, Sol. Phys., 84, 395

Wu, S. T., Li, B., Wang, S., & Zheng, H. 2005b, J. Geophys. Res. (Space Physics), 110, 11102

Xapsos, M. A., Barth, J. L., Stassinopoulos, E. G., et al. 2000, IEEE Transactions on Nuclear Science, 47, 2218

Zank, G. P., Li, G., Florinski, V., et al. 2004, J. Geophys. Res. (Space Physics), 109, 4107

Zank, G. P., Rice, W. K. M., & Wu, C. C. 2000, J. Geophys. Res., 105, 25079

Zhao, X. P., Plunkett, S. P., & Liu, W. 2002, J. Geophys. Res. (Space Physics), 107, 1223

Zuccarello, F. P., Jacobs, C., Soenen, A., et al. 2009, A&A, 507, 441